Compatibiliteit van ADS kandidaat-materialen
met vloeibaar metaal in een neutronenstralingsomgeving

ADS Candidate Materials Compatibility
with Liquid Metal in a Neutron Irradiation Environment

Joris Van den Bosch

Promotoren: prof. dr. ir. J. Degrieck, dr. A. Al Mazouzi
Proefschrift ingediend tot het behalen van de graad van
Doctor in de Ingenieurswetenschappen: Materiaalkunde

Vakgroep Toegepaste Materiaalwetenschappen
Voorzitter: prof. dr. ir. Y. Houbaert
Faculteit Ingenieurswetenschappen
Academiejaar 2008 - 2009

UNIVERSITEIT
GENT

ISBN 978-90-8578-241-4
NUR 971
Wettelijk depot: D/2008/10.500/61

Dit onderzoek werd uitgevoerd bij de onderzoeksinstelling
This research was performed at

SCK•CEN
Institute for Nuclear Materials Science
LHMA
Boeretang 200
B-2400 MOL

In samenwerking met
In collaboration with

Universiteit Gent
Vakgroep Toegepaste Materiaalwetenschappen
Faculteit Toegepaste Wetenschappen
Sint-Pietersnieuwstraat 41
B-9000 Gent

Examencommissie
Examining Board

Prof. dr. ir. R. Verhoeven, voorzitter
UGent, onderwijsdirecteur FirW

Prof. dr. ir. G. Van Oost, secretaris
UGent, vakgroep Toegepaste Fysica

Dr. A. Al Mazouzi, promotor
SCK•CEN, Institute for Nuclear Materials Science

Prof. dr. ir. J. Degrieck, promotor
UGent, vakgroep Toegepaste Materiaalwetenschappen

Prof. dr. H. Aït Abderrahim
UCL, EPL / SCK•CEN, Institute for Advanced Nuclear Systems

Prof. dr. ir Y. Houbaert
UGent, vakgroep Toegepaste Materiaalwetenschappen

Dr. ir. C. Latgé
CEA, Département de Technologie Nucléaire

Dr. ir. S.A. Maloy
LANL, Core materials and transmutation fuel group

TABLE OF CONTENT

PREFACE

I've learned that people will forget what you said, people will forget what you did,
but people will never forget how you made them feel.
Maya Angelou
(1928-…)

Good friends don't let you do stupid things……. Alone.
Anonymous

The experience of making a PhD at SCK•CEN has thought me a great deal. Of course the PhD work itself was very interesting and rewarding and I have to acknowledge that I was very lucky to have an exciting experimental materials science subject in the frame of future reactor systems. However, the past four years comprised of much, much more.

Thinking back, I need to mention changing promoters at UGent, changing departments even; unsubstantiated media circus about irradiation exposure at SCK•CEN; unfortunate decease of Paul Goovaerts; changing general management at SCK•CEN; discovery of a very bad financial position of the Institute combined with social uprising, strikes,…; restructuring of SCK•CEN; assassination of Litvinenko using Po^{210}; renovation of my office; re-opening of the debate on nuclear energy in Belgium; elections linked to possible large influence of the nuclear sector; government crisis; Luc Bens having a car accident; SCK•CEN's open days and finally the application for group leader of the structural materials expert group…
On the personal level, the last four years were almost as turbulent: I quit chiro after 20 years, Eveline and I bought a house, our first cat drowned in our inflatable swimming pool, both my grandfathers past away, my sister got married, my parents got divorced and our band Pikeys found the road to (local) success.

So, in a very dynamic, changing background, I had to realize, within the term of my PhD, a very ambitious project. This included a first of a kind irradiation experiment, building and licensing a new hot cell test set-up and managing to have a valuable scientific contribution to the knowledge of a strange phenomenon at the end of the ride.

Of course, this PhD could never have been anywhere near what it has become without the support of, cooperation and interaction with many, many people.

Therefore, in general, I would like to thank the management of SCK•CEN: Prof. Dr. Eric van Walle, Prof. Dr. Hamid Ait Abderrahim, Dr. Leo Sannen and Dr. Ir. Steven Van Dyck, for supporting the work where needed and for listening when I had something to say.
I absolutely need to thank my mentor/co-promoter Dr. Abderrahim Almazouzi (Abdou) for believing in me since day one, for introducing me to people, for pushing me, for supporting me, for trying to teach me patience, science,…..
In short: for being a good mentor.
Despite the sharp discussions and disagreements we sometimes had, I really liked working with you, Abdou.

Furthermore, I need to thank Prof. Dr. Ir. Joris Degrieck, my promoter at Ghent University, for the suggestions and ideas he gave me and for all his support at Ghent University. Despite my physical absence at the faculty in Ghent, Joris was always there when needed and I really appreciate this.

Actually, I should thank everyone at SCK•CEN and in the EUROTRANS-DEMETRA community that I got to know, since all of you played a part in the growth to who I am now. It would however not be correct not to mention a few persons by name since I absolutely couldn't have completed the work without them. Nancy Van der Borgt for practical matters of every day, Roger Mertens for the mechanical work and sample manufacturing, Philippe Benoit for his work on Twin Astir, Rik-Wouter Bosch, Ludo Eysermans and Luc Bens for the wonderful cooperation to complete cell 12, Serguei Gavrilov and Rafaël Fernandez for the fruitful discussions, Willy Claes for the operations regarding the irradiation in BR2 and for his help in getting cell 12 licensed and all people who made a contribution to the Astir irradiation.

Moreover, I need to thank my friends with whom I happily shared the office: Milena Matijasevic, Marlies Lambrecht, Xiaoqiang Li and Katelijne Verhiest. I honestly never came to our office with a bad feeling thanks to all of you.
Also special thanks to Marc, Johan, Enrico, Jean-Louis, Inge, Antonio, Paul, Roel, Jan and Leo for bringing life and color into every day. Mec-test sure had all the elements for a good reality soap.
Thanks to Sven, Ann, Wouter and Ben for the support in microstructural related work and for the interesting discussions at lunch.
Last but certainly not least, thanks to my friends Dani, Dmitry, Genaro and Giovanni for all the moments we will remember for the rest of our lives.

I also want to make use of this preface to have a look at the future and use the opportunity to wish my successor, Gunter, lots of success and courage in all his endeavors at SCK•CEN. I enjoyed working with Gunter as his graduation thesis mentor and therefore I'm very confident that I will enjoy working with him as a colleague and friend.

Of course, I should also thank my parents for my open and independent education, for giving me every opportunity to grow as a person, to learn from my mistakes and those of others and to discover the world with respect and responsibility for my surroundings.
Finally, thanks to Eveline for her patience and support when I locked myself in my office at home to write this PhD thesis and for always being herself.

Joris Van den Bosch
September, 2008

SAMENVATTING

Lood bismut eutecticum werd geselecteerd als koelmiddel en spallatie doelwit materiaal voor de toekomstige experimentele accelerator gedreven reactor, MYRRHA, beter bekend als een Accelerator Driven System (ADS). Dit nieuwe concept van reactor type zou wel eens één van de mogelijke oplossingen voor het kernafvalprobleem kunnen bieden, aangezien dit type reactor bedacht is om hoog radioactief afval en lang levende actinides te transmuteren.

De ADS technologie vereist echter veeleisende operationele condities. De structuurmaterialen moeten bestand zijn tegen temperaturen tussen 200 en 550°C en dit in contact met het vloeibare lood bismut eutecticum (LBE) en onder intense neutronen straling. Het contact met het vloeibaar metaal veroorzaakt niet enkel vloeibaar metaal corrosie maar kan eventueel ook leiden tot vloeibaar metaal verbrossing (liquid metal embrittlement of LME).

Daarom was de eerste doelstelling van deze doctoraatsthesis dan ook de karakterisatie van eventuele vloeibaar metaal verbrossing van T91, 316L en hun lassen in contact met vloeibaar lood bismut eutecticum. Daarenboven werden verscheidene experimentele staalsoorten onderzocht op vloeibaar metaal verbrossing. Deze experimentele stalen hadden allen een verhoogde concentratie silicium aangezien reeds aangetoond werd dat de toevoeging van silicium de corrosie weerstand in vloeibaar lood bismut eutecticum verhoogt.

Er werden trektesten en breuktaaiheidstesten uitgevoerd op de materialen in hun standaard toestand in de Limets 1 installatie, welke een goede controle toelaat van de vloeibaar metaal chemie (voornamelijk de zuurstofconcentratie) en de temperatuur.

De belangrijkste resultaten kunnen als volgt samengevat worden:

- 316L roestvast staal is niet vatbaar voor vloeibaar metaal verbrossing in de geteste omstandigheden;
- T91 staal lijdt aan vloeibaar metaal verbrossing onder bepaalde omstandigheden zoals bv. in geval van verhoogde hardheid door thermische behandeling en in aanwezigheid van spanningsconcentraties aan de oppervlakte door kerven of scheurtjes. Ondanks de vatbaarheid voor vloeibaar metaal verbrossing onder bepaalde omstandigheden, blijft de verbrossing van T91 staal eerder beperkt. De vloeigrens en treksterkte blijven ongewijzigd maar de totale verlenging neemt af in contact met vloeibaar LBE. Voorlopige breuktaaiheidstesten op

200 en 300°C hebben aangetoond dat de breuktaaiheid van T91 staal met maximaal 30% afneemt in contact met vloeibaar lood bismut eutecticum;

- De TIG en EB lassen van T91 met T91 en T91 met 316L verbrossen sterker in contact met vloeibaar LBE in vergelijking met hun respectieve basis materialen. De zone van de las die de hoogste hardheid heeft na warmtebehandeling (post weld heat treatment, PWHT) blijkt sterker vatbaar voor vloeibaar metaal verbrossing en dit voor alle bestudeerde lasverbindingen. In het geval van de T91 met T91 TIG en EB lassen evenals in het geval van de T91 met 316L EB las verbrost de zone waar het metaal gesmolten was het sterkst in contact met LBE. Voor de T91 met 316L TIG las daarentegen, verbrost de verbindingszone tussen het T91 basis materiaal en de 309 bebotering.
- De ferritische/martensitische/bainitische hoog silicium stalen worden zeer sterk verbrost onder alle onderzochte condities in contact met vloeibaar LBE op 350°C. Analyse van de breukvlakken toonde volledig brosse splijtbreuk wat erop wijst dat het vloeibaar metaal verbrossing model van Stoloff, Johnson, Westwood en Kamdar (SJWK model) het meest waarschijnlijke model is voor dit geval;
- Het SJWK model, ook bekend als het "absorptie geïnduceerde reductie in cohesie model" verklaart vloeibaar metaal verbrossing als zijnde een reductie van de interatomaire bindingsterkte van de atomen aan de scheurtip van het vaste metaal door de aanwezigheid van de vloeibaar metaal atomen. Dit model is consistent met de experimentele waarnemingen van de invloed van metallurgische parameters zoals temperatuur, korrelgrootte, vervormingsnelheid, etc. op vloeibaar metaal verbrossing.

Het tweede deel van deze thesis behandelt het concept, de realisatie en bestraling van een experiment waarbij de referentie materialen evenals hun las verbindingen en enkele specifieke legeringen (aangereikt Si staal) in contact waren met vloeibaar LBE. Het doel van dit experiment, het eerste in zijn soort wereldwijd, was het bestuderen van het afzonderlijke evenals het gecombineerde effect van neutronen bestraling en contact met vloeibaar LBE. De gerelateerde problemen op vlak van veiligheid, controle en werking van dit experiment werden aangepakt op een gecoördineerde manier met samenwerkingen tussen verschillende departementen en instituten zowel binnen als buiten het Belgische Studiecentrum voor Kernenergie waar dit werk werd verricht. Deze eerste bestralingscampagne maakte duidelijk dat het alles behalve een sinecure is om te werken met bestraald LBE.

Het bestralingsexperiment dat de naam Twin Astir meekreeg (dit staat voor ADS Steel T91 Irradiation tot 2 verschillende bestralingsdoses – vandaar Twin), ontving zijn eerste neutronen bestraling tijdens de tweede reactorcyclus van de Belgische BR2 reactor in april 2006. De kennis en expertise die werd opgebouwd in het MEGAPIE iniatief (MEGAPIE werd bestraald met de eerste protonen bundel slechts enkele maanden na Twin Astir) was hierbij van groot belang en droeg ongetwijfeld bij tot de realisatie en het vergunnen van Twin Astir.

Het Twin Astir experiment had tot doel om de meest invloedrijke parameters van vloeibaar metaal corrosie en/of vloeibaar metaal verbrossing in LBE op 350°C te onderscheiden en te kwantificeren en daarenboven te onderzoeken of er mogelijke synergiën optreden tussen deze parameters. Na bestraling bleek echter dat de opwarming van het lood bismuth eutecticum door gamma straling onderschat was. Dit effect bleek een onverwachte temperatuurstijging veroorzaakt te hebben en herbepaling van de temperatuur resulteerde in een effectieve bestralingstemperatuur van 460-490°C (voor de capsule bestudeerd in dit werk) ten opzichte van de oorspronkelijk geplande 350°C. Op deze verhoogde temperaturen treedt echter voornamelijk in het referentie staal T91 geen stralingsverharding op.
Desalnietemin werd de eerste lading proefstukken afkomstig van dit experiment succesvol ontmanteld en getest onder gecontroleerde omstandigheden in een hot cell die in de loop van deze thesis volledig ontworpen en uitgewerkt werd speciaal voor deze toepassing.

De meest voorname resultaten van dit bestralingsexperiment kunnen als volgt opgesomd worden:

- 316L roestvast staal is niet onderhevig aan vloeibaar metaal verbrossing onder de geteste omstandigheden. De treksterkte daalde met ongeveer 50 MPa na neutronen bestraling op 460-490°C terwijl de vloeigrens onveranderd bleef. Op 200°C vertonen de trekcurves van 316L bestraald op 460-490°C een aanzienlijke hoeveelheid ververvormingsversteviging wat in schril contrast staat met de materiaaleigenschappen van 316L staal bestraald op 200°C tot vergelijkbare dosissen en getest op 200°C.
- T91 staal was verzacht door de neutronen bestraling tot 1.5 dpa op 460-490°C waarbij de vloeigrens en de treksterkte met 50 tot 100 MPa daalden op 350°C. De bestraalde T91 was vatbaar voor vloeibaar metaal verbrossing bij een vervormingsnelheid van 1.10^{-6} s^{-1} wat resulteerde in een verlaging van de totale verlenging met ongeveer 50%. De vloeigrens en treksterkte bleven ongewijzigd door de vloeibaar metaal omgeving. Bij een vervormingsnelheid van 1.10^{-3} s^{-1} werd geen vloeibaar metaal verbrossing opgemerkt. Op 450°C (± bestralingstemperatuur) werd geen vloeibaar metaal verbrossing opgemerkt.

- TIG en EB lassen van T91 met T91 en T91 met 316L bleken allen vatbaar voor vloeibaar metaal verbrossing op 350°C onder de geteste omstandigheden. De ductiliteit van de T91/T91 TIG las na bestraling op 460-490°C was vergelijkbaar met deze van de T91/T91 TIG las die blootgesteld werd aan schommelende temperaturen in contact met vloeibaar LBE. De T91/T91 EB las leed daarentegen sterker aan vloeibaar metaal verbrossing na bestraling tot 1.5 dpa op 460-490°C wat zich vertaalde in een daling van zijn totale verlenging met ongeveer 3%. De T91/316L TIG las was minder verbrost in contact met LBE na bestraling op 460-490°C dan voor bestraling. Dit effect is te wijten aan de temperende werking van de bestraling op hoge temperatuur. Anderzijds, leed de T91/316L EB las sterker aan vloeibaar metaal verbrossing na bestraling waarbij amper enige ductiliteit overbleef.
- Alle bestudeerde hoog Si stalen ondergingen stralingsverharding na neutronen bestraling tot 1.5 dpa op 460-490°C en bleken zeer vatbaar voor vloeibaar metaal verbrossing. Voor alle vier de hoog Si stalen werd de totale verlenging verder gereduceerd waarbij ze braken op de vloeigrens of in het geval van het 2441 staal zelfs in het elastische gebied. De austenitische 2442 variant behield het meeste ductiliteit na bestraling van de bestudeerde hoog Si stalen maar zijn totale verlenging werd toch ook zeer sterk gereduceerd.

Gebaseerd op de trektesten van de bestraalde materialen kan gesteld worden dat de neutronen bestraling op 460-490°C in contact met laag zuurstof houdend vloeibaar LBE de kans op voorkomen van vloeibaar metaal verbrossing verhoogt ondanks het uitblijven van stralingsverharding. Dit fenomeen is vermoedelijk te wijten aan een thermisch corrosie effect op 460-490°C waarbij de oxidelaag opgelost wordt en goed contact bekomen wordt tussen het vaste metaal en het verbrossende vloeibaar metaal. Op dit ogenblik is het echter onduidelijk of neutronen bestraling de thermische corrosie in contact met LBE versterkt. Omwille van veiligheidsmaatregels en vergunningen was het tot zover niet mogelijk om oppervlakte interacties of breukvlakken van bestraald materiaal te bestuderen.

SUMMARY

Lead bismuth eutectic is selected to be both coolant and spallation target material for the future experimental accelerator driven system (MYRRHA). This new concept of reactor type might be one of the possible solutions for the nuclear waste problem as it is conceived to be able to burn up high level radioactive waste and long lived actinides.

The ADS technology however requires special operating conditions. The materials need to withstand temperatures ranging between 200° and 550°C under high neutron flux and in contact with the liquid lead bismuth eutectic (LBE). This liquid metal contact does not only result in liquid metal corrosion but might also facilitate liquid metal embrittlement (LME).
Therefore, the first goal of this PhD thesis was to characterize possible liquid metal embrittlement of T91, 316L and their welds in contact with liquid lead bismuth eutectic. Furthermore, several experimental steels which contain an elevated concentration of silicon to increase their corrosion resistance in LBE were examined for possible liquid metal embrittlement as well.

Tensile and fracture toughness tests of as received materials were performed in the Limets I facility where both the testing temperature as well as the chemistry of LBE, especially the oxygen content, can be controlled quite precisely.

The main results can be summarized as follows:

- 316L stainless steel is not prone to liquid metal embrittlement in LBE under the tested conditions;
- T91 steel does suffer from LME under certain conditions such as increased hardness by thermal treatment and the presence of surface stress concentrators or cracks. Despite the occurrence of LME under certain conditions, the embrittlement of T91 steel in liquid LBE is rather limited. The yield strength and ultimate tensile strength remain the same while the total elongation is decreased in liquid metal environment. Preliminary fracture toughness results at 200 and 300°C indicate a maximum reduction in fracture toughness by about 30% when tested in oxygen saturated liquid LBE;
- TIG and EB welds of T91 to T91 and T91 to 316L steel are more severely embrittled than the respective base materials. The area of the weld having the highest hardness after PWHT is prone to LME for all investigated welds. For the T91 to T91 TIG and EB welds as well as for the T91 to 316L EB weld, the fusion zone is embrittled by the LBE while for the T91 to 316L TIG weld, the

fusion zone between the T91 and the 309 buttering material is severely embrittled.

- The ferritic/martensitic/bainitic silicon enriched steels are very strongly embrittled when tested in liquid LBE at 350°C under all investigated conditions. Fracture surface analysis revealed fully brittle cleavage type failure which indicates that the model proposed by Stoloff, Johnson, Westwood and Kamdar (SJWK model) for liquid metal embrittlement is the most probable for this specific case;
- The SJWK LME model, also known as the "adsorption induced reduction in cohesion model" explains LME by a reduction of the interatomic bond strength between the atoms at the crack tip of the solid due to the presence of the liquid metal atoms. The model is consistent with observations made on the metallurgical parameters influencing LME such as temperature, grain size, strain rate, etc.

The second part of this thesis deals with the conception, construction and the irradiation of a set-up where the reference materials as well as their welds and some specific alloys (Si-enriched steels) were in contact with LBE.
The goal of this experiment, the first of its kind worldwide, was to study the separate and the combined effect of neutron irradiation and contact with liquid LBE. The issues related to the safety and the control of such experiment were tackled in a coordinated way between different departments and institutes inside and outside the Belgian nuclear research centre where this work has been performed. This first irradiation campaign made it clear that dealing with irradiated LBE is not an easy issue.

The irradiation experiment called Twin Astir, which stands for ADS Steel T91 Irradiation up to two doses (hence Twin) started receiving neutron irradiation during the second cycle, 2006 of BR2 in April 2006. The knowledge and expertise that was built up in the MEGAPIE initiative, which received its first proton beam on target only a few months later, was of great importance and facilitated the licensing and realisation of Twin Astir.

The Twin Astir experiment had the purpose to distinguish and quantify the most important influencing parameters on the liquid metal corrosion and/or embrittlement in LBE at 350°C and to examine possible synergistic effects of these parameters. However, it appeared post mortem that the gamma heating due to the presence of LBE (even in very low quantity) was under-estimated. It turns out that this effect induced an unexpected temperature enhancement and thus the actual irradiation temperature was reassessed to be about 460 - 490°C (for the capsule investigated in

this work) instead of the planned 350°C. At this elevated temperature, no radiation induced hardening occurs in the reference materials T91 and 316L.
Nevertheless, the first batch of the materials issued from this irradiation experiment, has been successfully dismantled and tested in controlled conditions inside a hot-cell which was totally conceived and equipped for this purpose during the accomplishment of this thesis.

The main results of the irradiation experiment can be summarized as follows:

- 316L stainless steel did not undergo any LME under the investigated conditions. The
  ultimate tensile strength was decreased by about 50 MPa due to neutron irradiation at 460-490°C while the yield strength remained unchanged. Significant work hardening was present in sharp contrast with 316L steel irradiated at 200°C up to similar doses;
- T91 steel was softened by neutron irradiation up to 1.5 dpa at 460-490°C resulting in a decrease of the yield strength and ultimate tensile strength by 50-100 MPa at 350°C. The irradiated T91 steel was prone to LME at a strain rate of 1.10^{-6} s^{-1}, showing a decrease in total elongation by about 50%. Yield strength and ultimate tensile strength were unaffected by the liquid metal environment. At a strain rate of 1.10^{-3} s^{-1} no LME was observed. At 450°C (± irradiation temperature) no LME was observed neither.
- TIG and EB welds of T91 to T91 and T91 to 316L were all prone to LME at 350°C under the tested conditions. The ductility of the T91 to T91 TIG weld after irradiation at 460-490°C was similar to that measured for the T91/T91 TIG weld pre-exposed under cycling temperature conditions. The T91/T91 EB weld however did suffer from an increased LME effect after neutron irradiation up to 1.5 dpa resulting in a further decrease of its total elongation by about 3%. The T91/316L TIG weld was less embrittled by the LBE after neutron irradiation at 460-490°C than before irradiation. This was attributed to the tempering effect of the high temperature irradiation. On the other hand, the T91/316L EB weld suffered increased LME effect after irradiation leaving hardly any ductility of the welded connection.
- All investigated elevated Si steels are hardened after neutron irradiation up to 1.5 dpa at 460-490°C and suffer from very strong liquid metal embrittlement. For all four examined steels, the total elongation is further reduced causing them to break at the yield point or in case of the 2441 steel even in the elastic region. The austenitic 2442 grade remains the most ductile of the studied elevated Si steels although its total elongation was also strongly decreased.

Based on the tensile results of the irradiated material it can be said that irradiation at 460-490°C in contact with initially oxygen depleted liquid LBE increases the occurrence of LME despite the absence of irradiation hardening. This is attributed to the thermal corrosion at 460-490°C which dissolves the oxide layer and creates good contact between the solid metal and the embrittling liquid metal. It is unclear at this stage whether the irradiation enhances the thermal corrosion in contact with LBE. Due to licensing and safety regulations it was not possible up to now to further examine surface layers or fracture surfaces.

SYMBOLS, ABBREVIATIONS & ACRONYMS

a	crack length
a_{bi}	blunting corrected crack length
A_{C1}-temperature	upper limit of the γ-region, start of α–γ transformation
A_{C3}-temperature	lower limit of the γ-region, start of γ–α transformation
AC	Alternating current
ADS	Accelerator driven system
a_f	final crack length
ASTM	American Standard for Testing of Materials
B	fracture toughness specimen thickness
b_o	original remaining ligament
BCC	Body centered cubic
B_N	nominal thickness of fracture toughness specimen after side grooving
BR2	Belgian reactor 2
C	compliance
C_c	Hardening embrittlement coefficient
CCD	Charge coupled device
CCT	Centre cracked tension
CFE	Common Format Equations
CMOD	Crack mouth opening displacement
CR	Cold rolled
CTOD	Crack tip opening displacement
CW	Cold worked
DBTT	Ductile to brittle transition temperature
DC	Direct current
DCM	Dissolution condensation model
DCT	Disc shaped compact in tension (specimen)
DEMO	Fusion power demonstration reactor
dpa	Displacement per atom
E	Young modulus
EAC	Environmental assisted cracking
EB	Electron beam (welding process)
EBW	Electron beam welding
EDM	Electron discharge machining
EDX	Energy dispersive X-ray analysis
E_i	crack initiation energy
EPFM	Elastic plastic fracture mechanics
EPMA	Electron probe micro analysis

EUROTRANS	EUROpean Research Programme for the TRANSmutation of High Level Nuclear Waste in an Accelerator Driven System
FCC	Face centered cubic
FF	Kaltenhauser ferrite factor
FR	Fast reactor
GTAW	Gas tungsten arc welding
HAZ	Heat affected zone
HCP	Hexagonal close packed
HEPA	High Efficiency Particulate Air
HLMC	Heavy liquid metal coolant
IASCC	Irradiation assisted stress corrosion cracking
ITER	International thermonuclear experimental reactor
JAEA	Japan Atomic Energy Agency
J_{el}	Elastic component of *J*-intergal
J_i	Ductile crack initiation energy
J_{Ic}	Critical value of *J*-integral
J_{pl}	Plastic component of *J*-integral
J-*R* curve	curve of *J*-integral vs. crack growth
K_I	Stress intensity factor for mode I cracking
K_{Ic}	Critical stress intensity factor for mode I cracking
LANL	Los Alamos National Laboratory
LBE	Lead bismuth eutectic
LCF	Low cycle fatigue
LFR	Lead cooled fast reactor
LHMA	Laboratory for high and medium activity
LIMETS	Liquid Metal Embrittlement Testing Station
LISm	Laboratory for Iron and Steel making
LLE	Lead lithium eutectic
LLFF	Long lived fission fragments
LMC	Liquid metal corrosion
LME	Liquid metal embrittlement
LMIE	Liquid metal induced embrittlement
LVDT	Linear Variable Differential Transformer
LWR	Light water reactor
m	Exponent of the geometry function
MA	Minor actinides
MCNP	Monte Carlo Neutron Photon
MEGAPIE-TEST	Megawatt Pilot Target Experiment
MHD	Magneto- hydrodynamic

M_f	Martensite finish (temperature at which martensite transformation stops)
M_s	Martensite start (temperature at which martensite starts to form)
MMA	Manual metal arc (welding)
MYRRHA	Multi-purpose hYbrid Research Reactor for High-tech Applications
NDR	Normalisation data reduction (fracture toughness assessment technique)
NHE	Non hardening embrittlement
OCAS	Onderzoekscentrum voor de aanwending van staal
OCS	Oxygen control system
ODS	Oxide dispersion strengthened
P	Force
PAG	Prior austenite grain
PCCv	Precracked Charpy V-notched specimen
PD	Potential drop
PIE	Post irradiation examination
P_{Ni}	Normalized force
PPCS	Power plant conceptual study
PVD	Physical vapour deposition
PWHT	Post weld heat treatment
PWR	Pressurised water reactor
RAFM	Reduced activation ferritic martensitic
RIS	Radiation induced segregation
RMSE	Root mean square error
RT	Room temperature
SAW	Submerged arc welding
SEM	Scanning electron microscope
SFA	Shear fracture appearance
SFE	Stacking fault energy
SFR	Sodium cooled fast reactor
SIA	Self interstitial atom
SIMS	Secondary ion mass spectrometry
SMAW	Shielded metal arc welding
SMIE	Solid metal induced embrittlement
SPT	Small punch test
SSRT	Slow strain rate testing
T91	Modified 9%Cr-1%Mo ferritic-martensitic steel
TEM	Transmission electron microscope
T_E	Onset temperature of embrittlement

T_i	Irradiation temperature
T_m	Absolute melting temperature
T_R	Ductility recovery temperature
T_t	Testing temperature
TIG	Tungsten inert gas (welding process)
TWIN ASTIR	Irradiation up to 2 doses (hence TWIN) of Ads Steel T91 Irradiation
UC	Unloading compliance
UHV	Ultra high vacuum
UTS	Ultimate tensile strenght
v	Displacement
v_{el}	Elastic displacement
v_{pl}	Plastic displacement
v'_{pli}	Normalised plastic displacement
W	Width of the fracture toughness specimen
YS	Yield strength
YSZ	Yttria stabilized zirconia

1 INTRODUCTION

If you can find a path with no obstacles, it probably doesn't lead anywhere.
Frank A. Clark
(1915-2003)

Those who cannot remember the past are condemned to repeat it.
George Santayana
(1863-1952)

In Chapter 1, we briefly discuss the possible applications of heavy liquid metal coolant for future reactor systems and place them within the current global energy perspectives.
We present a literature review of the liquid metal embrittlement phenomenon. First, the general phenomenon is discussed along with proposed models for the mechanism and later specified for the case of ferritic-martensitic and austenitic steels in contact with liquid lead bismuth.
Second, we make a brief summary of the effects of irradiation on the microstructure and mechanical properties of structural steels and finally, we discuss the very scarce available literature on the combined effects of irradiation of structural steels and contact with liquid lead bismuth.

1.1 APPLICATION OF LIQUID LEAD ALLOYS IN FUTURE REACTOR SYSTEMS

1.1.1 Global Energy Perspectives

In the beginning of the 21st century the realisation of the finiteness of fossil fuel supplies – which had not been a very effective driving force to reduce dependence of Western countries on oil and gas – was overtaken by the concern for possible global warming due to CO_2-emissions. In fact the concerns for global warming re-opened the debate on the use of nuclear energy in Western Europe. Global warming together with increasing oil, gas and electricity prices made the future energy debate into a hype which strongly influenced the public opinion on nuclear energy. International collaborations were formed to set out roadmaps to meet future energy demands while maintaining and improving the environment.

Chapter 1

Studies performed on a global or large scale all predict an increase in the average use of electricity per capita due to the expected increase of the applications of electric power and the increasing prosperity of developing countries [1],[2]. Combined with the expectancy of a strong increase in global population in the next 50 years, electricity production is facing serious challenges. Belgium's energy commission has limited its roadmap to 2030 which in terms of energy related R&D is near future and therefore leaves limited possibilities to the deployment of new technologies. However, the report of the Energy Commission stresses the importance to keep all options open and re-evaluate the nuclear phase out [3].

Although renewable energy sources offer the possibility of clean energy there are concerns about their economic efficiency and reliability which limits their application to a few tens of percents of the total energy production [1]. Therefore the main provision of long term reliable energy supply would be the development of new energy technologies capable of large-scale and economical replacement of fossil fuels within a reasonably short time scale. Nuclear energy, which has a negligible CO_2 emission, has proven its reliability and economic efficiency by the reactors operating today. However, the vast majority of current reactors are fuelled with U^{235} which in terms of resources is assessed to somewhat more than 0.7% of the total 5.5 10^6 tons of available natural uranium (based on the total identified resources of uranium at an extraction cost lower than 130 $/kg in the 2007 IAEA, NEA "Red Book"). In terms of energy equivalents this is less than the estimated resources of oil and gas, let alone coal [2]. Nuclear power can be deployed on a much larger scale however, using fast reactors capable of breeding their own fuel and therefore not relying as much on the available U^{235} resources or perhaps one day even by using fusion reactors. Fast reactors use neutrons given off by the fission reaction to "breed" more fuel from otherwise non fissionable fuel. The most common breeding reaction is the neutron capture of U^{238} which after two successive beta-decays is converted in to Pu^{239}. The term fast breeder reactor refers to a configuration which can produce more fissile fuel than it consumes. Moreover fast reactors could be used to burn high level radio-active waste thus decreasing the waste half- life time by several orders of magnitude. Fast reactors are however limited in the amount of waste they can treat due to the decrease of control and safety margins with increasing amount of trans-uranium elements in the core. To solve this problem dedicated waste burners better known as subcritical accelerator driven systems (ADS) could be built.

Due to the fact that this work is focused on the materials issues of reactor structural materials in contact with liquid lead alloys we will not go any further into the discussion on energy perspectives or neutronics of future nuclear systems. It is however considered useful within the frame of this PhD to give a brief overview of the possible applications of liquid lead alloys and the associated requirements on the structural materials in fusion reactors, fast reactors and accelerator driven systems.

1.1.2 Application of liquid lead or lead bismuth eutectic in GEN IV fast reactors

Generation IV nuclear energy systems are future, next-generation technologies that will compete in all markets with the most cost-effective technologies expected to be available over the next three decades. Comparative advantages include reduced capital cost, enhanced nuclear safety, minimal generation of nuclear waste, and further reduction of the risk of weapons materials proliferation. Generation IV systems are intended to be responsive to the needs of a broad range of nations and users.

The Lead-Cooled Fast Reactor (LFR) is one of the six most promising concepts within the GEN IV proposed systems selected by the Generation IV International Forum (GIF). It features a fast-spectrum lead or lead/bismuth eutectic liquid-metal-cooled reactor and a closed fuel cycle for efficient conversion of fertile uranium and management of actinides. Due to the relatively low global availability of bismuth the possible industrial application of the LFR should be operated using pure lead. A schematic representation of the LFR is depicted in Figure 1.1.

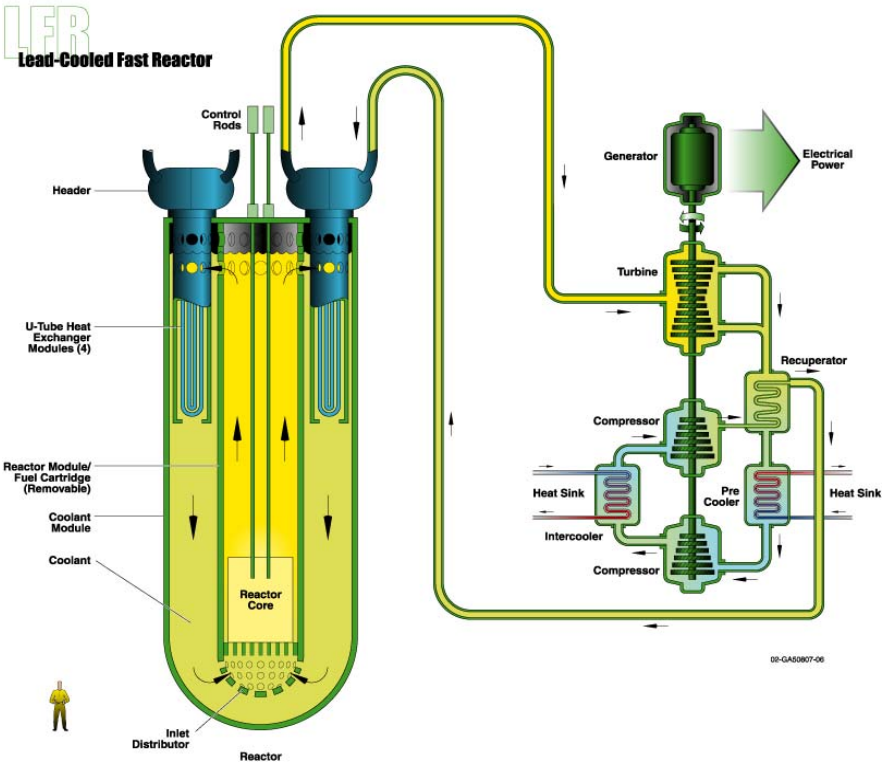

Figure 1.1: Schematic representation of the lead cooled fast reactor (LFR) [4].

The system has a full actinide recycle fuel cycle with central or regional fuel cycle facilities. Options include a range of plant ratings, including a battery of 50-150 MWe that features a very long refuelling interval, a modular system rated at 300-400 MWe, and a large monolithic plant option at 1200 MWe. The term battery refers to the long-life, factory fabricated core, not to any provision for electrochemical energy conversion. The fuel is metal-, oxide- or nitride-based, containing fertile uranium and transuranics. The LFR is cooled by natural or forced convection with a reactor outlet coolant temperature of 550 °C, possibly ranging up to 800 °C with advanced materials. The higher temperature enables the production of hydrogen by thermochemical processes.

With the exception of uncertainties in materials performance over very long service life in cores (20 years or longer) at temperature over the 500-550°C range, no apparent conceptual barriers (i.e. “show-stoppers”) exist for the eventual use of lead and LBE coolants in advanced nuclear applications [5]. In fact, considering the typical core lattice configurations, the LFR showed advantages over the Sodium cooled fast reactor (SFR) regarding behaviour in severe accidents [6]. This is due to the better natural circulation behaviour of an LFR design and the much higher boiling temperature of lead bismuth eutectic and lead (boiling points indicated in Table 2.10 of Chapter 2). Moreover, the chemical inactivity of lead excludes the possibility of fires or other strongly exothermic reactions with air, water and water vapour. This means that an LFR is a very robust system regarding safety. A drawback of the LFR is that due to its high density, lead or LBE is very heavy and therefore causes high stresses on ducts and pipes. The weight of the coolant limits the maximum size of pipes and ducts requiring higher flow velocities of the liquid metal coolant which in turn increases erosion-corrosion. For present steels a protective oxide layer or a coating is needed to minimize erosion and possible liquid metal embrittlement (LME) during normal operation. These layers and coatings are sensitive to coolant temperatures above 870 K for prolonged periods of time. For LFR's, corrosion and material characteristics of steels should be further investigated, in particular under irradiation conditions.

For applications in the higher temperature ranges an extensive R&D programme on materials and coolant technology is needed. A preliminary analysis of existing materials led to the following classification, depending on the upper operating temperatures [7]:

Class I. For temperatures below 600°C, it has been demonstrated that the existing technologies and some qualified nuclear structural materials (austenitic and

ferritic/martensitic steels) possess acceptable performance in short to medium durations and out of pile. These demonstrations need to be extended to longer durations and under irradiation.

Class II. For higher-temperature services envisioned in more advanced system concepts, materials and coolant technology developmental needs are much more extensive and the development much longer term. For reactor outlet temperature up to 650-700°C for higher efficiencies, ODS (oxide dispersion strengthened) steels and/or advanced F/M steels are potential candidates. These materials, categorised as Class II, may be used with an extension of the LBE coolant technology. For this temperature range, it is likely that Pb, rather than LBE, will be used, although the use of LBE is more established.

Class III. For operating temperature above 750-800°C in systems with more diverse energy products, including hydrogen production, refractory metals and alloys, ceramics and composites are potential candidates (Class III). These systems will require a very different coolant technology, and design, construction and operating methodology. Compatibility is no longer the key obstacle. Other issues, including irradiation stability, fatigue strength, fabrication, joint, costs, etc are challenging. The development of Class III materials are pursued by high temperature reactor and fusion technology development programmes. For this temperature range, Pb will likely be the only choice since LBE and the associated technologies no longer offer any intrinsic or experiential advantages.

1.1.3 Application of liquid lead bismuth eutectic in Accelerator Driven Systems (ADS)

The spent nuclear fuel and nuclear waste in general has always been the Achilles' heel of the nuclear industry. More specifically the public acceptance of the high level nuclear waste repository is a limiting factor in the possible large scale expansion of nuclear energy production. Driven by this issue a new concept of nuclear system was launched based on the coupling between the accelerator and nuclear reactor technologies.

The principle is that of absorption of a high energy hadron beam in a spallation target which can produce a high energy nuclear cascade. The spallation source is placed in a fissile medium so that neutrons coming from the spallation reaction will cause nuclear fissions which in turn will give an energy release several orders of magnitude higher than the energy delivered by the beam [8].
Using this concept an inherently safe nuclear system can be built by relying on neutrons delivered to the core by the spallation reaction instead of having a critical chain reaction to sustain the fission reactions in the core. Without going into details of neutronics and safety it is presumed understandable that an inherently safe machine such as an ADS can transmute (burn) a higher amount of long lived fission fragments (LLFF) and minor actinides (MA) than a critical fast reactor. This transmutation of waste can result in a decrease of the half-life of the high level waste by several orders of magnitude. As can be seen in Figure 1.2 the high level nuclear waste would reach the equilibrium radiotoxicity of uranium as found in nature after about 300 years instead of after 250 000 years after removal by transmutation of plutonium, neptunium, americium and curium.

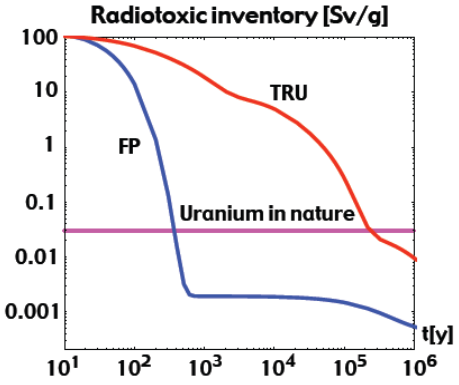

Figure 1.2: Radiotoxicity of spent LWR fuel with and without partitioning and transmutation (P&T).

Since 1998, SCK•CEN, in partnership with IBA s.a. and many European research laboratories, has been designing a multipurpose Accelerator Driven System (ADS) – MYRRHA – and is conducting an associated R&D support programme [9]. MYRRHA aims to serve as a basis for the European experimental ADS. In a first stage, the project focuses mainly on demonstration of the ADS concept, on safety research of sub-critical systems and on nuclear waste transmutation studies. Subsequently, MYRRHA will be used as a fast spectrum irradiation facility dedicated to research on structural materials, on nuclear fuel, on liquid metal technology and associated aspects on one hand and as a radio-isotope production facility on the other hand.

The system consists of a proton accelerator that supplies a 600 MeV × 3-4 mA proton beam to a liquid lead-bismuth eutectic (LBE) spallation target, delivering the primary neutrons, that in turn couples to a LBE cooled sub-critical fast core (depicted in Figure 1.3). Materials issues related to corrosion and irradiation damage of the lead-bismuth cooled sub-critical core are identical to those of the lead-bismuth cooled fast reactor. The material requirements for the spallation target are however more stringent due to the spallation induced production of hydrogen and helium in the structural material.

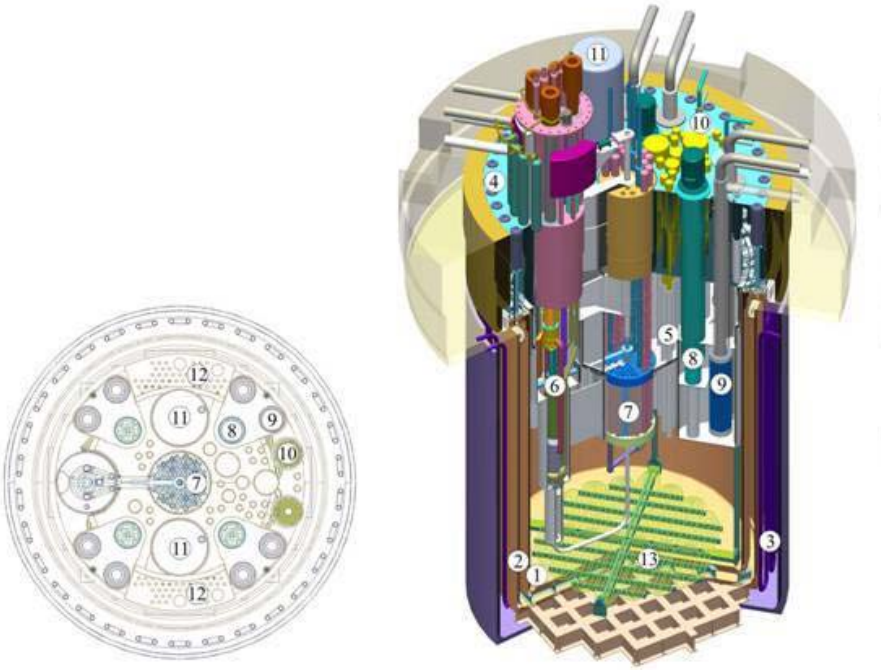

1. inner vessel
2. guard vessel
3. cooling tubes
4. cover
5. diaphragm
6. spallation loop
7. sub-critical core
8. primary pumps
9. primary heat exchangers
10. emergency heat exchangers
11. in-vessel fuel transfer machine
12. in-vessel fuel storage
13. coolant conditioning system

Figure 1.3: Schematic representation of MYRRHA (08/2008).

The structural materials for ADS and more specifically for MYRRHA need to withstand temperatures ranging between 200° and 550°C (normal operating temperature between 300 and 450°C) under high spallation neutron flux and in contact with liquid lead bismuth eutectic. It is clear that the candidate materials need to be able to fulfil challenging performances such as high thermal conductivity and

heat resistance, low thermal expansion, low DBTT shift, sufficient strength at elevated temperatures with limited loss of ductility and toughness, low swelling rate, high creep resistance and good corrosion resistance.

In the 1950's the 9-12 wt% Cr transformable steels with low carbon (< 0,1%) were developed for high temperature applications where high creep-rupture strengths were needed in combination with good oxidation and corrosion resistance. These steel types proved their worthiness in several industries, e.g. petroleum, aerospace and engineering. In the 1980's the ferritic-martensitic steels were further developed and used in fast breeder reactor programs because of their superior resistance to irradiation damage and appropriate mechanical properties combined with an acceptable cost.
In recent years, the commercially available ferritic-martensitic steel T91 has been considered to be very promising as a candidate material for ADS. The material exhibits good swelling resistance and good mechanical properties such as tensile, impact properties and creep resistance. T91 was therefore already tested in other projects e.g. SPIRE, TECLA and MEGAPIE-TEST.
On the other hand the well known austenitic stainless steel, AISI 316L is proposed to become the structural material for the sections of the ADS which undergo less irradiation and have a lower operating temperature due to its superior corrosion resistance and ductility in these conditions.

Accelerator-driven systems using lead-bismuth technology are presently under investigation in Europe (EUROTRANS), India, South Korea (HYPER) and Japan (J-PARC).

1.1.4 Application of liquid lead lithium eutectic in fusion reactors

The current development of fusion reactors is based on magnetic confined fusion of deuterium (D) and tritium (T) according to the following reaction:

$$D + T \rightarrow {}^4He(3.56MeV) + n(14.03MeV)$$

For the structural materials of the internals of fusion reactors the damage production caused by the 14 MeV neutrons is of great importance. This high energy particle causes not only displacement cascades in the lattice, it also causes transmutation of atoms in the matrix which leads to helium and hydrogen retention in the material. Irradiation damage, swelling and formation of helium bubbles will be considered more in detail in the paragraph on irradiation effects in ferritic-martensitic and austenitic steels. To give an idea on the magnitude of energy deposition and expected material damage in future fusion systems the currently estimated values are given in Table 1.1.

Table 1.1: Estimated energies and material damage for future fusion systems.

	ITER	DEMO	*Reactor*
Fusion Power	0.5 GW	2-2.5 GW	*3-4 GW*
Heat Flux (First Wall)	0.1-0.3 MW/m^2	0.5 MW/m^2	*0.5 MW/m^2*
Neutron Wall Load (First Wall)	0.78 MW/m^2	< 2 MW/m^2	*~2 MW/m^2*
Integrated wall load (First Wall)	0.07 MW/m^2 (3 yrs inductive operation)	5-8 MW.year/m^2	*10-15 MW.year/m^2*
Displacement per atom (end of life values)	<3 dpa	50-80 dpa	*100-150 dpa*
Transmutation product rates (First Wall)	~10 appm He/dpa ~45 appm H/dpa	~10 appm He/dpa ~45 appm H/dpa	

The tritium in the fusion reaction above is produced by the following nuclear reaction with lithium:

$$n + {}^6Li \rightarrow T + {}^4He + 4.78MeV$$

There are currently four different designs available for the tritium breeding blanket of the future commercial fusion power plant depending on the form in which the

lithium is present in the system [10]. Models A, C and D are using liquid lead lithium eutectic.

Model A is based on a liquid lithium-lead blanket with water cooling. The lithium serves as a tritium-generating material and the lead as a neutron multiplier in order to improve the conversion efficiency. The structural material is the reduced-activation ferritic-martensitic steel Eurofer which is very similar in microstructural properties to the ferritic-martensitic reference material for lead or lead-bismuth cooled nuclear systems. The in-vessel shield is water-cooled steel, as is the vacuum vessel.
In the blanket modules, the cooling water average pressure and temperature are respectively 15 MPa and 300 ºC, which is similar to the operating conditions of PWR fission plants. The power conversion system of this Model is based on the fully qualified PWR technology and its overall thermodynamic efficiency is similar to that of a PWR fission plant. For good maintenance characteristics, a segmentation of the blanket into large modules has been adopted.

Model C, depicted in Figure 1.4, has a lithium-lead blanket in which heat is removed by circulation of the lithium-lead itself and helium coolant passing through channels in the structure. This structure is mainly Eurofer, with oxide-dispersion-strengthened RAFM steel in the highest temperature zone (facing the plasma). The LiPb flow channels are lined by silicon carbide composite inserts, providing thermal and electrical insulation but no structural function. The thermal insulation allows higher temperature operation of the LiPb for improved thermodynamic efficiency, while the electrical insulation avoids MHD effects when pumping the LiPb at high velocity. The modules are large, stiff boxes with a grid structure inside, which are used as flow channels for the Pb-17Li and helium. High-pressure (8 MPa) helium gas is used to cool the first wall and the entire steel structure. For good maintenance characteristics, a segmentation of the blanket into large modules has been adopted.

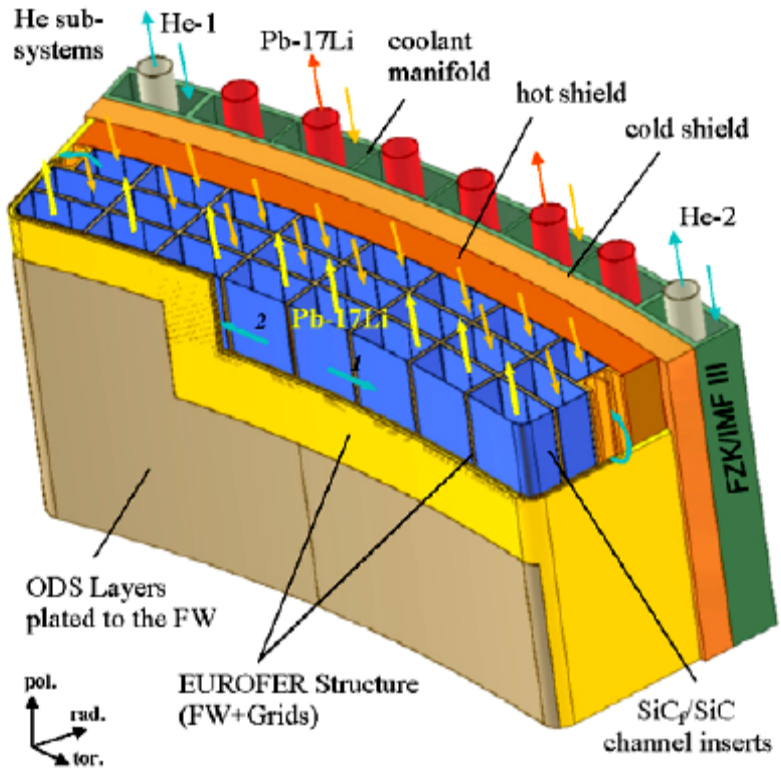

Figure 1.4: Dual-coolant blanket (model C), equatorial outboard blanket module [10].

The liquid-metal Pb-17Li serves as a coolant as well as the tritium-generating material. Its outlet temperature is maximised for efficiency reasons. It enters the modules at 460 °C and exits at 700 °C, which is above the maximum permissible temperature for steel. Therefore, the Pb-17Li channels are thermally insulated with a layer of SiC_f/SiC, which also serves as electric insulator for MHD reasons as indicated above.

The most advanced of the PPCS Plant Models, Model D, uses a lithium-lead blanket in which the LiPb itself is circulated as primary coolant. The structure is made by silicon carbide composite. The divertor structure is also made of silicon carbide composite, with tungsten armour, cooled by liquid lithium-lead. The objective for PPCS D is to reach very high blanket operating temperatures, and thus very high thermodynamic efficiency, as well as very low decay heat densities and low coolant pressures, accepting a higher development risk. The temperature of the coolant in the blanket modules is in the range 700 ºC – 1100 ºC. In order to simplify the lithium-lead flow path and to maximize the blanket coverage, a segmentation of the blanket in vertical, “banana-shaped” segments has been assumed for this model.

1.2 LIQUID METAL CORROSION (LMC)

Corrosion of steels in pure liquid Bi, Pb or LBE occurs primarily through dissolution of steel components into the liquid metals/alloys [11]. The main driving force for liquid metal corrosion is the chemical potential for dissolution of all solid surfaces in contact with the liquids [12]. The compositional and microstructural changes due to selective dissolution and intergranular corrosion can lead to material failures [13]. The dissolution rate depends on the liquid media, the ratio of the surface area of the solid metal to the volume of the liquid metal, the conditions of the surface, the content of impurities such as oxygen and nitrogen in the liquid metal and the compositions of the solid materials [11].

There are two types of corrosion (Figure 1.5), uniform and local. Uniform corrosion is characterized by the uniform damage at the surface of the solid phase by the liquid metal. For the local corrosion, the liquid metal penetrates into the solid metal in the areas where zones with a high density of crystal structure defects reach the surface. The local corrosion front moves along grain boundaries, the specific crystallographic directions, vacancies and pores, the previously formed defects. The penetration of the liquid metal into solid metals can redistribute the interstitial impurities between the solid and liquid phases [11].

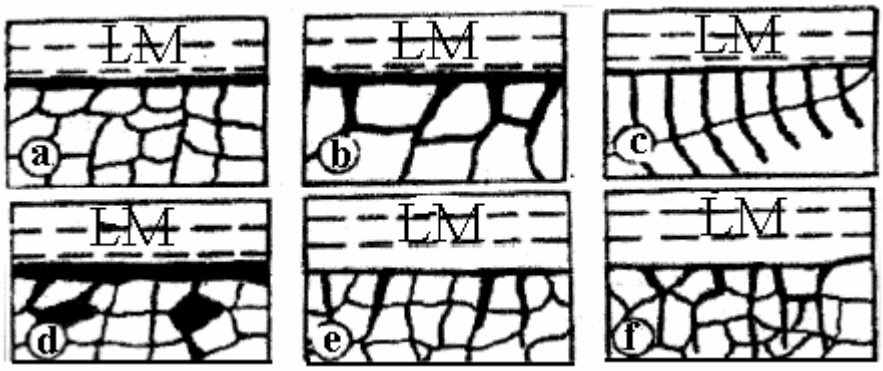

Figure 1.5: Diagram of corrosion damage of metals in liquid metal media: (a) uniform corrosion; (b) penetration along the grain boundaries; (c) along the specific crystallographic direction; (d) along vacancies and pores; (e) and (f): along previous formed defects [11]. LM represents the liquid metal.

When liquid metals flow over solid metal/alloy surfaces, the velocity of liquid metals accelerates corrosion. This is called flow accelerated corrosion. There are a number of mechanisms for interactions between the flow and dissolution [11]. The combination of different mechanisms results in four main types of flow accelerated

corrosion (see Figure 1.6): mass transport-controlled corrosion, phase transport-controlled corrosion, erosion-corrosion and cavitation-corrosion. Mass transport-controlled corrosion occurs when the flow velocity is low. The mass transfer rate (combined effects of convection and diffusion) is less than the dissolution rate of the solid metal into the liquid metal, and the corrosion rate is determined by the mass transfer rate. For these cases, the corrosion product concentration at the solid/liquid interface equals the saturation or equilibrium concentration. For multi-phase flows or high turbulent flows, the aggressive particles in the liquid moving along the protective film surface or the high shear stress at the interface can strip the protective films or wear them away, reducing the thickness of the protective film and leading to erosion corrosion. In the areas where the flow changes its direction sharply, such as sudden expansions or elbows, the liquid or the aggressive particles are thrown against the surface of solid metals, which results in a higher wear rate. Cavitation-corrosion occurs when there are cavitation bubbles in the flowing liquid metals and the bubbles collapse on solid metal surfaces. The collapse creates micro-jets of the liquid metal to the solid metal surface, producing high local pressure and destroying the surface. This behaviour can lead to brief high stress in the solid metal, causing localized corrosion fatigue damage and environmentally assisted micro-fractures of the solid metal.

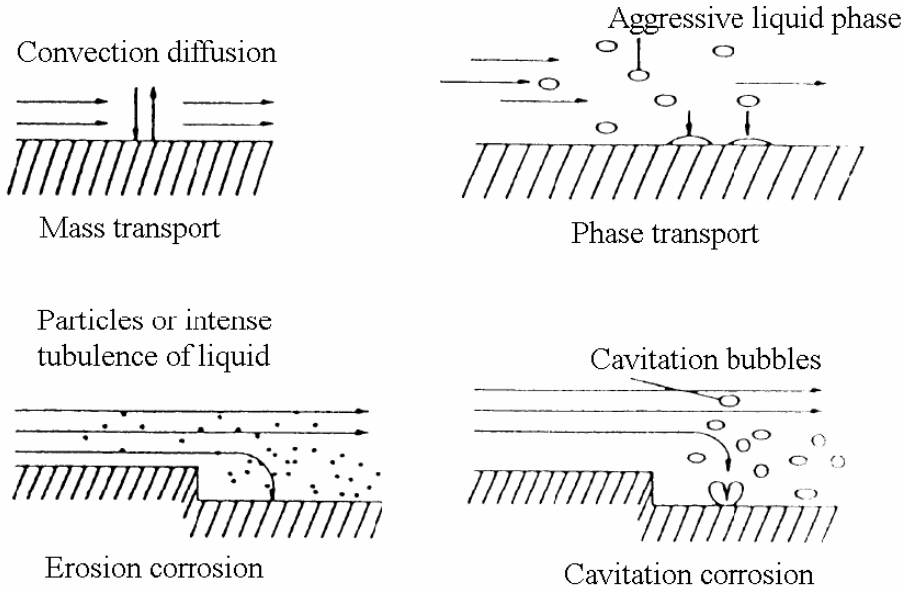

Figure 1.6: Representation of the four main types of flow affected corrosion [11]

However, in this work only stagnant liquid metal exposure conditions will be considered. Therefore, the solubility limit of metals and alloying elements in the liquid LBE can be considered as the most important parameter for LMC in the frame

of this work. Solubility data of metals in liquid lead and LBE are scarce. Generally, the saturation solubility of a metal in LBE, lead and bismuth can be written as:

$$\log(c_s, wppm) = A_c + \frac{B_c}{T(K)} \quad \textbf{(1.1)}$$

Where A_c and B_c are constant. Values of the two constants for Fe, Cr, and Ni in liquid LBE, bismuth, and lead are given in Table 1.2.

Table 1.2: Solubility data of Ni, Fe, and Cr in LBE, Bi, and Pb [11].

	Fe		Cr		Ni	
	A_c	B_c	A_c	B_c	A_c	B_c
LBE	6.10	-4380	5.08	-2280	7.53	-843
Bi	6.26	-3490	6.86	-3580	6.93	-2400
Pb (673<T<873)	4.34	-3450				
Pb (873<T<1020)	5.82	-4860				

Corrosion products dissolved into LBE at surfaces are transported in LBE for sustained corrosion or stops when the concentrations reach the saturation limits. For static corrosion tests, the transport process is mostly diffusion that depends on the corrosion product concentration gradient and the corrosion product diffusion coefficient in LBE. When the dissolution rate is less than the diffusion rate, diffusion is fast enough to take all the dissolved species and the corrosion rate is determined by the dissolution rate. When the dissolution rate is greater than the diffusion rate, the concentration at the interface is always at saturation and the corrosion rate is determined by the diffusion rate. In liquid metal systems there is good evidence that both cases described above occur [11], depending on the solution and solute.

The diffusion coefficient is a function of temperature. To our best knowledge, there are no experimental correlations for the temperature dependence of diffusion coefficients of Fe, Ni, and Cr in LBE. A single value for iron was reported in the literature [11]:

$$D_{Fe \rightarrow LBE} = 2.27 \pm 0.11 \times 10^{-9}\, m^2 s^{-1} \text{ at } 750°C \quad \textbf{(1.2)}$$

This value is almost same as that of iron in pure lead [11] at the same temperature. Therefore, Balbaud-Celerier and Barbier [11] assumed that the diffusion coefficient of iron in LBE equals that in pure lead, and can be calculated using the correlation for lead developed by Robertson [11]:

$$D_{Fe\rightarrow Pb}\left[m^2 s^{-1}\right] = 4.9\times10^{-7}\exp\left(\frac{44100\pm6300}{RT}\right) \quad \textbf{(1.3)}$$

Treating the liquid metal as a continuum, the hydrodynamic theory of diffusion developed a correlation between the diffusion coefficient and the dynamic viscosity by balancing the driving force and the friction force exerted on an atom that has hard sphere shape [11]. The Stokes-Einstein equation is:

$$D\left[m^2 s^{-1}\right] = \frac{kT}{6\pi r\mu} \quad \textbf{(1.4)}$$

Where k [J K^{-1}] is the Boltzmann constant and r [m] is the radius of the diffusion atom. Comparing to the experimental results [11], it seems that the Stokes-Einstein equation (Eq. 1.4) is suited to calculate the species diffusion coefficient in LBE.
In an oxygen control system, the diffusion of oxygen in LBE is particularly important. This is shown by the effect of the oxygen content in lead on the corrosion behaviour of the structural material, depicted in Figure 1.7.

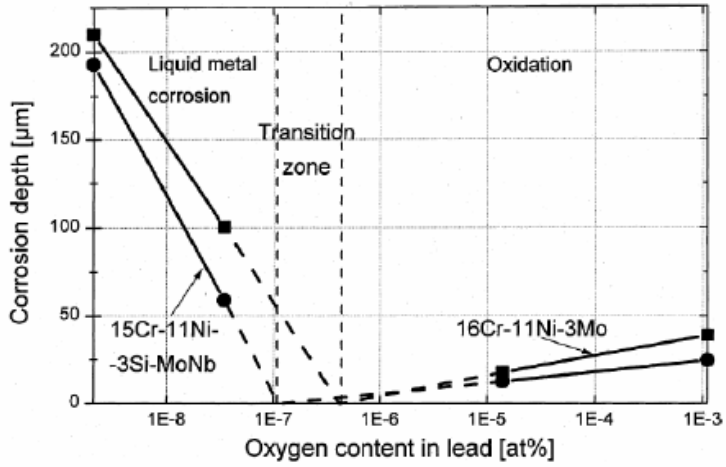

Figure 1.7: Corrosion behaviour of steels in flowing lead after exposure for 3000 h at 550°C [11].

However, the main emphasis of this work is on the mechanical properties of the candidate structural materials in contact with LBE which are much more affected by liquid metal embrittlement than by liquid metal corrosion. Therefore, we will further focus on liquid metal embrittlement.

1.3 LIQUID METAL EMBRITTLEMENT (LME)

Although liquid metal embrittlement (LME) has been observed a long time ago, the mechanism is not yet fully understood due to its complexity. Despite the fact that many interpretations of LME have been formulated [14]-[24], the prediction of its occurrence remains problematic. Moreover various parameters such as metallurgical state, surface state, composition, solubility, temperature, strain rate, stress concentrators, etc. are known to influence the risk of LME [17], [20], [21].
In this section the general phenomena known to occur in certain solid metal/ liquid metal couples will be described along with the parameters that strongly influence the LME. In the second section the most important models found in the literature that explain the liquid metal embrittlement phenomenon will be explained and critically reviewed in the light of the former presented literature. The last section discusses the most relevant but relatively scarce literature on the very specific case of T91 and 316L structural steels in contact with LBE or Pb.

1.3.1 General phenomena occurring in contact with liquid metals

There are several mechanisms by which a liquid metal may degrade a solid metal. Some liquid metals like aluminium are very reactive and will attack many other metals by forming intermetallic compounds. In some other cases the attack is confined to particular states or constituents of a solid alloy. For instance above 750°C zinc preferentially dissolves the nickel in the grain boundaries of austenitic stainless steels while lithium reduces grain boundary carbides in carbon steels [22]. In more inert systems, degradation of the solid is known to occur through grain boundary penetration by the liquid metal. Solid polycrystalline zinc and aluminium disintegrate into separate grains even when unstressed after a period in contact with liquid gallium at 30°C [20]. The processes described above are however not considered as cases of classical liquid metal embrittlement in this work and will therefore not be discussed further in the frame of LME.

Definition

Liquid metal embrittlement, LME, has been given several different definitions, one more general than the next. The most commonly used definitions are given in Table 1.3.

When examining the literature this is often confusing since several authors use the term liquid metal embrittlement for all processes leading to accelerated mechanical failure in liquid metal environment. This does not strictly conflict with some of the general definitions given in Table 1.3 and can therefore not be avoided as long as little more is known about the specific mechanism of liquid metal embrittlement.

Table 1.3: Definitions of Liquid Metal Embrittlement according to several authors.

M. Kamdar, 1973 [14]	Drastic modification of fracture behaviour of a non oxidised solid metal covered by a film of liquid metal. (yield stress and plastic deformation behaviour remain unchanged) The phenomenon only manifests itself in specific solid metal – liquid metal couples.
F. Shunk, W. Warke, 1974 [24]	Deterioration of mechanical properties of a solid metal or alloy subjected to a minimum stress while wetted by a liquid metal.
M. Nicholas, C. Old, 1979 [23]	Decrease in total elongation of a normally ductile solid metal when subjected to stress while being in contact with liquid metal.
P. Gordon, 1982 [25]	Fracture of a normally ductile solid metal in perfect contact with a liquid metal under influence of abnormally low stresses. (brittle fracture when it occurs in the elastic domain)
E. Glickman, 1999 [26]	Reduction of ductility and fracture toughness of metals when simultaneously subjected to stresses and wetting by liquid metals.
E. Rabkin, 1999 [27]	Brittle rupture of an intrinsically ductile metal under limited constraint when in contact with specific liquid metal environments.
B. Joseph, F. Barbier, 1999 [17]	Brittle fracture or loss in ductility of a usually ductile material in presence of liquid metal, possibly in absence of stress. (ref. Al_{solid}-Ga_{liquid})

Mechanism

LME failure occurs by nucleation of a crack at the wetted surface of the solid and its subsequent propagation with little resistance into the bulk. The process does not involve bulk chemical or structural modification of the solid. In severe cases, the ductility may be so reduced that the normal ultimate tensile strength is not achieved and thus the load to produce failure is decreased. This differs considerably from other degradation processes encountered in liquid metal environments mentioned above.

Despite several reviews [14][15][16][17][22][23] describing the phenomenological features of LME and effects of numerous variables such as grain size, strain rate, temperature, metallurgical state, etc., a qualitative explanation of LME has not yet been found and its prediction is still uncertain. The next few pages we will describe the most important features commonly ascribed to LME and their most important influential variables before coming to the hypothetic models explaining the phenomenon.

Elastic & plastic behaviour

When comparing engineering stress – engineering strain curves of solid metals tested in liquid metals and in inert environment or air, two main trends are discussed in the literature. The first one, by Westwood [18] and Stoloff [29], claims that until fracture occurs, the stress-strain behaviour of the solid metal is the same as that in the unwetted condition. The second one, by Dmukhovskaya and Popovich [30] states that there is an initial promotion of plastic flow and consequently a different plastic behaviour of the solid material before rupture. In both cases however, the elastic domain and the yield stress of the solid are said to be unchanged in presence of liquid metal.

Fracture behaviour

By definition LME causes a decrease in ductility but other mechanical properties are usually unaffected. Elastic moduli and yield stress always remain the same. The UTS however might not be reached in some severe cases as mentioned before.

Some authors [20], [22], [23], [28] mention that intergranular failure is the most common type of failure but they acknowledge that some cases of transgranular fracture have been observed. Kamdar specifies furthermore that there is little indication of crack branching or striation to indicate slow crack propagation. It must

be noted however that these authors include some clear cases of intergranular corrosion in their study and that they do not pay much attention to the crystal structure of the investigated materials.

LME induced cracks propagate along grain boundaries or across grains at variable speeds depending on the testing conditions. Propagation rates may reach several meters per second if substantial amounts of elastic strain energy are present in the stressed solid [20]. However, if little strain energy is available the crack propagation rate will be low and will depend upon the extension rate of the sample.

The presence of liquid metal at the moving crack tip appears necessary for fast fracture. However, in high strength brittle metals, a crack initiated in the liquid may propagate in a brittle manner in the absence of liquid metal. In low strength metals, a transition may occur from brittle to ductile failure under circumstances of loss of liquid metal at the crack tip. Although less frequent than brittle fracture, embrittlement can also occur by a ductile dimpled rupture mode in certain steels, copper alloys and aluminium alloys. The embrittlement then manifests itself as the degradation of the mechanical properties of the solid [28].

Fracture is not limited to polycrystalline metals. Single crystals of zinc and cadmium are embrittled by liquid metal and fracture in a brittle cleavage mode [28].

Temperature

LME usually occurs just above the melting point of the liquid and causes a transition in fracture behaviour similar to the ductile to brittle transition in bcc metals as temperature increases [23]. At a sufficiently high test temperature, a brittle to ductile transition occurs when embrittlement ceases and ductility of the solid is restored. The phenomenon leads to a decrease in ductility within a certain temperature interval which is often referred to as the ductility trough, as schematically illustrated in Figure 1.8.

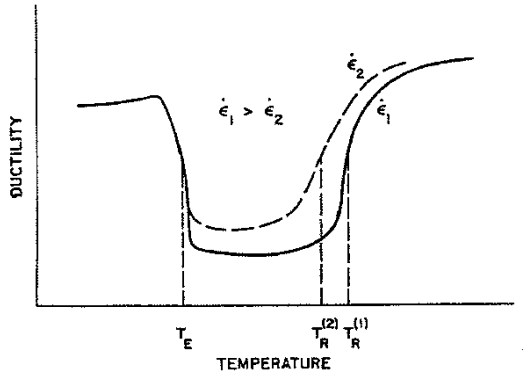

Figure 1.8: Schematic representation of ductility vs. temperature behaviour typically related to LME [23].

The transition at the upper end of the ductility trough does not occur at a sharply defined temperature but depends on the testing conditions. It is not predictable on a theoretical basis, in terms of diffusion or in terms of dissolution. It is generally accepted that a significant increase in ductility with temperature counteracts the tendency to brittle failure in a liquid metal environment [28].
These brittle to ductile transition temperatures have been reported for zinc-mercury, aluminium-mercury, brass-mercury, titanium-cadmium and steel-lead combinations [28].

Strain rate

Generally, as mentioned before, ductile metals which comprise relatively low elastic strain energies under plastic deformation, will show a nearly linear relation between crack propagation and strain rate. This is confirmed by Glickman who mentions the nearly linear relation between crack propagation and strain rate for the copper – bismuth system [17].

With increasing strain rate the upper temperature of the ductility trough, T_R, is increased, as illustrated in Figure 1.8 [22]. The effects of strain rate appear to be related to the increase in the yield stress of the embrittled solid metal with increasing strain rate [28].
At slow strain rates, thus in conditions favourable for intense stress relaxation, the only effect of adsorption of the active media is to ease plastic flow, i.e. to inhibit LME [31]. With a decrease in strain rate, the upper temperature of the ductility trough, T_R, therefore drops which leads to narrowing of the embrittling temperature range or even to its disappearance.

The effects of strain rate on the shift of T_R temperature has been reported for cadmium – gallium, zinc – mercury, aluminium – mercury, zinc – indium, brass – mercury and titanium – cadmium embrittlement couples [28]. Usually, changes in strain rate by orders of magnitude are required to change the T_R temperature by 50 to 100°C.

Stress

Some definitions of LME, stated in Table 1.3, mention a certain minimal stress as a prerequisite for LME. This stress can be either an applied external stress or residual stress present in the material. This causes a problem since it is often unclear whether the studied solid metal is free of stress or contains high stress concentrations.
LME would occur only above a certain threshold stress. That is not reported by all authors, perhaps because some may have worked on a system that requires a very low threshold stress.

Embrittlement by liquid metals can be achieved in simple tension, bending and torsion. In general, it will not occur under compressive stresses. Thus, a sheet of high strength aluminium wetted on one surface with mercury will break in a brittle manner if bent so that the wetted surface is in tension but it will not break if bent plastically so that the wetted surface is in compression. However, in the latter instance, when the applied stress is released, cracking may occur from residual tensile stresses [20].

Creep and delayed failure tests under constant load have been conducted to study the effects of time dependent processes, such as diffusion penetration of the grain boundaries as a possible cause of embrittlement. Delayed fracture has been reported for notch insensitive aluminium – copper and beryllium – copper alloys in liquid mercury [28]. Penetration of mercury did not occur and embrittlement was independent of time to failure but failure time increased with an increased stress level of the tests. In notch sensitive zinc tested in liquid mercury, the time to failure was very sensitive to the stress level, with complete failure occurring instantly at a stress slightly higher than a threshold stress. Penetration of mercury was also not observed in this study
These tests indicate that time dependant diffusion penetration or dissolution processes are not the cause of LME.

Pressure

The pressure of gravity alone has influence on the extent of cracking. If a test sheet specimen is held in the vertical plane and a tensile stress applied in the horizontal direction, the crack produced by LME propagates less in the upward direction than in the downward direction.
To verify this, an experiment was conducted by bend testing aluminium in contact with mercury [20]. A tube was used in such a manner that a 30 inch head of liquid mercury could be maintained in the machined notch. The resulting crack propagated at a faster rate and the crack length was nearly tripled.

Composition of the liquid metal

The effect of alloying the liquid metal on the susceptibility to LME can be significant. It can embrittle the solid where it had no embrittling effect before or if it does embrittle already, it can alter the severity of the LME. However, substantial amounts of alloying are needed to have significant effects. No evidence was found that small additions in the order of ppm of an active component had any effect on the LME phenomenon.
For example, cadmium is not embrittled by mercury at room temperature but its ductility and fracture stress decrease if the liquid is alloyed with more than 5 to 10% of indium. The opposite effect is observed for the embrittlement of silver [23].

Nicholas *et al.* [23] also states that the concept of low melting metals acting as inert carriers for embrittling species may explain certain experimental observations found in literature. Absence of embrittlement of a certain solid metal – liquid metal couple could be due to the T_R temperature for the couple being less than the melting point of the liquid metal. However, additions of the embrittler to a lower melting carrier could result in LME.
An example of this is the observation that aluminium is not embrittled by tin – zinc solders at 250°C and only slightly embrittled by mercury at room temperature but is severely embrittled by mercury – 1.3% tin and mercury – 3% zinc at room temperature [18].

Composition of the solid metal

The effect of alloying on the susceptibility to LME has been studied for a wide variety of metals. The results are different from one author to the other. Some additions are reported to increase the effect of LME, others are reported to slow down the crack propagation speed or remove the embrittling effect entirely.

It is commonly accepted that the effect of alloying elements is manifested at the level of grain boundaries [17].

Microstructure of the solid

LME depends strongly on the thermal and mechanical history of the solid. This is clearly related to the underlying microstructure. The effect of grain size is discussed by several authors and has an undisputable effect on the liquid metal embrittlement process. However the nature of this effect is unclear due to contradictory statements by different authors.

According to Glickman [26], Joseph [17] and Kamdar [14] the embrittling effect is increased with increasing grain size. Kamdar and Joseph are more specific and mention that the fracture stress decreases linearly with the reciprocal of the square root of the grain size, thus following the well known Cottrell-Petch relationship of grain size dependence on fracture stress. Glickman observes that for copper in LBE, an increase in the grain size leads to a reduction in total elongation and an increase in crack propagation.

Nicholas and Old [23] however, come to the conclusion that the influence of the grain size on the LME process depends on the system studied. For the couples copper – mercury and brass – mercury, the increase of grain size favours the embrittlement but the opposite is observed for aluminium in contact with a tin – zinc alloy.

Furthermore, the authors disagree on the effect of grain size on the ductility recovery temperature, T_R. According to Nichols and Rostoker [32] the T_R temperature is increased with increasing grain size linear to *log(d)*. However, Kamdar concludes that T_R decreases with increasing grain size linear to $d^{-1/2}$.

The hardness of the solid metal can also affect its susceptibility to LME. It is generally accepted that the hardest materials are more severely embrittled. However, this may be offset if the hardness increase is achieved by cold working since cold working can decrease the grain size.

Empirical rules for the prediction of LME

Based on a systematic study of a large number of solid metal / liquid metal couples, Rostoker *et al.* [20] conclude that neither the melting temperature of the embrittler, nor the chemical reactivity, nor the shape of the thermodynamic phase diagram allows prediction of LME. They do propose two empirical rules for the occurrence of LME:

- Low mutual solubility of liquid metal embrittler and solid metal;
- Absence of intermetallic compound formation.

These two empirical rules are however not to be used as an axiom since a long list of exceptions to these rules can be found in the literature.
Kamdar [14] comes to very similar empirical rules on the basis of his own study and adds a third empirical rule for the occurrence of LME to the two of Rostoker mentioned above:

- Similar values of electronegativity of the solid metal and liquid metal.

Furthermore, Kamdar concludes that LME is not influenced by the relative atomic sizes of solid and liquid metal atoms.

These empirical rules, despite many exceptions, do support the notion of specificity of LME which is a point of discussion throughout literature and which is discussed in the next paragraph.

Specificity of solid metal – liquid metal couples

Rostoker [20] claimed in 1960 that LME doesn't manifest itself apart from a certain (unknown) number of specific solid metal – liquid metal couples. He states that only certain liquid metals can cause catastrophic brittle failure of solid metals or alloys and draws up a table of susceptible and non susceptible couples based on his own experience.
This "specificity" of LME has been a point of discussion since.
Contradictive statements on certain couples can be found throughout the literature. Shunk *et al.* [24] mentions that steel and lead are described as being an embrittling couple as well as a non embrittling couple. Nicholas mentions about the copper – mercury couple that LME has been observed in the case of large grain copper material but it has not been observed for fine grained copper.
These examples show that it is very difficult to conclude whether a solid metal – liquid metal couple is embrittling even after several tests. Shunk *et al.* [24] conclude that the concept of specificity can not be justified, neither on the basis of experiments nor on the basis of available theory.

Solid metal surface effect

In several definitions of LME stated in Table 1.3, reference is made to "wetting", "perfect contact between the liquid metal and the solid" and even to "non oxidized steel". All these terms are related to the solid metal surface condition. For LME to occur, the liquid metal has to be in close contact with the solid metal atoms.
As mentioned by several authors an oxide layer on the surface of the solid metal can prevent LME from occurring [14],[18],[21]. However, many metals which are known to have a dense oxide layer are strongly embrittled by certain liquid metals [15],[17],[18]. The oxide layer will be ruptured under stress however due to the presence of dissolved oxygen in certain liquid metals such as Pb alloys, repassivation could occur. This apparent contradiction underlines the importance of the occurring phenomena at the initiation stage of LME failure.

1.3.2 Models explaining LME

As mentioned before, since little is known about LME, the true mechanism of the phenomenon has not yet been found (or at least has not been agreed upon). Several authors have tried to propose a model for LME based on their proper findings combined with available literature.
In the following, we will discuss these models and their shortcomings based on the phenomenological features of LME described in section 1.3.1 above. The first four models we discuss are the most commonly accepted ones. However, for reasons of completeness, it was considered to be useful to also include three other models often found in literature.

Reduction in surface energy model (Rostoker, Rehbinder)

The so called "reduction in surface energy model" is based on the concept that the surface free energy is reduced by adsorption of a surface active substance. The model was first proposed by Rozhanskii and Rebinder (quoted in Rehbinder and Shchukin [33]) who mostly worked on organic surface active liquids but later expanded their work to liquid metal embrittlement and hydrogen embrittlement. They showed that the adsorption of surface active substances results in a decrease in fracture strength.

The reduction in surface energy approach uses the Griffith equation which considers the energy balance between the decrease in potential energy of a stressed body owing to the release of stored elastic energy and the work done by moving the newly formed crack surfaces and the increase in surface energy due to the formation of new crack surfaces.
Griffith [20] treated the problem of fracture in an isotropic solid containing a thin sharp elliptical crack of length 2C within the body of the specimen and oriented in a plane normal to the stress axis. This led Griffith to show that the stress required to fracture a purely elastic material is related to the surface energy by the following equation:

$$\sigma = \left(\frac{2E\gamma_e}{\pi\left(1-\nu^2\right)C} \right)^{1/2} \qquad \textbf{(1.5)}$$

Where σ is the externally applied tensile stress, ν is the Poisson ratio, E is the Young's modulus and γ_e is the specific surface energy.

It can be seen from Equation 1.5 that if the surface energy is reduced due to adsorption of a liquid metal at the crack tip, the applied stress required for fracture is equally reduced.

The use of Griffith's equation was promptly criticised because it was derived for purely elastic material behaviour and could therefore never account for crack tip plasticity.
A different approach to this problem was proposed by Gilman [34], who showed that by assuming the material to be perfectly plastic, the fracture energy can be written according to the following equation:

$$\gamma_f = A\gamma_e \qquad \textbf{(1.6)}$$

Where A is a constant equal to the ratio of the cohesive strength, σ_o, to the yield strength, σ_y, which in the case of steels is about 100. Using this equation, small changes in γ_e leads to large changes in the fracture energy. Experimental results have been successfully explained using this approach [16].

It was shown by Rostoker [20] that brittle fracture by wetting and reduced surface energies are associated thru the use of the Petch-Stroh relationship between fracture stress and grain size:

$$\sigma_F = \sigma_0 + Kd^{-1/2} \qquad \textbf{(1.7)}$$

Where

$$K = \left[\frac{6\pi G\gamma}{1-\nu}\right]^{1/2} \qquad \textbf{(1.8)}$$

By using this equation, which is very similar to the Cottrell-Petch equation, the effect of grain size and strain rate on LME can be explained as well as the change of the slope of the curve of grain size versus fracture strength when testing in surface active media.

To explain the initiation of fracture, Rostoker [20] suggests that the crack nucleus is generated as a result of sub-surface slip. Only those dislocation pile-ups whose stress fields reach the liquid metal-solid metal interface can take advantage of the low-energy surface generation. The suggested mechanism is based on visual observation that cracks can nucleate on intersections of slip planes in MgO crystals.
Crack propagation is assumed to occur by progressive rupture of atomic bonds and the creation of new surface. No plastic deformation of the material would be needed for the crack to propagate.

Despite the strong support for the reduction in surface energy model due to good correlations with experimental observations, several rather severe limitations to the theory are left unanswered.
Lack of accurate surface energy data has prevented more thorough verification and application of this model to other LME examples. Furthermore, it is unclear how the reduction in surface energy model can account for the effects of various metallurgical and physical variables known to affect the occurrence of LME.
Finally, the model is strongly based on thermodynamic considerations to the problem of LME. The attempts to explain the phenomenon on an atomic scale in the frame of the model are insufficient and do not provide insight into the mechanisms of embrittlement on an atomic scale. The reduction in surface energy is therefore regarded by many authors as a necessary but not sufficient condition for LME [14],[15],[16],[18].

Adsorption induced reduction in cohesion model (Stoloff, Johnson, Westwood, and Kamdar)

The adsorption induced reduction in cohesion model was independently proposed by Stoloff and Johnson on one hand and Westwood and Kamdar on the other. It is therefore sometimes referred to as the SJWK model in review papers [17].

The adsorption induced reduction in cohesion model is an extension of the surface energy reduction model and focuses on the effect of the liquid metal on the strength of interatomic bonds at the crack tip [14]. Consider the crack shown in Figure 1.9.

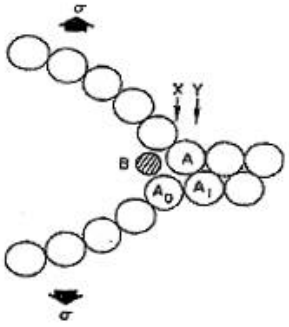

Figure 1.9: Displacement of atoms at the tip of a crack;
the bond A-A_0 constitutes the crack tip and B is a liquid metal atom (schematic) [14].

Crack propagation will occur by repeated breaking of bonds of the type A-A_0, A-A_1, etc. These bonds might be expected to have potential energy separation distance curves of the form U(a) as indicated in Figure 1.10.

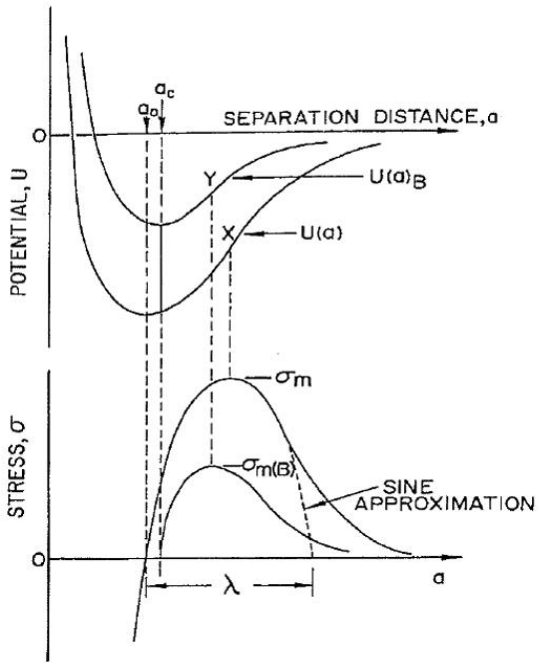

Figure 1.10: Schematic potential energy, U(a) and $U(a)_B$, and resulting stress, σ(a) and $\sigma(a)_B$, versus separation distance curves for bonds of type A-A_0 (Figure 1.9) in the absence and presence of chemisorbed atom B. For spontaneous chemisorption of B, $a_c = a_0$. For strain-activated chemisorption, $a_c > a_0$ [14].

In Figure 1.10 a_0 is the equilibrium distance between atoms across the fracture plane. The stress, σ, between atoms A and A_0 varies as (dU/da) from σ=0 at $a=a_0$ to a maximum value of $\sigma=\sigma_m$ at the point of inflection of the curve U(a). A tensile stress of magnitude σ_m acting at the crack tip would cause the bond A-A_0 to break. Assuming that the actual σ(a) curve can be approximated by one half of a sine curve, and that its wavelength, λ, represents the effective range of interatomic forces, it can be shown that [34]:

$$\sigma_m = \left(\frac{E\lambda}{\pi a_0} \right) \qquad \textbf{(1.9)}$$

If the work done in breaking A-A_0 bonds is then equated to the surface free energy of the subsequently created fracture surfaces, γ, it can also be shown that [34]:

$$\sigma_m = \left(\frac{E\gamma}{a_0} \right)^{1/2} \quad \textbf{(1.10)}$$

Next, assume that the liquid metal atom B at the crack tip reduces the strength of the bond A-A_0. The chemisorption reaction involved in the process may occur spontaneously or only after atoms A and A_0 have been strained to some critical separation distance, a_c. In any case, the model assumes that the bond A-A_0 becomes inherently weaker. This leads to a change in the form of its potential energy separation curve, which may now for better understanding be considered similar to $U(a)_B$ in Figure 1.10. As the applied stress is increased, the stress acting on A-A_0 may exceed its now reduced breaking stress, $\sigma_{m(B)}$. This causes the bond to break and the crack to propagate to point Y in Figure 1.9. Consequently atom B comes in contact with freshly created surface and may chemisorb thus weakening bond A-A_1. This procedure is then repeated until failure of the specimen.
The cracking process is limited by the arrival of liquid metal atoms at the crack tip and it is assumed that the liquid metal is able to keep up with the propagating crack tip.

According to these hypotheses, crack initiation will also be facilitated by the adsorption of liquid metal B atoms at the surface. Moreover, if chemisorption is strain activated, it will occur preferentially at sites of stress concentration such as the vicinity of piled-up groups of dislocations at high angle grain boundaries, surface notches and surface microcracks.

An alternative approach to explain the adsorption induced reduction in cohesion model is to first determine the true fracture surface energy for the cleavage plane, γ, of a particular solid metal which is directly related to σ ($\sigma=\sigma_m$ in Equation 1.10) and then show that γ is reduced in the presence of an active liquid metal.
Consider the propagation of a semi-elliptical crack of length C in a thin plate under the action of tensile stress σ_a, perpendicular to the length of the crack. The maximum tensile stress acting at the crack tip, σ_c, can then be written as [14]:

$$\sigma_c = 2\sigma_a \left(\frac{C}{R} \right)^{1/2} \quad \textbf{(1.11)}$$

Where R is the radius of the crack tip. The minimum radius of curvature having physical significance is given by $R=a_0$. For such an atomically sharp crack to propagate, σ_c must exceed σ_m (Equation 1.10 and Figure 1.10) and the applied stress necessary to achieve this, $\sigma_a=\sigma_P$ from Equations 1.10 and 1.11 is:

$$\sigma_P = \left(\frac{E\gamma}{4C} \right)^{1/2} \quad \textbf{(1.12)}$$

In practice, most cracks are not atomically sharp but are blunted by plastic relaxation in the vicinity of the crack tip. Therefore, the radius of curvature at the tip increases from $R=a_0$ to some larger value, $R=R_1$. Nevertheless, to propagate a plastically blunted crack, the stress acting on the bond $A\text{-}A_0$ at the tip must exceed σ_m.
Assuming $R_1/a_0=\rho$, then from Equations 1.11 and 1.12 it can be shown that for a blunted crack:

$$\sigma_P = \left(\frac{E\rho\gamma}{4C} \right)^{1/2} \quad \textbf{(1.13)}$$

In other words, the energy involved in propagating a blunted crack is simply $\rho\gamma$, where ρ is a dimensionless, variable ratio (R_1/a_0) dependent on the amount of plastic relaxation at the crack tip, and therefore on temperature, propagation rate, yield stress, metallurgical composition and structure, etc.
It is important to remark that this analysis, independently also made by Gilman [34] and Stoloff and Johnston [29], suggests that the crack propagation energy is directly related to the surface free energy, γ, and should not be calculated as the sum of the surface free energy plus a plastic relaxation energy term, p.
Considering again the situation in Figure 1.9, it can be seen that to propagate the crack from X to Y under a reduced stress due to the presence of embrittling liquid metal atom B, it is only necessary to decrease the strength of bond $A\text{-}A_0$. This means that the embrittling action of B is independent of the radius of the crack tip. Therefore it is suggested by Kamdar [14] to define a coefficient of embrittlement, η, relating the energy absorbed in breaking bonds at the crack tip in the presence and absence of an embrittling phase. The total energy involved in the propagation of a crack in a metal would then be written as $\eta\rho\gamma$, where η and ρ are simple and independent ratios, η being an environmental variable and ρ a plastic relaxation variable.

The adsorption induced reduction in cohesion model is widely accepted and although many questions remain unanswered, it has been used extensively to account for experimental results [16]. Although the acceptance of the model is not based on actual measurements of decreased bond strength, fractographic studies have been used to validate the adsorption induced reduction in cohesion model. If LME failures occur by tensile decohesion than fracture surfaces are expected to be microscopically flat and featureless with little or no plastic deformation. Such surfaces have indeed been reported. However this is not always the case in LME

studies. In many cases of LME, fracture is accompanied by extensive localised plasticity, ductile tearing and the formation of a dimpled fracture surface.

In later work, Kamdar [28] states that the reduction in tensile cohesion is predominantly responsible for the occurrence of embrittlement, although both tensile as well as shear cohesion are reduced. Embrittlement can also occur by the adsorption induced reductions in the shear strength of the atomic bonds at the crack tip. Kamdar [28] uses this second type of reduction in cohesion mechanism to explain the occurrence of a minority of LME cases where the fracture surface is clearly dimpled while ductility and elongation to fracture are clearly diminished. This second mechanism is actually the model proposed by Lynch which we discuss in the next section.

Enhanced dislocation emission model (Lynch)

This model, based on ductile fracture behaviour, was proposed by S.P. Lynch [35] and is therefore often referred to as the Lynch model.

The enhanced dislocation emission model, like the SJWK model, is also based on the decrease of interatomic bond strength due to chemisorption or adsorption of liquid metal atoms at the crack tip. The model however significantly differs from the SJWK model, since in the enhanced dislocation emission model the interatomic shear strength is decreased and not the interatomic tensile strength as in the SJWK model.

According to Lynch there is insufficient time for diffusion or dissolution processes in liquid metal embrittlement due to the fast crack propagation in several cases. Furthermore, many embrittled couples have very limited or no mutual solubility. Even in tests where diffusion of atoms ahead of cracks was allowed to occur, subsequent transcrystalline cracking in inert environment was ductile [35]. This leads Lynch to the conclusion that LME is due to chemisorption.
The chemisorption can only have a limited number of effects [35]:

- chemisorption reduces the stress required for tensile separation of atoms at crack tips;
  (ref. adsorption induced reduction in cohesion model)
- chemisorption hinders the nucleation or egress of dislocations at the crack tip [36];
- chemisorption facilitates the nucleation or egress of dislocations at the crack tip [35],[37],[38],[39],[40].

The first two possibilities favour tensile decohesion at atomically sharp crack tips while the last, Lynch's model, promotes localised slip.

Detailed fractographic study is used to support the idea that chemisorption facilitates the dislocation nucleation. The presence of dimples (sometimes extremely small <0.1 μm) on fracture surfaces, the evidence of considerable strains adjacent to fracture surfaces and extensive slip around crack tips, particularly on planes intersecting the crack tip are used as arguments to support the proposed theory.

Figure 1.11 illustrates the difference between ductile crack growth in inert environment and in liquid metal environment as described by Lynch [35].

In inert environments, if dislocation nucleation at the crack tip is very difficult relative matrix slip, crack growth by slip will not occur until near surface dislocation sources are activated on slip planes which:

- exactly intersect the crack tip;
- are at angles greater than 90° to the crack.

Near surface sources which meet the above requirements and which can be activated at low strains are probably uncommon. Therefore, large strains and large plastic zones develop around the crack before significant crack growth occurs. Fractures are not parallel to particular crystallographic planes probably because the egress of dislocations which produced crack growth occurs in a chaotic fashion at tips of cracks and voids.

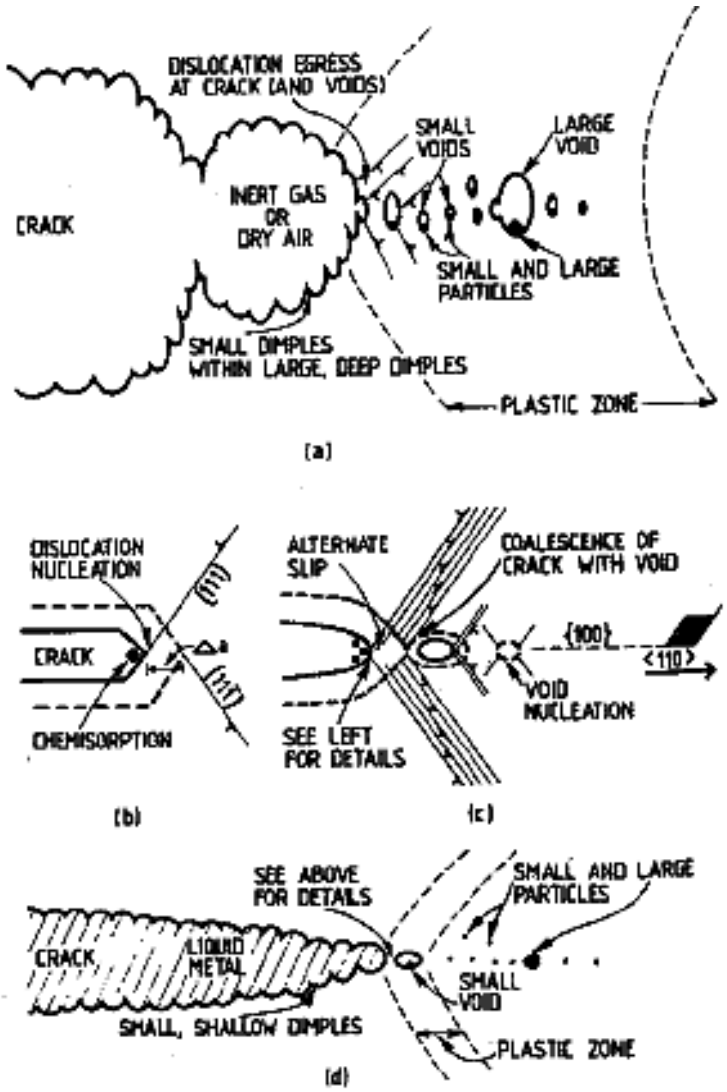

Figure 1.11: Diagrams illustrating crack growth according to the Lynch model in (a) inert environments, and (b)-(d) liquid metal environments [35].

In liquid metal environments however, nucleation of dislocations at crack tips occurs readily compared with extensive matrix slip and crack as soon as dislocations are nucleated and move away from crack tips. It is hereby assumed that nucleation of dislocations is a more difficult process than their subsequent movement and that the local shear stress is sufficient for their continued movement once nucleation occurs. Roughly equal amounts of slip on planes either side of the crack should occur since more dislocations emitted on one side would create a larger back stress counteracting further dislocation nucleation on the more active side. Now, if some

general matrix slip occurs and produces nucleation and growth of voids just ahead of cracks, then cracks growing predominantly by alternate slip will link up with voids. This way, dimpled fracture surfaces, having much more shallow dimples, will be produced.

Void nucleation at sites other than particles, e.g. dislocation cell boundaries, is regarded possible and is given as a justification of the proposed mechanism for LME in pure materials [35].

Lynch attributes the decrease in embrittlement with increasing temperature to the more rapid occurrence of desorption, compound formation or dissolution at the solid metal / liquid metal interface at higher temperatures.

The comparison of LME, stress-corrosion cracking and hydrogen embrittlement [37],[38],[39],[40] leads Lynch to suggest that the proposed mechanism is applicable to embrittlement produced by other environments.

Although the fractographic analysis performed by Lynch certainly appear to be very thorough and the arguments are rather convincing, several limitations to the model do exist.
It is not clear whether some of the chemical cleaning methods are completely unreactive with the solid metal. Despite the repeated proof that the replicating techniques used in his study do not introduce artefacts, the use of the term "dimple" for sometimes very shallow relief in fracture surfaces and the lack of independent support for the reported observations do undermine the credibility of the model.
Gordon [25] has also pointed out that the enhanced dislocation emission model can not account for the delayed failure observed in some LME studies. Lynch has explains this as follows: crack initiation sometimes involves the slow development of a notch of critical depth and acuity by injection of dislocations facilitated by adsorption [17].
Kapp [16] has shown that in torsion tests on notched alpha brass specimens, crack propagation occurred along the plane of maximum tensile stress. This is inconsistent with the enhanced dislocation emission model which predicts that fracture occurs along the plane of maximum shear stress. It should be noted however, that the crack initiation in liquid metal environment did occur in the plane of maximum shear stress and at a lower torque and angle of twist than in inert environment [16].
However, the most important limitation to the model was emphasised by Kamdar who notices that adsorption effects on dislocations will be limited to several atomic spacings due to electronic screening effects and will therefore not be felt at larger distance in the bulk of the solid ahead or in the vicinity of the crack tip. According

to him, these effects are secondary in importance when compared to breaking of inter-atomic bonds where liquid metal is continuously absorbed at the tip of a propagating crack.

Stress assisted dissolution model (Robertson, Glickman)

This model is often referred to as the dissolution-diffusion based model of Robertson. It was later modified by Glickman, under the name dissolution-condensation model (DCM), in an attempt to solve the models shortcomings.

The stress assisted dissolution model of Robertson is based on the concept that the presence of liquid metal at the crack tip results in dissolution of the solid metal at the crack tip. The local dissolution is enhanced by stress and capillarity effects. The dissolved atoms than diffuse through the liquid metal filled crack away from the crack tip allowing the crack to propagate.

The main purpose of this theory was to give an expression for the crack propagation rate. The model makes no reference to the crack initiation stage. It uses only macroscopic, thermodynamic and elastic concepts to come to an equation that is intended to explain the observed crack propagation rates.

So, consider a crack of length 2L, of thickness 2r and with a tip radius, r, subject to an applied stress, σ_a. The stress distribution around the crack tip establishes a gradient in the chemical potential at the tip, which causes a diffusion flux through the liquid away from the crack tip. The magnitude of the stress at the tip of a long, narrow crack due to the applied stress, σ_a can be written as:

$$\sigma = 2\sigma_a \sqrt{\frac{L}{r}} \qquad \textbf{(1.14)}$$

In the presence of an unstressed, flat surface, the concentration of the solute in the liquid metal is equal to the equilibrium concentration, C_0. However, inside a crack in a stressed material, the concentration of the solute in the liquid metal will be the equilibrium concentration, C_0, plus an excess concentration due to the applied stress, σ, at the crack tip, $\Delta C(\sigma)$, plus the excess concentration due to capillarity, $\Delta C(\gamma)$.
After calculations by Robertson (referred to in [17]), the excess concentrations are given by:

$$\Delta C(\sigma) = \frac{C_0 2\Omega L \sigma_a^2}{ErkT} \quad \textbf{(1.15)}$$

$$\Delta C(\gamma) = -\frac{C_0 \Omega \gamma}{kTr} \quad \textbf{(1.16)}$$

Where Ω is the atomic volume of the solid, E is the Young's modulus of the solid metal, k the Boltzmann factor, T the temperature in Kelvin and γ the solid-liquid interfacial energy.
Consequently, the concentration of solute at the crack tip is:

$$C = C_0 + \frac{C_0 \Omega}{kTr}\left(\frac{2L\sigma_a^2}{E} - \gamma\right) \quad \textbf{(1.17)}$$

The flux, J, of the solute atoms away from the crack tip is given by Fick's first law:

$$J = -D\left(\frac{\delta C}{\delta x}\right)_{x=0} \quad \textbf{(1.18)}$$

Where D is the diffusion coefficient of the solid in the liquid.

The velocity of the crack is defined by:

$$v = -\Omega J \quad \textbf{(1.19)}$$

Thus, the expression for crack propagation rate becomes:

$$v = \left(\frac{C_0 D \Omega^2 \gamma}{kT}\right)\frac{1}{r^2}\left(\frac{2L\sigma_a^2}{E\gamma} - 1\right) \quad \textbf{(1.20)}$$

The effect of capillarity, as expressed by the (-1) in Equation 1.20, provides a threshold stress for crack propagation. Setting *v* equal to zero gives the classical Griffith criterion for the critical stress to obtain propagation.

We can now deduce the maximum crack velocity from Equation 1.20: the tip radius cannot be less than about the interatomic distance of the lattice atoms, d. Furthermore, σ, cannot be greater than E. If γ/r is small compared to E/2, than we can write the maximum crack propagation rate as the product of three terms:

$$v_{\max} = \frac{1}{2k}\frac{\Omega^2 E}{d}\frac{C_0 D}{T} \quad \textbf{(1.21)}$$

In Equation 1.21, the first term is a numerical constant, the second term is determined only by the properties of the solid and the third term depends on the interaction of the solid and the liquid and contains most of the temperature dependence of the crack velocity.

Although the model does predict a maximum crack velocity in the same order as those observed in several investigations of LME, there is not a lot of support for the model and several authors have criticized the stress assisted dissolution model by Robertson [16], [17].
Popovich [41],[42] remarks that according to the model of Robertson, the degree of embrittlement must increase with increasing solubility of the solid metal in the liquid metal. This does not agree with experimental observations of LME. Moreover, Popovich states that as the solution process becomes more important, the crack is blunted and the embrittlement would be suppressed.
Kamdar [14] points out that the third term in Equation 1.21 increases as temperature increases. Therefore, the crack velocity would increase with increasing temperature which is not in agreement with the observed behaviour of most embrittlement couples.
The assumption that solubility will increase under an applied stress is also questionable [16]. While it is conceivable that a stressed solid will dissolve more easily into a liquid, the solvating ability of the liquid is not expected to be affected by stress.

In defence of these arguments, Robertson remarks that in all of the discussion, the crack tip radius, r, has been left as an unspecified parameter. The tip radius will depend on the differential rates of dissolution and on the dynamic yielding around the tip. This yielding behaviour can vary significantly with composition, heat treatment and temperature.
However, since it is very difficult to predict the behaviour of r with varying T, it is not at all clear how the crack velocity would vary with temperature.

According to Glickman [43], the model of Robertson is oversimplified because it does not take into account the possibility of relaxation of the elastic stresses during blunting of the crack.
For Glickman, the nucleation and subcritical growth of cracks which take place along grain boundaries are associated with selective dissolution of solid metal atoms at the crack tip. This dissolution is enhanced by the adsorption of liquid metal atoms, which favours the nucleation of dislocations. These dislocations are creating an atomic roughness at the solid-liquid interface which enhances dissolution of solid metal atoms from the crack tip (see Figure 1.12).

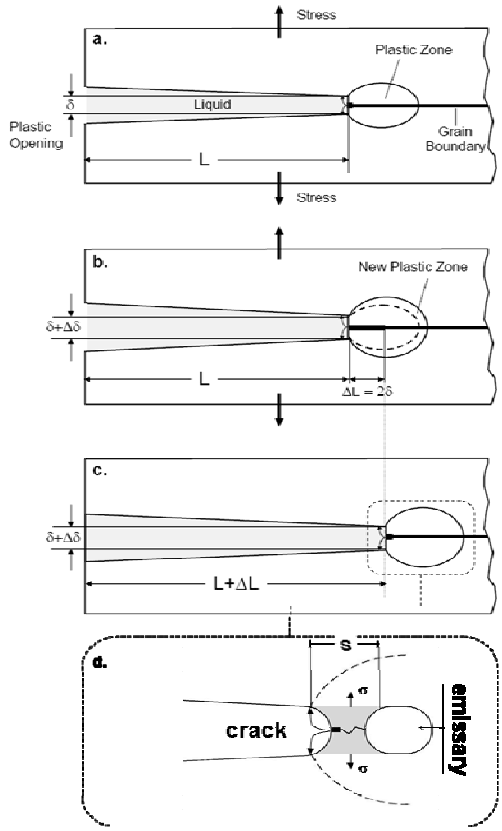

a, b, c: Crack extends by emitting a short thin channel (shown in black) into the GB, or into the localized slip band, and periodic blunting to the equilibrium δ(L). Small arrows show direction of diffusion in liquid metal that fills the major crack; fast mass transfer in the channel is by the admetal promoted surface diffusion.

d: Stress induced dissolution by DCM causes thinning of the 'internal neck' (shown by grey), triggering its strain controlled instability, rupture, and thus fast crack extension in the plastic zone. The emissary void forms due to high strain ahead of the crack.

Figure 1.12: Crack extension by Dissolution –Condensation Mechanism (a-c) and by combination of DCM with the strain controlled instability in the plastic zone (d). Schematic [43].

According to Glickman there are three kinetic stages for microcrack failure:

1. Crack initiation, which results from selective dissolution of the grain boundaries in the melt. The melt filled grooves are formed where grain boundaries exit to the surface.
2. Crack precritical propagation which is the controlling stage of failure according to Glickman. It is a slow crack propagation whose duration depends on the crack rate during this stage and the critical length, l_c, at the moment of transition from subcritical to hypercritical growth. The rate of subcritical growth does not depend on the crack length. The variation in subcritical crack growth with applied stress is described as follows:

$$v = \frac{\delta L}{\delta \tau} \approx \alpha(\sigma - \Delta) \qquad \textbf{(1.22)}$$

   Where L is the crack length, α the crack mobility, σ the applied stress, Δ the threshold stress of subcritical growth and τ the time.
3. Crack supercritical propagation which is due to the achievement of a certain critical deformation level in the plastic zone near the crack tip.

In Glickman's model for LME, the accelerated fracture under the influence of surface active melts is associated with the simultaneous influence of two factors:

- The exceptionally high diffusion of the melt filling the crack, which ensures fast removal of dissolved atoms from the crack tip by diffusion.
- The high degree of atomic roughness of the metal – melt interface which is related to the low specific surface energy at the interface. Due to the high degree of atomic roughness, the dissolution rate is increased.

In comparison with the initial model by Robertson, the model proposed by Glickman presents some improvements. Glickman's model makes a difference between nucleation and propagation and has better interpretation of the effect of temperature. However, the model still faces the problem that high solubility of the solid in the liquid enhances the embrittlement, which is in strong contradiction with the majority of experimental data.

Glickman discards this argument by stating that the mechanism still works when solubility tends to zero due to reaction of impurities which form compounds soluble in the melt. He also proposes another possible explanation, with the mass transfer from crack tip to the metal bulk by volume or grain boundary diffusion or even along the melt-metal interface.

Enhanced Work hardening model

The enhanced work hardening model was proposed by Popovich and Dmukhovskaya. The model is based on the decrease of surface energy by the Rebinder effect in combination with enhanced plastic flow. The enhanced work hardening model is therefore constructed on the combination of a thermodynamic and an atomistic approach. It is a purely qualitative model which does not give any quantitative expressions for time to rupture or crack propagation rate.

Popovich stresses that not all forms of liquid metal embrittlement are based on the same mechanism [41]. For metals and alloys whose mechanical properties are influenced by the presence of liquid metals where dissolution of the solid or diffusion of the liquid into the solid are not observed, he suggests the following mechanism [41],[42],[44],[45]:

1. Adsorption of active liquid metal causes easing of plastic deformation in the surface layers of metal caused by a reduction in surface energy at the boundary between the phases.
2. Surface active media, including liquid metals, promote the occurrence of plastic deformation in the surface layer not only as a result of easing the outlet of dislocations to the surface but also as a result of reducing the stress for the origin and start of dislocations. In the case of ductile materials this eliminates the barrier effect of the surface and increases their ductility.
3. The increased generation of dislocations under conditions limiting relaxation (low temperature, high strain rate, low defect packing energy) favours an increase in dislocation density in the surface layers of the metal. This means stronger local work hardening.
4. Strengthening of the surface layer by work hardening promotes the nucleation of microcracks at smaller degrees of deformation than in the absence of surface active media.
5. After the crack passed thru the strengthened layer, its further development will be retarded in the more ductile matrix. However, the crack will resume after an increase in its opening to a value less than in vacuum since the influence of the medium on deformation of the local zone near the tip of the crack is similar to the influence on the free surface. As a result of this, crack propagation will occur with lower energy consumption.

Within the framework of this model, the possibility of appearance of LME is determined by two factors: reduction in surface energy and the properties of the solid under specific conditions of plastic deformation.

Popovich explains the experimental results discussed in section 1.3.1 by the fact that coarse grain structured materials are more strain hardened and less relaxed when the average grain size is increased. Actually, decreased strain hardening in fine grain structures is explained by the easier movement of dislocations in fine grain structures as a result of the presence of a multitude of boundaries with high energy disorientation. The model's prediction corresponds with the observations that LME is more severe at high strain rates, relatively low temperatures and with high average grain sizes.

The enhanced work hardening model has a number of similarities with Lynch's one. Most of the comments that have been made about the enhanced dislocation emission model are still relevant here. Therefore, we will now focus on the main differences between the two proposed models based on ductile failure.
Popovich proposes that the adsorbed liquid metal, besides the nucleation of dislocations, promotes new slip planes and work hardening, the latter not being developed in Lynch's model. Moreover, according to Popovich, the influence of the dislocations can be felt at a great distance from the crack which is impossible according to Kamdar because of electronic screening effects [17].

Hancock and Ives' model

Hancock and Ives have proposed a model in which embrittlement results from the interaction of dislocation pile-ups and liquid metal atoms diffusing ahead of the crack tip [16]. They studied the embrittlement of a copper aluminium alloy in mercury.
Embrittlement was associated with extensive localised plasticity and fracture surfaces were faceted and featureless.
The model is based on plastic flow occurring around the crack tip during loading which results in the formation of dislocation pile-ups at grain boundaries immediately ahead of the crack. Crack growth would then be caused by the combination of liquid metal atoms, which penetrate short distances ahead of the crack tip and the stresses resulting from the dislocation pile-ups.

The advantages of the model are that it can qualitatively predict the effects of temperature, strain rate, solid metal composition, microstructure and prior cold work. The magnitude of the stress concentrations at dislocation pile-ups ahead of the crack depends on the number of dislocations and the amount of stress relaxation that can take place.
With increasing temperature, the amount of stress relaxation is increased due to increasing dislocation mobility and therefore, embrittlement will be suppressed. The

transition from brittle to ductile behaviour at elevated temperatures can thus be accounted for.
At high strain rates, insufficient time is available to allow stress relaxation by dislocation movement and embrittlement is therefore observed up to higher temperatures.

Despite the advantages of this model, it has several severe limitations [16].
First, the model assumes that LME failure is always intergranular. It can therefore not explain the occurrence of LME in single crystals nor the reported cases of transgranular failure. It is questionable whether dislocation pile-ups at sub grain boundaries or slip plane intersection points in single crystals will induce sufficient stresses to cause crack initiation. Second, it is very uncertain whether diffusion ahead of the crack tip could occur at the very fast crack growth rates often observed in LME.

Grain boundary penetration model (Gordon & An, Rabkin)

The observations of delayed failure in liquid metal environment (both SMIE and LMIE) of 4140 steel by indium led Gordon and An [25] to suggest a mechanism involving stress-aided embrittler diffusion penetration of the base metal grain boundaries. The model suggests that crack initiation is preceded by stress assisted diffusion of the embrittling atoms into the base metal along the grain boundaries.
In the case of single crystals, diffusion occurs along sub grain boundaries and dislocation arrays.

The presence of embrittler atoms in the diffusion zone increases the difficulty of slip and reduces the resistance to cracking. Once a critical concentration of embrittling atoms is present in the diffusion zone, crack initiation occurs. At high stresses and temperatures, diffusion occurs more rapidly and crack initiation times are reduced. At low temperatures the rate of diffusion becomes rate limiting.
The instantaneous failure observed in some LME couples is said to occur at temperatures high enough such that the loading time is longer than the time required for the formation of a diffusion zone and crack initiation.

The dependence of embrittlement on temperature, strain rate and grain size are explained by the influence of these variables on the diffusion process. At high temperatures bulk diffusion of the embrittler into the solid metal becomes more favourable and thus reduces the concentration of embrittler along the grain boundaries. Embrittlement is therefore suppressed, leading to a brittle to ductile transition at high temperatures [23]. At high strain rates insufficient time is available

for diffusion to occur and higher temperatures are required for bulk diffusion to suppress embrittlement [18]. The effect of grain size on embrittlement can be explained by considering the grain boundary area. The smaller the grain size, the larger the grain boundary area and therefore the lower the concentration of embrittler in the diffusion zone.

The grain boundary penetration model by Gordon and An was originally proposed by M.A. Krishtal (mentioned in the conclusions of Gordon and An [25]) and has been used to explain several experimental observations. It does however have various limitations.
A mathematical analysis of the model has never been carried out. Therefore, the possibility of embrittler atom diffusion into the base metal to a sufficient extent has not been confirmed. Furthermore, experimental results have shown that embrittlement is most severe in couples showing limited mutual solubility.

Driven by the observation that simple grain boundary diffusion (ref. Gordon and An) is too slow to supply sufficient embrittler atoms from the liquid phase in cases of fast LME fracture, Rabkin [27] proposed a slightly different model to explain LME by grain boundary penetration. The suggested model combines features of the Gordon model and of the "adsorption induced reduction in cohesion" or SJWK model.

The Rabkin model is based on the complete wetting of grain boundaries by the melt which causes grain boundary disordering and formation of grain boundary quasi-liquid phase in the single phase regions of the phase diagram. Theses disordered grain boundaries exhibit a diffusivity which is comparable to that in the liquid phase and therefore high enough to supply the gradual decohesion zone at the crack tip with sufficient embrittling atoms.

The model of Rabkin does account for a possible explanation of high velocity cracks sometimes encountered in LME. It is however based on full grain boundary wetting and penetration of the liquid metal into the solid. This is experimentally observed for the aluminium – gallium and copper – bismuth couples studied by Rabkin but as mentioned before, LME is often observed in couples showing limited or no mutual solubility. In fact, to our believe, Rabkin discusses intergranular corrosion of metals by liquid metals in stead of liquid metal embrittlement.

LME Models overview

To summarize the features, support and limitations of the LME models discussed here, an overview is given in Table 1.4.

Despite the existence of these proposed models, many if not all of these models can not be verified by quantitative measurement or straightforward application and the mechanism can only be "felt" intuitively or be supported by fracture surface observations.

Table 1.4: Comparison of principal features of existing models for LME [16]

Model	Principal features	Support	Limitations
Reduction in surface energy	▪ Thermodynamic approach based on reduction in surface energy for fracture in liquid metal environments ▪ Failure is usually intergranular	▪ Experimental support ▪ Can account qualitatively for effects of many experimental observations, e.g. temperature, strain rate and grain size	▪ Lack of surface energy data prevents qualification of embrittlement ▪ Does not consider mechanism of embrittlement on atomic scale
Adsorption induced reduction in cohesion	▪ Adsorption of liquid metal reduces cohesive strength across atomic planes ▪ Failure is by transgranular or intergranular cleavage	▪ Can account qualitatively for effects of many experimental observations, e.g.; temperature, strain rate and grain size ▪ Fractographic support	▪ Difficult to quantify ▪ Can not account for all experimental observations
Enhanced dislocation emission	▪ Adsorption of liquid metal atoms facilitates nucleation and movement of dislocations ▪ Failure is by localised ductile microvoid coalescence	▪ Experimental support ▪ Strong fractographic support ▪ Many similarities with other environmentally assisted cracking phenomena	▪ No mathematical analysis ▪ Based on fractographic analyses which are difficult and complicated to carry out ▪ Lack of independent support ▪ adsorption effects on dislocations are limited to several atomic spacings
Stress assisted dissolution	▪ Crack growth is through stress assisted dissolution of solid metal in liquid metal at crack tip	▪ Limited experimental support	▪ Lack of experimental support ▪ Predicts wrong dependence of LME on liquid metal composition

Enhanced work hardening	▪ Adsorption of liquid metal atoms facilitates nucleation and movement of dislocations ▪ Enhanced dislocation activity results in work hardening and exhausts plasticity ▪ Cracking is intermittent	▪ Experimental support for discontinuous crack growth ▪ Can account qualitatively for effects of many experimental observations, e.g. temperature, strain rate and grain size	▪ No mathematical analysis ▪ Lack of experimental support for enhanced work hardening
Hancock and Ives	▪ Liquid metal diffuses along grain boundaries ahead of crack tip and reacts with dislocation pile-ups to reduce fracture stresses	▪ Correctly predicts that LME fracture is accompanied by extensive plasticity ▪ Mathematical analysis has shown that rapid LME cracking is feasible under these conditions ▪ Can account qualitatively for effects of many experimental observations, e.g. temperature, strain rate and grain size	▪ Can not account for transgranular fracture of fracture of single crystals ▪ Lack of experimental support for concept of liquid metal diffusion ahead of crack tip
Grain boundary penetration	▪ Stress assisted diffusion of liquid metal along grain boundaries ahead of crack tip ▪ Presence of embrittler ahead of crack tip increases difficulty of slip and reduces resistance to cracking	▪ Can account qualitatively for effects of many experimental observations, e.g. temperature, strain rate and grain size	▪ No mathematical analysis ▪ Lack of experimental support for concept of liquid metal diffusion ahead of crack tip ▪ Can not account for transgranular fracture or fracture of single crystals

1.3.3 Liquid metal embrittlement in lead alloys

A lot of work has been performed on liquid metal embrittlement of leaded steels [46]-[49] which have a better machinability. In these steels the embrittler is internally present due to formation of low melting constituents [49]. By comparing leaded and non-leaded steel, Warke *et al.*[47] clearly found a ductility trough as can be seen in Figure 1.13. The most important findings in the research of LME in leaded steels are that lead embrittlement was found to be common to a wide variety of leaded steels ranging from low to high carbon steels and from plain carbon steel to high alloy steels. Furthermore, the brittle to ductile transition temperature, characterizing the high temperature end of the ductility trough, did not vary in any systematic fashion in function of investigated parameters. The T_R temperature varied for all investigated leaded steels between 650 and 900 F [46] (± 350°-480°C). The T_E temperature extended some 200 F below the melting point of lead (± 240°C).
Breyer and Gordon [48] found two methods for eliminating the lead embrittlement. First, in contrast to the general trend mentioned in 1.3.1 they found that prior cold deformation reduced the susceptibility to embrittlement. Second, the addition of rare earth elements, such as Ce, La, Nd and Pr, was found to strongly reduce the embrittling effect of lead in high strength steels. In contrast to the addition of Sb, Zn, Sn and Bi, which increased the LME effect, particularly the addition of cerium eliminated the lead embrittlement.

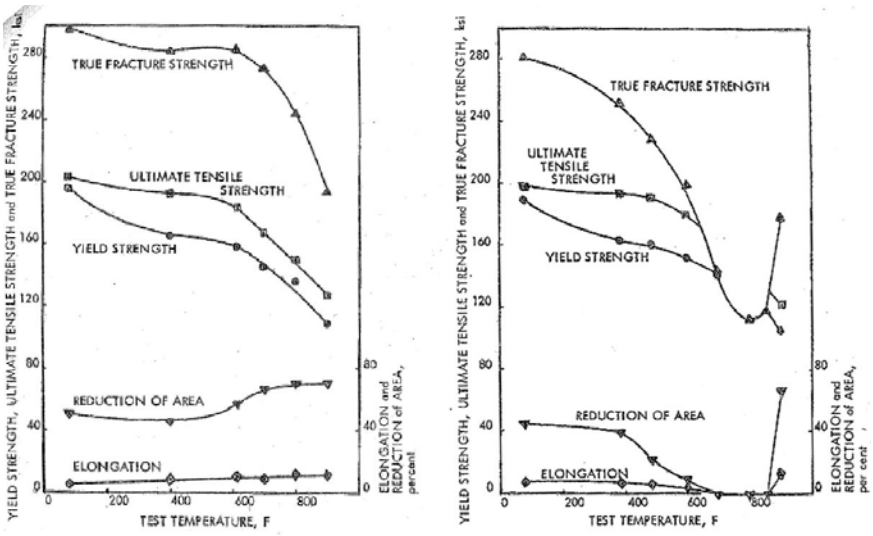

Figure 1.13: Elevated temperature tensile properties of non-leaded (left) and 0.30 % leaded (right) 4145-I steel with a nominal room temperature strength of 200 000 psi (± 1780 MPa) [47].

In leaded steels, the embrittler is added by pneumatically blowing solid lead into the liquid steel during casting. In our case however, the liquid metal is in external contact with the steel.

Smooth plain carbon steel specimens tested in liquid lead, showed recovery of ductility at approximately 510°C. In similar steel, fracture mechanics type test specimens containing sharp notches tested in liquid lead, the brittle to ductile transition occurs at approximately 650°C. Transition temperature in this case depends on the presence or absence of a stress raiser in the specimen and on the type of test method used [28].

However, in this section, we will further focus on the review of liquid metal embrittlement studies performed to verify the suitability of structural steels when in contact with liquid lead alloys for nuclear applications. More specifically, the focus will be on 316L and T91 in contact with liquid lead bismuth eutectic.

As will be seen in the following sections on LME of austenitic steels and ferritic-martensitic steels, the LME effect is not strongly present and there is no immediate catastrophic failure when stress is applied in contact with liquid lead alloys. This has very often been attributed to the lack of wetting of the liquid metal on the oxidised steel surface. Wetting studies have pointed out that lead alloys do not wet oxidised steel [50]. Furthermore, the addition of Li to Pb does not affect the wetting of deoxidised steel but it does improve the wetting of oxidised steel. To accommodate the uncertainty in results due to the difficulty of achieving wetting a variety of mechanical tests on different specimen geometries have been performed as well as several techniques to achieve wetting of the liquid metal on the surface of the solid.

In this section, we will divide the results based on the material type (austenitic and ferritic-martensitic) and furthermore, we will divide the available results based on the separate testing method. The separation between austenitic and ferritic-martensitic steels is motivated by the vast differences between these two microstructures: austenitic steels have an FCC crystal structure, 12 different slip systems, large grains, high nickel content, high work hardening capability, etc. whereas ferritic-martensitic steels have a BCC lattice, 48 different slip systems, small martensite laths, low nickel content and different flow properties than austenitic steels.

1.3.3.1 Liquid metal Embrittlement of austenitic stainless steels in lead alloys

Tensile testing

Fazio *et al.* [51] performed tensile tests on 316L after a pre-exposure in flowing, low oxygen LBE (between 3.10^{-10} and 7.10^{-8} wt% of oxygen dissolved in the LBE) for 1500 hours at 400°C. None of the tests showed any decrease in ductility or strength of the material. Furthermore, the examined fracture surfaces were fully ductile. Examination of the corrosion layer at the sample outer surface did reveal Ni depletion and consequent ferritisation to a maximum depth of 14 μm.

Low cycle fatigue testing

Low cycle fatigue testing of 316L was done both in air and PbBi at 260°C [52]. After an initial hardening, 316L softened under LCF conditions. However, the extent of softening was not influenced by the environment. As shown in Figure 1.14, the fatigue lives for 316L at lower total strain amplitudes in PbBi appeared to be similar in comparison with the results in air. At high strain amplitudes of 0.50% and 0.60%, there was a weak influence of the PbBi environment on the cycle number to crack initiation.

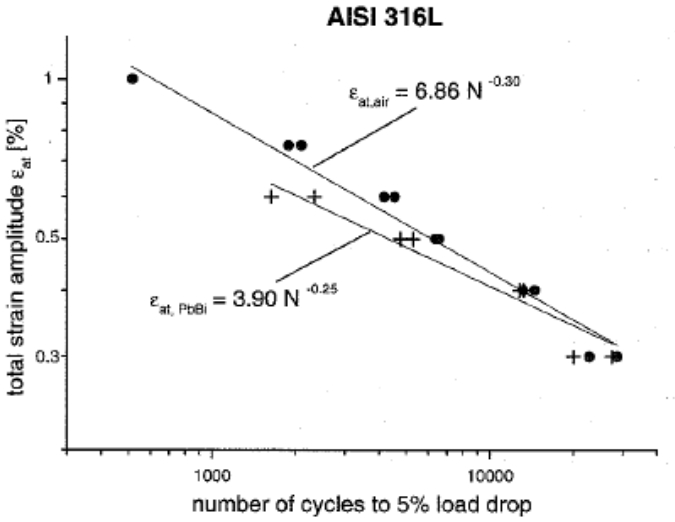

Figure 1.14: Total strain amplitude vs. cycle number to 5% load drop for crack initiation curves for 316L stainless steel in air and PbBi at 260°C [52].

The data were analyzed according to the Coffin-Manson law [52] and for 316L the Coffin-Manson exponent in PbBi was 0.25 compared to 0.30 in air. This lower exponent indicated different fatigue fracture mechanisms in air and LBE.
It is thought that the good fatigue resistance of 316L in LBE is caused by the formation of stable protective oxide layers on the surface of 316L during testing [52].

1.3.3.2 Liquid metal Embrittlement of ferritic-martensitic steels in lead alloys

Tensile testing

The vast majority of experimental data on LME research of T91 in contact with LBE concerns tensile data. The problem of wetting or intimate contact between the liquid LBE and the base metal leads to a lack of reproducibility and is discussed in most papers. Several methods are used to attempt to avoid the uncertainty of liquid metal wetting at the surface. Among these methods the most common are pre-exposure in stagnant LBE, pre-exposure in flowing LBE and use of a chemical soldering flux.
Apart from the effect of wetting enhancing techniques on the occurrence of LME of T91 in LBE, the effect of the presence of surface defects and thermally hardening of the T91 steel are discussed.

Di Gabriele *et al.* [53] tested T91 in the standard condition in contact with LBE without any surface modifications and found a significant environmental assisted cracking (EAC) effect at 300°C but no degradation of the mechanical properties at 500°C. They attributed the difference to the rate of formation of a passivating oxygen layer on the newly cracked surface which was sufficiently fast to prevent embrittlement at 500°C. Examination of the fracture surfaces of samples tested at 300°C, showed clear evidence of several initiation sites of LME as can be seen in Figure 1.15. The fracture surfaces of samples tested at 500°C were fully dimpled.

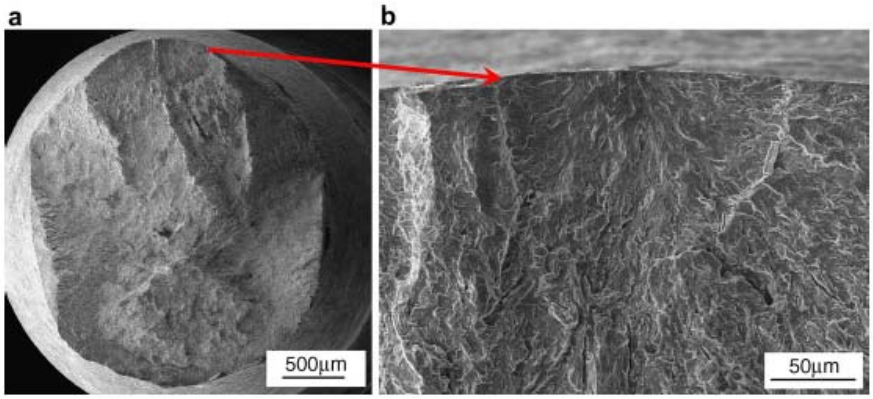

Figure 1.15: (a) Fracture surface of specimens of the as-received ferritic steel T91 after rupture under tensile load in LBE at 300 °C with a strain rate of 10^{-6} s^{-1}; (b) detail of the initiation of the brittle fracture [53].

Guerin *et al.* [54] studied the influence of wetting and liquid metal corrosion (LMC) of T91 in contact with LBE on the tensile properties of T91. They strongly linked the LMC to the wetting of the T91 surface by partial, local removal of the native oxide layer. No intergranular penetration of LBE into T91 was observed.
A corrosion study as a function of temperature led them to the conclusion that the native oxide layer of T91 remains present at temperatures below 350°C and therefore prevents wetting below 350°C. An LME effect was found on notched specimens in the standard metallurgical state, strongly dependent on the liquid and gas phases in contact. The reduction in strength and ductility passes through a maximum at 350 °C before beginning the ductility recovery at 400°C. The embrittling influence of LBE is maximized under He-4%H_2, suggesting a synergy effect of LBE and hydrogenated helium.
Tensile tests at 200°C did not show any effect of LME.

Fazio *et al.* [51] performed tensile tests on T91 after a pre-exposure in flowing, low oxygen LBE (between 3.10^{-10} and 7.10^{-8} wt% of oxygen dissolved in the LBE) for 1500 hours at 400°C. The total elongation and reduction of area of the T91, corroded in LBE, was significantly less than that of the non corroded T91 when tested in LBE at 400°C and a strain rate of 3.10^{-1} s^{-1}. However, yield and tensile strength remained the same.
Corrosion examination of the surface revealed transgranular and intergranular dissolution of steel elements, indicating good wetting. The fracture surface was predominantly dimpled however on one side, the periphery showed a flat surface with the presence of microcracks.

The problem with the use of pre-exposure in low oxygen LBE or purging with He + 4% H_2 to obtain reducing conditions and favour wetting is that these methods can be quite time consuming and do not guarantee successful intimate contact between the liquid and the solid metal. To overcome this problem, Auger *et al.*[55] has examined the possibility of using physical vapour deposition (PVD) of PbBi onto the surface and the use of soft chemical fluxing.

In the first case, the oxide layer of the sample was first removed by ion sputtering in an UHV chamber and verified by depth profiling chemical analysis. In a second step, a layer of PbBi with a thickness of a few hundreds of nanometres was applied on the surface on the oxide free sample by PVD.

Following PVD deposition, the sample was tensile tested at 340°C. The results revealed a partial embrittlement which was considered due to the very limited amount of PbBi available on the surface. The periphery of the sample's fracture surface was clearly broken in a brittle manner. This led the authors to conclude [56] that martensitic T91 steel is prone to LME by Pb–Bi but that this behaviour can easily be hindered by the passivation layer of these steels unless special means of oxide removal is used. No special metallurgical state is needed to induce embrittlement. The fracture mode was little influenced by prior austenitic microstructure but seemed to be a mix of transgranular and intergranular cracking with respect to martensitic platelets. Prior plastic deformation seems to be required before cracking can be observed and cracking seems to propagate without initiation incubation time.

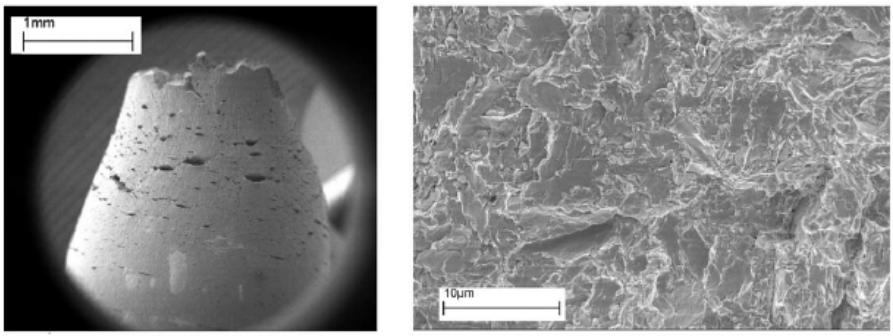

Figure 1.16: In case of direct T91-LBE contact obtained by ion beam sputtering in a UHV chamber prior to deposition of lead–bismuth, LME effects are produced: (left) multicracking of the gauge length of the specimen, as a result of transgranular failure initiated from the surface and (right) top view of a transgranular rupture faces of a crack initiated at the surface [56].

The second method applied by Auger *et al.* [55] to obtain wetting, is the use of a soft soldering flux (mixture of zinc chloride with 7 wt% of ammonium Chloride). The oxide film is dissolved in the flux and then the specimen is coated with liquid Pb–Bi protected from air by the flux to prevent re-oxidation. Quasi-cleavage cracking was also observed using this surface preparation technique, however, in these tests,

intimate contact is only partially reached on the overall specimen surface. The areas in direct contact seem to be sufficient to induce brittle cracking. The fluxing method is far more practical and seems to produce the same results. However, impurities introduction at the interface may modify the severity of embrittlement in an uncontrolled manner and constitutes the main drawback of the method. Indeed, one finds traces of fluxes by EDX analysis on the surface of the specimen, coming most likely from residual flux due to the soldering process. Nevertheless, no contamination was detected along the cracks.

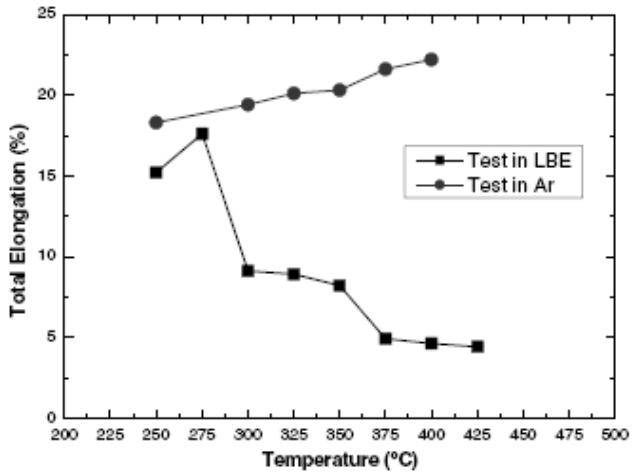

Figure 1.17: The total elongation versus testing temperature for Group-I specimens tested in LBE (where the embrittlement occurs) and in Ar [57].

Dai *et al.* [57] also examined the embrittlement effect of LBE on martensitic steel T91 by performing slow-strain-rate tensile (SSRT) tests in static LBE with about 1 wppm oxygen at temperatures ranging from 250 °C to 425 °C. In contrast to the previous work we discussed, performed on cylindrical tensile specimens, Dai *et al.* uses dog bone shaped specimens, cut by electron discharge machine (EDM) cutting. However, no chemical fluxing was used to promote wetting in these experiments.
Two groups of samples were used. Group-I samples with microcracks on the lateral surfaces resulting from the EDM cutting, indicated clearly LBE embrittlement effect at temperatures between 300 and 425°C (see Figure 1.17), while Group-II samples without microcracks (electro-polished + mechanically polished to remove micro-cracks at the surface) did not show any LME effect. The LBE embrittlement effect occurred after the necking of specimens started. The yield and ultimate tensile strengths and uniform elongation were not affected. SEM observations showed the specimens ruptured in a brittle fracture mode when the embrittlement occurred. The difference in fracture appearance can clearly be seen in Figure 1.18, where the fracture surface of a sample tested in argon (left column) is compared to the fracture surface of a sample tested in LBE (right column).

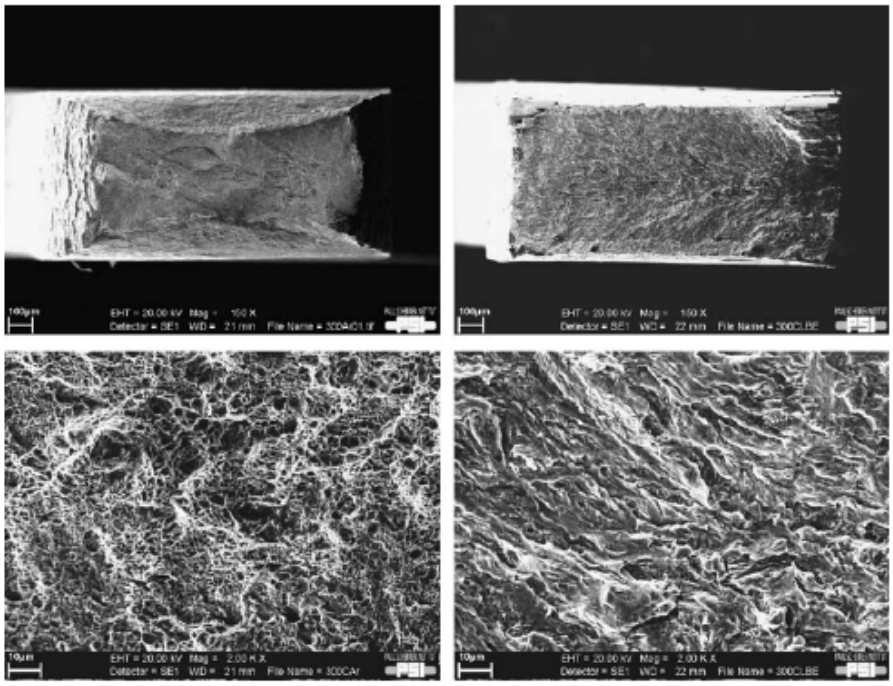

Figure 1.18: Fractographs of Group-I specimens tested at 300 °C in Ar (left column) and in LBE (right column) [57].

It was concluded by Dai *et al.* that the requirements for the susceptibility of LBE embrittlement effect on the T91 steel are: surface cracks or flaws, wetting and a certain level of stress concentration at crack tips. Dai *et al.* state that based on their observations, the adsorption induced reduction in cohesion model, discussed in 1.3.2, is the proper one [57].

Long *et al.* [58] examined the susceptibility of EDM cut, rectangular T91 specimens to LME after different heat treatments. They re-austenitised the steel by heating it to 1050°C for 60 minutes and used three tempering conditions (2 hours of tempering time):

- Tempering at 760°C, which is the normal tempering treatment of T91 and could be compared with the standard T91 material;
- Tempering at 600°C;
- Tempering at 500°C.

The lowering of tempering temperatures does not change the prior austenite grain (PAG) size but does change the precipitate structure. In HT500 (Figure 1.19a and b) the precipitates were mostly located inside the laths and the PAG boundaries were almost free of precipitates. With the tempering temperature increasing to 600°C (HT600, Figure 1.19c and d), dense and relatively small precipitates formed in the laths and also a lot of precipitates appeared at PAG and lath boundaries.

Tests were performed at a strain rate of 1.10^{-5} s^{-1}, at temperatures between 150°C and 500°C and with a maximum oxygen concentration of 1 wppm in the LBE.
The standard tempering condition revealed significant decrease of total elongation in the range of 300 to 450°C. The material that was tempered at lower temperature, demonstrated more pronounced embrittlement, (HT600: embrittled between 150 and 400°C; HT500 embrittled between 150 and 450°C) reflected by wider and deeper ductility-troughs which suggests that martensitic steels with higher strength are more susceptible to LBE embrittlement. This is in agreement with the general statements on the influence of hardness and strength on LME as discussed in 1.3.1.

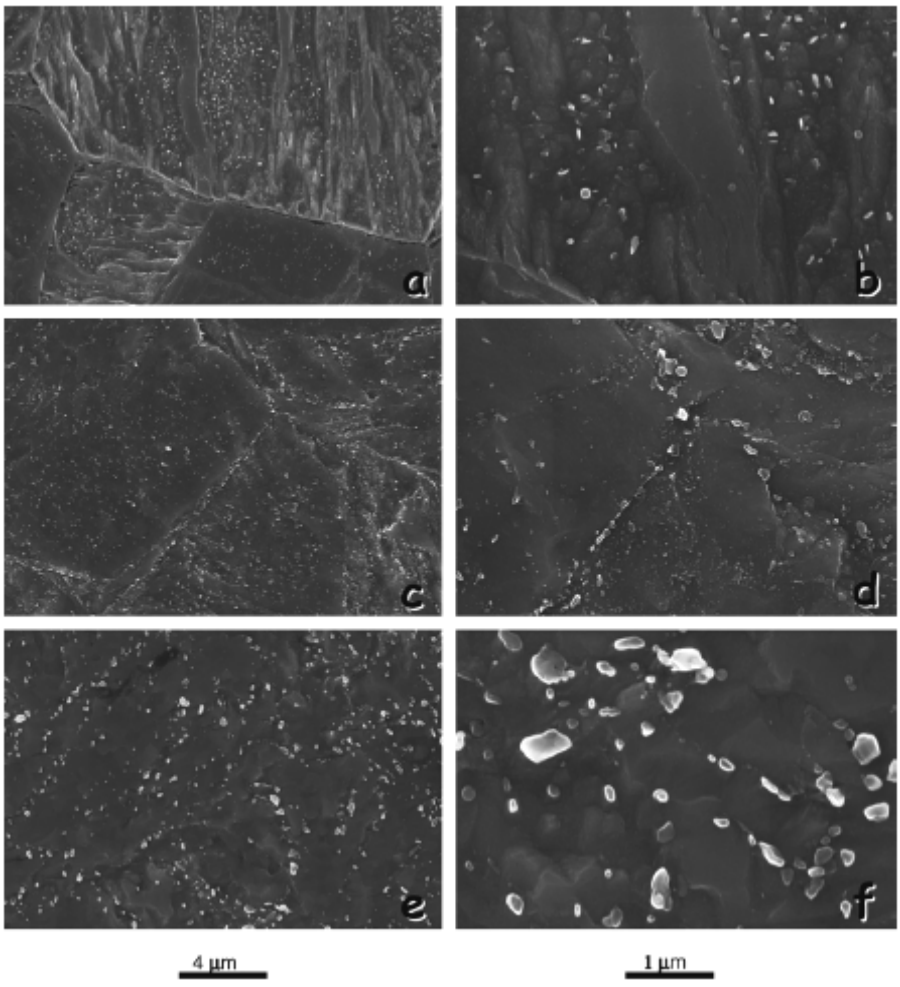

Figure 1.19: SEM observation on the distribution of carbide precipitation in: (a) the HT500, (c) the HT600 and (e) the HT760 specimens. Graphs (b), (d) and (f) are of a higher magnification for (a), (c) and (e) respectively. The scales at the bottom are for the graphs in the left and right columns [58].

Bend testing

Glasbrenner *et al.* [59] thoroughly investigated U-bent T91 specimens exposed to LBE, Bi and Pb-17Li at 300°C for 1000h. They used T91 steel both in the standard condition (±240 $HV_{0.05}$) and in a hardened condition, called T91* (420 $HV_{0.05}$) by lowering the tempering temperature to 500°C. The aim was to investigate possible preferential penetration of one of the elements into the matrix along grain boundaries.
T91 steel in the standard condition did not show any LME neither in the straight, nor in the bent part of the specimen. Furthermore, no corrosion attack was visible. T91* also did not show any corrosion attack, nor LME after exposure to LBE. It is mentioned also here that this might be due to the presence of the oxide layer which has not been affected. However, T91* exposed to both Bi and Pb-17Li showed severe corrosion attack on both the straight and bent part of the sample. Furthermore, signs of LME are present on the bend part of the specimen but the absence of failure is attributed to the stress distribution in U-bent specimen geometry.

Small Punch testing

Serre *et al.* [60] studied the sensitivity of T91 to LME by using the small punch test (SPT) at 300°C, both in air and in contact with LBE. In this test, a tungsten carbide ball is punched into a disc. The loading mode is initially biaxial and is considered to be an intermediate between uniaxial tensile testing and triaxial testing of notched specimens. The surface of the specimens are mechanically polished up to 1200 grit and subsequently electropolished. No special techniques were used to remove the native oxide of the T91. T91 was used in the standard condition as well as in the thermally hardened condition (no tempering, ±380 HV_{10} and tempering at 500°C, ±400 HV_{10}).

In its standard condition T91 did not undergo any embrittlement during SPT when in contact with LBE at 300°C. The disc shaped specimen deformed very similar under both environmental conditions showing circular cracks. Both thermally hardened varieties did however show significant embrittlement in contact with LBE at 300°C. When tested in air, the T91 tempered at 500°C did already show some mechanical behaviour deviating from the expected ductile behaviour. Fracture surface analysis did show a fully ductile fracture for the tests in air. The radial crack component was clearly more important in these materials when tested in contact with LBE and the fracture surface analysis showed predominant transgranular brittle cleavage fracture with occasional areas of intergranular brittle fracture.

Low cycle fatigue testing

Vogt *et al.* [61] examined the low cycle fatigue resistance of smooth, cylindrical T91 specimens in air and in LBE at 300°C. The stress response to strain cycling was nearly the same for tests in air as in LBE. However, similar to the effect of LBE on the fatigue resistance of ferritic-martensitic MANET-II steel [52], they found a strong reduction in fatigue resistance of T91 when in contact with LBE. This decrease in fatigue resistance can be seen in Figure 1.20 and is said to be at least a factor two [61]. This strongly suggests a role of LBE on crack initiation and propagation. Furthermore, in LBE, a further reduction in fatigue resistance was observed after the introduction of a hold time (Figure 1.20) and after pre-exposure of the samples to low oxygen LBE at 600°C.

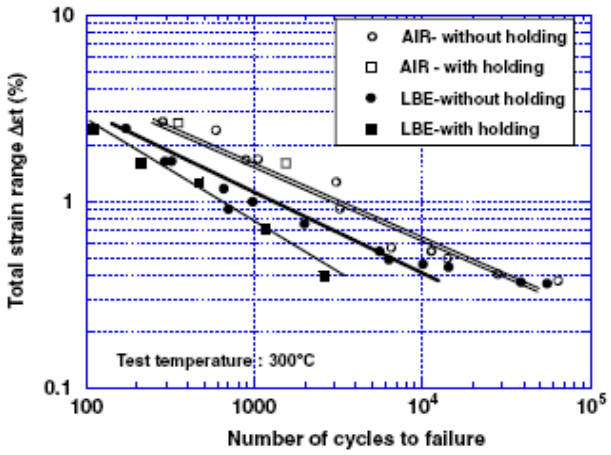

Figure 1.20: Fatigue resistance of T91 according to the environment and the mechanical loading conditions [61].

In contrast to specimens tested in air, fracture surfaces of the specimens fatigued in LBE were flat and perpendicular to the loading axis regardless the applied strain range. Furthermore, they only exhibited a single crack initiation site whereas specimens tested in air clearly showed several initiation sites of which the propagating cracks later coalesced. The presence of fewer but larger cracks when fatigued in LBE is explained by the fact that LBE would assist the propagation of the first short crack so that nucleation and propagation of other cracks would be prevented. The grain boundary resistance to crystallographic growth vanishes according to Vogt, when LBE is present at the crack tip, allowing easy extension of the crack into the bulk.

The oxide layer present on the T91 surface after pre-exposure in oxygen saturated LBE at 470°C appeared to limit the LBE-fatigue damage by preventing contact between the LBE and the steel.

Heinzel *et al.* [62] on the contrary found no effect of LBE on the fatigue life time of T91 at 550°C. The absence of any LME effect was attributed to the temperature which would have been above the upper limit of the ductility trough of the T91-LBE couple.

Fracture toughness testing

Due to the opaque and conducting nature of liquid LBE, none of the conventional methods for determination of plane strain fracture toughness of T91 in LBE could be used. Furthermore, the standard precracking procedure by fatigue recommended in ASTM-1820 discards any insurance of liquid metal wetting at the crack tip.
Therefore Auger *et al.* [63] used CCT geometry specimens to be able to visually follow the crack extension using a relatively simple CCD camera. Instead of precracking the CCT specimens prior to testing, they are treated with a chemical flux allowing wetting to be achieved at the notch root.
The most important drawbacks of this method are firstly that one can only measure crack advancement on the surface, which may differ significantly from the crack advancement in the centre of the specimen. Secondly, the specimen geometry is loaded in plane stress condition instead of the mostly used plane strain fracture toughness condition. This means the obtained fracture toughness results are mostly qualitative and are more indicative for the behaviour of cladding tube material than for structural components.

The loading sequence used is to load the sample for 30 to 60 seconds duration at constant cross-head displacement rate (0.04 mm/min). Then the specimen is unloaded to 10% of the maximum load reached during the loading sequence. The crack length is then measured optically and the overall sequence repeated until one of the two cracks reaches the edge of the sample. The force and displacement are recorded during the experiment and correlated with the crack length at any time in the post test analysis. The reported fracture mechanics results are based on one single experiment of the T91/LBE combination in comparison with reference measurements. The embrittlement effect of LBE on T91 in this geometry, using the chemical fluxing method to achieve wetting, had been proven reproducible at various cross-head speeds.

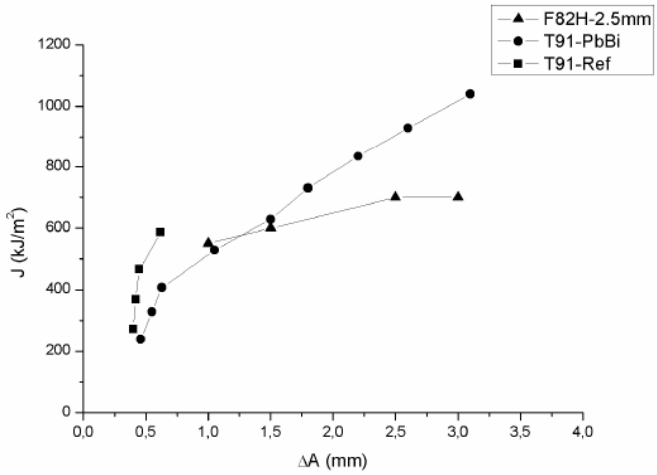

Figure 1.21: J - Δa curve of T91 reference and T91 in contact with PbBi at 160°C. The triangles represent the F82H reduced activation martensitic steel data with 2.5 mm thickness [63].

T91 was tested in air and in LBE at 160°C. In case of ductile rupture in air, blunting at the crack tip lead to a CTOD that increased rapidly up to a point where extended shear band plastic deformation prevented further analysis. In contact with LBE however, the CTOD saturated at a lower value and remained nearly constant as the crack propagated. Furthermore, stable crack growth extended to very large crack sizes before extended plastic deformation by shear band formation occurred.

J-Δa analysis of T91 in air in the CCT geometry proved impossible beyond Δ=±1 mm due to the extended shear band localization. This effect is attributed to the specimen geometry in conjunction with the martensitic material type where the work hardening rate is low. Therefore the results are only presented up to that limit in Figure 1.21.When T91 is in contact with LBE, the shear band localization occurs at a later stage and thus the test is valid up to Δa=±3 mm.
The energy needed to propagate a crack seems to be affected by the liquid metal as shown in Figure 1.21. However, in the used specimen geometry, crack propagation could not be followed to a sufficient length. Due to this restriction, it is difficult –if not impossible- to reliably evaluate the fracture toughness difference in the two environments.

To avoid the problem of shear band localization, Long *et al.* [64] have performed 3-point bending tests on T91 both in argon and in LBE environment. They used the multi-specimen technique to derive the relationship between crack length and bending displacement. The tests could then be performed using the single specimen

technique with the application of the derived relationship between crack length and bending displacement from the multi-specimen technique.

The T91 steel only illustrated a slight embrittlement effect between 200 and 400°C, displaying a reduction in J-value by 20-30% compared to the tests in argon atmosphere (see Figure 1.22).

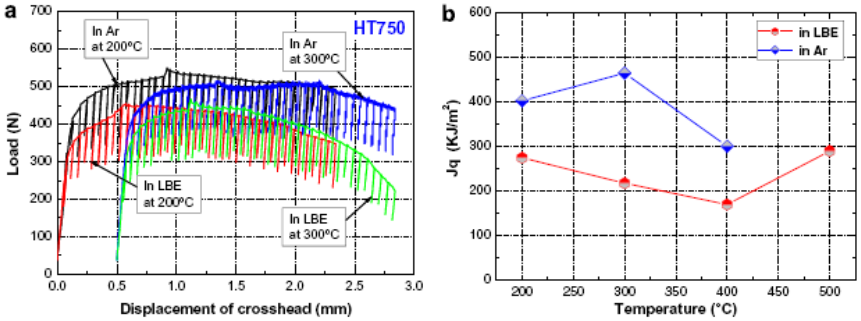

Figure 1.22: (a) Load–displacement curves of the HT750 specimens tested in Ar and in LBE at 200 and 300°C (shifted by 0.5 mm in X-axis); (b) Jq-values derived from tests at 200–500 °C in Ar (up to 400 °C) and LBE [64].

In addition, they performed thermal treatments to increase the hardness of the T91. Specimens were normalised as usual but tempering was performed at lower temperatures, being 500 and 600°C. This led to an increase of the yield stress to respectively 905 and 1205 MPa (compared to 510 MPa for standard T91). These heat treatments were performed to simulate the effects of hardening by irradiation. Although it is well established that the microstructural cause of the hardening is very different and that hardening by thermal treatment can not replace irradiation hardening studies, it can give a first impression of the possible effects.
Both the T91 steel tempered at 500°C (see Figure 1.23) and the one tempered at 600°C (see Figure 1.24) showed significant embrittlement in LBE at temperatures between 200 and 500°C, displaying a reduction in J-values of more than 50% [64].

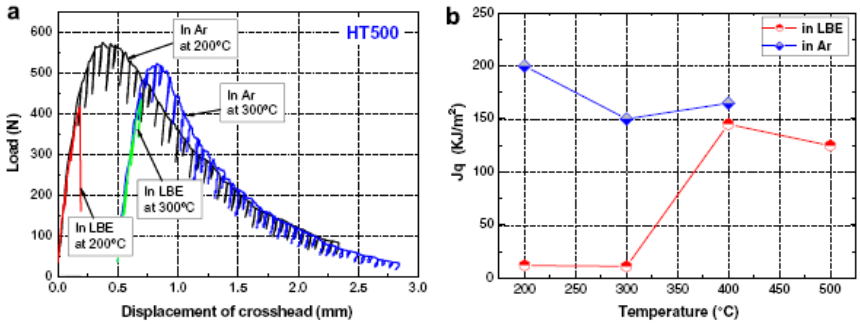

Figure 1.23: (a) Load–displacement curves of the HT500 specimens tested in Ar and in LBE at 200 °C and 300 °C (shifted by 0.5 mm in X-axis); (b) Jq-values derived from tests at 200–500 °C in Ar (up to 400 °C) and LBE [64].

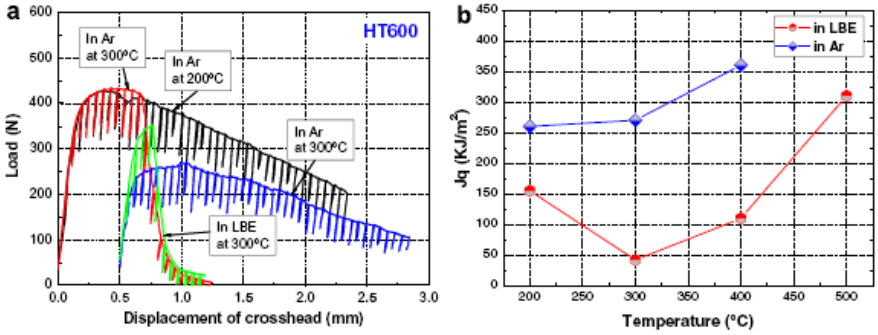

Figure 1.24: (a) Load–displacement curves of the HT600 specimens tested in Ar and in LBE at 200 °C and 300 °C (shifted by 0.5 mm in X-axis); (b) Jq-values derived from tests at 200–500 °C in Ar (up to 400 °C) and LBE [64].

1.4 IRRADIATION EFFECTS IN FERRITIC-MARTENSITIC AND AUSTENITIC STAINLESS STEELS.

Several types of neutron irradiation spectra are encountered in ADS, fission and fusion reactors. However, based on the discussion of the influential factors on LME in the previous section, it is clear that we should focus on the effects of irradiation which modify the mechanical properties or change the composition of the irradiated structural steel.

In addition to the displacement damage (displacement of atoms from their equilibrium lattice positions by energetic neutron-atom collisions and the formation of Frenkel defects) caused by both fast and thermal neutrons, the effects of transmutation caused by high energy, fast neutrons in fusion and high energy protons and neutrons in the spallation target area of an ADS should be considered.

In this section, we will summarize the most important aspects of displacement damage and transmutation on the properties of ferritic-martensitic and austenitic structural steels.

1.4.1 Irradiation induced microstructural changes

When high energy particles collide with the matrix atoms of a structural material, several reactions can occur. In case of neutron irradiation, the neutrons can be absorbed, an elastic collision reaction can take place which can be compared with the collision effects of billiard balls and at very high energies (fusion neutrons or spallation neutrons) the intersected atom can be separated into smaller atoms, which is called transmutation.
Although the absorption of neutrons can also lead to changes in the chemical composition of the structural materials and thus also cause microstructural changes in the material, we will explain the displacement damage and transmutation more in detail in the next paragraphs.

1.4.1.1 Displacement damage

Under irradiation, materials are bombarded by neutrons which affect and modify their microstructure. The atom displaced by the high energy neutron, called the primary recoil atom or knock-on atom, transfers energy to surrounding atoms, often displacing them from their normal lattice site. These atoms, in turn may also cause

displacements, resulting in a displacement cascade. The large amounts of defects created in the cascade recombine immediately after the collision took place. This is called the quenching phase. Depending on the temperature of irradiation, the amount of defects being annihilated by recombination is estimated to be around 90% as depicted in Figure 1.25. The actual number of defects that survive the displacement cascade and their spatial distribution in the solid will determine their effect on the irradiated microstructure.

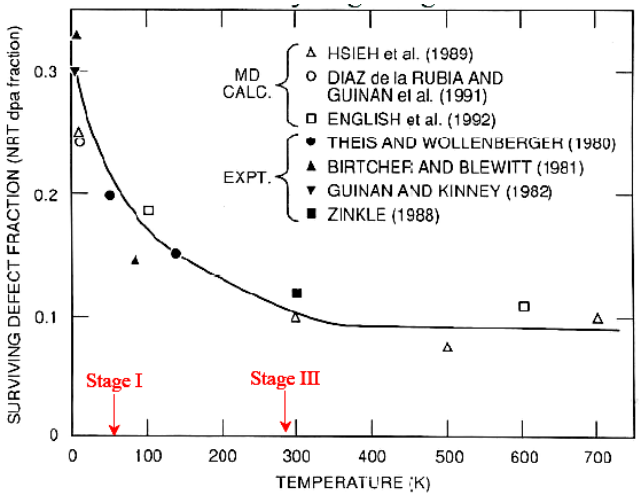

Figure 1.25: surviving defect fraction (NRT dpa fraction) as function of temperature [65].

The extent of the displacement damage is expressed in terms of how often an atom is displaced from its lattice position during the irradiation as displacements per atom or dpa. The commonly accepted model to calculate the dpa is described by ASTM E693 and is referred to as the NRT dpa (for Norgett, Robinson and Torrens, the originators of the model) [85].

The possible defects created due to neutron irradiation in crystalline structures are vacancies, self interstitial atoms (SIA), dislocation loops (interstitial or vacancy type), line dislocations, stacking fault tetrahedra, cavities (voids or bubbles) and precipitates (caused by radiation induced segregation). The defects that do not recombine in the quench phase migrate to sinks in the microstructure, where they are absorbed. These sinks could be surfaces, grain boundaries, precipitate-matrix interfaces, dislocations and existing cavities. If vacancies and interstitials are absorbed equally at sinks in the microstructure, the effects will be small. However, if they are accepted preferentially at sinks, the damage will accumulate and properties can be strongly affected.
Clusters consisting of interstitials can evolve into dislocation loops and vacancy clusters can develop into vacancy loops, microvoids or cavities.

As in non active materials, the temperature of the material has a large influence on the mobility of the created defects. With increasing temperature, the mobility of defects is increased. These "recovery stages" can be measured using electrical resistivity measurements. Five recovery stages are distinguished:

- Stage I: Initiation of self-interstitial atom migration (correlated and uncorrelated);
- Stage II: Long-range migration of SIA clusters and SIA-impurity complexes;
- Stage III: Vacancy migration (longstanding controversy on stage III behaviour);
- Stage IV: Migration of vacancy clusters and vacancy-solute complexes;
- Stage V: Thermal dissociation of (displacement cascade-produced) vacancy clusters.

For austenitic stainless steels, the typical microstructural features observed in the "low-temperature" regime, between the onset of stage III (50°C) and stage V (300°C) are small defect clusters ("black spots"), faulted dislocation loops and network dislocations. The observable densities of "black spots", faulted loops and network dislocations are nearly independent of irradiation temperature in the low temperature regime (see Figure 1.26). The black spot density begins to decrease at temperatures above 250°C and there are indications that the network dislocation density may simultaneously increase slightly [66]. Radiation produced cavities and precipitates are generally not observed in the low temperature regime. The degree of radiation induced solid segregation (RIS) is minimal due to the limited point defect mobility and the high sink strength associated with the high density of small defect clusters that are formed at low doses.

The microstructure is relatively insensitive to variations in the damage rate or He/dpa ratio in this temperature regime and reaches a "saturation" level at relatively low doses [66].

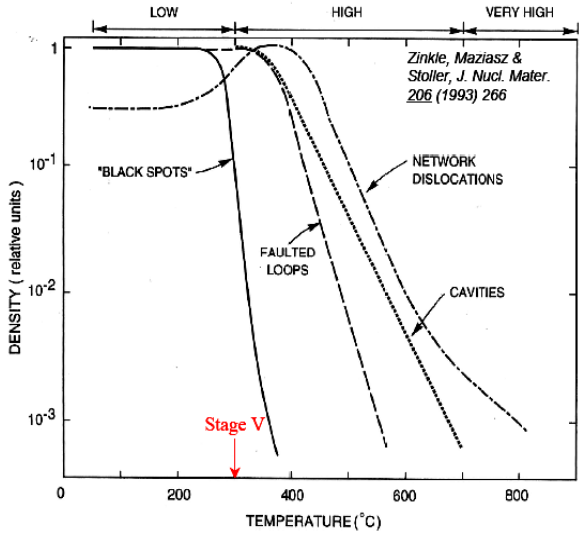

Figure 1.26: Temperature dependence of the experimentally observed "saturation" densities of the various microstructural components in neutron irradiated austenitic stainless steel [66].

At temperatures above the onset of stage V (300°C for austenitic stainless steels) up to about 700°C, the microstructural evolution during irradiation is complex and consists of cavities (helium bubbles and/or voids), dislocation loops, network dislocations and various types of precipitates. As shown in Figure 1.26, saturation densities of helium bubbles, voids, dislocation loops and network dislocations all decrease with increasing temperature in this regime. There is some evidence that the network dislocation density may reach a local maximum at a temperature near 350°C as shown in Figure 1.29 of the section on irradiation hardening, but this needs to be verified by other high dose studies [66]. High irradiation damage levels (> 10 dpa) are often required to reach a "steady state" defect microstructure in this high temperature regime due to extensive interactions between the individual microstructural components. The specific details of the microstructural evolution are sensitive to numerous parameters, including damage rate, alloy composition and He/dpa ratio.

In the very high temperature regime, above 700°C, all radiation induced defect clusters except gas pressurized bubbles are thermally unstable. Therefore, the microstructure in this temperature regime is essentially identical to the unirradiated steel microstructure, aged at the same temperature.

In ferritic-martensitic steels such as T91, the onset temperature of different defect mobility stages is slightly different, however the principles explained above and the irradiation defect types are very similar. For pure iron [67], which also has the BCC

crystallographic structure, the stage I recovery takes place between 20 and 150 K. Between 150 to 200 K stage II recovery takes place and from 200 to 300 K stage III recovery. Above this temperature, the recovery in high purity specimens is nearly complete (99% recovery). A small stage near 520 K, observed at higher irradiation doses is sometimes called stage IV. This stage is considered to be related to the rearrangement of small point defect clusters [67].

1.4.1.2 Transmutation

In addition to displacement damage, (high energy) neutrons can cause transmutation reactions with atoms of the irradiated steel and thus produce solid and gaseous reaction products. The solid products are usually other metal atoms and with a few exceptions, are not expected to produce detrimental effects to the material properties [85].
The gases produced are helium and hydrogen. Helium is produced primarily by an (n,α) reaction. This means a neutron interacts with the nucleus of a lattice atom to form a new atom nucleus and a helium ion (α-particle). Hydrogen is usually formed by a (n,p) reaction which is similar to the (n,α) reaction, however, instead of forming a helium ion, a proton (hydrogen ion) is formed. Depending on temperature, the formation of gases in the material by transmutation can lead to significant changes in the material properties (helium embrittlement) and even the materials dimensions (swelling). Swelling will be further discussed in 1.4.3.

1.4.2 Irradiation hardening

The irradiation induced microstructural defects discussed in the previous section form obstacles which hinder dislocation motion and therefore influence the mechanical properties of the irradiated material. Similar to the hardening mechanisms of point defects, dislocations, grain boundaries, precipitates, etc. in non irradiated materials, the SIA's, dislocation loops, vacancy loops and precipitates formed under irradiation will increase the yield stress of the material.

It should be obvious that since the temperature has a large influence on the mobility of the microstructural defects and therefore also on their recombination probability, that the temperature will have large influence on the change of the yield stress, $\Delta\sigma_Y$, of irradiated materials. Below 400 to 500°C (depending on the steel), irradiation induced microstructural changes lead to lattice hardening resulting in an increase in yield stress and ultimate tensile strength and a decrease in the uniform and total

elongation. The magnitude of the hardening decreases with increasing temperature until it disappears between 400 and 500°C [85].

Figure 1.27 shows changes in properties of several ferritic-martensitic steels as function of temperature. Most often, the presented results are for tests where the irradiation temperature, T_i is about equal to the testing temperature, T_t. The $\Delta\sigma_Y$ generally decreases for increasing T_t. The presented results for T_i<220°C are usually tested at room temperature [68].
There is significant irradiation hardening in ferritic-martensitic steels for irradiation temperatures up to 365°C. Above this irradiation temperature, scatter increases and both hardening and softening can occur, depending on the specific properties of both the material itself and the irradiation.

In Figure 1.28, the irradiation induced change of the yield stress is plotted as function of dpa for ferritic-martensitic steels, similar to T91, after neutron irradiation at 325°C up to 9 dpa. In these tests, T_i=T_t. The curves show a significant increase in yield strength up to 2 dpa with a slower increase at higher displacement damages.

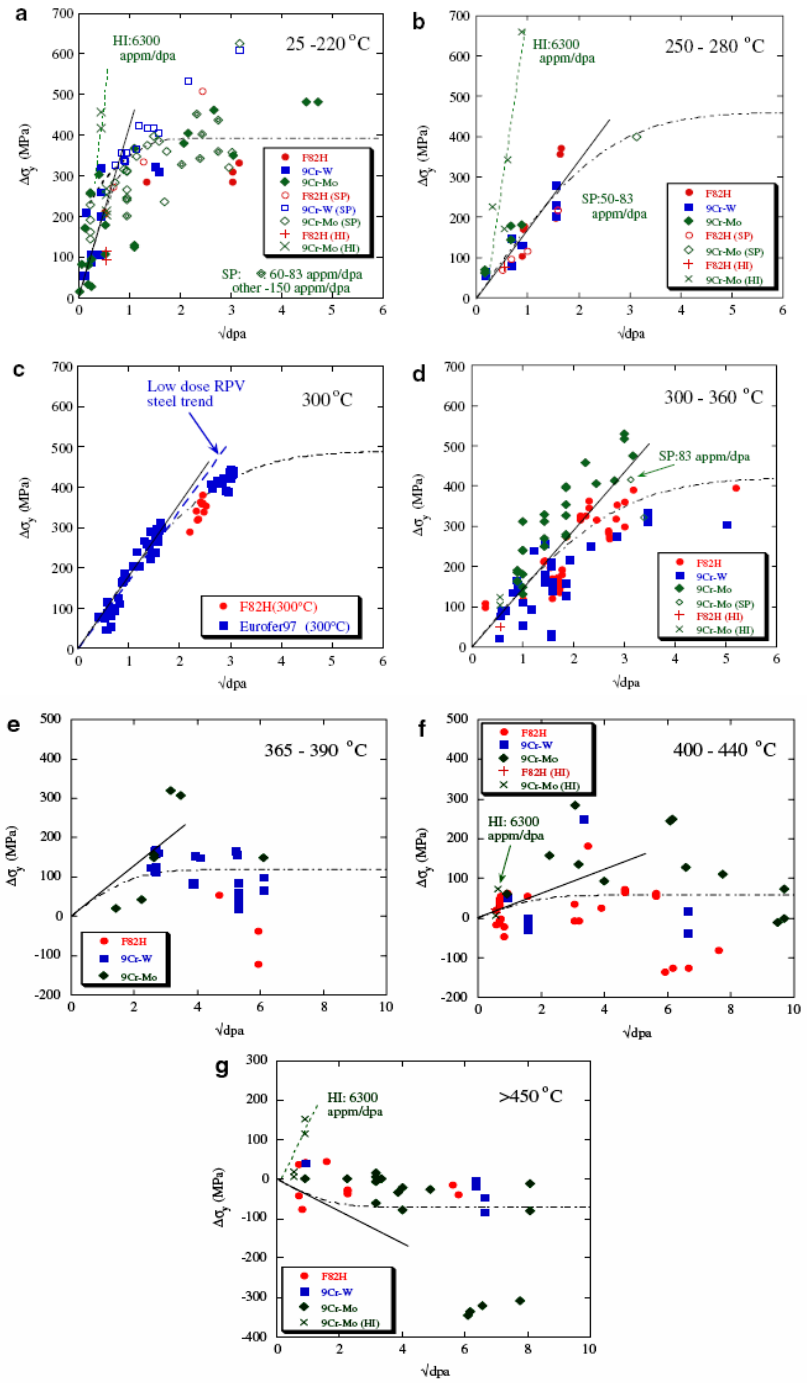

Figure 1.27: The √dpa dependences of $\Delta\sigma_y$ for the temperature bins: (a) 25–220 °C (nominal 120 °C); (b) 250–280 °C (nominal 265 °C); (c) 300 °C; (d) 300–360 °C (nominal 330 °C); (e) 365–390 °C (nominal 380°C); (f) 400–440 °C (nominal 420 °C); and (g) >440 °C (nominal 500 °C) [68].

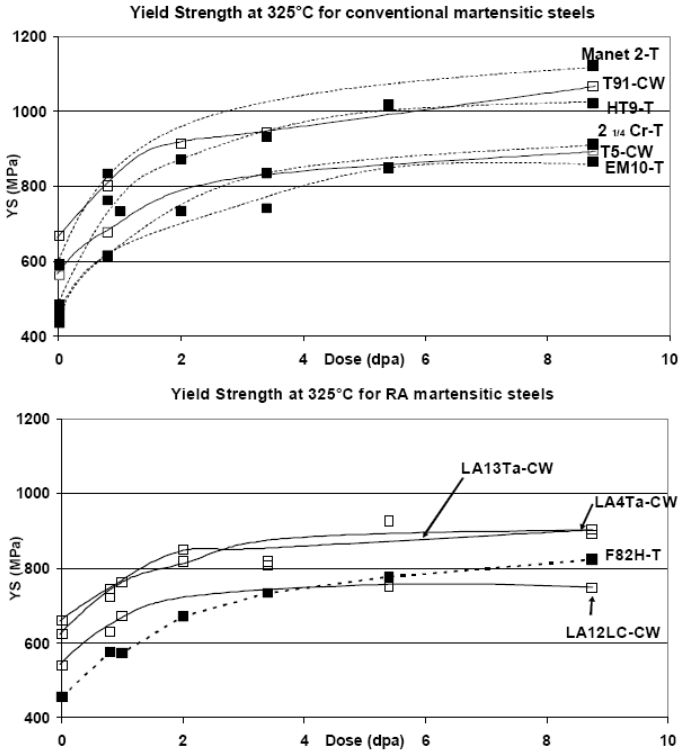

Figure 1.28: Evolution of the yield strength for (a) conventional and (b) reduced activation martensitic steels as a function of the irradiation dose [69].

In austenitic stainless steels, such as 316L, the irradiation hardening will be significant below 350°C with a sharp decline in $\Delta\sigma_Y$ above 350°C. In the low temperature regime, work hardening will be negligible or entirely absent.

The yield stress increase is plotted in Figure 1.29 as function of temperature for 316 under conditions where $T_i=T_t$. The behaviour of 316L should be similar to that of 316. However, due to the higher carbon content of 316, it has a higher yield and tensile strength. Furthermore, RIS phenomena might have a significant influence on the difference between 316 and 316L in the high temperature regime. The results for 316 stainless steel, presented in Figure 1.29 should therefore only be seen as an indication of the behaviour of 316L as function of temperature.

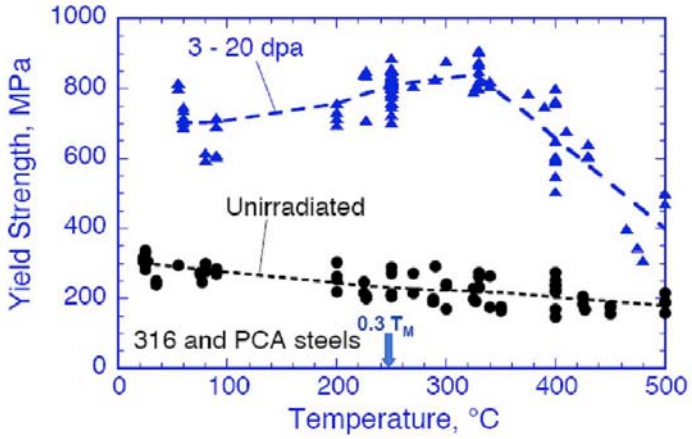

Figure 1.29: Yield strength of 316 austenitic stainless steel (irradiated vs. unirradiated) as function of temperature (T_{irr}=T_{test}) [70].

1.4.3 Irradiation induced swelling

Swelling is explained by assuming dislocations act as biased sinks for interstitials, meaning that excess vacancies must be absorbed by neutral sinks. The latter sinks are envisioned as gas atom clusters that act as void nuclei. These void nuclei will than allow bias driven void growth when they reach a certain critical size [85].
For void swelling to occur, the temperature must be high enough for the vacancies to be mobile and low enough for vacancy supersaturation to occur.

The extensive experimental data for the austenitic stainless steels [71],[85] have shown that the magnitude of the swelling depends on the major and minor elemental composition and initial thermomechanical treatment. However, these factors only affect the incubation or transient dose before the swelling in the austenitic steels accelerates to a constant rate of about 1% per dpa, independent of the irradiation temperature for temperatures in the peak swelling range (about 0.3 – 0.5 T_m) as can be seen in Figure 1.30.

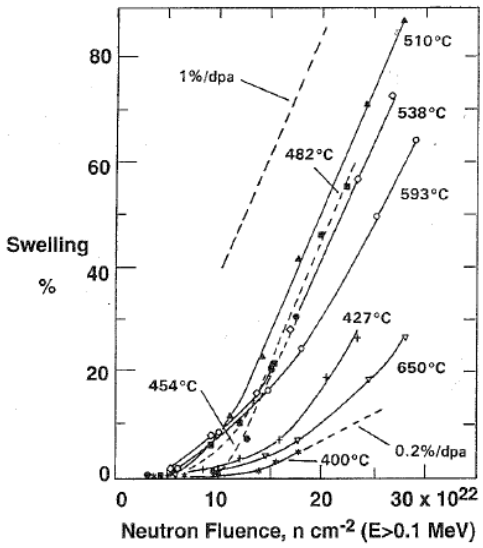

Figure 1.30: Stress free swelling of solid rods of 20% cold worked 316 during a materials test irradiation in the open core of EBR-II. The lack of scatter is due to repeated measurements and reinsertion of single specimens to further irradiation at each temperature [71].

The swelling behaviour of ferritic, bainitic and martensitic steels has also been extensively studied up to very high displacement damages and these swelling rates appear to be much lower than those observed in austenitic steels (see Figure 1.31). Garner *et al.* obtained a steady state swelling rate of ~0.2%/dpa. The reason for the low swelling rates usually observed for ferritic/martensitic steels was attributed to the longer transient stage for the bcc structure relative to the fcc structure of austenitic stainless steels [71]. The transient stage is dominated by void nucleation which indicates that nucleation is more difficult in the bcc structure. Furthermore, Garner *et al.* found the occurrence of swelling to temperatures as high as 650°C, which is well above the peak swelling temperature.

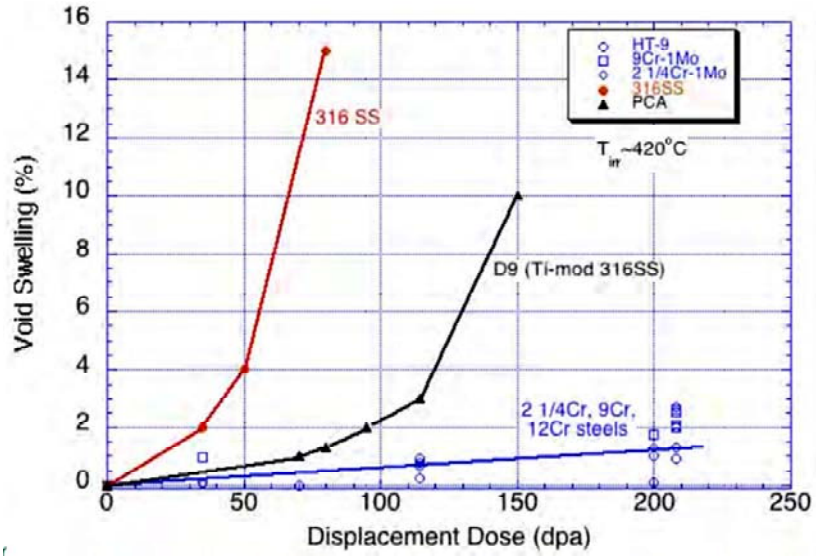

Figure 1.31: Comparison of void swelling behaviour in neutron irradiated austenitic and bainitic/martensitic/ferritic steels [71], [85].

1.4.4 Irradiation induced embrittlement

All previously discussed irradiation effects (displacement damage, transmutation, hardening and swelling) have an influence on the macroscopic mechanical properties of the structural materials. These effects lead to a decrease in the fracture toughness and in case of Charpy tests to a lowering of the upper shelf and an increase of the ductile-to-brittle transition temperature (DBTT) of the material.
In this section we describe the framework to better assess several different mechanisms of irradiation embrittlement, including irradiation hardening and various non-hardening embrittlement (NHE) processes.

Brittle fracture occurs in BCC alloys when the elevated normal stress ($\sigma_n = M\sigma_y$) in front of a notch or crack tip exceeds a critical local fracture stress for transgranular cleavage (σ_c) or intergranular (σ_{ig}) fracture over a critical microstructural volume of material (V*), or $\sigma_n(V^*) \geq \sigma_c$. Here, σ_y is the yield stress and M is a constraint factor that varies between about 2 and 4 depending on the notch/crack geometry and the alloy strain-hardening rate.

At low irradiation temperatures (< 375 – 400 °C), and in the absence of high levels of helium embrittlement, the increase in DBTT is due to irradiation hardening and can be correlated with changes in yield stress ($\Delta\sigma_y$), as $\Delta DBTT = C_c\Delta\sigma_y$ [68]. For Charpy impact tests. the value of the hardening-embrittlement coefficient, C_c

depends on both $\Delta\sigma_y$ and the elastic cleavage transition temperature and upper shelf energy of a particular unirradiated alloy.

As shown above in Figure 1.26, at high irradiation temperatures (> 440 °C) there is typically either little or no hardening, or even some degree of softening, with $\Delta\sigma_y \leq 0$. However, an increase in DBTT may still occur in this temperature regime as the result of reductions in the critical local fracture stress for transgranular cleavage due to irradiation enhanced thermal aging processes [68]. Such NHE processes include precipitation or coarsening of brittle phases, grain boundary segregation of solutes, such as phosphorous, and instabilities in the tempered martensitic substructure [68].
In 8–10Cr martensitic steels containing significant quantities of tungsten, a primary non-hardening embrittlement mechanism is the precipitation of brittle Laves phases on prior austenitic grain boundaries (PAGs). Purely thermal NHE occurs at 500 °C and above but it appears that radiation enhanced diffusion decreases the lower leg of the time–temperature NHE C-curve to about 400 °C or less. This is a concern, since combinations of $\Delta\sigma_y$ and NHE may give rise to very large increases in DBTT. Significant NHE is signaled by a large, or alternatively, negative (when $\Delta T > 0$ and $\Delta\sigma_y < 0$) values of C_c and often, a transition occurs from transgranular cleavage to intergranular fracture.

The accumulation of helium and hydrogen on PAGs may also lead to NHE. In some cases this may be difficult to distinguish from a corresponding high concentration of hydrogen. The distribution of helium on the grain boundaries is critical. For example, a coarse distribution of large bubbles would be expected to have a modest effect on the DBTT increase, while a monolayer-type film of boundary would likely be most damaging.
As noted above, NHE mechanisms are generally associated with a transition from a transgranular cleavage to intergranular local fracture mode. While oversimplified, a conceptual model of the competing effects transgranular fracture versus intergranular fracture is very useful. The model states that the transgranular fracture continues to be the fracture path of least resistance as long as it has a lower critical stress than that for intergranular fracture in BCC metals. Thus, gradual weakening of the PAGs by helium (and/or other mechanisms) would not be reflected in intergranular fracture until σ_{ig} falls below σ_c, where the increase in DBTT depends synergistically on both $\sigma_{ig} - \sigma_c$ (<0) and $\Delta\sigma_y$ [68]. Of course in reality the transition would not be abrupt and the conceptual model is oversimplified.

1.5 IRRADIATED STRUCTURAL STEELS IN CONTACT WITH LIQUID LEAD ALLOYS

The experience on irradiations in contact with liquid lead bismuth eutectic is mostly related to the military fast reactor programmes performed during the Cold War. As mentioned before, the only practical experience with lead bismuth cooled reactors was the operation of the Russian alpha class submarine. However, both the US and Russia had military programmes based on liquid lead bismuth cooled reactors.
Unfortunately, the material research performed in these programmes is not available in open literature.

The available experience for civil application in the materials research development of lead or lead bismuth cooled fast reactors is still very limited.
Recently, Sapundjiev *et al.* [72] has performed SSRT tests in LBE on tensile specimens irradiated in water. Both the tests and the irradiation (up to about 1.5 dpa) of the examined T91 and 316L steels were performed at 200°C. The SSRT tests were performed at a strain rate of 5.10^{-6} s^{-1}. No effects of the LBE environment were found in this work. The author did remark that the irradiation hardening effect in the studied material ($\Delta\sigma_Y$ 316L: 155 MPa; $\Delta\sigma_Y$ T91: 260 MPa) was far less than observed in the studies performed on thermally hardened T91 ($\Delta\sigma_Y$ >500 MPa for HT500) [58],[64] which did show LBE embrittlement. Furthermore, the samples used in this study did not have any surface stress concentrators in contrast to the EDM cut samples in [58],[64]. Apart from the hardening effect and the absence of surface stress concentrators, one needs to keep in mind that these samples were irradiated in water and subsequently tested in LBE. The oxide layer which was built up during irradiation in water is thicker than the native oxide layer present on the non irradiated sample and might also have had an important role in prevention of liquid metal wetting in these tests. Unfortunately, no examinations were made to characterize the oxide layer on the sample before and after testing in LBE.

At the Paul Scherrer Institute (PSI), Switzerland, liquid-solid reaction under irradiation (LiSoR) experiments [73]-[77] were performed with the aim of better understanding the effects of LBE corrosion and embrittlement on structural steels. The LiSoR setup is basically an LBE loop with a test section irradiated with 72 MeV protons [73]. The flow velocity of the LBE in the test section is about 1 m/s. The test section of the loop consists of a T91 tube and a T91 tensile specimen. The specimen was stressed in tension to a mechanical load of 200 MPa during irradiation to simulate the effects of the mechanical load and irradiation at the beam window of a spallation target. The inside of the tube and the specimen were both manufactured

by EDM cutting. The specimen was mechanically polished up to 1000 grit paper whereas the inside of the tube was used as cut.

LiSoR 2 was irradiated for 34 hours at a proton beam current of 49 μA and was terminated after the detection of an LBE leak in the irradiated section [73]. There was no thermocouple directly attached on either the tube or the tensile specimen or in the irradiated area. Therefore, the actual temperature was not known during irradiation. Calculations performed after irradiation revealed temperatures as high as 780°C and resulting thermal stresses above the yield for both the tube and the specimen. This meant both the tube and the specimen had been subjected to thermal fatigue deformation. The produced radiation damage was 0.1 dpa.
Examination of the crack in the tube revealed that the fracture was initiated on the inside and propagated to the outside. The crack which lead to the LBE leak was very probably initiated by microcracks detected on the inside of the tube and attributed to the EDM cutting process. The T91 tensile specimen however, did not show any microcracks on its surface. The brittle fracture features of the crack in the tube were attributed to LBE embrittlement effects. Conditions of LiSoR-2 were however to be considered as accidental conditions since both temperature and stresses were too high.

For LiSoR-3 [75], the inside of the new test section tube was mechanically reworked to obtain a smooth and crack free inner surface. Furthermore, the wobbling of the 72 MeV beam was modified to get a maximum temperature at the inner wall of the test section to be around 342°C. LiSoR-3 operated for 264 hours under proton irradiation with a beam current of 15.5 μA. The corresponding total radiation damage was about 0.146 dpa.
Detailed SEM-EDX examination of the surface of the specimen revealed there was no dissolution of steel elements into the LBE, nor penetration of LBE into the T91 steel matrix. Furthermore, it was seen that an oxide layer formed on the sample surface during proton irradiation. Despite the relatively short irradiation duration of 264 hours, an oxide layer had formed on the area in the beam foot print. SIMS analyses clearly showed that oxides were formed during irradiation on the tensile specimen and on the tube. The oxides exhibited a duplex structure: the outer layer consisting of magnetite and the inner layer of iron chromium spinel. The thickest layer of around 400 nm of magnetite was revealed in the irradiated area [76].

Tensile tests and TEM investigations were performed on T91 from both the test section tube and the inner-tensile stresses specimens from LiSoR-2 to -4 [74]. Due to the higher temperature in both LiSoR-2 and -4, the irradiation hardening was limited. Tensile tests in LBE as function of strain rate on specimens outside of the

beam footprint (0 dpa) revealed a clear tendency that embrittlement becomes more pronounced at lower strain rate. Therefore, subsequent tests on irradiated samples were performed at a strain rate of 1.10^{-5} s^{-1} (lower limit of the tensile rig). Specimens irradiated in LiSoR-2 up to 0.07 dpa and tested in LBE at 300°C, showed a clear embrittlement effect although the high temperature of LiSoR-2 caused the absence of hardening. The author mentions the embrittlement might be attributed to the presence of microcracks at the surface as seen in [57].

Tensile tests performed on specimens from the test section tube and the inner tensile stressed tensile specimen irradiated in LiSoR-4, illustrated significant hardening and a clear LBE embrittlement effect as can be seen in Figure 1.32. However, from the results presented, it is difficult to see a clear irradiation dose dependence of LBE embrittlement [74]. This is attributed to the fact that many higher dose samples were irradiated at high temperatures and do not show radiation hardening which is believed to promote embrittlement of martensitic steels in LBE as discussed above in 1.3.3.2.

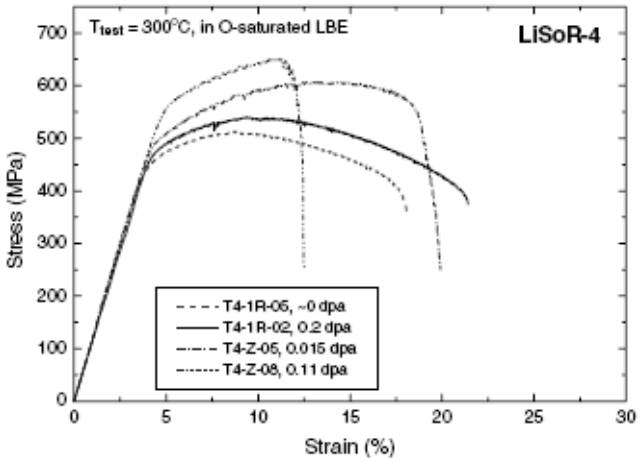

Figure 1.32: Tensile curves of four samples of LiSoR-4 tested at 300°C in oxygen-saturated LBE at a strain rate of 10^{-5} s^{-1} [74].

TEM investigations revealed the presence of small defect clusters and loops in the inner tensile stressed specimen of LiSoR-3 and LiSoR-4 whereas the dislocation structure of the inner tensile stressed specimen of LiSoR-2 consisted of dislocation tangles and dislocation networks. These findings can be well correlated to the irradiation temperature and stresses on the specimen. Furthermore, these observations support the hardening observations of the tensile tests [74].

The LiSoR-5 experiment [77] was irradiated by a 72 MeV proton beam (as for all LiSoR experiments) at a maximum beam current of 30 µA for a total time duration of 724 hours.

The temperature in LBE during irradiation was 360°C and the temperature on the surface of the sample was 380°C. The total irradiation dose in the specimen was 0.75 dpa. After 180 days of decay, the dose rate of the irradiated specimen was about 27 Sv/h. The T91 coming from the LiSoR-5 irradiation was examined by secondary ion mass spectrometry (SIMS), scanning electron microscopy (SEM), energy dispersive X-ray analysis (EDX) and electron probe micro analysis (EPMA). SEM investigation revealed no corrosion attack of the LBE. Both EPMA and SIMS revealed the presence of a double layered oxide layer with a maximum thickness of about 1.5 µm in the irradiated area, comprising of an outer layer of Fe_3O_4 and an intermediate layer of $FeCr_2O_4$. The authors make the final remark that well planned irradiation experiments under relevant conditions are required and will gain in importance [77].

Dai *et al.* [78] examined two stressed capsules made of the austenitic steel 316LN and the martensitic steel 9Cr2WVTa, which were irradiated in SINQ Target-4 in contact with LBE up to 16.7 and 12.2 dpa at calculated temperatures of 315 and 225°C respectively. They discovered no cracks in the 316LN capsule but also added that the stress in the capsule wall was relaxed quickly after irradiation started. Cracks were observed in the EB weld and its vicinity in the 9Cr2WVTa capsule. These cracks were both on the inside (attributed to the high stress in the brittle EB weld) of the capsule as well as the outside (attributed to LME in contact with LBE). The corrosion depth was found to be less than 10 µm for both capsules but the corrosion of the 9Cr2WVTa was still slightly more severe than this of the 316LN capsule.

Although the MEGAPIE (1 MEGAwatt Pilot Experiment) project has finished the irradiation campaign of the first liquid lead bismuth target at PSI, the post irradiation examination (PIE) will only be started in 2009.

At Los Alamos National laboratory (LANL), USA, a systematic study of the interaction between liquid metal corrosion and irradiation has been started [79]. This irradiation and corrosion experiment (ICE) facility uses low energy proton irradiation and enables testing of materials under a wide range of different conditions and environments with the benefit of relatively quick tests due to low sample activation and the absence of polonium. These data can later be compared to data gained from neutron irradiation experiments which take much longer. The first ICE experiment has been conducted, however the sample analysis (SEM/WDX, AFM/MFM/CAFM, Nanoindentation and TEM) will be performed as soon as the sample activity is below about 350 Bq [79].

2 MATERIALS

Materials are like people. It's their defects that make them interesting
Charles Frank
(1911 - 1998)

Chapter 2 discusses the metallurgy, microstructure and mechanical properties of the as received materials which are investigated in this PhD.
First, we review the physical metallurgy of the selected candidate structural materials T91, 316L and we explain the reasons for their selection.
The base materials: T91, 316L and the silicon enriched experimental steels, used in this work, are each characterized in detail in terms of their microstructure and mechanical properties in the as received condition.
Second, we review the metallurgy of welding high chromium steels. We discuss welding ferritic-martensitic steels and austenitic stainless steels in both similar and dissimilar material welds and explain the most common occurring problems in these types of welds. Furthermore, the characterisation of the microstructure and mechanical properties of the investigated TIG and EB welds are discussed in detail.
Third, we briefly review the properties of the liquid lead bismuth and lead lithium eutectic which will further on be used as testing and irradiation environment

This PhD was performed within the frame of the 6th European Framework Programme EUROTRANS and the Belgian (SCK•CEN) MYRRHA materials support programme. Since the ferritic-martensitic steel T91 and the austenitic stainless steel 316L were designated as candidate reference materials for both these programmes, they are the main focus in this PhD thesis. Both the T91 and 316L base materials as well as their TIG and EB welds were investigated.
The Si enriched experimental steels, investigated in this work, were developed due to the better corrosion resistance of ferritic-martensitic steels with elevated silicon content in liquid LBE [80]-[83].

2.1 BASE MATERIALS

2.1.1 Metallurgy of high chromium steels

2.1.1.1 Physical metallurgy of high chromium steels

For a good understanding of the metallurgy of high chromium steels, it is considered useful to make a quick overview of the physical metallurgy of the basic iron-carbon alloys before looking at the more complex alloys such as the high chromium alloys.

Fe and Fe-C

Pure iron can exist in two possible crystallographic forms, body centred cubic or bcc and face centred cubic or fcc. From room temperature up to 910°C pure iron has a bcc crystal structure. In this temperature interval the material is called α-iron or ferrite. Above 910°C the ferrite transforms very rapidly into austenite or γ-iron (fcc), which is stable up to 1390°C. At 1390°C the iron transforms again to the bcc form, which is then called δ-iron. This bcc form remains stable up to the melting point of the iron at 1535°C. However, pure iron is almost never used as a structural material because of its relatively poor mechanical properties.

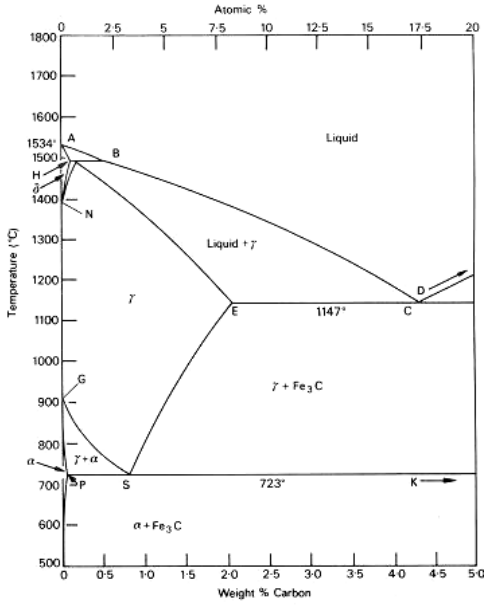

Figure 2.1: Iron-carbon equilibrium phase diagram.

The iron-carbon alloy is referred to as steel. Carbon atoms are much smaller than the iron atoms and they will therefore be present in the material as interstitial atoms. The phase diagram in Figure 2.1 shows that the solubility of carbon is much greater in austenite (max. 2 wt% at 1130°C) than it is in ferrite (max. 0,025 wt% at 723 °C). This is due to the larger interstitial cavities available in γ-iron. The larger solubility of carbon in austenite is very important for the metallurgy of steels. It creates the possibility to obtain different microstructures and influence the properties of the material by heat treating the steel and by varying the cooling rate. Another effect of the carbon is the creation of carbides in the microstructure. These carbides can limit the growth of the grains and serve as a strengthening mechanism by hindering or stopping dislocation movements.

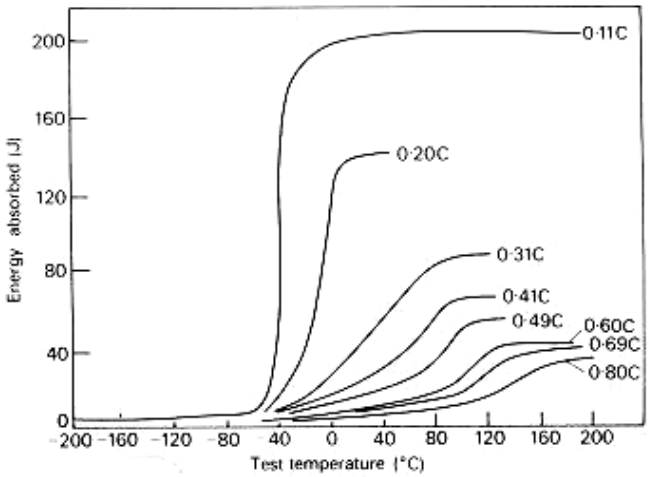

Figure 2.2: Effect of carbon on DBTT [84].

Figure 2.2 shows the influence of the carbon content on the DBTT (ductile to brittle transition temperature). It was found that 0.1 wt% of carbon in the steel results in the best DBTT. This is explained by the observation that the migration of the carbon to the grain makes the material very hard and brittle.

Fe-C-Cr

The pseudo-binary Fe-Cr diagram is shown in Figure 2.3 for the case of 0.1 wt% of carbon in the system.

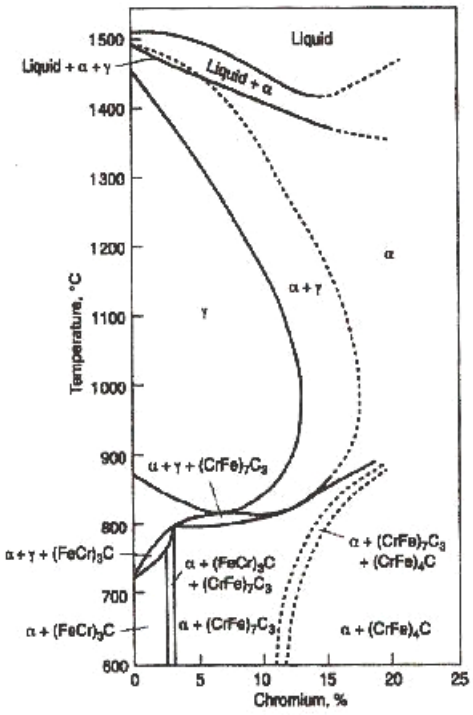

Figure 2.3: Phase diagram of the Fe-Cr system containing 0.1 wt% C [85].

The figure clearly shows that chromium is an α-geneous element because it restricts the existence of the γ-loop. For Chromium contents above 13 wt% the system becomes fully ferritic over the entire temperature range whereas between 12 and 13 wt% Cr there is still an α+γ region. Notice that in the Fe-Cr diagram of Figure 2.3 the δ-phase is no longer mentioned because in this system the ferrite can exist from the melting temperature down to room temperature.

Cr is a strong carbide former. It increases the strength of the steel and the temperature of quenching and decreases the critical velocity of cooling. Chromium is added to steel to increase corrosion resistance and oxidation resistance, to increase hardenability, or to improve high-temperature strength. Complex chromium-iron carbides solve slowly into the austenite. Therefore, sufficient heating time must be allowed for, prior to quenching. But all these characteristics of Cr-alloyed ferritic-martensitic steel alone were not enough to select the optimal Cr-content for ADS and GENIV candidate materials.

The influences of the chromium content of the steel on the properties after irradiation were examined by irradiating several steel grades with a different Cr-content. Figure 2.4 shows the DBTT shift as a function of chromium content for several steel grades irradiated to 7, 10 or 36 dpa. It is obvious that although all high chromium steels exhibit a low DBTT shift, the minimal DBTT shift due to irradiation is given by 9% Cr content.

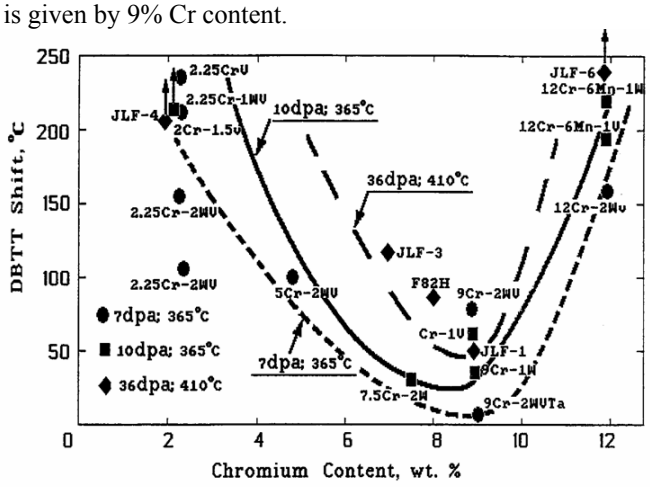

Figure 2.4: Effect of Cr-content on DBTT [85].

It is well known that under the influence of irradiation steels can show a certain amount of swelling. This was discussed in section 1.4 on irradiation damage. Figure 2.5 shows the percentage of swelling as a function of the chromium content of the material. It can be seen in the figure that the lowest irradiation induced swelling occurs for material with a Cr content between 5 and 10% [86]. These findings form the most important arguments for the selection of the 9 wt% Cr materials as candidates for the regions of ADS applications which undergo high irradiation doses.

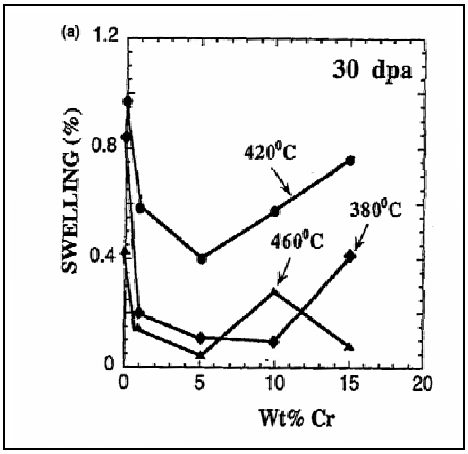

Figure 2.5: Effect of Chromium content on irradiation induced swelling [86].

This does however not explain the selection of AISI 316L as a candidate material for ADS. The reason for its selection is not entirely because of the physical metallurgy of the steel. The austenitic stainless steel 316L cannot be used at high temperatures due to creep and high swelling rates at elevated irradiation doses. However, the material has been extensively studied in materials programmes for reactor applications in the past and therefore a very large materials database supports its selection for components exposed to relatively low irradiation doses and temperatures. Furthermore, at lower temperatures, the corrosion resistance of 316L steel was found to be better than this of T91. This is shown in Figure 2.6 which gives the corrosion rates in stagnant lead bismuth eutectic (LBE) with a dissolved oxygen content of about 11 wt.% as a function of temperature for T91 and 316L. The materials were exposed for 175, 500, 1250, 2300 and 3000 hours at temperatures from 425°C to 600°C under 5% H_2 and Ar cover gas atmosphere. Severe corrosion occurred at temperatures above 500°C where three corrosion modes were distinguished: stable oxide film mode, transition mode, and final dissolution mode featuring Cr and Ni leaching and material loss. The principle corrosion mechanisms were uniform penetration and dissolution of the penetrated volumes. At temperatures above 500°C, T91 had a better corrosion resistance compared to A316L. The transition corrosion mode continued 2–3 times longer for T91 material due to residual oxides found even after 3000 h of exposure. At low temperatures (<450°C) both materials showed good corrosion resistance but A316L performed better than T91 with corrosion rates 2–5 times lower [87].
Furthermore, due to the available extended database on the behaviour of 316L under irradiation it is considered to be an interesting candidate for liquid metal cooled applications.

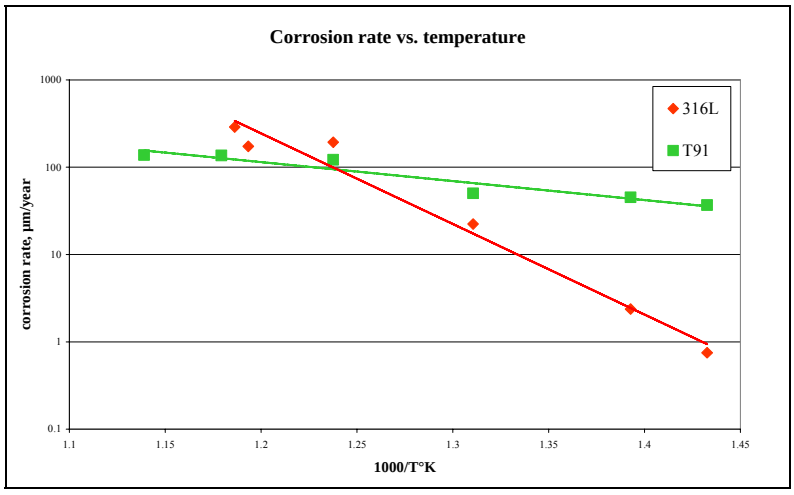

Figure 2.6: Comparison of the corrosion rate for T91 and 316L in LBE as function of the temperature [87].

Alloying elements in steels

Alloying elements can influence the Fe-C equilibrium diagram. The austenite stabilizing elements or γ-geneous elements are C, N, Ni, Mn and Cu. They extend the austenite phase field. Ferrite forming elements or α-geneous elements are Mo, Nb, V, W, Si, Ti, Al and Cr which contract the γ-phase field by stabilizing the ferrite phase.

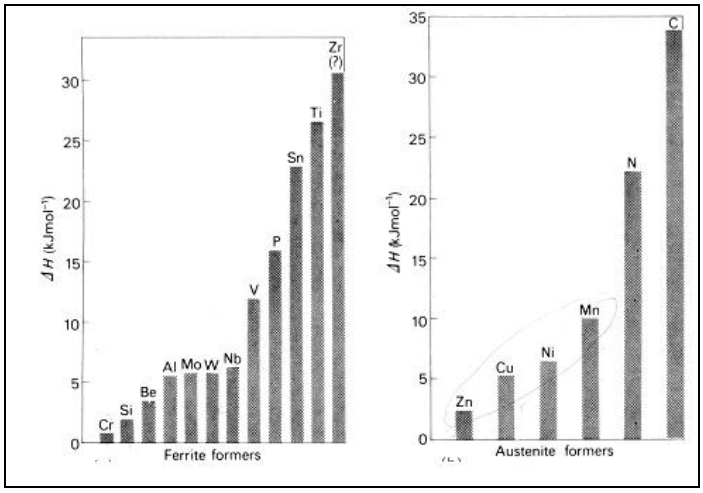

Figure 2.7: Degree of influence on the formation energy of ferrite, thus (left) and austenite (right) [84].

In steels in which the austenite transforms to ferrite and carbide by slow cooling, the alloying elements are divided into three categories:

The first category consists of the elements which enter only into the ferrite phase such as nickel, phosphorus and silicon. Their solubility in cementite or in alloy carbides is very low.

In the second group, the elements which can form stable carbides or enter the ferrite phase can be found. At low concentration they will go into solid solution in the cementite phase or into the ferrite. At higher concentration however, they will form alloy carbides which are more stable than cementite. This group consists of elements already mentioned like chromium, molybdenum, vanadium, tungsten and niobium. Some of these elements like W and Mo produce substantial solid solution hardening of ferrite as well.

The third group is formed by only a few elements which enter to the carbide phase, like nitrogen which forms carbo-nitrides with iron and many alloying elements.

For a fixed carbon content (0.1 wt % C), as the alloying element is added, the γ field is either expanded or contracted depending on the particular solution.
If vanadium is added, the γ field is contracted and in the material vanadium carbides will be formed because of their equilibrium with ferrite over much of the ferrite field. Nickel does not form carbides in steel. It remains in solution in the ferrite phase, strengthening and toughening the ferrite.
Nickel also increases the hardenability and toughness of steels.
Phosphorus increases strength and hardness and decreases ductility and notch impact toughness of steels. It should however be controlled to low levels in the steel because of the tendency of phosphorous to segregate to the grain boundaries at higher concentrations and thus weaken the intergranular bonds.
Manganese is generally beneficial to surface quality, especially in resulfurized steels. It contributes to strength and hardness, but much less than carbon does. Increasing the manganese content also decreases ductility and weldability, but less than carbon. It has a significant effect on the hardenability of steel.
Sulphur decreases ductility and notch impact toughness especially in the transverse direction. Weldability decreases with increasing sulphur content. Sulphur is found primarily in the form of sulphide inclusions and therefore needs to be controlled to low levels.
Silicon is one of the principal deoxidizers used in steelmaking. It is less effective than manganese in increasing as-rolled strength and hardness. Silicon improves strength and promotes large grain sizes.
Boron is added to fully killed steel to improve hardenability. Boron-treated steels are produced to a range of 0.0005 to 0.003%. Whenever boron is substituted in part for other alloys, it should be done only with hardenability in mind because the lowered alloy content may be harmful for some applications. Boron is a potent alloying element in steel. A very small amount of boron (about 0.001%) has a strong effect on hardenability. It is most effective in lower carbon steels, but it is not good for nuclear applications as it produces He which significantly increases the embrittlement of the material after irradiation.

It should be noted that cementite is only stable up to about 1.5 % of Cr or 0.6 % of V and for higher content on the diagram (Figure 2.8), several alloy carbides replace cementite. For 9% Cr steels, it is recommended that the concentration of V should not be higher then 0.2 %, because then cementite will be replaced by V_4C_3 carbides, which are very brittle.

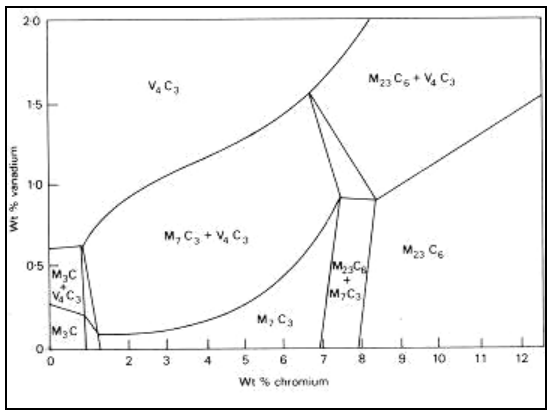

Figure 2.8: Carbide constitution in steel as a function of vanadium and chromium content [84].

V, Nb, Ta and Ti form carbides, nitrides or carbonitrides (VC, VN, Nb(CN)) at higher temperature than those at which M_2X precipitates, so they are more stable and increase the resistance to overaging. During creep or exposure at lower temperature, the precipitation of VN is more likely than this of VC due to reduced solubilities of the former. Soluble V, Nb, Ta and Ti also produce solid-solution strengthening and retard growth of sub-grains at the highest tempering temperatures [85].

Both Nb and V are added to the alloy to improve its high temperature strength properties. Microstructural work showed that the strength of the modified alloy comes from two factors. First, fine $M_{23}C_6$ precipitate particles nucleate on Nb(C, N), which first appear during the heat treatment. Second, the vanadium enters the $M_{23}C_6$ and retards its growth at the service temperature. The finer distribution of $M_{23}C_6$ adds to the strength and its retarded growth holds the strength for long periods of time at the service temperature [85].

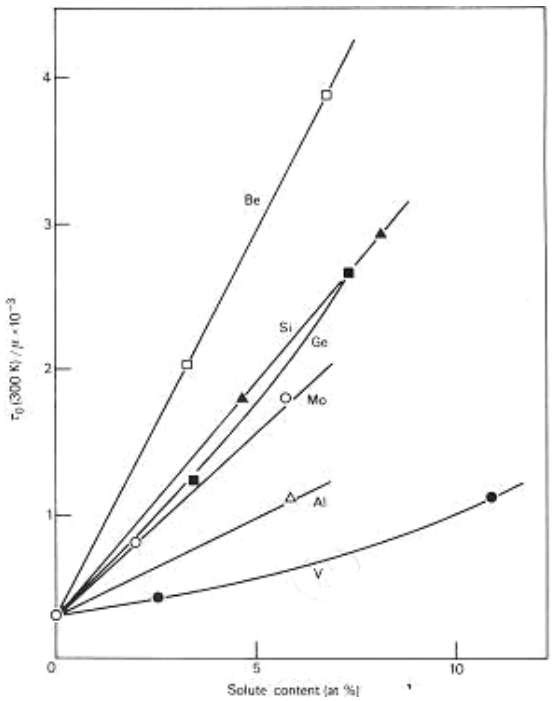

Figure 2.9: Effect of alloying elements on strengthening [84].

Figure 2.9 shows that vanadium has a weak strengthening effect on α-iron at low concentration (<2 at%), while silicon and molybdenum are much more effective strengtheners. These alloying elements are also usually added for other reasons. Silicon is added to achieve deoxidation, manganese to combine with sulphur and molybdenum to promote hardenability. The effect of increasing molybdenum content is effectively demonstrated in a series of steels containing 0.1 wt% C (Figure 2.10).

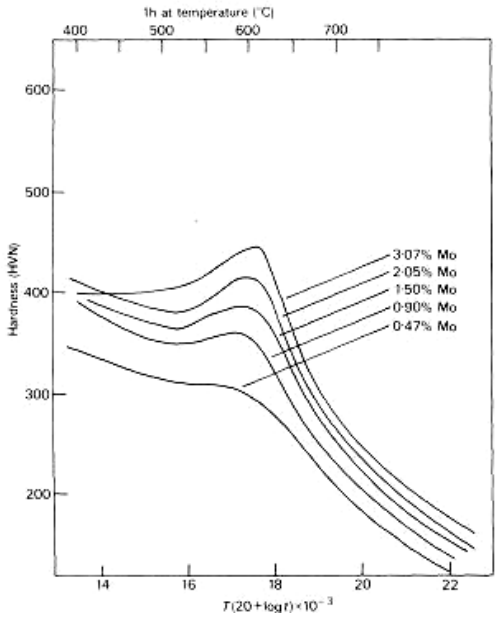

Figure 2.10: Effect of molybdenum on the tempering of quenched 0.1 wt% C steels [85].

The formation of alloy carbides between 500 and 600 °C is accompanied by increasing strength of the as-quenched martensite which is referred to as secondary hardening. The carbides responsible for secondary hardening in the case of tungsten and molybdenum are the isomorphous hexagonal carbides Mo_2C and W_2C. However, the secondary hardening effect of tungsten is less than for molybdenum, probably because of the slower diffusivity of tungsten. Alloy steels which exhibit secondary hardening can provide high strength levels on tempering between 500 and 700 ° C, with better ductility than at lower tempering temperatures.

2.1.1.2 Heat treatment of High Chromium steels

A clear distinction needs to be made between the purpose of the heat treatment for ferritic-martensitic steels and the austenitic steel grades. This is due to the nature of the steel structure that needs to be obtained after the treatment. In ferritic-martensitic steels the γ–α transformation is very important as well as the martensite start, M_s and martensite finish, M_f temperatures. These temperatures are very strongly influenced by the chemical composition of the steel. Therefore, heat treatments (hold times, hold temperatures and cooling rates) will differ slightly for different ferritic-martensitic steel grades.

Austenitic steels on the other hand have a composition which leads to avoiding the γ–α transformation. The needed heat treatment will therefore be significantly different from that of the ferritic-martensitic steel grades.

Ferritic-Martensitic steel

The heat treatment to obtain good ferritic-martensitic steel consists of two parts: normalisation and tempering.

The first part, the homogenization or normalisation treatment, is intended to evenly spread the alloying elements throughout the material and to obtain a homogeneous grain size. This treatment needs to be performed at temperatures above the austenitisation temperature (within the γ-phase). If the temperature would remain below the A_3-temperature and thus remain in the α-phase during the normalisation, one would obtain only ferrite grain growth of the as cast structure without the possibility to have the needed γ-α transformation upon cooling. This would lead to a decrease in mechanical properties and is highly unwanted.
The austenite present in the sample above the A_3-temperature needs to be transformed to martensite by means of cooling. Martensite is a supersaturated solid solution of carbon in a tetragonal iron matrix with bcc structure. It is formed by a diffusionless shear transformation leading to the characteristic martensite laths which appear in polished and etched sections. Some 9% Cr steels are fully martensitic. Alloying elements have some influence on the M_s temperature. If the M_s temperature is close to or below room temperature, it results in the presence of retained austenite, which increases the toughness of high chromium transformable steels, but it also decreases the strength. The composition of the steel must be adjusted not only to control the constitution but also to maintain the M_s and M_f temperature range above ambient temperature. The M_s and M_f temperature for high chromium steels range from 250 to 350 °C and 80-190 °C , respectively, but much higher temperatures M_s ($\leq$ 450 °C) and M_f ($\leq$ 260 °C) were determined for some reduced activation steels [85].

The second part of the heat treatment is the tempering. The tempering of the martensite is at temperatures 740-780°C, below the A_{C1} temperature, where the α-γ transformation starts. It is done to avoid re-austenisation and to obtain good combination of strength and toughness. The austenite stabilizing elements decrease A_{C1}, while ferrite forming elements increase it.
Retarded softening occurs during tempering of low carbon Cr steels at temperatures to about 500°C, while pronounced softening occurs at 500-550°C. The hardness changes at different tempering temperatures can be correlated with microstructural changes as follows [85]:

- < 350 °C –A fine dispersion of M_3C (Fe_3C) precipitates forms and grows to dendrite morphology and then to a plate like Widmanstatten distribution. The Chromium content of Fe_3C increases to 20 % with the possibility of M_7C_3 being formed in situ from the Cr-enriched Fe_3C. These effects slow down the growth rate of the Fe_3C and retard softening.
- 450-500 °C – Fine needles of M_2X on the dislocations within the martensite laths and retard softening.
- 500-550°C- The M_7C_3 and M_2X phases coarsen with rapid decrease in hardness.
- >550 °C - The M_7C_3 and M_2X are replaced by Cr rich $M_{23}C_6$ precipitates, which nucleate on the martensite lath and prior austenite grain boundaries and the rate of decrease in hardness slows down. The dislocation density decreases to the as-quenched martensite.
- ≥ 650 °C – The $M_{23}C_6$ precipitates at the tempered lath martensite boundaries grow, leading to reduction in dislocation density and sub-grain formation across the martensite laths.
- ≥ 750 °C – The sub-cells within the martensite laths grow into fairly equiaxed sub-grains with very little lath martensite structure. $M_{23}C_6$ precipitates continue to grow and there is still some presence of dislocation networks.
- 700-780 °C - All the carbon in the steels is precipitated as $M_{23}C_6$ on tempering for more then 1 h.

Austenitic steel

The ratio of γ–geneous elements (often expressed by the Ni equivalent) to α–geneous elements (often expressed by the chromium equivalent) determines whether a steel will have an austenitic microstructure. The absolute amounts of alloying elements can differ significantly. We will further discuss the 316L austenitic grade, since it is the austenitic steel grade of interest for this work.

316L contains between 10 and 14 wt% of nickel and between 16 and 18 wt% of chromium. It also contains molybdenum for increased corrosion resistance, particularly for resistance to pitting corrosion, and for increased high-temperature strength. The alloy 316L is the reduced carbon version of 316 and this makes it better resistant to temperatures in the 538°C to 816°C range. The composition of 316L leads to a stable austenitic microstructure at room temperature because Ni is a strong γ-geneous element. Because the material will not undergo a phase transformation under influence of cooling after annealing, the heat treatment can be completed in one single treatment. This treatment, called solution annealing, will be

performed at sufficiently high temperature (1050°C-1100°C) to achieve good diffusion properties of the alloying elements in the steel. The purpose is to get a homogeneous distribution of the precipitates and solid solution strengtheners. Cooling rates are not critical because the material will remain austenitic over the entire temperature range. However, in certain cases changes in phase stability due to cold working or thermal treatment can promote the formation of martensite.

Long term heat treatments at temperatures between 500°C and 800°C are also known to have a possible detrimental effect on the corrosion properties of the 316L alloy due to the formation and coarsening of the $M_{23}C_6$ carbide precipitates at the grain boundaries, causing sensitization.

Additional time during heat treatments might promote the formation of other intermetallic phases such as chi (χ), Laves (η), and sigma (σ) phase. The maximum formation rate of these phases has been determined to be around 820°C and can be enhanced by cold work. Do note that all these phases can be reverted back into solution in the austenite phase at temperatures above 1100°C.

2.1.2 T91 base material

2.1.2.1 Chemical composition

The ferritic-martensitic steel T91 (Grade 91 Class 2 / S50460), according to ASTM standard A387-Ed99 was delivered as hot rolled and heat treated plate with a thickness of 15 mm by Industeel, ArcelorMittal group.
The required chemical compositions and the measured composition of T91 are illustrated in Table 2.1.

Table 2.1: Chemical composition of T91 delivered by Industeel, all percentages are in weight percent.

T91 Industeel (heat nr. 55883)					
elements	ASTM chemical requirements Heat analysis	Heat analysis (Industeel)	ASTM Chemical requirements Product analysis	Product analysis (Industeel)	Lab analysis (LISm & OCAS)
C	0.08-0.12	0.097	0.06-0.15	0.102	0,1025
Si	0.20-0.50	0.218	0.18-0.56	0.235	0.22
Mn	0.30-0.60	0.386	0.25-0.66	0.401	0.38
P	< 0.020	0.020	< 0.025	0.019	0.021
S	< 0.010	0.0005	< 0.012	0.0007	0.0004
Cr	8.00-9.50	8.873	7.90-9.60	8.895	8.99
Mo	0.85-1.05	0.871	0.80-1.10	0.889	0.89
Ni	< 0.40	0.115	< 0.43	0.121	0.11
Al	< 0.04	0.009	< 0.05	0.010	0,0146
Cu		0.080		0.080	0.06
Nb		0.077		0.079	0,06
Ti		0.003		0.004	0,0034
V	0.18-0.25	0.195	0.16-0.27	0.202	0,21
W					0,01
Pb					< 10 ppm
Sn					0,004
As					0,008
B					< 1ppm
N	0.030-0.070	0.0440	0.025-0.080	0.0480	0,0442
Fe	balance	balance	balance	balance	balance

In addition to the chemical analysis of the producing company, chemical analysis was also performed by the laboratory for iron and steel making at Ghent University and OCAS n.v. The concentrations were measured at LiSm using a spark spectrometer. For a more accurate value, the carbon, nitrogen and sulphur were measured by OCAS using the combustion method and the chromium and boron were additionally measured by LISm using wet chemistry.

2.1.2.2 Heat treatment

As described earlier, ferritic-martensitic steels have to be used in normalized and tempered condition. Thus for T91, the normalizing treatment consisted of heating the alloy to 1050°C; holding for 1 minute per millimetre, thus 15 minutes and then water cooling to room temperature. This treatment produced a fully martensitic structure.
The tempering treatment consisted of heating the normalized steel to 770°C, holding for three minutes per millimetre of thickness, thus 45 minutes and then air cooling in still air to room temperature.

2.1.2.3 Microstructure

Specimens of T91 were examined metallographically by optical microscopy. They were prepared by mechanical polishing using a Struers Roto Pol-11 to 1µm fine grain and were etched with Villela's reagent. The martensitic microstructure, characterized by the martensite laths, is shown in Figure 2.11.

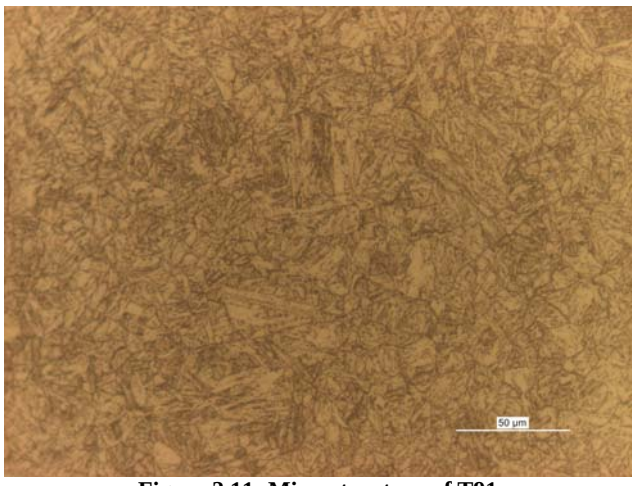

Figure 2.11: Microstructure of T91

The prior austenite grain size of the T91 grade is relatively hard to determine with sufficient confidence. In order to be able to characterize its microstructure better, a series of EBSD measurements (electron backscattering diffraction) were performed.

Figure 2.12: Image quality map of EBSD measurement on T91

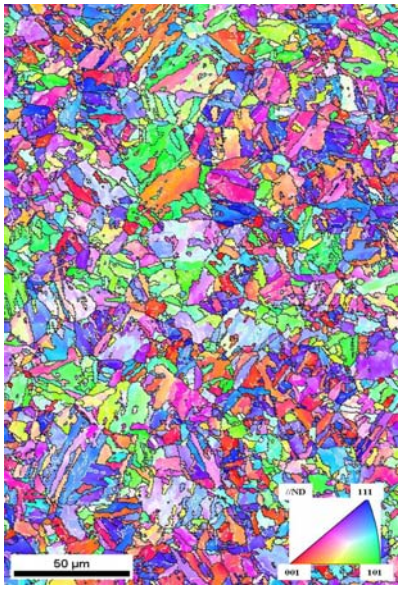

Figure 2.13: Inverse pole figure map of EBSD measurements on T91

Figure 2.12 shows the image quality map of one of the EBSD measurements. This map is obtained by plotting the image quality factor of all measured spot. This image quality factor is a number given to a measurement as an indication of the certainty in the determination of the diffraction pattern. This means that a measurement inside a grain will lead to a high quality factor (plotted in the map as a light point) whereas a measurement on a grain boundary will lead to a low image quality factor (plotted in the map as a dark point) due to the scattering of the electrons. This image quality map in fact results in an image of the microstructure.
The average prior austenite grain size was identified to be 20µm using these image quality maps.
The inverse pole figure map, illustrated in Figure 2.13, shows the orientation of the grains in the T91 material. The base triangle of the inverse pole figure is indicated in the lower right corner of the figure. It can be seen that the 111 orientation corresponds to the blue colour, the 101 or Gauss-orientation corresponds to the green and the 001 orientation to the red colour in the map. The figure shows that the T91 material does not have a preferential grain orientation.

Because of the small size of the martensite laths and of the present carbides in the ferritic-martensitic structure of T91, transmission electron microscopy (TEM)

observations were made to further characterize the T91 microstructure. For this purpose, specimens were prepared using the 1 mm technique. The samples were first polished mechanically up to ~100 µm of thickness and than etched using Jet-polishing with Tenupol (Struers 3) at 0°C with a chemical solution of 10% Perichloric Acid and 90% of methanol. The material was examined using a JEOL 3010 EX, 300 KeV, transmission electron microscope.

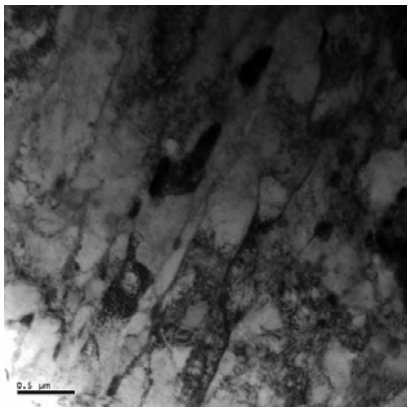

Figure 2.14: Transmission electron micrograph of T91; bright field image of the global structure.

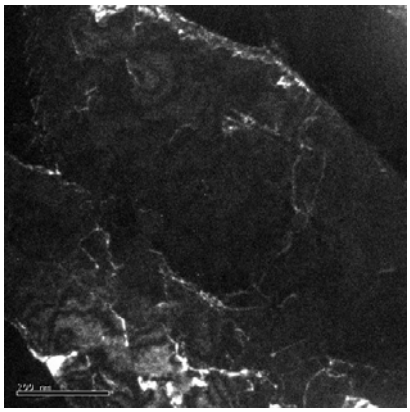

Figure 2.15: Transmission electron micrograph of T91: dark field image showing dislocations in a martensite lath.

Figure 2.14 and Figure 2.15 show transmission electron micrographs of the structure of T91. The martensite laths can be clearly seen. At both the prior austenite grain boundary and the subgrain boundaries precipitates have been formed. The larger precipitates are of the $M_{23}C_6$ type. These $M_{23}C_6$ precipitates form the majority of the precipitates but also M_6C type precipitates are present at the grain boundaries. Small coherent vanadium carbo-nitrides VN(C) are also present inside the martensite laths but these can not be seen in the figure. The dislocations inside one of the martensite laths are illustrated in the dark field image of Figure 2.15.

2.1.2.4 Mechanical properties

2.1.2.4.1 Hardness

Although the hardness of a material does not reveal that much information about its mechanical behaviour, it can be used as a good indication. Hardness values allow quick comparison of several materials. Moreover, hardness gives the best insight in the structure of welds which will be discussed later and as mentioned in 1.3.1, materials with an increased hardness are reported to have a higher susceptibility to LME.

The hardness of T91 was measured with a Wolpert DIATESTOR 2n using 5 kgf. The average hardness at the skin of the plate was 244 Hv whereas the hardness at the centre of the plate was on average 226 Hv.

2.1.2.4.2 Tensile properties

To characterize the mechanical properties of T91 as function of temperature, we performed tensile tests at temperatures ranging from -150°C up to 450°C. These tests were performed using small cylindrical tensile specimens machined in L-direction with a diameter of 2.4 mm and a gauge length of 12 mm. The strain rate we used for these tests was 10^{-4} s^{-1}.

Figure 2.16 shows the obtained tensile curves of tests of T91 at temperatures between -150°C and 450°C. The trends in the mechanical behaviour as a function of temperature can clearly be seen. The strength and elongation properties decrease with increasing temperatures but around 400°C the total elongation of the material begins to increase again with temperature. The results of the analysis of the tensile data are summarized in Table 2.2.

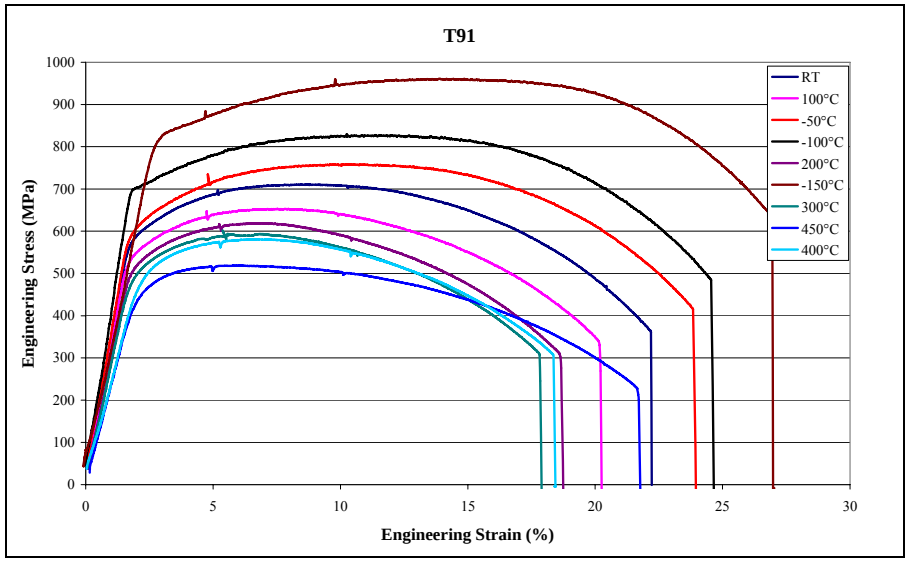

Figure 2.16: Stress-Strain curves of T91 tested at different temperatures between -150°C and 450°C.

Table 2.2: Results of tensile tests on T91 at different temperatures.

Specimen	temperature (°C)	$\sigma_{y0,2}$ (MPa)	σ_{uts} (MPa)	ε_u (%)	ε_t (%)	Area reduction (%)
T91-6	-150	811	957	10.97	24.90	61.3
T91-4	-100	704	827	9.18	23.39	69.8
T91-3	-50	595	756	8.22	22.71	73.7
T91-1	RT	580	708	6.66	21.13	77.5
T91-2	100	536	650	5.61	19.18	78
T91-5	200	511	616	4.79	17.55	79.2
T91-7	300	488	590	4.51	16.69	76.2
T91-9	400	478	580	4.35	17.11	75.5
T91-8	450	440	520	3.71	20.95	78.5

Comparison between T91 and other 9% Cr steels [88],[89]

In 2.1.1.1 it was discussed that 9% Cr steels have very promising properties for the envisaged application. Here we want to compare the 9% Cr steel used in this PhD to other 9%Cr steels investigated in the nuclear energy sector.

Figure 2.17 illustrates the comparison between the T91 from the SPIRE program and the T91 material from the Demetra project which is used in this PhD. The figure shows that the strength of the "Demetra T91" is higher than this of the T91 material from SPIRE. The comparison between T91 from Demetra with most other 9%Cr steels used in nuclear research is shown in Figure 2.18.

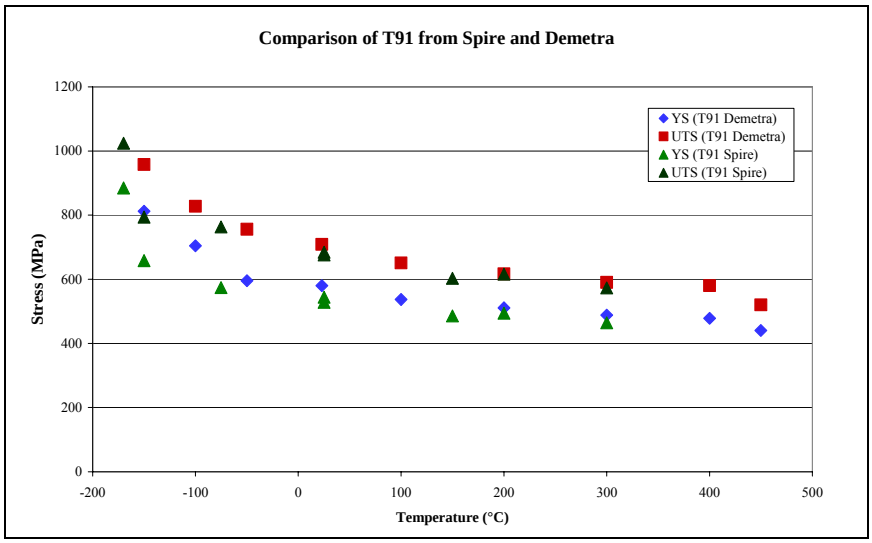

Figure 2.17: Comparison between the tensile strength of T91 from SPIRE and Demetra.

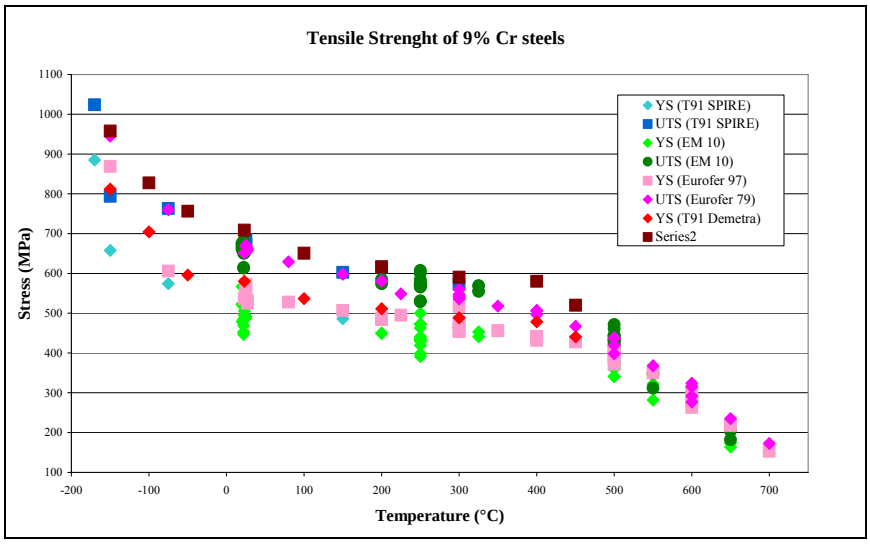

Figure 2.18: Comparison between the tensile strength of 9% Cr steels used in nuclear research.

Figure 2.19 and Figure 2.20 respectively show the comparison of the elongations between T91 from Demetra and SPIRE and the comparison between the T91 from Demetra and the other commonly used 9%Cr steels. Notice that the elongations of the T91 from SPIRE [89] are longer than those of the Demetra material.

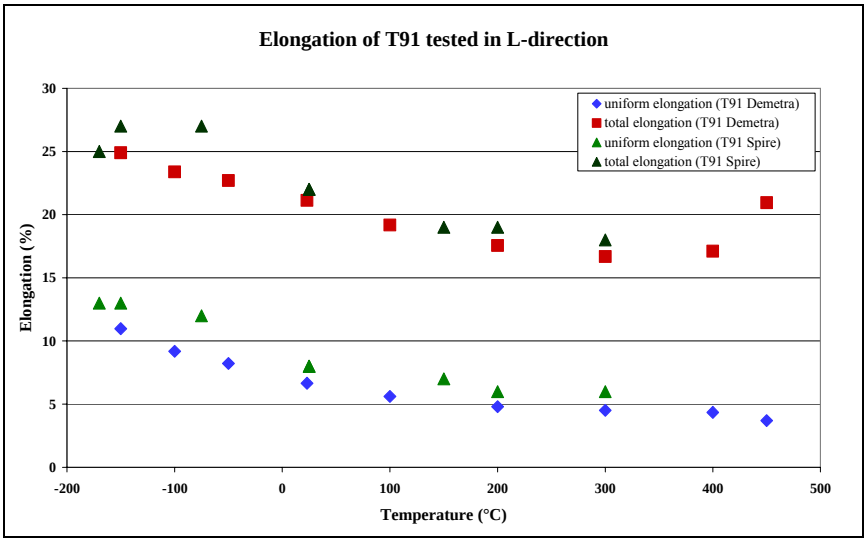

Figure 2.19: Comparison between the elongations of T91 from SPIRE and Demetra, tested parallel to the rolling direction (L-direction).

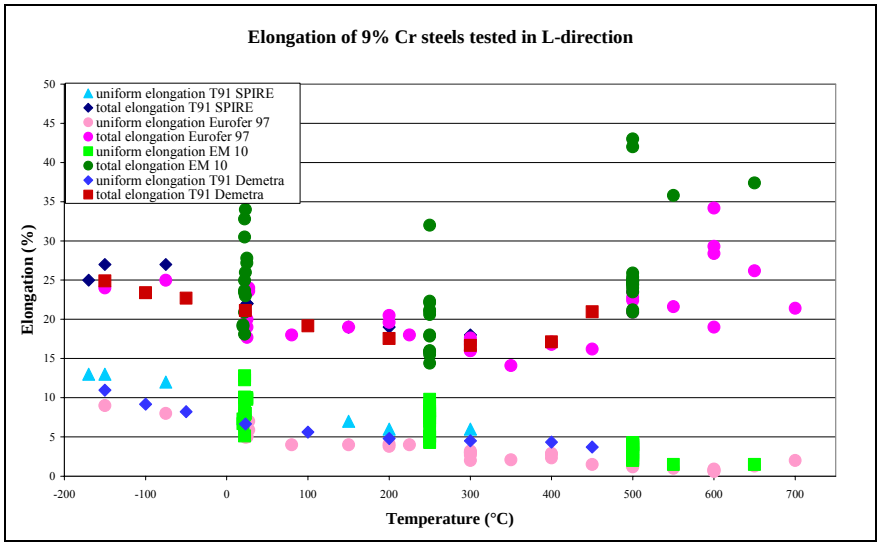

Figure 2.20: Comparison between the elongations of 9%Cr steels used in nuclear research, tested parallel to the rolling direction (L-direction).

2.1.2.4.3 Charpy impact properties

The Charpy properties of T91 were tested using KLST subsize specimens. These specimens have a length of 27 mm, a height of 4 mm and a width of 3 mm. They were taken in both T-L and L-T orientation.

The Charpy impact test is used as a means of quality control, in order to qualify the fracture toughness behaviour of a material without dedicated fracture toughness experiments. In fact, the Charpy impact tests could allow determination of [90]:

- the flow properties
- the microcleavage fracture stress
- the crack arrest performance
- the characteristic transition temperatures

The Charpy impact tests were performed on the Wolpert 50J. machine in Cell C2, tup DIN-4 mm 10 kNcorr, with a velocity of 3.852 m/s. The impact tests were performed at temperatures ranging from -140°C to 400°C according to the requirements of ASTM E23 standard [90]. The specimen to be tested was heated or cooled to the test temperature and acclimatized for about 20 minutes in the conditioning chamber. Then the test piece was transported to the anvil and tested within 3 seconds. The actual test temperature was corrected for the temperature loss. During the test, the load as a function of time was recorded.

In Figure 2.21 the transition curves based on the dial energy of the T91 material used in this work (T91 Demetra) are compared to those of other 9% Cr steels used in other research dedicated to future nuclear installations. The results depicted in Figure 2.21 confirm that the material has no strong orientation of its microstructure as shown in 2.1.2.3, since there is no orientation dependent DBTT transition. Both test orientations have very similar DBTT temperatures and the upper shelf energies are very similar in value.

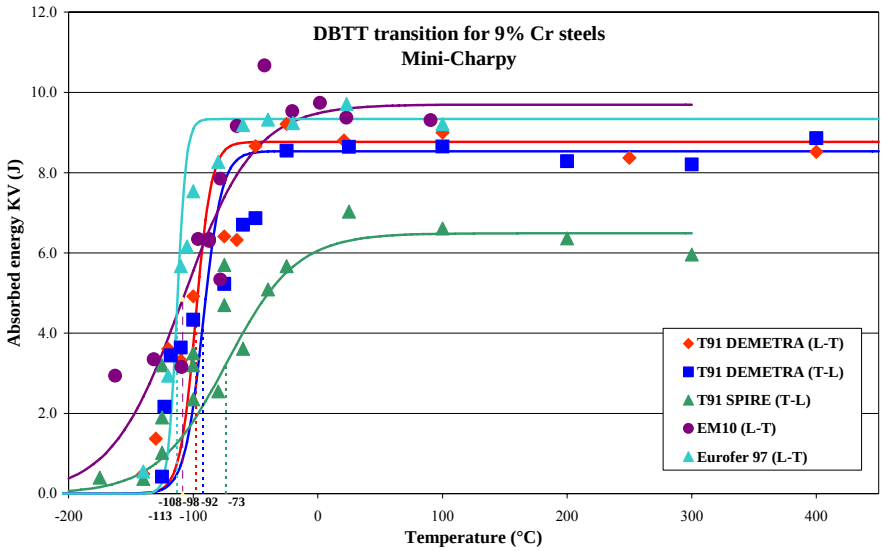

Figure 2.21: DBTT transition curves of common used 9% Cr steels in nuclear research.

2.1.3 316L base material

2.1.3.1 Chemical composition

The austenitic stainless steel 316L (S31603), according to ASTM A240-Ed02 was delivered as hot rolled and heat treated plate with a thickness of 15 mm by Industeel, ArcelorMittal group.

The required chemical compositions and the measured composition of the 316L material are illustrated in Table 2.3. As for the chemical composition of T91, this of 316L was confirmed by chemical analysis performed at Ghent University and OCAS n.v.

Table 2.3: Chemical composition of 316L delivered by Industeel, all percentages are in weight percent.

316L Industeel (ASTM A 240 Ed.02)				
elements	Heat analysis (Industeel)	ASTM Chemical requirements Product analysis	Product analysis (Industeel)	Lab analysis (LISm & OCAS)
C	0.016	0.030	0.015	0.0185
Si	0.641	0.75	0.643	0.67
Mn	1.840	2.00	1.842	1.81
P	0.026	0.045	0.027	0.032
S	0.0030	0.030	0.0028	0.0035
Cr	16.822	16.00-18.00	16.687	16.73
Mo	2.086	2.00-3.00	2.075	2.05
Ni	10.170	10.00-14.00	10.256	9.97
Al				0,0183
Cu				0.23
Nb				0,000
Ti				0,0058
V				0,07
W				0,02
Pb				<10 ppm
Sn				
As				
Zr				
B				<1ppm
N	0.0250	0.10	0.0261	0.0293
Fe	balance	balance	balance	balance

2.1.3.2 Heat treatment

The austenitic stainless steel was solution annealed followed by a water quench. The solution annealing heat treatment was done at 1050°C - 1100°C.

2.1.3.3 Microstructure

316L was examined metallographically by optical microscopy. The specimens were prepared by mechanical polishing using a Struers Roto Pol-11 to 1µm fine grain and etched with a chemical solution of 100 ml HCl, 33 ml HNO_3 with a few drops of H_2SO_4. The microstructure of 316L is depicted in Figure 2.22.

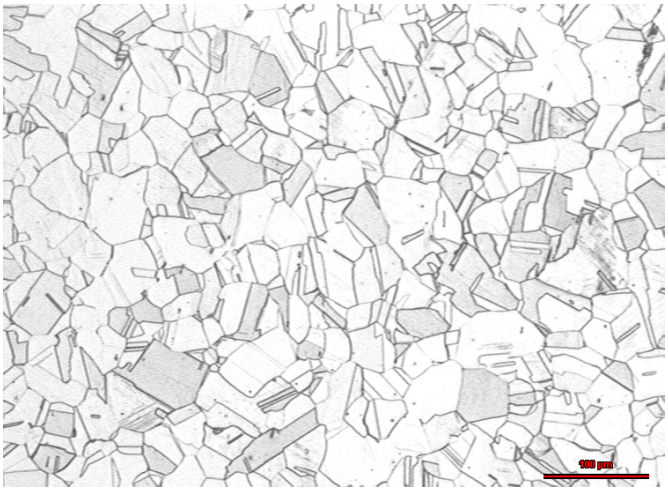

Figure 2.22: Optical micrograph of 316L

Because of the clearly defined grains in the austenitic steel, it is relatively easy to determine the grainsize. The 316L material under consideration has an average grain size of 24µm.

2.1.3.4 Mechanical properties

2.1.3.4.1 Hardness

The hardness of 316L was measured with a Wolpert DIATESTOR 2n using 5 kgf. The average hardness at the skin of the plate was 193 Hv whereas the hardness at the centre of the plate was on average 146 Hv.

2.1.3.4.2 Tensile properties

The tensile properties for 316L were investigated between -150°C and 450°C, using small cylindrical specimens in L-direction with a gauge length of 12 mm and a

diameter of 2.4 mm. The tests were performed at a strain rate of 10^{-4} s^{-1}. The test results are depicted in Figure 2.23 and the values of the tensile properties are stated in Table 2.4.

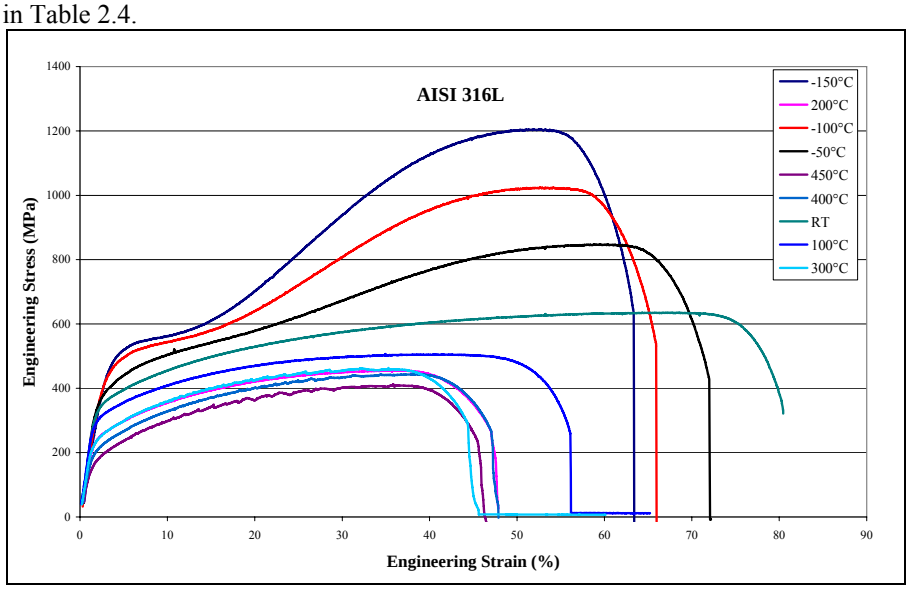

Figure 2.23: Stress-Strain curves of AISI 316L tested at temperatures between -150°C and 450°C.

Table 2.4: Results of tensile tests on AISI 316L at temperatures between -150°C and 450°C

Specimen	temperature (°C)	$\sigma_{y0,2}$ (MPa)	σ_{uts} (MPa)	ε_u (%)	ε_t (%)	Z (%)
316L-1	-150	423	1208	46.03	59.39	78.8
316L-2	-100	375	1022	47.12	62.97	79.6
316L-4	-50	330	845	54.94	69.93	84
316L-7	RT	308	639	67.65	78.79	84.6
316L-8	100	274	505	37.97	54.85	84.1
316L-10	200	222	455	32.19	47.70	84.6
316L-9	300	212	462	30.89	43.15	74.2
316L-6	400	181	443	35.68	45.78	77.2
316L-5	450	150	408	32.13	44.91	85.5

2.1.3.4.3 Charpy impact properties

The stainless steel 316L has an austenitic microstructure as mentioned before and therefore this material does not exhibit a ductile to brittle transition temperature. However Charpy impact tests can give a first estimate of the fracture toughness of

this material. Note that the results should not be seen as fracture toughness since it has been shown that the results of fracture toughness tests do not coincide with Charpy impact test results. The results of the impact tests on 316L are illustrated in Table 2.5.

Table 2.5: Charpy impact test results of 316L tested in L-T direction.

Specimen N°	Temp. (°C)	E Dial (J) corr.	Shear Fract. App. (%) Estim.
L631-12	22	11.7	100
L631-11	-100	15.0	100

2.1.4 Si enriched materials

The silicon enriched steels used in this work are all experimental steels which have no commercial applications so far. These materials were developed with the aim to improve corrosion resistance in LBE. Several authors have pointed out the improved corrosion resistance of elevated Si steels in LBE [80]-[83]. We did not examine any corrosion in flowing LBE in the frame of this work and focussed on the mechanical properties of these Si enriched steels.
The Si enriched T91, which we called T91-Si in this work was provided by JAEA, Japan. The four higher Si containing steels, named 2439, 2440, 2441 and 2442, were provided to us by LANL, USA. Furthermore, we had 2 experimental steels, named L413 and A078, fabricated by LISm, Ghent University.
All Si enriched steels were produced in small quantities (100-200 kg) in a vacuum induction furnace. They were all hot rolled into plates with a thickness between 15 and 25 mm and given the proper heat treatment.
Unfortunately the amount of Si enriched material available to us was only a small amount of the experimental batch and therefore the amount of tests had be to kept to minimum.

2.1.4.1 Chemical compositions

The compositions of the experimental Si enriched steels were analysed by different laboratories. Furthermore, not all elements were always measured. The T91-Si was analysed by JAEA, Japan, the 2439-2442 were analysed by LANL, USA and the L413 and A078 were analysed by OCAS, ArcellorMittal, Belgium. The obtained chemical compositions are listed in Table 2.6. In Table 2.6, the elements indicated by "-" were below the detection limit of the applied method. Elements which do not have anything mentioned in the table were not measured at all.

Table 2.6: chemical composition of experimental Si enriched steels (wt%).

	C	Cr	Ni	**Si**	Mo	Mn	Al	V	W	Nb	P	S	N	Cu
T91-Si	0.13	8.10	0.99	**1.45**	0.86	0.52	0.003	0.20	-	0.074			0.054	
2439	0.19	11.58	0.48	**2.75**	1.03	0.37	0.042	0.31	0.48		0.004	0.004		
2440	0.19	13.52	0.51	**4.83**	1.00	0.38	0.043	0.31	0.45		0.004	0.004		
2441	0.21	18.35	0.51	**5.27**	1.04	0.43	0.045	0.3	0.46		0.005	0.004		
2442	0.03	18.25	14.16	**5.2**	1.96	1.44	0.009	-	-		0.001	0.004		
L413	0.01	18.40	8.5	**1.00**		1.56					0.033	0.02	0.08	
A078	0.029	19.70	9.98	**4.85**	-	1.08	0.033	0.028		-	0.008	0.0045	0.051	0.22

2.1.4.2 Heat treatments

The T91-Si, 2439, 2440 and 2441 have either martensitic or ferritic structures and were normalised and tempered. The 2442, L413 and A078 have a fully or partially austenitic structure and were solution annealed.

T91-Si was normalised at 1050°C for 30 minutes followed by air cooling. The tempering treatment was done at 750°C for 30 minutes, followed by air cooling.
2439, 2440 and 2441 were all normalised at 1050°C for 1 hour, followed by air cooling and tempered at 760°C for 1 hour, followed by air cooling.

The solution annealing treatment of all three austenitic grades (2442, L413, A078) consisted of a heating to 1050°C for 1 hour followed by air cooling.

2.1.4.3 Microstructure

All Si enriched steels were examined by optical microscopy after polishing up to 1μm paper. The ferritic-martensitic steel grades were etched using Villela's reagent whereas the austenitic grades were etched using an aqueous solution of HCl and HNO_3 in a 1:1:1 ratio.

The optical microscopy images of T91-Si, 2439, 2440 and 2441 are depicted in Figure 2.24. It is clear that T91-Si has a fully martensitic microstructure which is very similar to this of T91 showed in Figure 2.11 in 2.1.2.3. 2439 has a martensitic-bainitic microstructure whereas both 2440 and 2441 are fully ferritic with large grains typical of high Si electrical steels.

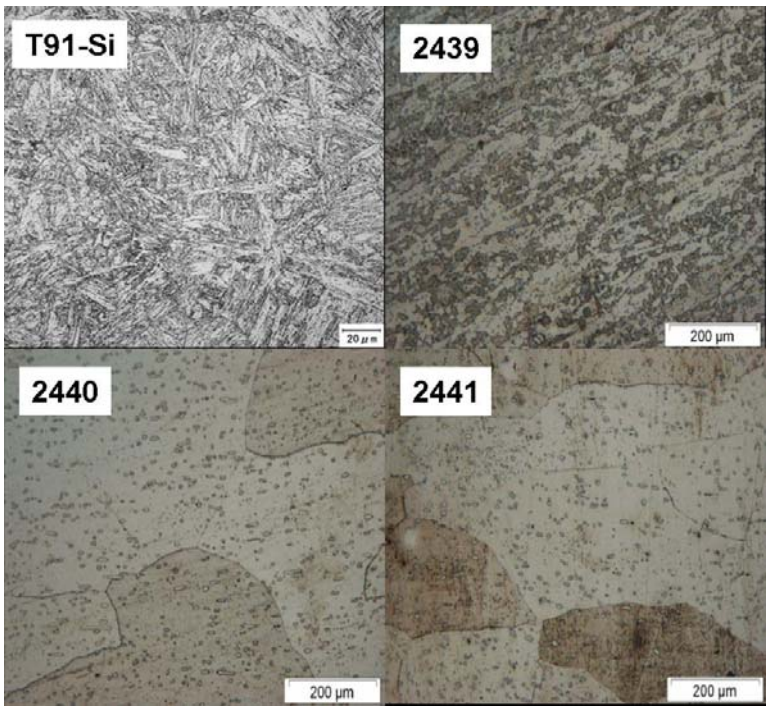

Figure 2.24: Microstructure of martensitic (T91-Si), martensitic-bainitic (2439) and ferritic (2440, 2441) Si enriched experimental steels.

The ferritic microstructures of both 2440 and 2441 could be expected based on the M_s temperatures of these steels, calculated using the Payson and Savage formula [91]. It is clear that the higher alloying content of 2440 and 2441 lowered the M_s temperature.

To have "numbers" giving an indication on the nature of these high Si steels, we summarized several typically used "numbers" in Table 2.7.

These values have to be used as an indication only since they have many restrictions. For instance, the Cr_{eq}, Ni_{eq}, C_{eq} and FF were empirically formulated to predict the content of ferrite in welds. Therefore, the used equations and their meaning will be discussed more in detail in 2.2.1.2 on the welding of high chromium steels. Experimental determination of the SFE by Li *et al.* [92] showed very good agreement with the value produced by the Pickering equation for SFE of L413. Therefore, this equation was also used for the determination of the SFA of the other Si enriched steels. It can immediately be seen however from the negative values for SFE in Table 2.7 that the Pickering equation is certainly not universally applicable.

Table 2.7: Cr_{eq}, Ni_{eq}, C_{eq}, ferrite factor, SFE and M_s of the Si enriched steels compared to those of T91 and 316L.

	Cr_{eq}	Ni_{eq}	C_{eq}	ferrite factor (FF)	SFE (mJ/m^2) (Pickering equation)	M_s
T91	11.83	4.48	2.23	7.16	53	462.8516
T91-Si	13.29	6.5	2.356	8.18	50	446.159
2439	20.65	6.66	3.348	21.94	61	318.002
2440	25.48	6.7	3.859	34.58	35	270.614
2441	32.40	6.72	5.137	43.55	23	98.824
316L	21.52	12.23	4.882	-16.38	25	43.86105
2442	31.64	14.88	6.103	-2.16	-32	-100.64
L413	20.4	11.58	4.683	-16.32	9	52.315
A078	29.54	12.73	5.643	3.58	-28	-41.3093

The optical microscopy images of the austenitic Si enriched steels are depicted in Figure 2.25. Based on the values of the ferrite factor in Table 2.7, one could expect a small fraction of ferrite in the microstructure of A078. The optical microscopy did however not reveal any ferrite. All three microstructures are fully austenitic in the solution annealed state.

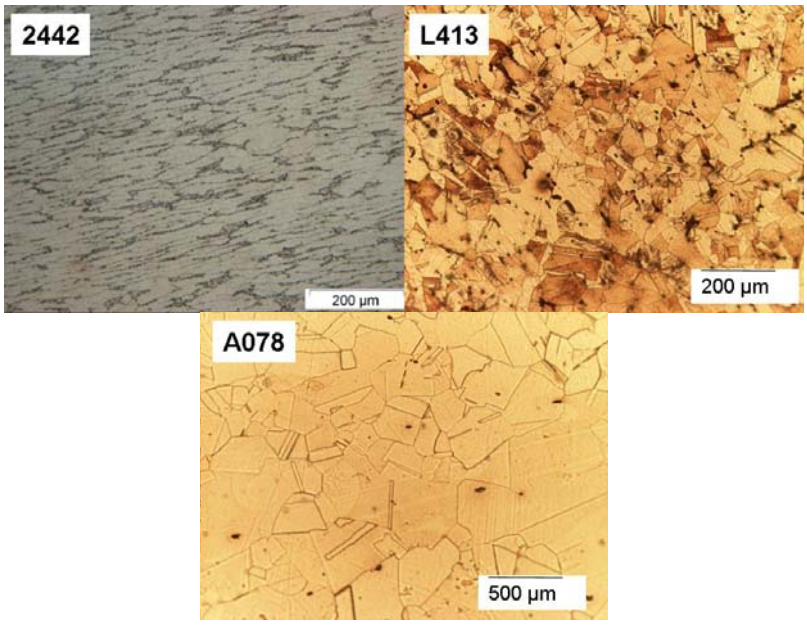

Figure 2.25: Microstructure of austenitic Si enriched experimental steels.

2.1.4.4 Mechanical properties

2.1.4.4.1 Hardness

The hardness of all Si enriched steels was measured with a Wolpert DIATESTOR 2n using 5 kgf. The average hardness measured at at least 6 points per material is listed in Table 2.8.

Table 2.8: Vickers hardness of Si enriched experimental steels

Material	2439	2440	2441	2442	L413	A078
Hardness Hv	261	337	323	281	370	296

2.1.4.4.2 Tensile properties

The tensile properties of the Si enriched steels were not systematically measured in air as function of temperature as we did for both T91 and 316L due to the limited amount of available material. The material was however tested in LBE and where necessary, reference tests in air or Ar + 5%H_2 were performed. These results will be discussed further on in Chapter 5.

The tensile properties of T91-Si as function of temperature were however tested at JAEA and sent to us. Their results are depicted in Figure 2.26. The strength values are approximately 200 MPa higher than those of the standard T91 while the ductility in air remains comparable.

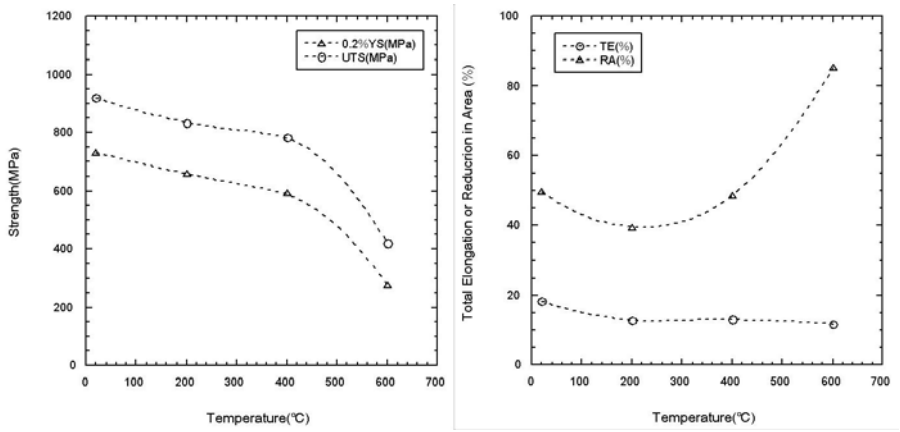

Figure 2.26: Strength and ductility of T91-Si as function of temperature. Courtesy of Y. Kurata, JAEA.

2.1.4.4.3 Charpy impact properties

DBTT temperatures were determined for all ferritic/bainitic/martensitic Si enriched steels. The Charpy tests on T91-Si were performed at JAEA on full size charpy specimens whereas we determined those of the 2439, 2440 and 2441 grades using subsize mini charpy specimens. The austenitic steels do not have a DBTT and where therefore not impact tested. The results of the dial energy are all represented in Figure 2.27.

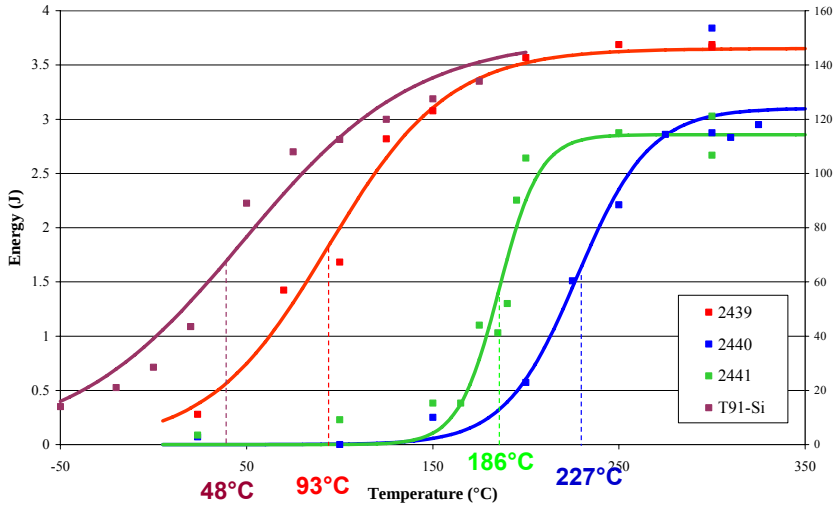

Figure 2.27: Charpy transition curves of the ferritic/bainitic/martensitic Si enriched experimental steels. T91-Si determined using full size Charpy (energy scale on right); 2439-2441 determined using sub-size KLST (energy scale on left).

2.2 WELDS

Four weldments produced by two welding techniques were investigated. Two weldments of T91/T91 and two mixed welds of T91/316L. Tungsten inert gas (TIG) in combination with Shielded Metal Arc Welding (SMAW) and Submerged Arc Welding (SAW) and Electron Beam (EB) welding were applied. The thermodynamic relevant parameters of T91 and 316L for any welding method are summarized in Table 2.9.

Table 2.9: Thermodynamic data for T91 and 316L relevant to the welding process.

Material	Melting temp. (°C)	Thermal conductivity at room temperature (W/mK)	Thermal expansion coefficient at room temperature (10^{-6}/K)	Specific heat (J/kgK)	Latent Heat of fusion (J/kg)
T91	1500	22,1	10,4	444,8	$2{,}6.\ 10^5$
316L	1375	13,49	15,2	500	$3{,}3.10^5$

Before going into details on the examined welds, we will first explain the necessary techniques and most common problems in welding high chromium steels.

2.2.1 Metallurgy of Welding

Although welding is a very common technique it is considered useful to make a quick overview of the metallurgy of welds in general and more specifically of the various welding techniques discussed within this PhD.

2.2.1.1 General

Welding is the term used for the connection technique between two metals, similar or dissimilar, by melting off and mixing both ends by which possibly a third melt is added in the form of an electrode or welding rod. Adding material when welding is not always required as opposed to soldering. When soldering, the metals that are to be connected are not molten but the added material, the solder, is added in molten form and makes the physical connection after solidification. The distinction between the two techniques has to be clear because the fact that both connected materials have to be molten to make the weld, influences both mechanical and microstructural properties of the welded connection.

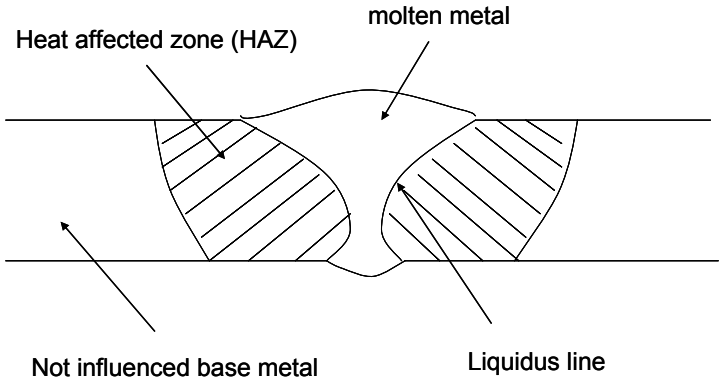

Figure 2.28: schematic representation of a welded connection.

Figure 2.28 depicts a schematic representation of a welded connection that is visualised by etching. After etching one can distinguish rather easily the material that was molten and the possible different welding passes that were applied. The line that separates the material in the weld that was molten during welding from the material that did not melt is being called the liquidus line. Immediately next to the liquidus line is the zone of the material that was not molten but was subjected to an 'abnormal heat treatment' under influence of the adjacent weld. In most carbon steels this area of the connection called the heat affected zone (HAZ) can also be visualised rather easily by etching. In weldments of austenitic steels it is however very difficult if not impossible to visualise the HAZ by etching.

When welding the following points have to be regarded:

- The pieces to be connected need to be heated and partially molten;
- Possibly a third material needs to be added ;
- The liquid phase needs to be protected from interaction with the surrounding atmosphere.

The methods to achieve these three points differ for each welding technique and will be looked at more in detail for the techniques used for the welds studied within this PhD.

2.2.1.1.1 TIG Welding

The commonly used acronym TIG stands for tungsten inert gas. The Anglo-Saxon acronym GTAW can also be found which stands for gas tungsten arc welding. The welding technique uses an electric arc between a refractory tungsten electrode and the material to be welded to melt the ends of the work piece. The filler material is added manually or automatically in the form of a wire or bar by placing it into the

electric arc. The technique uses an inert gas of He or Ar or a gas mixture to prevent the liquid phase during welding from oxidising. The principle of the TIG welding process is shown in Figure 2.29.

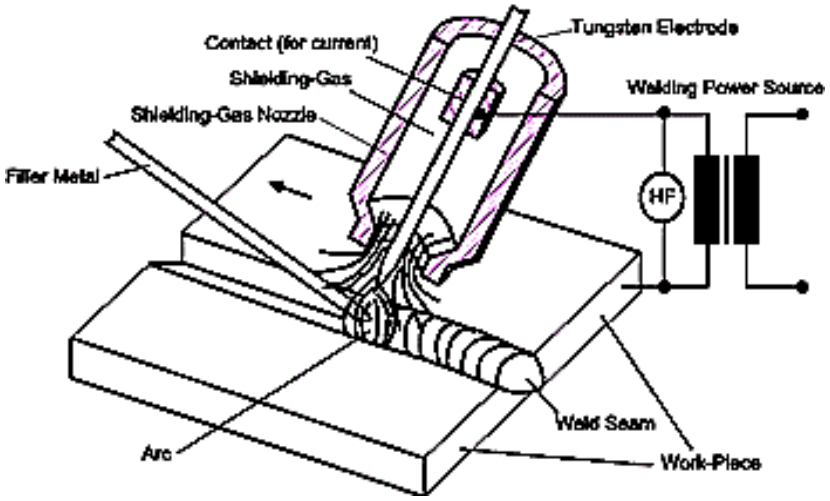

Figure 2.29: Principle of TIG welding

Note that the "TIG welds" examined in the frame of this work are not performed by strictly applying the TIG welding process. Therefore the other applied techniques will also be explained further here.

2.2.1.1.2 Shielded metal arc welding (SMAW)

Shielded metal arc welding (SMAW), also known as manual metal arc (MMA) welding or informally as stick welding, is a manual arc welding process that uses a consumable electrode coated in flux to lay the weld. An electric current, in the form of either alternating current or direct current from a welding power supply, is used to form an electric arc between the electrode and the metals to be joined. When drops of metal are molten from the electrode they are surrounded by a thin film of flux or slag which protects them from the surrounding atmosphere. As the weld is laid, the flux coating of the electrode disintegrates, giving off vapours that serve as a shielding gas and providing a layer of slag, both of which protect the weld area from atmospheric contamination. Whereas the inert gas in TIG welding serves merely as a protection from the surrounding atmosphere, the role of the flux in shielded metal arc welding is much more complex. Other than protection from oxides and nitrides the flux is used to actively alter the chemical composition of the weld metal.

Because of the versatility of the process and the simplicity of its equipment and operation, shielded metal arc welding is one of the world's most popular welding

processes. It dominates other welding processes in the maintenance and repair industry, and though flux-cored arc welding (the flux is inside the hollow electrode and 'floats' to the surface when molten) is growing in popularity, SMAW continues to be used extensively in the construction of steel structures and in industrial fabrication.

2.2.1.1.3 Submerged arc welding (SAW)

Submerged Arc Welding requires a continuously fed consumable solid or tubular (with metal core) electrode. The molten weld and the arc zone are protected from atmospheric contamination by being “submerged” under a blanket of granular fusible flux. When molten, the flux becomes conductive and provides a current path between the electrode and the work piece.
SAW is normally operated in the automatic or mechanized mode allowing much faster welding and more constant welding parameters, however, semi-automatic (hand-held) SAW guns with pressurized or gravity flux feed delivery are available. Deposition rates approaching 45 kg/h are possible compared to 5 kg/h (max) for shielded metal arc welding. Currents ranging from 200 to 1500 A are commonly used; currents of up to 5000 A have been used (multiple arcs).
DC or AC power can be utilized, and combinations of DC and AC are common on multiple electrode systems. Constant Voltage welding power supplies are most commonly used, however Constant Current systems in combination with a voltage sensing wire-feeder are available.

2.2.1.1.4 EB welding

Electron beam welding (EB) is a fusion welding process in which a beam of high-velocity electrons is applied to the materials being joined. The work pieces melt as the kinetic energy of the electrons is transformed into heat upon impact, and the filler metal, if used, also melts to form part of the weld. Pressure is not applied, and a shielding gas is not used, though the welding is often done in conditions of a vacuum to prevent dispersion of the electron beam.

As the electrons strike the work piece, their energy is converted into heat, instantly vaporizing the metal under temperatures near 25,000 °C. The heat penetrates deeply, making it possible to weld much thicker work pieces than is possible with most other welding processes. However, because the electron beam is focused, the total heat input is actually much lower than that of any arc welding process. As a result, the effect of welding on the surrounding material is minimal, and the heat-affected zone is small. Distortion is slight, and the work piece cools rapidly, and while normally an advantage, this can lead to cracking in high-carbon steel. Almost all

metals can be welded by the process, but the most commonly joined are stainless steels, super alloys, and reactive and refractory metals. The process is also widely used to perform welds of a variety of dissimilar metals combinations. However, attempting to weld plain carbon steel in a vacuum causes the metal to emit gases as it melts, so deoxidizers must be used to prevent weld porosity.

The amount of heat input, and thus the penetration, depends on several variables, most notably the number and speed of electrons impacting the work piece, the diameter of the electron beam, and the travel speed. Greater beam current causes an increase in heat input and penetration, while higher travel speed decreases the amount of heat input and reduces penetration. The diameter of the beam can be varied by moving the focal point with respect to the work piece—focusing the beam below the surface increases the penetration, while placing the focal point above the surface increases the width of the weld.

The three primary methods of EB welding are each applied in different welding environments.
The method first developed requires that the welding chamber has a hard vacuum. As a result, the chamber must be small to prevent it from being crushed under atmospheric pressure. Material as thick as 15 cm can be welded, and the distance between the welding gun and work piece (the stand-off distance) can be as great as 0.7 m. The disadvantages of this method are the amount of time required to properly evacuate the chamber and the cost of the entire machine.
It is also possible to perform EBW in a soft vacuum, under pressure of about 0.1 mbar. This allows for larger welding chambers and reduces the time and equipment required to evacuate the chamber, but reduces the maximum stand-off distance by half and decreases the maximum material thickness to 5 cm.
The third EBW mode is called nonvacuum or out-of-vacuum EBW, since it is performed at atmospheric pressure. The stand-off distance must be diminished to 4 cm and the maximum material thickness is about 5 cm. However, it allows for work pieces of any size to be welded, since the size of the welding chamber is no longer a factor.

2.2.1.2 Welding high chromium steels

2.2.1.2.1 Welding T91

T91 is a modification of 9Cr-1Mo steel. This 9Cr-1Mo-NbV steel was co-developed by Combustion Engineering and the Oak Ridge National Laboratory (ORNL) in the late 1970's. The standard composition range for the steel together with the chemical

composition of the steel used in this study (T91 heat nr. 55883) were given in Table 2.1 in 2.1.2.1.

The composition of the steel was designed to produce a fully martensitic microstructure during air cooling. This means that issues related to the handling during the welding process and between the welding operation and the completion of the post weld heat treatment (PWHT) are important concerns.

The heat treatment of ferritic-martensitic steel, as mentioned in 2.1.1.2 requires normalizing at a minimum temperature of 1040°C, followed by air cooling to room temperature and tempering at 730°C or higher. A cooling rate of 6°C/min or higher from the normalization temperature avoids the formation of pro-eutectoid ferrite. Notice that very low cooling rates associated with very thick sections could result in ferrite formation and subsequent reduced strength. The steels martensite start (M_s) temperature is around 400°C and the martensite finish (M_f) temperature is around 200°C. When heat treated to meet the requirements of the specifications for T91, the as tempered microstructure consists of fine prior austenite grains containing a lath martensite structure with a high dislocation density which is stabilized by $M_{23}C_6$ carbides and MX (Nb,V) carbo-nitrides.

Martensitic stainless steels can be welded (with the exception of the high sulphur machining grade 416) but caution needs to be exercised as they will produce a very hard and brittle zone adjacent to the weld. Cracking in this zone can occur unless much care is taken with pre-heating and with post weld heat treatment (PWHT). These steels are often welded with austenitic filler rods to increase the ductility of the deposit. Considerable effort has gone into the development of the 9Cr-1Mo-V steel consumables to optimize strength and toughness in weldments.
A recent publication has been released by EPRI as a guideline to weld T91 [93]. One of the important issues described in the EPRI document is a list of five weld metal compositions for three welding processes: GTAW, SAW, SMAW. The compositional ranges differ for several elements but those of nickel and manganese are of special importance. These two elements influence critical temperatures such as the onset temperature for austenite formation (A_{c1}) and the M_s and M_f temperatures. The base metal specification allows a maximum of 1% (Ni + Mn) whereas it is possible to have much higher levels in the filler metal. When Ni + Mn reaches 1.4%, the A_{c1} decreases to 780°C, the M_s decreases to below 350°C, and the M_f decreases to below the required preheat temperature for welding of 200°C. Up to 20% of retained austenite has been observed in the filler metal at 200°C [94].
Cooling the weldment to room temperature prior to the PWHT is one way to avoid the formation of fresh, untempered martensite after the PWHT. However,

maintaining preheat temperature prior to PWHT is essential for minimizing the probability of hydrogen cracking in the heat affected zone of the weld. Moreover, it makes more efficient use of energy resources and may be desirable for practical reasons depending on the welded component size and the available facilities for material handling and heat treating.

The relatively low A_{c1} could also pose problems since there is no actual upper temperature limit specified for PWHT and temperatures up to 780°C have been employed in practice [95]. This temperature is very close to the A_{c1} for high Ni + Mn filler metals.

As a guideline, Santella has calculated the effect of major alloying elements on the A_{c1} for T91 using computational thermodynamics [94]. The analysis revealed that Ni + Mn concentration has the strongest influence. The curve in Figure 2.30 could be used to estimate the upper PWHT temperature based on the decrease of the A_{c1}.

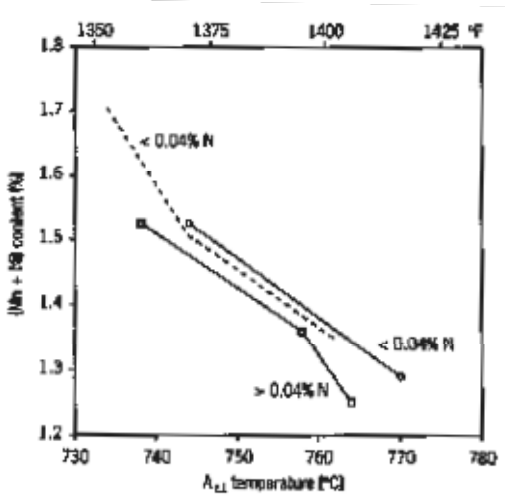

Figure 2.30: Influence of nitrogen, nickel and manganese on the A_{c1} temperature [95].

Although 9-12% Cr steels normally have a fully martensitic microstructure, some have the tendency to form delta ferrite during the welding process. The potential for δ-ferrite formation can be estimated by either the determination of the chromium equivalent (Cr_{eq}) and the nickel equivalent (Ni_{eq}) used to represent the composition of the steel in the Schaeffler diagram as can be seen in Figure 2.31 or by the Kaltenhauser ferrite factor (FF) or trough the analysis of the phase diagram obtained with thermodynamic calculations. The formulas employed for 9-12% Cr steels to calculate the Cr_{eq} and Ni_{eq} in order to use the Schaeffler diagram in Figure 2.31, and the Kaltenhauser ferrite factor, FF are [97]:

$$Cr_{eq} = \%Cr + 2\,\%Si + 1.5\,\%Mo + 5\,\%V + 1.75\,\%Ti + 0.75\,\%W \quad \textbf{(2.1)}$$

$$Ni_{eq} = \%Ni + \%Co + 0.5\,\%Mn + 0.3\,\%Cu + 25\,\%N + 30\,\%C \quad \textbf{(2.2)}$$

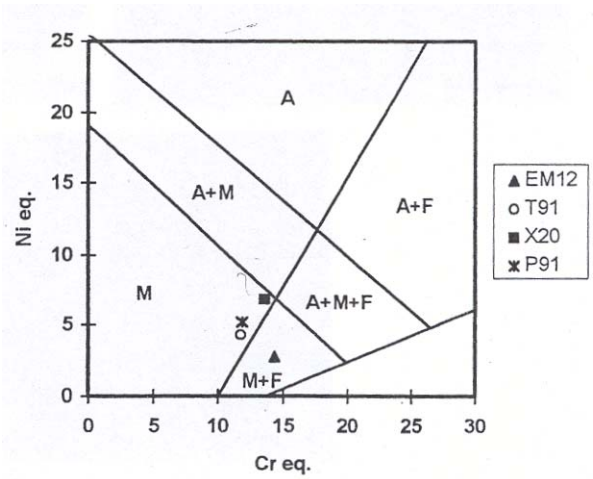

Figure 2.31: Schaeffler diagram showing the location of several 9-12 Cr steels compositions [97].

$$FF = \%Cr + 6\,\%Si + 8\,\%Ti + 4\,\%Mo + 2\,\%Al + 4\,\%Nb - 2\,\%Mn - 4\,\%Ni - 40\,\%(C + N) \quad \textbf{(2.3)}$$

Although the composition of T91 in the Schaeffler diagram is entirely in the martensite area (M), it is rather close to the martensite and δ-ferrite area (M+F). Therefore, for welds subjected to elevated temperatures where the evolution of heating and cooling is dependant on the type of welding process applied, the Schaeffler diagram itself is not sufficiently reliable.

A ferrite factor less than 8 is accepted to give rise to a fully martensitic microstructure whereas a FF higher than 11 will result in the formation of significant amounts of δ-ferrite [97]. T91 with a chemical composition within the ASTM requirements has a FF<8 and should not show any δ-ferrite formation.
This is again confirmed by looking at the equilibrium phase diagram for T91, depicted in Figure 2.32, which was obtained with the aid of Thermo-Calc [97]. Although equilibrium phase diagrams will not show the formation of metastable structures such as martensite, they give an important insight in the evolution of the microstructural phases at elevated temperatures.

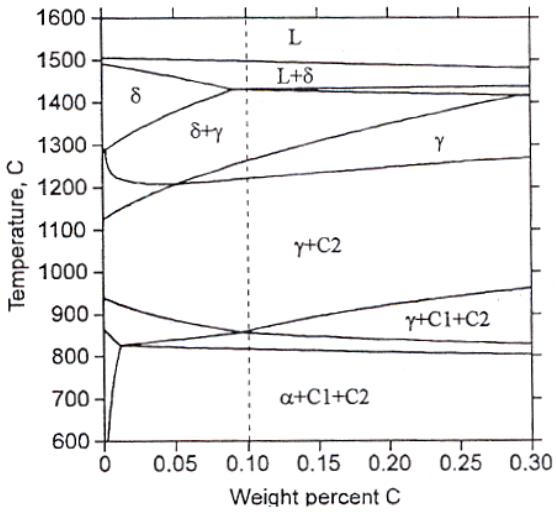

Figure 2.32: Section of the Fe-C phase diagram for T91 as obtained with Thermo-Calc [97].

In Figure 2.32, in addition to the ferrite (α) and austenite (γ) phases, the carbides $M_{23}C_6$ (C1) and MC (C2) are also included. In order to understand the evolution of the phases in T91 steel with temperature one has to consider the dashed line in Figure 2.32 corresponding to the weight percent of carbon in T91. One can see that there exists a wide range of temperatures (800-1200°C) in which the material will have a fully austenitic microstructure and therefore will exhibit a fully martensitic structure upon air cooling after an austenitising treatment.
The risk of the occurrence of δ-ferrite can only occur in the areas of the HAZ that were heated above 1200°C and subsequently rapidly cooled. For this reason welds of T91 need to undergo slow cooling. The resulting microstructure of the weld metal is however in some cases not fully martensitic [98]. The HAZ has the characteristic morphology of a grain growth region close to the weld interface and a grain refined region farther away from the weld interface [99].

Although the experience from the power generating industry in welding T91 tubes has been favourable, the issue of welding procedures for thick section vessels of T91 still copes with some problems which should not be overlooked [100].
The hardness profile after PWHT of a T91 welded joint typically has a hardness dip in the fine grained region of the HAZ close to the base material (intercritical zone). This softened zone in a weldment is usually very thin. Nevertheless it determines the creep rupture strength of the weld when transversal stresses are dominant [101]. Under such conditions, the supporting effect of neighbouring regions with higher strength decreases more and more as the operating time increases and the fracture mode becomes increasingly intergranular. Therefore cross weld creep tests of T91

show a shift in fracture location from the base material to the fine grained HAZ. This phenomenon is known as type IV cracking and displayed in Figure 2.33. The shift in fracture location is stress and temperature dependent [102]. Notice that such a decrease in creep rupture strength is of importance only in welds with the principle stress acting in cross weld direction.

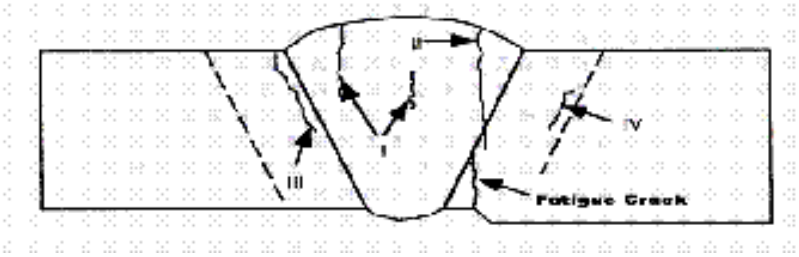

Figure 2.33: Schematic weld crack classification: Type I – Oriented Transverse or Longitudinal, located in the weld, remains in the weld; Type II – Similar to Type I but grows out of the weld; Type III – Located in the Coarse-Grained HAZ; Type IV – Located in the Fine-Grained/Intercritical HAZ .

The problem of type IV cracking is shared by all ferritic steels and becomes a problem in the case of T91 at temperatures above ~565°C. It results in the formation of circumferential cracks around the outer edges of the heat affected zone. It is a consequence of the fact that the creep rupture strength of the normalized and tempered base material decreases substantially with increasing tempering temperature (~above 800°C) and increases progressively with austenitising temperature (above ~900°C) as can be seen in Figure 2.34.
The figure shows the rupture lives at 570°C and 600°C of T91 plate given a standard normalizing treatment followed by five minutes at the temperatures indicated -to simulate the microstructure variation across the HAZ- then a typical PWHT of 1 hour at 730°C. The austenite transformation temperature (A_{c1}) in this case is around 830°C with full transformation by ~930°C. The weld therefore exhibits a severe minimum in rupture life at the outer edge of the HAZ where the material has been severely overtempered, intercritically transformed or transformed to fine grained austenite [102].

Therefore it seems necessary when forming vessels from rolling plate for longitudinal seam welding for good toughness in the weld seam to aim toward high nickel contents in the filler. As mentioned above, the effect nickel has on the critical temperatures must be regarded when establishing the welding procedures. Moreover the high nickel content in the weld may not be desired in certain environments such as LBE due to the preferential dissolution of the nickel which could lead to the early degradation of the vessel weldments.

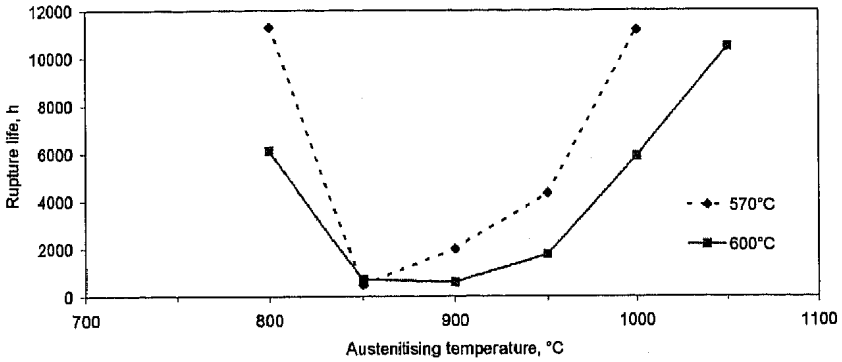

Figure 2.34: Effect of austenitising temperature on rupture life of P91 material [102].

Reheat cracking is another common type of failure that can occur in (P)T91 weld joints. The Cr-Mo steels are generally most susceptible to this type of failure but we must note that the advanced Cr-Mo steels such as T91 have been designed to be less sensitive to reheat cracking.
This type of cracking is found in the coarse grained regions of the heat affected zone (HAZ) beneath the weld and in the coarse grained regions within the weld metal. The fracture is typically intergranular and is attributed to the precipitation of Nb and V carbides during the PWHT which causes the grain boundaries to become weaker than the precipitation hardened matrix.
Stress concentrations, impurities, hydrogen, poor weld process, and/or poor PWHT in combination or as stand-a-lone propagators can lead to various degrees of reheat cracking. The cracking itself occurs in the PWHT cycle between 540°-600°C where the grain structure of T91 Cr-Mo alloy weld joints characteristically weakens.

2.2.1.2.2 Welding 316L

The austenitic stainless steels within the 300 series contain approximately 18 wt% Cr and 8 wt% Ni. The 316L type has an elevated Mo concentration and the carbon content is kept below 0.03 wt%. The molybdenum gives the steel an improved corrosion resistance, particularly to resist pitting corrosion. The reduced carbon content gives the steel an improved weldability and increases the resistance of weldments to corrosion due to the lower risk of sensitisation. The chemical composition of 316L as described by the ASTM as well as the composition of the steel under study in this work was shown in Table 2.3 in 2.1.3.1.

The austenitic grades are all very readily welded (with the exception of the free-machining grade 303). All the usual electric welding processes can be used and a full range of welding consumables is readily available.

The most well known problem in weldments of austenitic stainless steels is the loss of corrosion resistance due to intergranular corrosion or sensitisation. This is due to the limited solubility of carbon in the alloy. As well known, Cr has a very large affinity to carbon. This causes the solubility of carbon in the austenite to decrease. In addition, the presence of nickel further reduces this solubility limit.
Austenitic stainless steels are generally delivered in the solution annealed condition. This however means that the carbon in the steel is kept in an oversaturated condition and that elevated temperatures cause the carbon to precipitate in the form of chromium carbides. The precipitation of these carbides demands the diffusion of both Cr and C. The formation of the carbides therefore causes a depletion of Cr and C in the close vicinity of the forming precipitate. At temperatures of 500-700°C carbon already has a significant diffusion rate as opposed to the chromium. Due to the large diffusion speed of carbon, the differences in C concentration will be annihilated very fast however the Cr concentration difference does not equalise so fast. After welding, the areas around the precipitates that are depleted in Cr to beneath 13 wt% are no longer corrosion resistant. These precipitates are often located on the grain boundaries hence the intergranular corrosion.

The lower amount of carbon in the 316L variety will automatically lower the possibility for Cr carbides to be formed during welding and therefore lower the risk of sensitisation. The sensitisation is caused by the lack in diffusion of Cr and when keeping the weldment at higher temperatures for longer periods the concentration difference will be annihilated. Therefore it should be noted that if a fabrication has become sensitized during welding the effect can be reversed and the material restored to full corrosion resistance by a full solution treatment.

Besides possible sensitization, the chemical composition of 316L seems to influence the solidification mode and the risk of slag inclusions which have an effect on both the corrosion and mechanical properties of the weldment.
Minor changes in composition within the ASTM compositional requirements can alter the way in which 316L solidifies during welding. Possible solidification modes are shown in Figure 2.35. These modes are austenitic, austenitic-ferritic, ferritic-austenitic and ferritic. The majority of 316L chemistries will provide welds that are austenitic, austenitic-ferritic or ferritic-austenitic.

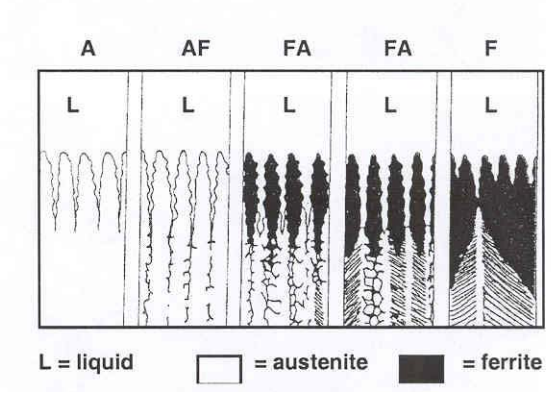

Figure 2.35: Solidification modes in AISI 316L;
A: austenite; AF: austenitic-ferritic; FA: ferritic-austenitic; F: ferritic.

The austenitic weld will solidify completely to austenite without any further high temperature transformations. The austenitic-ferritic weld solidifies as austenite and ferrite is formed from the melt retained between the austenite dendrites. In the ferritic-austenitic weld, ferrite solidifies first and austenite forms between the ferrite dendrites. The austenite subsequently grows into the ferrite, resulting in a significant decrease in the volume fraction of ferrite. At room temperature the weld is substantially austenite with a small volume of retained ferrite. The ferritic-austenitic solidification is the preferred solidification mode due to the higher solubility of the slag forming elements such as calcium, aluminium and silicon in ferrite than in austenite. This reduces the risk of slag inclusions. However, too much ferrite creates preferential corrosion sites and reduces the resistance to pitting corrosion of the weld.

Although several equations exist to calculate the chromium and nickel equivalent, the equation developed by Hammar and Svensson especially for austenitic stainless steels shows an excellent correlation between composition and solidification mode. The equivalents are as follows [103]:

$$Cr_{eq} = \%Cr + 1.5\,\%Si + 1.37\,\%Mo + 2\,\%Nb + 3\,\%Ti \quad \textbf{(2.4)}$$

$$Ni_{eq} = \%Ni + 22\,\%C + 0.31\,\%Mn + \%Cu + 14.2\,\%N \quad \textbf{(2.5)}$$

Solidification mode can be predicted by the ratio of Cr_{eq}/Ni_{eq}. For $Cr_{eq}/Ni_{eq} < 1.5$ the mode is austenitic or austenitic-ferritic. From $1.5 \leq Cr_{eq}/Ni_{eq} \leq 2.0$, solidification is ferritic-austenitic and for values > 2.0, solidification is ferritic.

Based on a TIG welding study performed by Swagelok using 21 different heats of 316L, it was found that a composition with a $Cr_{eq}/Ni_{eq} \geq 1.45$ provided acceptable

welds with minimal slag formation. In addition, corrosion resistance of welded 316L remained high when the amount of ferrite measured in the weld was under 3% or when $Cr_{eq}/Ni_{eq} \leq 1.55$ [103]. The 316L under study in this work has a Cr_{eq}/Ni_{eq} value of 1.77 and is therefore predicted to be easily weldable but the pitting corrosion resistance of the weld is expected to be less than this of the base material.

Regarding the influence of the applied welding technique the reheating effect accompanied by multi-pass welding processes such as TIG welding of thick structures seems to have a negative effect on the low temperature toughness of the 316L weld material [104]. This effect is attributed to the formation of intermetallic compounds near δ-ferrite phase.
The weld metal of type 316L stainless steel processed by reduced pressure electron beam welding however does not have this reduction in low temperature toughness, which is considered to be due to the single pass welding process.

2.2.1.2.3 Mixed T91/316L welding

Welding together of different metals can be carried out, although some extra precautions need to be taken. Note that the possible problems mentioned above are still present in the case of the mixed weldment but the welding metallurgy is complicated by the often relatively strong difference in composition and microstructure between the materials to be joined.

It is usually recommended that over-alloyed austenitic welding rods, such as Grade 309, should be used to minimise dilution effects on the stainless steel component. The microstructure obtained from the composition of the weld deposit resulting from dissimilar grade welding can be derived from the Schaeffler diagram (Figure 2.36) or from its successors by De Long (Figure 2.37) and more recently the WRC diagram (Figure 2.38). Australian standard AS/NZS 1554.6 contains a table giving the pre-qualified consumables for each combination of dissimilar metal welds.

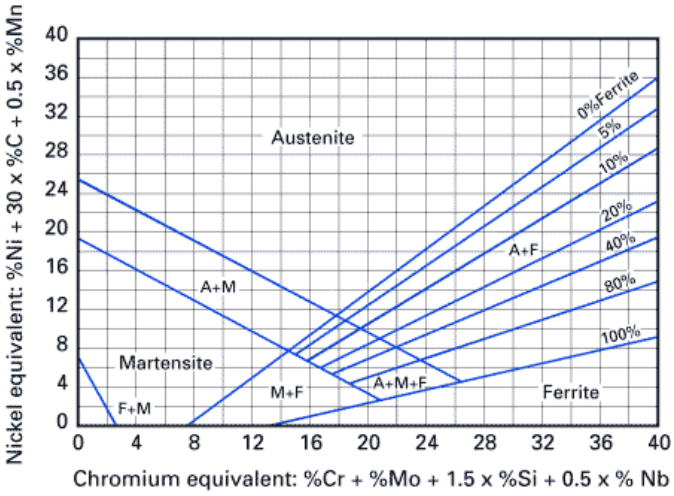

Figure 2.36: Schaeffler diagram.

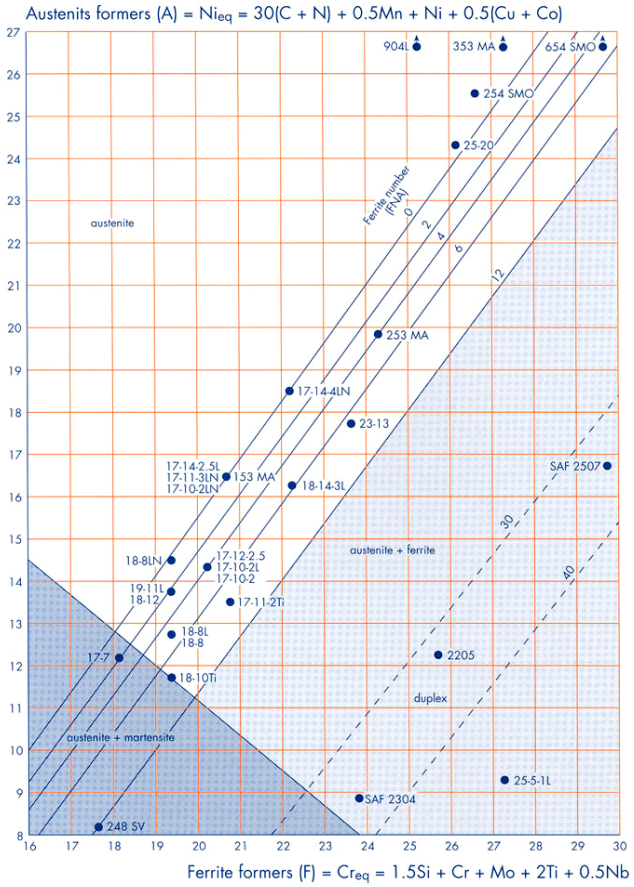

Figure 2.37: De Long diagram.

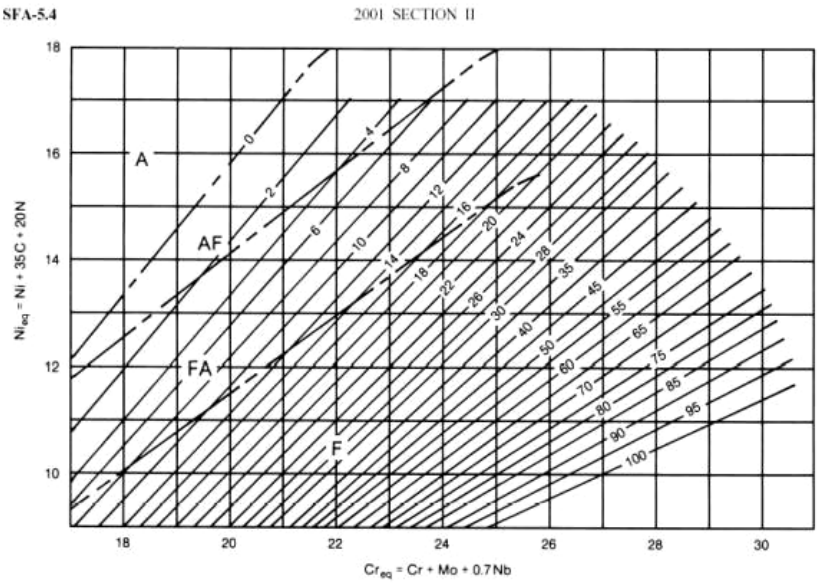

Figure 2.38: WRC-1988 (FN) Diagram for Stainless Steel Weld Metal.

In the case of mixed weldments, literature references tend to be either very scarce or relatively insignificant due to the specificity of the combination of the materials to be joined, the filler material and the applied welding technique.

At this point, it is worth to stress the importance of specific research regarding the possible problems of the envisaged mixed weldments. Especially when applied in neutron or neutron/proton irradiation environments up to relatively high dpa possible effects such as sensitization due to radiation induced segregation, preferential dissolution and possible problems due to differential swelling should not be overlooked.

2.2.2 T91/T91 welds

2.2.2.1 T91/T91 TIG weld

The T91/T91 TIG weld comprises in total 10 weld passes.
The first two passes were realized using manual gas tungsten inert gas welding (GTAW) with a Thermanit MTS3 TIG wire (AWS ER90S-B9), Ø 2.4 mm and a minimal preheating temperature of 220°C. Passes 3 – 6 were realized by manual shielded metal arc welding (SMAW) using a Chromo 9V electrode (AWS E9015-B9), Ø 2.5-3.2-4 mm with a minimal preheating temperature of 220°C. Passes 7 - 10 were done by submerged arc welding (SAW) under a bed of Marathon 543 flux with a Thermanit UP MTS3 wire (AWS EB9 proposed), Ø 2.5 mm and a preheating temperature of minimum 230°C.
The PWHT consisted of a maximum heating rate of 105°C per hour up to 750°C were the material was kept for 1 hour and 10 minutes. The applied cooling rate was a decrease in temperature of maximum 100°C per hour down to 80°C when the weldment was removed from the furnace and cooled down to ambient temperature without temperature control.

2.2.2.1.1 Microstructure

The T91/T91 weld specimens were prepared by mechanical polishing using a Struers Roto Pol-11 to 1 µm fine grain. Etching of the T91 welds was done using Villela's reagent.
The T91/T91 TIG weld is fully martensitic. After etching the different welding passes can clearly be distinguished. The evolution of grain sizes due to the different temperatures obtained in the HAZ is however difficult to distinguish.

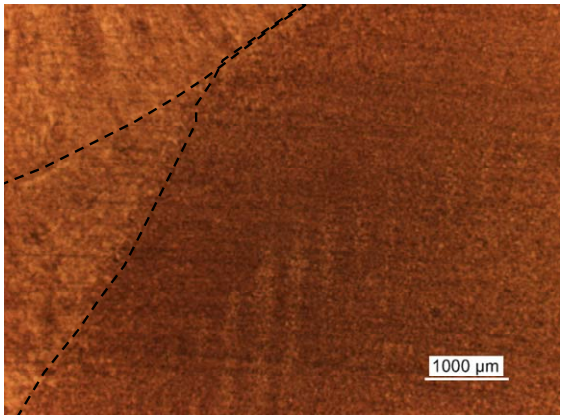

Figure 2.39: Martensitic microstructure of the HAZ. The upper left shows part of two welding passes whereas the lower right bottom shows the microstructure of the base material.

Figure 2.39 shows the microstructure of the HAZ. The upper left in the figure shows the weld whereas the lower right bottom of the picture shows the microstructure of the base material. On the left hand side one can distinguish two welding passes indicated by dashed lines. No porosities, micro-cracks or slag inclusions were found in this weld.

2.2.2.1.2 Mechanical properties

2.2.2.1.2.1 Hardness profile

Hardness measurements were performed across the welded joint to assure its quality. The indentations were made both on the upper, wider side of the weld as on the lower, more narrow side which is indicated respectively by line 1 and line 2 and can be seen in Figure 2.40. Note that the TIG welds have been given a proper heat treatment at the welding company as mentioned earlier. The hardness profile after PWHT of the welded T91 seam has the typical hardness dip in the fine grained region of the HAZ close to the base material (intercritical zone) as can be seen in the figure. This softer region is known to determine the creep rupture strength of the weld when transversal stresses are dominant. The hardness values across the weld do correspond to the expected values for this type of weld and therefore confirm the quality of the performed PWHT.

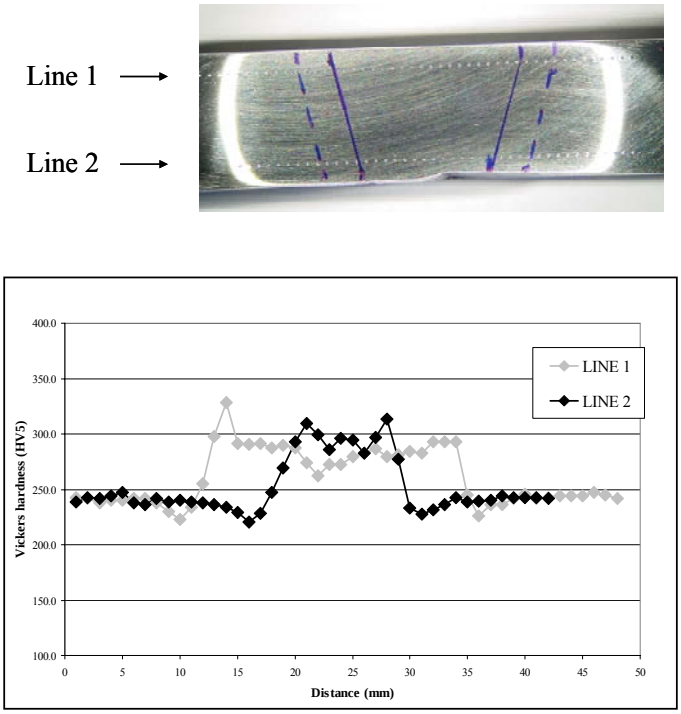

Figure 2.40: Hardness profile across the weld; Left: picture of welded joint with indentations; Full lines indicate weld area, dashed lines indicate HAZ; Right: Vickers hardness profile as measured across the weld.

2.2.2.1.2.2 Tensile tests

We performed tensile tests on mini tensile specimens with a gauge length of 12 mm and a diameter of 2.4 mm, which were taken across the weld. The tests as function of temperature were performed at a strain rate of 3.10^{-4} s^{-1}. To evaluate the mechanical properties of the TIG weld, these tests were compared to those performed on the T91 base material. The results are depicted in Figure 2.41. It is clear that the TIG weld has slightly higher strength and comparable though slightly lower elongation. This complies with the expected behaviour of a good T91/T91 TIG weld.

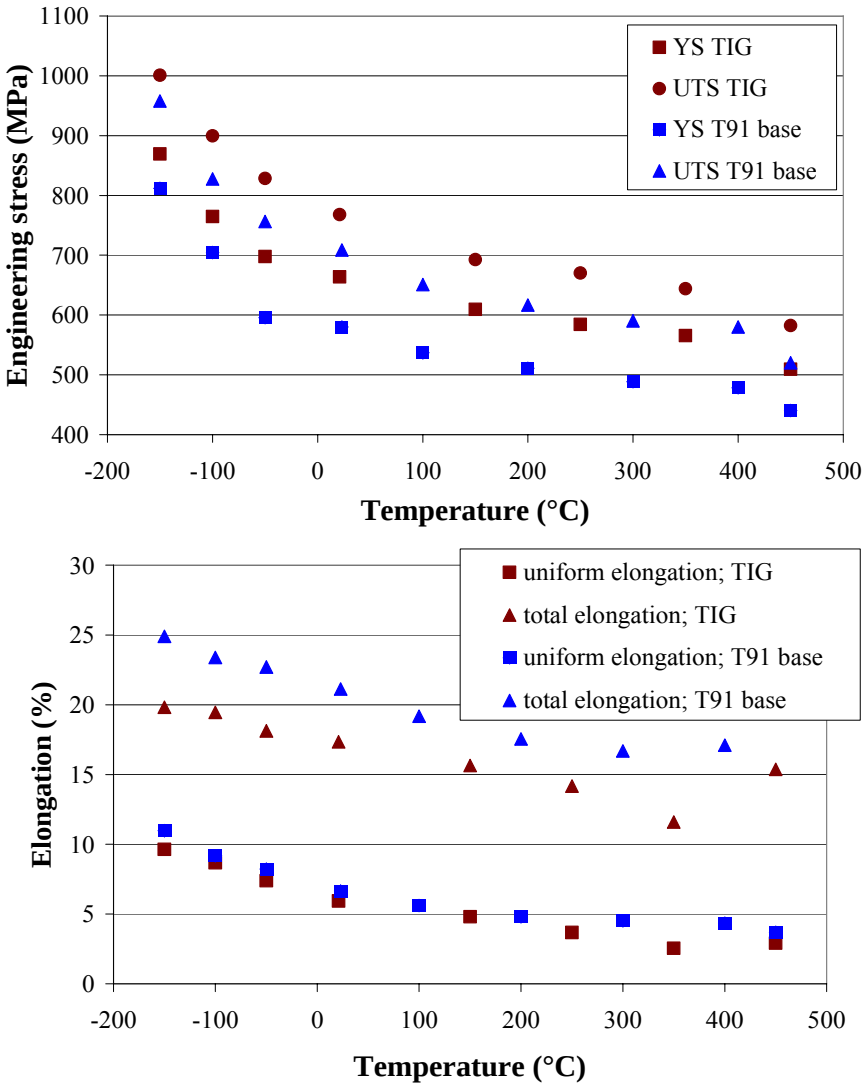

Figure 2.41: Tensile properties of T91 base material vs. T91/T91 TIG (specimens across the weld). Above: YS and UTS as function of temperature; Below: Total and uniform elongation as function of temperature.

2.2.2.2 T91/T91 EB weld

The electron beam weld was performed by FZK using an EBW 1001/10-60 CNC from PTR Präzisiontechnik, Maintal, Germany. The welding machine has a maximum voltage of 60 kV and a maximum current of 167 mA. The vacuum chamber has a dimension of 580 mm by 350 mm with a height of 500 mm. Prior to welding, the parts to be welded were decreased and fixed together by TIG. When placed in the vacuum chamber, the chamber is pumped down to about 6.10^{-3} mbar. Applied electrical tension during EB welding for the weldments under investigation was 60 kV, at a current of 62 A. The used welding speed was 10 mm/sec. The weld was made available to us in the as welded condition.

2.2.2.2.1 Microstructure

Similar to the preparation of the T91/T91 TIG weld, the EB weld specimens were prepared by mechanical polishing using a Struers Roto Pol-11 to 1 µm fine grain. Etching of the T91 welds was done using Villela's reagent. The T91/T91 EB weld is fully martensitic.

Due to the process of electron beam welding the actual weldment can be kept relatively small.

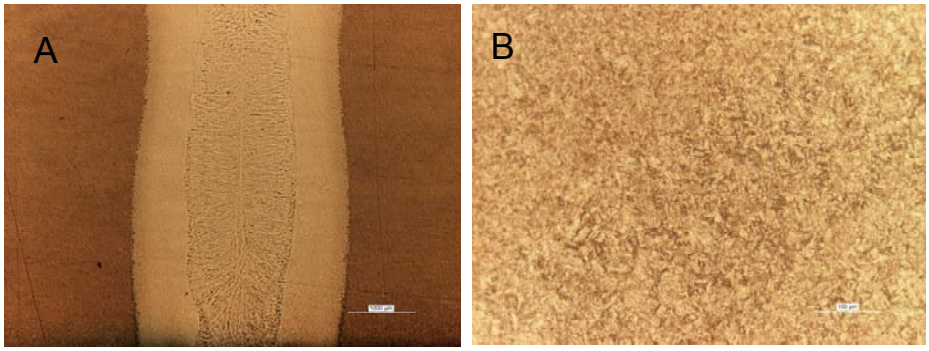

Figure 2.42: Electron beam weld of T91. A: microstructural overview of the weldment; B: ferritic martensitic microstructure in the heat affected zone.

In Figure 2.42A, a general overview of the weldment is shown. Note that the width of the EB weld and heat affected zone of this 15 mm thick welded plate is only a few millimetres.

The heat affected zone of this type of weldments is therefore very small and differences in grain size between the grains in the HAZ on the side of the base material and the grain size in the HAZ on the side of the weld can be kept to a minimum. The EB weldment is expected to have significantly smaller influence on the mechanical behaviour of the material compared to a traditional TIG weld due to

the narrow weld and the constant chemical composition across the weld. The microstructure in the HAZ is depicted in Figure 2.42B.

The chemical composition of the EB welded joint as measured by EDX does not vary across the weld as opposed to the composition of the TIG welded joint. This is illustrated in Figure 2.43 which shows the composition profile across the TIG weld (Figure 2.43A) as well as across the EB welded joint (Figure 2.43B).

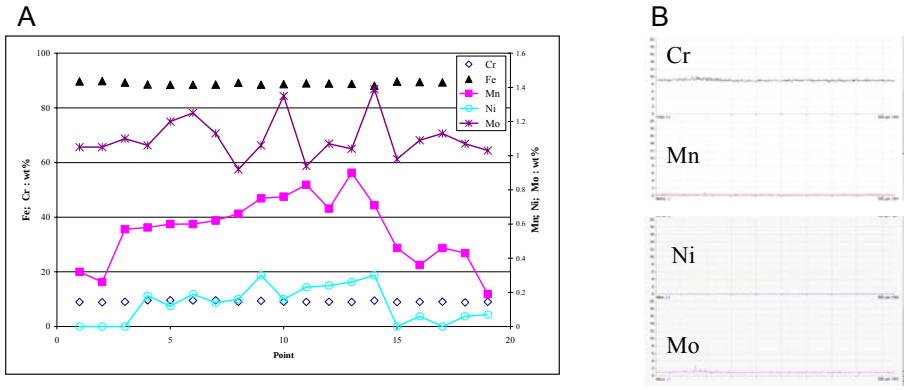

Figure 2.43: Chemical composition across the T91/T91 welded joints as measured by EDX. A: Cr, Fe, Mn, Ni and Mo measured at 20 equidistant points across the T91/T91 TIG weld; B: Cr, Mn, Ni, Mo-composition across the T91/T91 EB welded joint.

2.2.2.2.2 Mechanical properties

2.2.2.2.2.1 Hardness profile

As mentioned earlier the electron beam welds were supplied in the as welded condition and needed to be given an appropriate PWHT. Figure 2.44 shows the Vickers hardness measurements across the electron beam weld before and after PWHT. The PWHT consisted of a heating ramp of 100°C per hour and a holding time of 1h 10' at 750°C. The cooling was done at a maximum rate of 100°C per hour.

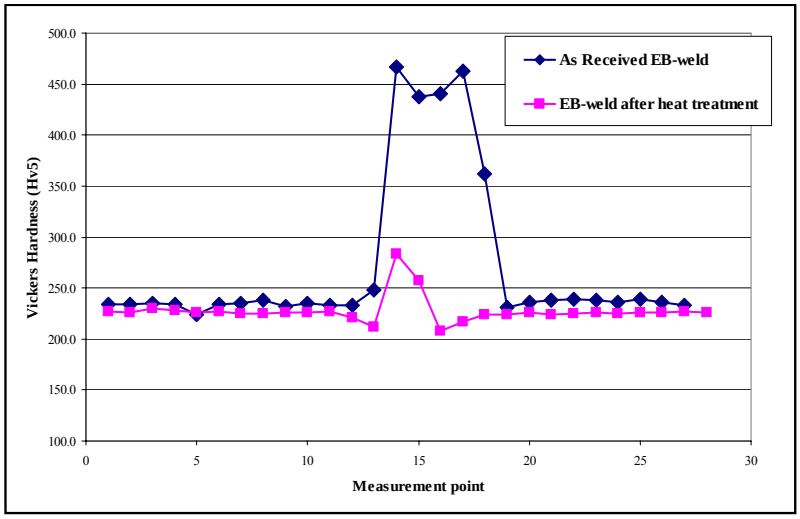

Figure 2.44: PWHT thermal profile and hardness measurements of T91/T91 EB before and after PWHT.

Due to this PWHT the hardness maximum has been decreased from 466 Hv to 283 Hv without significantly softening the base material. Again here the hardness profile after PWHT of the welded T91/T91 seam has the typical hardness dip in the fine grained region of the HAZ close to the base material (intercritical zone) as can be seen in Figure 2.44. Note that the width of the zone influenced by the EB weldment also narrows due to the PWHT. This is thought to be the optimum heat treatment for this welded joint. Longer holding times tend to increase softening of the base material whereas shorter holding times result in a smaller decrease of the hardness peak.

2.2.2.2.2.2 Tensile tests

Similar to the tensile tests performed on the T91/T91 TIG weld as function of temperature, we performed tensile tests as function of temperature both on the heat treated and the as received EB weld. The results of these tests are depicted in Figure 2.45. At first sight, there is little difference in mechanical behaviour between the heat treated and as received weld. It should however be noted that the EB weld, including HAZ is only a few millimetres wide while the tensile sample has a gauge length of 12 mm. The influence of the weld is therefore small.

Despite the small influence, it can be seen that the heat treatment has improved the mechanical properties of the weld as expected from the hardness profile.

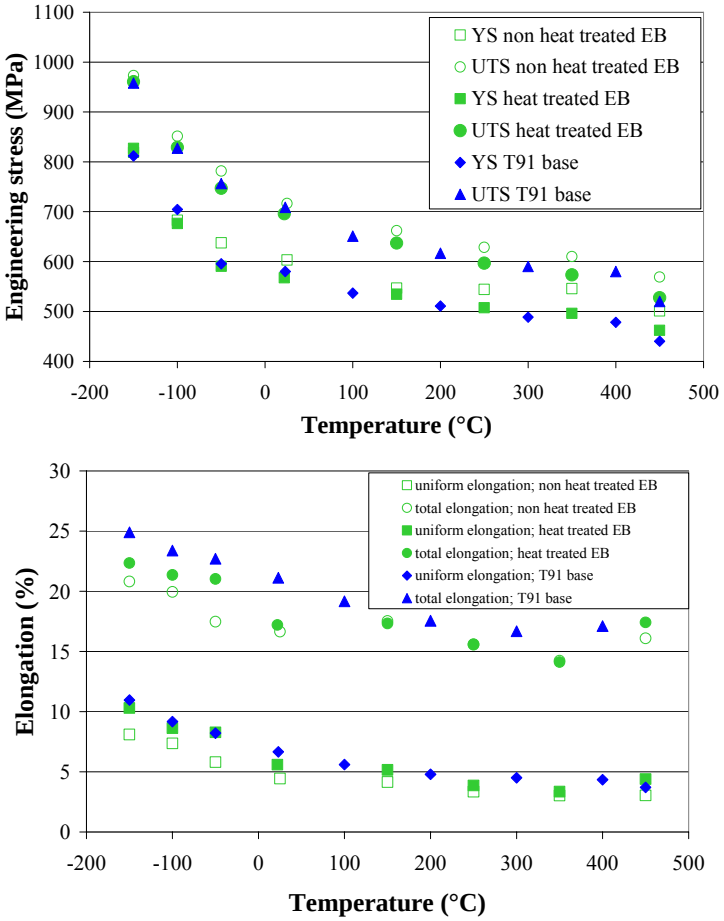

Figure 2.45: Tensile properties of T91 base material vs. T91/T91 EB (specimens across the weld). Above: YS and UTS as function of temperature; Below: Total and uniform elongation as function of temperature.

2.2.3 T91/316L welds

2.2.3.1 T91/316L TIG welds

The T91/316L weld is performed in two phases. At first a high alloyed 309 alloy is welded by SAW on to the T91 in five passes using an Arosta 309S electrode, Ø 2.5-3.2 mm and preheating the T91 steel to a minimal temperature of 250°C. This procedure is called beurrage or buttering. After the buttering, a PWHT was performed in order to relieve stresses by heating up the plate starting from room temperature at a maximum heating rate of 100° per hour up to 740°C and holding it for 45 minutes. Cooling was performed at a controlled rate of maximum 95°C per hour down to 50°C when the plate was removed from the furnace. The profile of the PWHT is shown in Figure 13.
In a second phase the actual connection weld is made between the 316L plate and the over alloyed 309 side of the T91 plate. This weld comprises of 11 passes in total. The first two passes are performed using manual TIG welding with respectively an LNT 316L, Ø 2.4 mm and a Nortal Inox 20-10-5, Ø 2.4 mm, AQ 8447 electrode.

2.2.3.1.1 Microstructure

The 316L/T91 TIG weld joint which is schematically represented in Figure 2.46, consists of four zones: the base materials: T91 and 316L steel, the filler material in 316L alloy and the buttering material in 309 alloy.

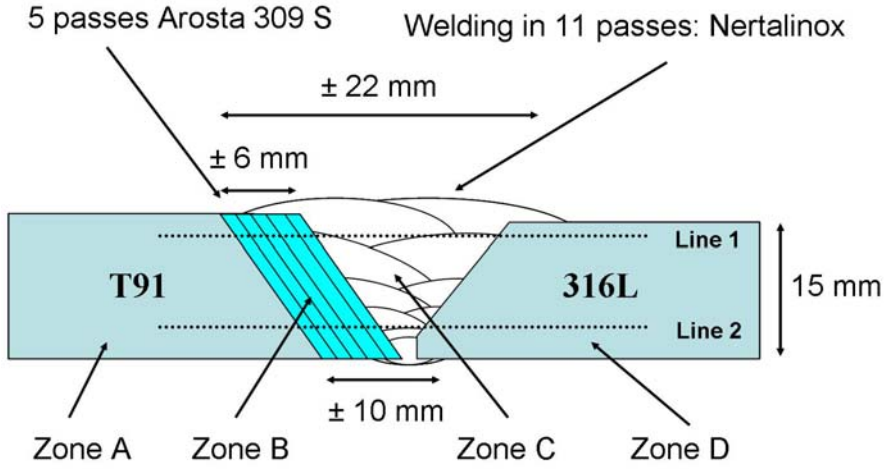

Figure 2.46: Schematic representation of 316L/T91 TIG weld joint.

The weld joint was mechanically polished in order to analyze its microstructure. At first, it was etched using Villela's reagent to reveal the microstructure of the T91

steel (zone A in Figure 2.46), and then electro-polished (97% acetic acid, 3% perchloric acid) to reveal the microstructure of the austenitic steels (zones B, C and D in Figure 2.46). The sample was observed by optical microscopy and by Scanning Electron Microscopy (SEM). Figure 2.47 shows the micrographs of the different zones of the 316L/T91 TIG weld joint.

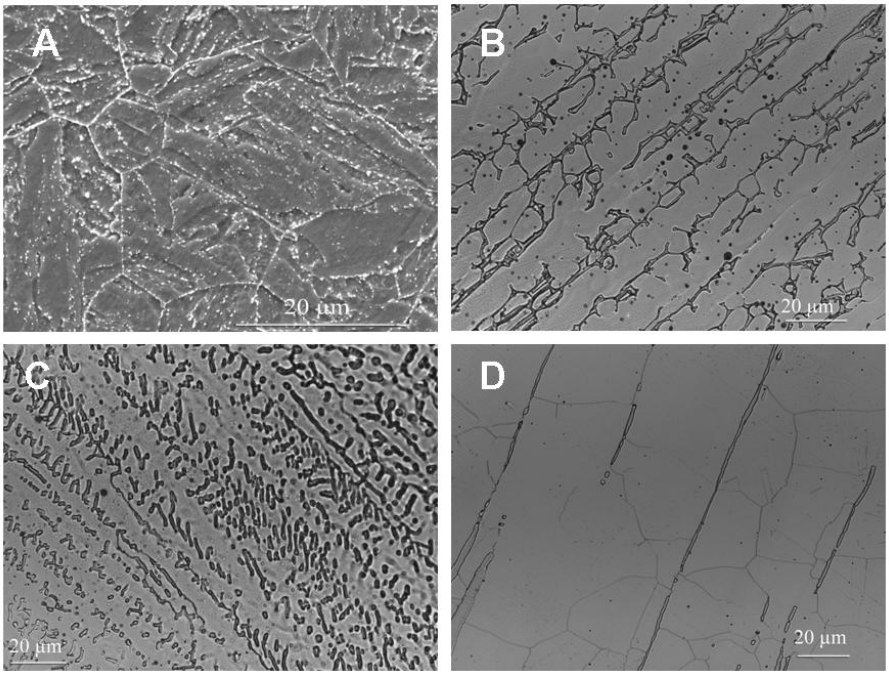

Figure 2.47: Micrographs of the different zones of the 316L/T91 TIG weld joint; A: T91 base material; B: 309 filler material; C: 316L weldment; D: 316L base material with δ-ferrite.

The microstructure of the T91 steel (zone 4) consists of a tempered martensite (Figure 2.47A). The microstructure of the 309 filler material (zone 3) is dendritic (Figure 2.47B) as well as this of 316L filler alloy, with dendrite morphology depending on the pass number (Figure 2.47C and Figure 2.47D). The microstructure of the 316L base material consists of austenite grains and delta ferrite islands (Figure 2.47E) which was confirmed by X ray diffraction. The presence of delta ferrite is related to the composition of the steel, especially its relatively low Nickel content. No porosity or micro-crack was observed at the interface between the different zones.

2.2.3.1.2 Mechanical properties

2.2.3.1.2.1 Hardness profile

We performed indentation tests at room temperature across the weld on the upper side of the weld (line 1), as well as on the lower part (line 2) (Figure 2.46).
The hardness profile across the welded joint is illustrated in Figure 2.48. In the graph, the T91 base metal is located on the left side of the profile.

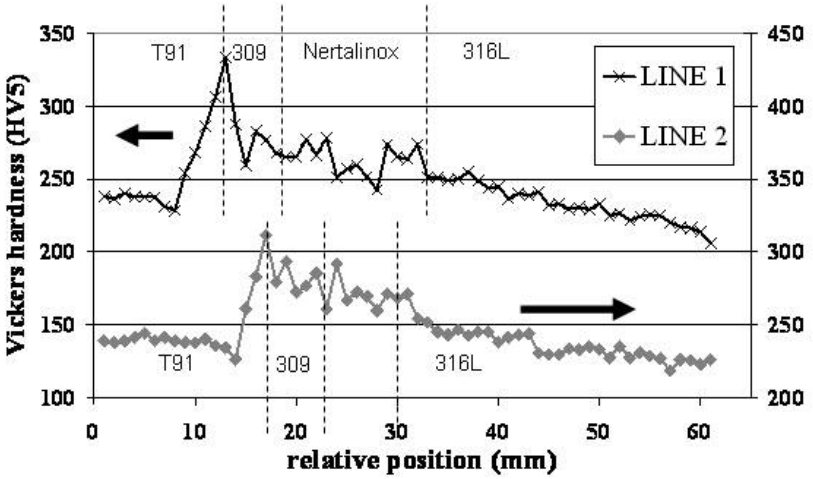

Figure 2.48: Vickers hardness measurement across the T91/316L weldment. T91 base metal is located on the left side of the profile, 316L on the right.

2.2.3.1.2.2 Tensile tests

We did not perform any tensile tests as function of temperature of T91/316L TIG weld specimens due to the complex nature of the weld. First of all, the weld, including its HAZ is wider than 12 mm (gauge of the used specimens) and secondly, when testing across the weld there are in fact 4 different materials involved which makes useful interpretation very difficult.
Specimens were however machined along various orientations along the T91/316L TIG weld and tested both in Ar + 5% H_2 (reference) and in LBE at 350°C. These results will be discussed in detail in Chapter 6 and Chapter 7.

2.2.3.2 T91/316L EB welds

The T91/316L EB weld was fabricated by FZK, Germany using the same equipment and procedure as for the T91/T91 EB weld which was explained in 2.2.2.2.

2.2.3.2.1 Microstructure

The microstructure of the T91/316L EB weld itself is clearly martensitic which is due to the higher fraction of melting of T91 compared to 316L during welding. This is entirely according to expectations due to the higher heat conductivity of T91 and the relatively close melting points of the two materials as illustrated in Table 2.9. Note that again here as it was in the case of the T91/T91 EB weld, the EB weld together with the HAZ is only a few millimetres wide. No microcracks were seen in the welded joint.

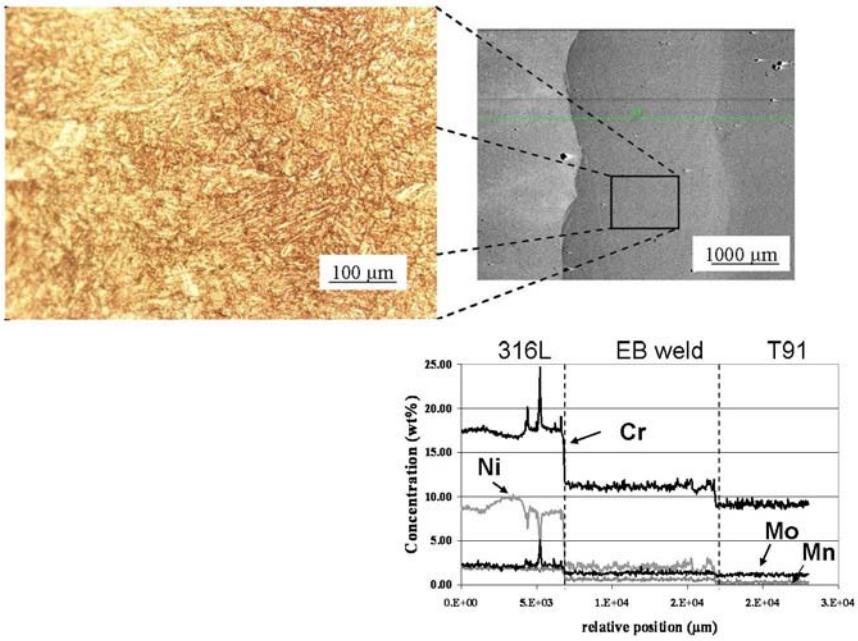

Figure 2.49: Martensitic microstructure of the weldment and chemical composition across the T91/316L EB welded joint as measured by EDX.

The compositional profile as measured by EDX across the mixed weld is depicted in Figure 2.49 as well as the martensitic microstructure of the weldment itself. As Figure 2.49 shows, the chemical composition changes very sudden at the interfaces between base metal and weldment but remains rather constant within the weldment itself. This type of compositional profile may pose problems in terms of sensitisation of the 316L after ageing.

2.2.3.2.2 Mechanical properties

The T91/316L EB weld was supplied by FZK in the as welded condition as mentioned before and like the T91/T91 EB welded joint needed a proper PWHT. The difficulty for this joint however is that the 316L base material is normally in a solution annealed condition and heat treatment causes the material to soften significantly. On the other hand the T91 martensitic steel needs a heat treatment to release the thermal stresses resulting from welding. This results in a delicate balance to optimise the mechanical properties of the welded joint. Figure 2.50 shows the Vickers hardness across the T91/316L EB welded joint before and after PWHT. It was chosen to decrease the welding stresses in the T91 as much as possible without softening the 316L too much.

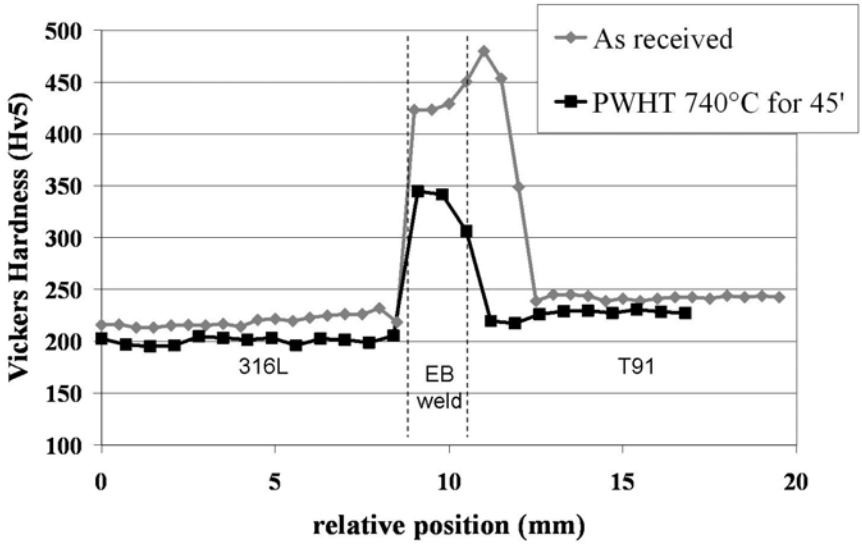

Figure 2.50: Hardness measurements of T91/316L EB before and after PWHT.

Due to the difficult interpretation of tensile results of a bimetallic joint no tensile tests were performed. Nor were any tests performed on the separate zones of the T91/316L EB weld because this would just be like testing the base material due to the small zone influenced by the weld.

2.3 PB, PBBI & PBLI EUTECTIC

In this PhD, the emphasis is on the mechanical properties of the candidate structural materials when in contact with the heavy liquid metal coolant (HLMC). The examination of the thermodynamical properties of these HLMC's was outside the scope of this work. It is however considered useful to briefly summon the most important properties of the coolant which will have an influence on the "boundary conditions" of the applied solid metal – liquid metal system. The focus in this section will be on lead bismuth eutectic, but we will mention several properties of lead and lead lithium eutectic to have a more complete view on the coolant criteria and to understand the preference for LBE.

2.3.1 Lead

Lead (Pb) [105] is not so expensive ($470-$510) a tonne. Due to a low neutron absorption cross-section (< 0.17 barn) and due to a high atomic mass (A = 207.18), it has very good reflecting properties for neutrons with $E_n < 20$ MeV. Moreover it is one of the best shields against high energy gamma-rays. Natural lead consists of four stable isotopes: 1.4 at.% $^{204}Pb_{82}$, 24.1 at.% $^{206}Pb_{82}$, 22.1 at.% $^{207}Pb_{82}$, 52.4 at.% $^{208}Pb_{82}$. After neutron capture followed by β-decay ($\tau_{1/2}$ = 3.25 h), the last of them yields the stable $^{209}Bi_{93}$, which, in its turn, can capture a neutron and produce the α-radioactive Po-210: $^{209}Bi_{83} + {}^{1}n_0 \rightarrow {}^{210}Bi_{83}^{*} \rightarrow {}^{210}Po_{84} + e$ ($\tau_{1/2}$ = 138.4 d). This can cause some worries in the lead coolant circuit.

Pure lead has the highest melting temperature (327 °C) among the considered HLMC. An oxide film (PbO) very rapidly appears on the surface of the liquid lead even in dry air. The oxidation rate is sharply increases at 700-900 °C. A higher solubility of metals in the liquid lead and its eutectic alloys makes them more corrosion active than liquid alkali metals. However, the affinity of lead to oxygen is significantly lower than those of alkali metals, refractory metals and basic components of steels (excluding nickel).

Lead contracts at solidification for about 3.6 vol. %. Therefore special means should be designed to prevent the structure damage that can be caused by this contraction in the case of accidental freezing of the coolant system.

Graphite is not soluble in the lead at temperatures lower 700 °C and can be used for the liquid lead containers. Gases H_2, N_2 and CO_2 are hardly soluble and Ar, He are

insoluble in the liquid lead and can serve as a "cover-gas" to protect the lead surface against oxidation. The vapours of Pb (like those of other heavy metals) are toxic.

Different design options of the fast nuclear reactor BREST cooled by liquid lead are now under study in Russia.

2.3.2 Bismuth

Bismuth (Bi) [105] is far more expensive than lead: price range in 1999 was $7385-$8598 a tonne. Moreover, the world mine production of bismuth is not so high as for lead - about 4560 tonnes of Bi per year.

Bi has five times lower neutron absorption cross-section than Pb and even better neutron reflecting properties. An important disadvantage of Bi in comparison with Pb is by three orders of magnitude higher production of α-radioactive Po-210, due to the thermal neutron capture followed by β-decay. This requires special means of protection during maintenance of the liquid bismuth coolant circuit.

Bismuth is more active chemically than lead: when Bi is heated in air to sufficiently high temperatures, it burns. The corrosion attack of the liquid bismuth on metals is stronger than that of the liquid lead at the same temperature.

The melting temperature of the pure bismuth is only by 56 °C lower than that of lead. It expands at solidification (and contracts in melting) for 3.32 vol. %.

A higher corrosion activity, a higher rate of radioactive polonium production and a relatively high price make the pure bismuth significantly less attractive than the pure lead. A project of using U-Bi eutectic as self-cooling nuclear fuel have been analysed in USA in 40-50x.

2.3.3 Lead Bismuth Eutectic

Lead-Bismuth Eutectic (*LBE*) [105], [106] contains 44.5 wt. % Pb and 55.5 wt.% Bi; so it should be at least by 40 % less expensive than the pure bismuth[1]. Its neutron properties are between those of Pb and Bi. The main disadvantage is a relatively high production of the radioactive polonium (Po-210), mainly due capture of the thermal neutrons by Bi. This polonium forms in LBE intermetallic compounds PbPo

[1] B.W. Spencer indicated a price of 0.55 $/lb ~ $1200 a ton for the delivered LBE.

and Bi_2Po_3. The last compound is not stable. At temperatures below 600 °C polonium exists in the non-saturated LBE melt in the form of PbPo, therefore the rate of release of the radioactive polonium from LBE is very close to that from the liquid lead under the same conditions (temperature, Po-concentration).

The presence of Pb significantly reduces chemical activity of Bi in LBE, however it remains higher than that of lead. The most important advantage of LBE is the lower melting temperature (123.5 °C) than that of lead (see the phase-diagram of the Pb-Bi system in Figure 2.51).

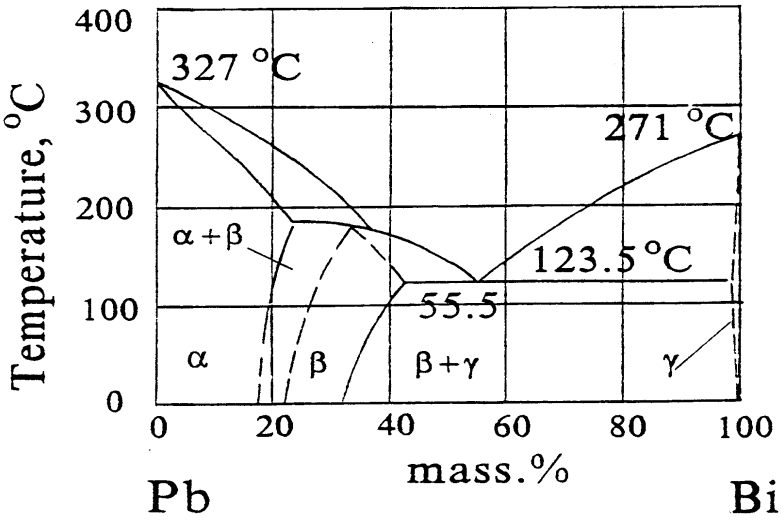

Figure 2.51: Phase diagram of the system lead-bismuth [105].

The corrosion attack of HLMC on structural materials is strongly increased with temperature, therefore it can be significantly reduced by decreasing the operation temperature. The HLMC melting temperature limits the minimum operation temperature. As a matter of fact, the operation temperatures must be at least 20-30 °C higher than the melting temperature, in order to ensure non-precipitation of the eutectic components in the case of variation of the chemical composition in the coolant circuit caused by chemical and nuclear reactions.

A change of the LBE volume in solidification is rather small (it is virtually zero due to mutual compensation of the effects of Bi and Pb), therefore it is possible to freeze and to thaw it repeatedly in ordinary steel pipes even when closed at one end.
Recently, Glasbrenner (referred to in [106]) showed that recrystallization at the level of a crystal grain is responsible for the expansion of LBE after freezing. In their experiments, two phases were identified immediately after rapid solidification of LBE:

- β-phase: an intermetallic compound with 42 at.% Bi (at the freezing point) and a hexagonal closed packed structure;
- γ-phase: a solid solution of Pb in Bi (~0.4 at.%Pb) with a rhombohedric structure.

The β-phase formed at freezing is not stable at room temperature. With time it is partly transformed into a β-phase with a lower Bi content (about 35 at.%) and γ-phase. As the γ-phase needs much more volume, the transformation produces an expansion of the material.
Measurements of this kind of LBE expansion performed at room temperature by Gröschel et al. (referred to in [106]) showed that it is reduced by a factor of 6 when slow cooling is used to 60-90 °C (333.3-363.3K) in the place of quenching.
Thus, in quasi-equilibrium processes a volume change close zero can be recommended for fusion of the pure LBE.

The high radioactive polonium production will require special means of protection during the maintenance of the LBE coolant circuit and will enhance the costs of its exploitation in comparison with the liquid lead variant.

Since the second half of the sixties, the LBE coolant has been used in nuclear propulsion reactors of some Russian submarines.

2.3.4 Lead Lithium Eutectic

Lead-Lithium Eutectic (LLE) [105] (99.3 wt.% Pb + 0.7 wt. % Li)[2] was considered as a candidate for coolant-breeder of the blanket in some projects of a fusion reactor. The phase diagram of the system "lead-lithium" is presented in Figure 2.52.

Because of a relatively high atomic fraction of lithium (~17 at.%), its effectiveness in the spallation source will be lower than in the case of the pure lead. Moreover, a significant amount of the radioactive tritium ($\tau_{1/2}$ = 12.3 y) can be produced in the result of the neutrons capture by Li [3] followed by α-decay: $^{6}Li_3 + {}^{1}n_o$ -> He + T; $^{7}Li_3 + {}^{1}n_o$ -> He + T + $^{1}n_o$. Lithium nucleus that absorbed a proton becomes two helium nuclei.

[2] In literature this eutectic is more known as the alloy *Pb-17Li* or Pb(83)Li(17) (i.e. *83 at.% Pb + 17 at. % Li*).

[3] Natural lithium contains *7.5 at. %* $^{6}Li_3$ and *92.5 %* $^{7}Li_3$. The microscopic cross-section of the thermal neutron absorption by the first is *941 barn*; the second has a neutron energy threshold of about *1 MeV*.

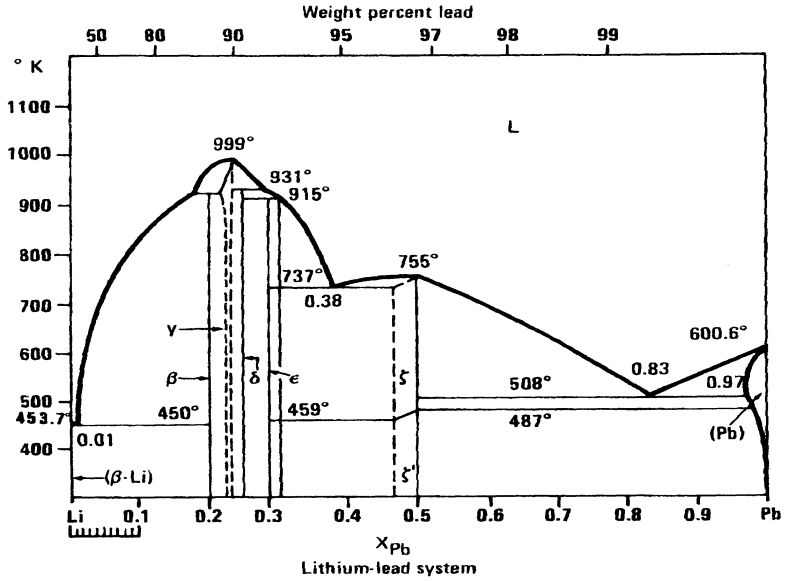

Figure 2.52: Phase diagram of the lead-lithium system [105].

The melting temperature of the LLE is about 250 °C. In the pure eutectic, Li is present in the form of the intermetallic compound PbLi, therefore its chemical activity is lower than that in the pure liquid lithium. A very high affinity of Li to oxygen can require about oxygen free conditions in the coolant circuit, in order to exclude a formation of the lithium oxide Li_2O. This also makes the oxide protective layers on the passivated surfaces of the steel structures ineffective, as in the case of the Pb-2.5Mg eutectic coolant. A number of studies have been performed in the 70-80's on the compatibility of steels with the liquid LLE in the framework of the International Co-operation on Fusion Reactors.

The brief review performed above allows concluding that LBE is the most attractive due to a complex of its properties: a high effectiveness of spallation, a low neutron absorption cross-section, the lowest melting temperature, good thermal properties, and a negligible change in density at solidification and melting. However, the "polonium problem" is more serious in the case of LBE.

In Table 2.10, we summon the thermodynamic properties of Pb, Li, Bi, PbBi and PbLi.

Table 2.10: Thermodynamical properties of lead (Pb), lithium (Li), lead-lithium eutectic and lead-bismuth eutectic (* T=500°C) [107].

Parameter	*Pb*	*Li*	*Bi*	*Pb-0.7Li*	*Pb-Bi*
Atomic weight (g/mol)	207.18	6.941	208.98	173.16	208.18
Neutron (th) absorption (Barn)	0.17	-		12.3	
Melting temperature (°C)	327.4	180.69	271.0	235	123.5
Latent heat of melting (kJ/kg)	23	0.00208	50.2	33.9	38.1
Volume change at melting (%)	+3.5	-	-3.32	+3.5	0.0
Density (kg/m^3)*	10430	~515	9910	9150	10200
Thermal expansion (K^{-1})*	$1.12 \cdot 10^{-4}$	$0.56\ 10^{-4}$		$1.23 \cdot 10^{-4}$	
*Heat capacity * (J kg^{-1}K^{-1})*	147			188	146.5
Thermal conductivity (W/mK)	15.4	0.847	13.3	17.1	13.2
Kinetic viscosity (m^2/s)*	$1.76 \cdot 10^{-7}$	-	$1.42 \cdot 10^{-3}$	$1.25 \cdot 10^{-7}$	
Surface tension (N/m)*	0.44	0.28		0.43	
*Solubility of Fe * (at%)*	$2.72 \cdot 10^{-4}$	-.		-	
Boiling temperature (°C)	1745	1347	1490	~1600	1670
Latent heat of boiling (kJ/kg)	860	-	855.2	~900	856.7
Saturation pressure (bar)	$5.1 \cdot 10^{-6}$	-		$2 \cdot 10^{-8}$	

Chapter 3

3 DEVELOPMENT OF EXPERIMENTAL TESTING FACILITIES

Give us the tools and we will finish the job.
Sir Winston Churchill
(1874 – 1965)

Be careful about reading health books. You may die of a misprint.
Mark Twain
(1835-1910)

Chapter 3 describes the experimental testing facilities that were specially built at SCK•CEN to allow mechanical testing in liquid metal environment under well controlled conditions.
First, we will describe the liquid metal embrittlement testing station 1 (LIMETS 1) which was built in the frame of the PhD of Danislav Sapundjiev and which was also used to perform all non-active tensile tests in LBE in this PhD.
Second, we will describe the instrumented hot cell (cell 12) which was constructed initially to perform tests in liquid LLE, but was modified to allow testing in liquid LBE on samples irradiated in contact with LBE in Twin Astir (Chapter 4). This hot cell contains LIMETS II, the modified version of LIMETS I to allow testing active specimens, as well as some specifically designed tools to allow dismantling of LBE filled irradiated capsules. In this section, we will also briefly discuss the polonium issue which signifantly complicated practical matters as well as significantly increased the necessary paperwork.

3.1 LIMETS I

The Limets 1 facility has been extensively described in the PhD thesis of Danislav Sapundjiev [108]. Here, we will give a summary of the most important characteristics of the installation and the testing procedure. The general characteristics of the Limets 1 facility are summarized in Table 3.1.

Table 3.1: Specifications of Limets 1.

Parameter	Range of values
Max. test temperature	550°C
Max. pressure	3 bar
Displacement rates	3.10^{-6} – 9.10^{-2} mm/s
Max. Displacement	30 mm
Number of loading units	1
Autoclave volume	3.6 l
Dumptank volume	3.8 l
Melting tank volume	3.8 l
Vessel material	316L
Duct material	316L
Valves and filters material	316L
Testing modes	Constant load
	Constant elongation (SSRT, tensile)
	Low cycle fatigue
Total electrical power	10 kW

Limets 1 can be seen as the combination of a liquid metal containing system and a gas conditioning system or oxygen control system. The liquid metal containing system consists of all parts, such as ducts and vessels, designed to contain or convey liquid metal. The gas conditioning system is designed to allow modification of the oxygen content in the liquid metal and to allow the build up of pressure where needed. A scheme of the Limets 1 testing facility is depicted in Figure 3.1.

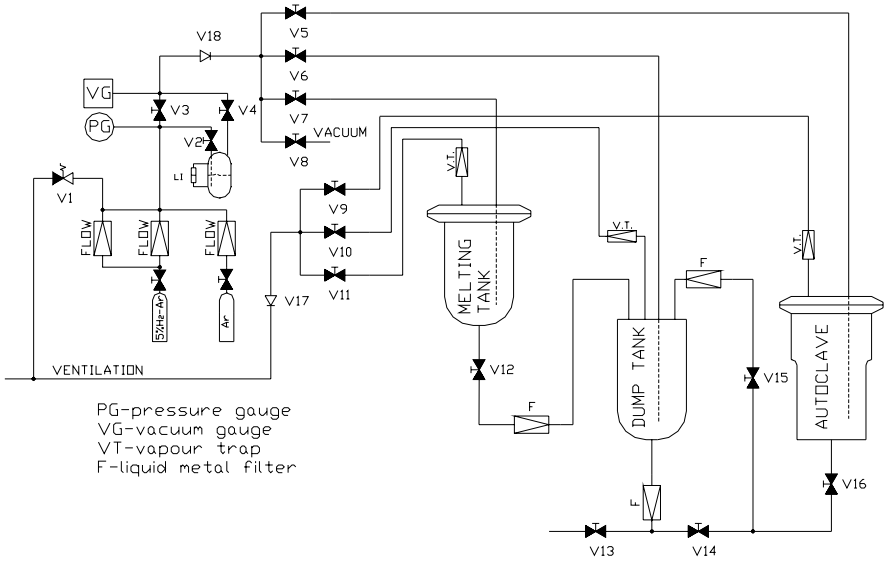

Figure 3.1: Principle scheme of LIMETS 1 installation.

3.1.1 Liquid metal containing system

Limets 1 is based on the three vessel concept to allow clean and slag free filling and conditioning of the liquid metal. The system consists of a melting tank, dumptank and testing autoclave. These vessels are connected by ducts, valves and filters, allowing liquid metal transfer from one tank to the other. In the following, the main features of each of the vessels and the liquid metal transfer system are discussed in detail.

3.1.1.1 Melting tank

The sole purpose of the melting tank is to allow clean and slag free filling of the dumptank.
Initially, the cleaned and degreased LBE ingots were molten in the open melting tank at about 150°C to minimise the oxidation rate of the liquid metal. Impurities and oxides floated to the surface due to the buoyancy and were manually removed with a ceramic ladle. Subsequently, the lid was closed and the tank evacuated using a rotary pump. After evacuating, the tank was purged with Ar + 5% H_2 to reduce the oxides left in the melt.
After bubbling with Ar + 5% H_2 for a few days, the liquid metal was transferred to the dumptank using gravitational force (melting tank placed above the dumptank). To ensure slag free metal in the dumptank, a small fraction of melt is left inside the melting tank.
After the transfer, the melting tank is slightly pressurised and cooled down to room temperature.

3.1.1.2 Dumptank

The liquid metal is stored in the dumptank for prolonged periods of time, during shut down and in between tests. The liquid metal is conditioned and adjusted to the desired oxygen content in the dumptank. This can be achieved by purging the liquid metal with a gas mixture containing hydrogen and water vapour at a ratio giving the desired oxygen potential.
The dumptank is equipped with an yttria stabilized zirconia solid electrolyte oxygen sensor using Ni/NiO powder as a reference system.

Under standard conditions, the dumptank is kept at 350°C under continuous gas bubbling. When a significant reduction in oxygen potential is needed, the temperature is raised to 450°C to facilitate reduction.

Before every test, the liquid metal is transferred from the dumptank to the testing autoclave by applying hydrostatic over pressure in the dumptank. After the test, the liquid metal is pushed back into the dumptank, again by application of hydrostatic over pressure.

3.1.1.3 Testing autoclave

The most versatile and complex of the three vessels is the testing autoclave. It needs to allow opening and closing and still guarantee sufficient leak tightness.
All gas pipes, pulling rods and level indicators are brought in through the lid of the autoclave which can be lifted from the vessel using a mechanical actuator. The lid is closed by using a C-ring flange. The force of the pulling rod is brought out of the autoclave by a metal below connection. The temperature in the autoclave is measured by a thermocouple which is inserted in a stainless steel finger into the autoclave vessel. When testing in gas, an additional thermocouple is inserted into the autoclave and attached to the sample. The autoclave is filled and drained through its bottom.

3.1.1.4 Liquid metal transfer

All ducts and filters, designed to have liquid metal flowing thru, are kept at a temperature of 200-250°C. Thermal gradients and frequent heating and cooling cycles should be avoided as much as possible. A thermal gradient between the liquid metal and the standard temperature of the ducts is however used to follow the flow and estimate the flow speed of the liquid metal. It is clear that the only way to verify whether the metal is flowing is to monitor pressure and temperature change.

3.1.2 Oxygen control system

The oxygen control system of Limets 1 is built to supply gas with specific hydrogen to water vapour ratio to reach the desired oxygen content of the LBE for each particular experiment. Furthermore, the gas supply is needed for cleaning, pressurisation and evacuation of the three vessels. The system consists of valves, flow meters, a water chamber, pressure and vacuum gauges and a rotary vacuum pump. The OCS of Limets 1 can serve one vessel at a time.

The oxygen content in the system is measured by an yttria stabilized tetragonal zirconia (YSZ) sensor working as a solid ionic conducting membrane. The sensor contains Ni/NiO powder mixture as reference system. The calibration of the oxygen sensor was performed in the dumptank of Limets 1 and shows very good agreement between theoretical prediction and experiment at 325°C and above [108].

To prevent ingress of atmospheric air, the system is always maintained at a gas overpressure of about 0.15 bar.

3.1.3 Testing procedure

The specimen (tensile or DCT) is attached in the pulling grips after ultrasonic cleaning in ethanol. The upper head of the tensile rig is always set in the same starting position, allowing the minimal resistance of the metallic bellow and maximal total displacement range. The lower, passive head of the tensile machine is then screwed until the force read out of the load cell reaches 100-200 N.

After closing and tightening the flange, the autoclave is evacuated down to about 5.10^{-2} mbar and subsequently purged with a gas mixture of argon and 5% hydrogen. This procedure of evacuation and purging is repeated 3 times.

The heaters of the autoclave are then started (dumptank and ducts are remained at respectively 350°C and 200°C). Data acquisition of the temperature is started simultaneously, keeping record of the thermal history of every specimen.
The liquid metal transfer takes place once the autoclave temperature reaches above 150°C. The level of the liquid metal is monitored by a low level and high level indicator and can be monitored by the temperature change of the two thermocouples in the autoclave.

Once the transfer is completed and the level of the liquid metal is sufficiently high to submerge the entire sample, the temperature is set to the desired testing temperature and the oxygen level is adjusted using the OCS. As soon as both the liquid metal temperature and oxygen signal have stabilized, the test can be started.

After the sample is broken, the autoclave is cooled down to below 350°C and the liquid metal is transferred back to the dumptank. The autoclave is left to cool down to room temperature and opened.

Observation of the remaining solidified LBE gives confirmation of the oxygen conditions of the past test. The solidified LBE must have a lustrous, metallic appearance.

The test data are analysed and one half of the specimen is cleaned in a solution of acetic acid, hydrogen peroxide and ethanol in a ratio of 1:1:1 to allow analysis of the fracture surface in the SEM.

3.1.3.1 Tensile testing in liquid metal environment

Tensile testing in the liquid metal environment inside the autoclave of the Limets 1 facility is based on to the ASTM standard E 8M. However, this standard does not include any liquid metal environment and therefore does not strictly apply to tensile testing in liquid metal environment.
No additional extensometer or visual observation of the deformation can be used due to the opaque and conducting nature of the LBE.

3.1.3.2 Fracture toughness testing in liquid metal environment

Due to the opaque and conducting nature of LBE, none of the conventional online crack advancement methods could be applied to the fracture toughness assessment in liquid metal environment. Therefore, new or unconventional methods had to be used to determine the plane strain fracture toughness of structural materials in liquid metal environment.

Initially, we spent quite a lot of effort developing methods to measure the crack tip opening displacement (CTOD) of a specimen submerged in LBE. We were however not successful in accurately online measuring the CTOD of the submerged specimen.
Annex A15 of ASTM E-1820 describes a "normalisation method" which was developed to allow fracture toughness testing in aggressive environments or elevated temperatures where the use of a clip gauge is not possible. This "normalisation method" means that only the initial and final crack length and the load-displacement record are needed to be able to calculate the *J*-integral. This inspired us to look for other, similar normalisation methods in the open literature. We found three methods which will be explained in the following sections. The fracture toughness results obtained by these methods will be discussed further in Chapter 5.

3.1.3.2.1 Normalisation data reduction (NDR)

The normalization data reduction (NDR) technique for characterizing the upper shelf fracture toughness of steels in the ductile regime, in terms of critical toughness (J_{Ic} or J_Q) and *J-R* curve is described in annex A15 of ASTM E1820.

3.1.3.2.1.1 Normalization of force and displacement data

The necessary information for this analysis is the force-CTOD data and the initial and final crack length. Each value P_i up to, but not including the maximum force $P_{\max}$, is normalized using:

$$P_{Ni} = \frac{P_i}{WB\left[\frac{W - a_{bi}}{W}\right]^{\eta_{pl}}} \quad \textbf{(3.1)}$$

Where a_{bi} is the blunting-corrected crack length, calculated by:

$$a_{bi} = a_0 + \frac{J_i}{2\sigma_Y} \quad \textbf{(3.2)}$$

and where σ_Y is the flow stress (average of yield and ultimate tensile strengths) at the test temperature. The *J*-integral J_i is calculated from:

$$J_i = \frac{K_i^{\,2}\left(1-\nu^2\right)}{E} + J_{pli} \quad \textbf{(3.3)}$$

In the equation above, the stress intensity factor K_i , plastic eta-factor η_{pl} and the plastic component of the J-integral J_{pli} are calculated according to annex A3 of ASTM E-1820, by using the initial crack length a_0 .

For a DCT specimen, K_i is calculated as follows:

$$K_i = \frac{P_i}{\left(BB_N W\right)^{\frac{1}{2}}} f\left(a_i / W\right) \quad \textbf{(3.4)}$$

where

$$f\left(\frac{a_i}{W}\right) = \frac{\left[\left(2+\frac{a_i}{W}\right)\left(0.76+4.8\left(\frac{a_i}{W}\right)-11.58\left(\frac{a_i}{W}\right)^2+11.43\left(\frac{a_i}{W}\right)^3-4.08\left(\frac{a_i}{W}\right)^4\right)\right]}{\left(1-\frac{a_i}{W}\right)^{\frac{3}{2}}} \quad \textbf{(3.5)}$$

η_{pl} is calculated from:

$$\eta_{pl} = 2 + 0.522\frac{b_0}{W} \quad \textbf{(3.6)}$$

Where $b_0 = W - a_0$ is the original remaining ligament.

J_{pli} can be calculated as follows:

$$J_{pli} = \frac{\eta_{pl} A_{pl}}{B_N b_0} \quad \textbf{(3.7)}$$

Where A_{pl} is the area A as shown in Figure 3.2.

In addition to the normalization of the force, the displacement has to be normalized for each value of v_i up to, but not including $P_{\max}$, using the equation:

$$v'_{pli} = \frac{v_{pli}}{W} = \frac{(v_i - P_i C_i)}{W} \quad \textbf{(3.8)}$$

Where C_i is the specimen elastic load line compliance based on a_{bi} (Equation 3.2)

C_i can be calculated using:

$$C_i = \frac{1}{EB_e}\left(\frac{1+\frac{a_i}{W}}{1-\frac{a_i}{W}}\right)^2\left[2.0562 + 9.6496\left(\frac{a_i}{W}\right) - 13.7364\left(\frac{a_i}{W}\right)^2 + 6.1748\left(\frac{a_i}{W}\right)^3\right] \quad \textbf{(3.9)}$$

The final force displacement pair also has to be normalized using the equations above, but instead of using the initial crack length, the final crack length a_f has to be used.

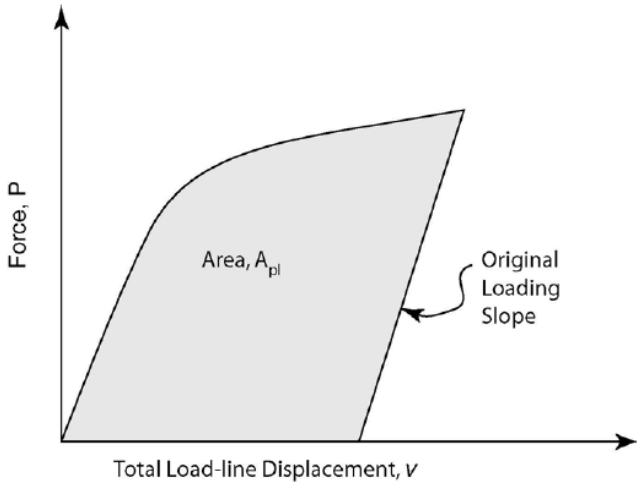

Figure 3.2: Definition of area for J calculation.

Typical normalized data are shown in Figure 3.3.

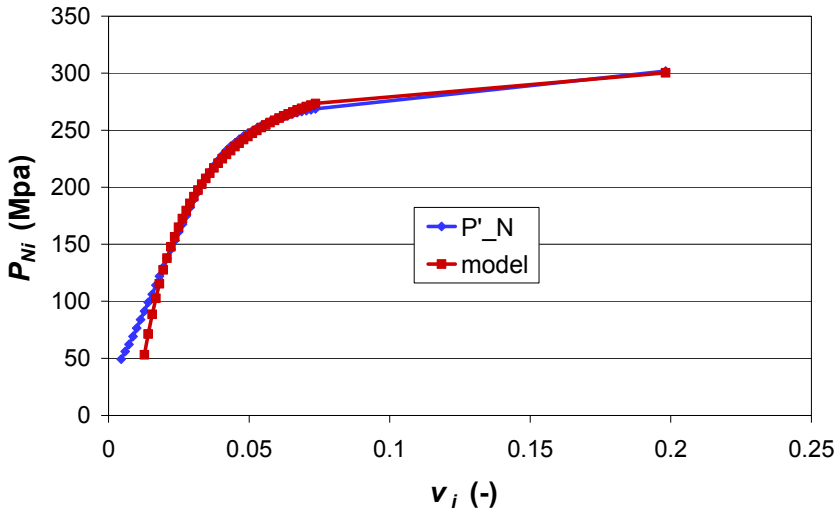

Figure 3.3: Typical normalized fitted data for NDR method

3.1.3.2.1.2 Fitting of model

After the normalization of force and displacement data, the data that meets the condition $v_{pli}/W \geq 0.001$ must be fitted with the analytical normalization function:

$$P_N = \frac{a + b \cdot v'_{pli} + c \cdot v'_{pli}}{d + v'_{pli}} \qquad \textbf{(3.10)}$$

Where *a*, *b*, *c* and *d* are the fitting coefficients. The maximum deviation between the model and the normalized data of the final fit must be less than 1%. The fitting was done by means of the SOLVER tool found in EXCEL, where the sum of the root mean square error (RMSE) between the model and the normalized data was minimized. In Figure 3.4, the fitted data is shown that corresponds to the normalized data.

Once the fitting function has been established, all the selected P_{Ni}, v'_{pli} and a_i are forced to lie on Equation 3.10 by adjusting individual crack lengths through an iterative procedure, starting from the first data point with $v_{pli}/W \geq 0.002$. The required minimum difference between the fitted and measured P_N values is ± 0.1%. Each step is accomplished by using the crack length resulting from the previous data point. The comparison between fitted and normalized data is shown in Figure 3.4.

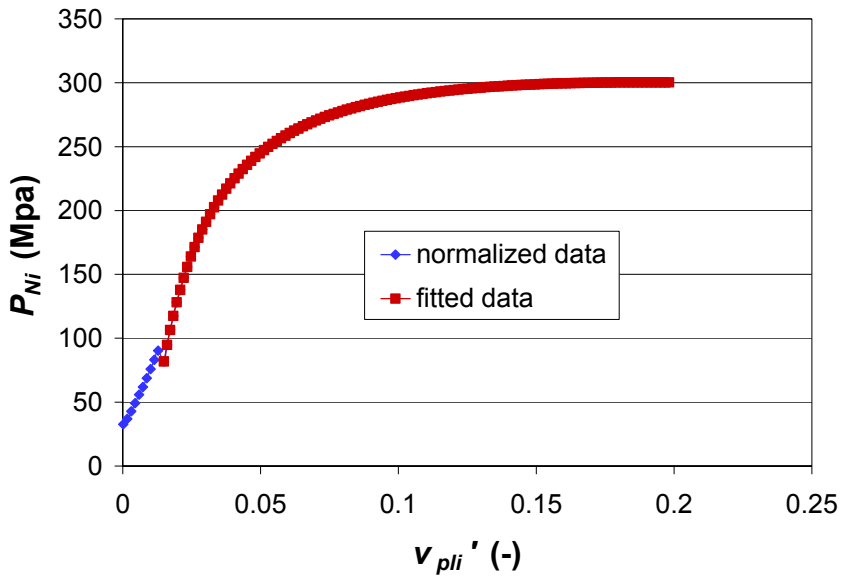

Figure 3.4: comparison between fitted and normalized data for NDR

Having determined the force, displacement and crack length for each data point, the *J*-integral for each data point and the *J*-*R* curve can be calculated using Equation 3.3 where:

$$J_{pli} = \left[J_{pl(i-1)} + \left(\frac{\eta_{(i-1)}}{b_{(i-1)}} \right) \frac{A_{pl(i)} - A_{pl(i-1)}}{B_N} \right] \left[1 - \gamma_{(i-1)} \frac{a_{(i)} - a_{(i-1)}}{b_{(i-1)}} \right] \quad \textbf{(3.11)}$$

and where

$$\gamma_{(i-1)} = 1.0 + 0.76 \frac{b_{(i-1)}}{W} \quad \textbf{(3.12)}$$

3.1.3.2.2 Chaouadi method

The fracture toughness analysis method described by R. Chaouadi [138] is a method for the calculation of the *J-R* curve, based on two observations.
The first observation originates from Charpy V-notch tests, where the ductile crack extension is correlated with the Shear Fracture Appearance (SFA) as shown in Figure 3.5a and where there is a one to one correlation between the SFA and the normalized energy, E/E_{USE}, normalized to the upper shelf energy (Figure 3.5b).

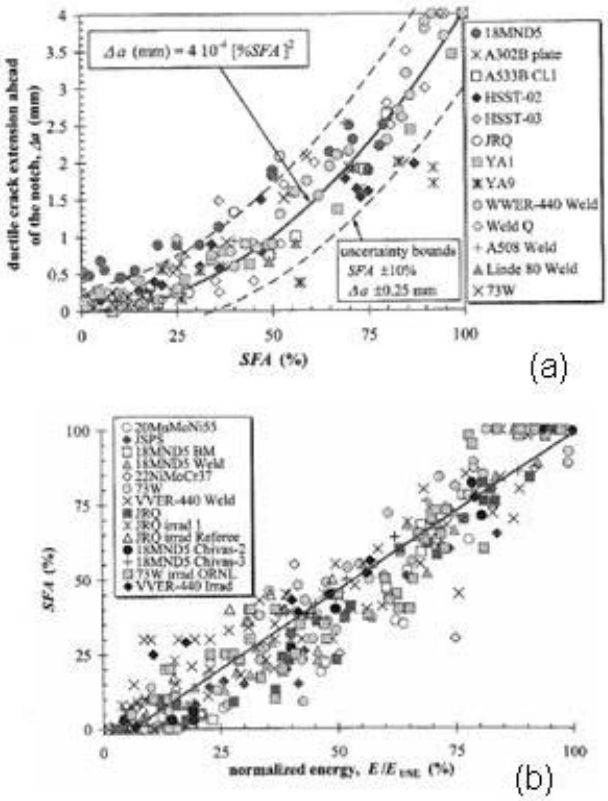

Figure 3.5: - (a) Correlation between ductile crack extension and SFA; (b) Correlation between SFA and normalized absorbed energy [138].

The second observation is that a single generic curve can fit the data of the *J-R* curve of any ductile tearing metal (Figure 3.6). The only difference between different materials is the energy at initiation, the initiation toughness J_i. J_i represents the physical initiation toughness, rather than the engineering parameter J_{Ic}.

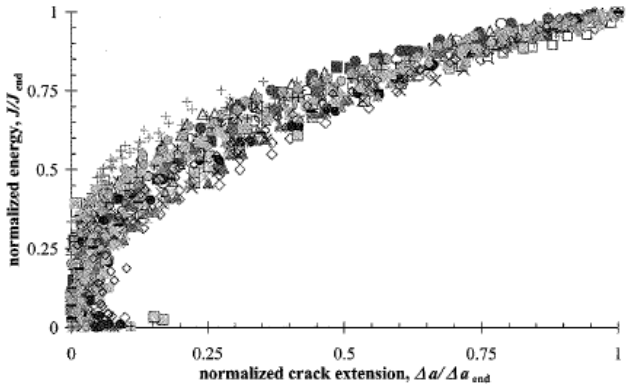

Figure 3.6: - Normalized crack energy of various materials [138].

Putting both observations together, the curve in Figure 3.6 can be represented by:

$$\frac{\Delta a}{\Delta a_{end}} \approx \left(\frac{E - E_i}{E_{end} - E_i} \right)^2 \qquad \textbf{(3.13)}$$

Where:
E is the absorbed energy, meaning the area under the load-displacement diagram and E_i is the crack initiation energy.
E_i is not known. It is assumed that the crack initiates at a load equal to the average of the yield and the maximum force.

$$F_i = \frac{F_y + F_m}{2} \qquad \textbf{(3.14)}$$

For the calculation of the J-integral value, the equation for J as recommended by Annex A3 of ASTM E1820 for DCT specimens was used. This method is similar to the calculation of J_i as explained in the section on the NDR method.
Afterwards, Δa is recalculated in a second iteration step, using the following equation:

$$\frac{\Delta a}{\Delta a_{end}} = \left(\frac{J - J_i}{J_{end} - J_i} \right)^2 \qquad \textbf{(3.15)}$$

The advantage of this method is the ease of use and the fact that there are no parameters to be fitted. Instead, all the parameters are unambiguously derived from experimental data.

3.1.3.2.3 Donoso method

The method by Donoso *et al.* [139] generates the *J-R* curve in closed analytical form, using the Common and Concise Formats.
In this method, a crack growth law for plastic displacement is proposed, that relates the crack growth, Δa and the normalized plastic displacement:

$$\frac{\Delta a}{W} = l_0 \left(\frac{v_{pl}}{W} \right)^{l_1} \quad \textbf{(3.16)}$$

An other key equation for the application of this normalization method is the Common Format Equation (CFE):

$$P = \Omega^* \cdot G(b/W) \cdot H(v_{pl}/W) \quad \textbf{(3.17)}$$

Where $G(b/W)$ is a function that depends on the geometry of the specimen, and $H(v_{pl}/W)$ is a hardening function and a material property. Both geometry and hardening functions are written as a power law expression of normalized ligament and plastic displacement:

$$G(b/W) = B \cdot C \cdot W \cdot \left(\frac{b}{W} \right)^m \quad \textbf{(3.18)}$$

$$H(v_{pl}/W) = \sigma^* \left(\frac{v_{pl}}{W} \right)^{\frac{1}{n}} \quad \textbf{(3.19)}$$

In order to use this equation, quite a lot of parameters have to be determined. The meaning of the different parameters and how they are to be determined is explained in the next few paragraphs.

3.1.3.2.3.1 n and σ*

The Ramberg-Osgood equation describes the relationship between stress and strain near the yield strength of the material. This equation can be written as [140]:

$$\frac{\varepsilon}{\varepsilon_0} = \frac{\sigma}{\sigma_0} + \alpha \left(\frac{\sigma}{\sigma_0} \right)^n \quad \textbf{(3.20)}$$

Where α is the Ramberg-Osgood coefficient and n is the hardening exponent. The parameters in the equation above were obtained by fitting tensile test data of T91 steel and 316L stainless steel at 200 and 300°C. Figure 3.7 shows the comparison

between the equation and tensile test data of T91 at 200°C, together with the obtained values for α and n.

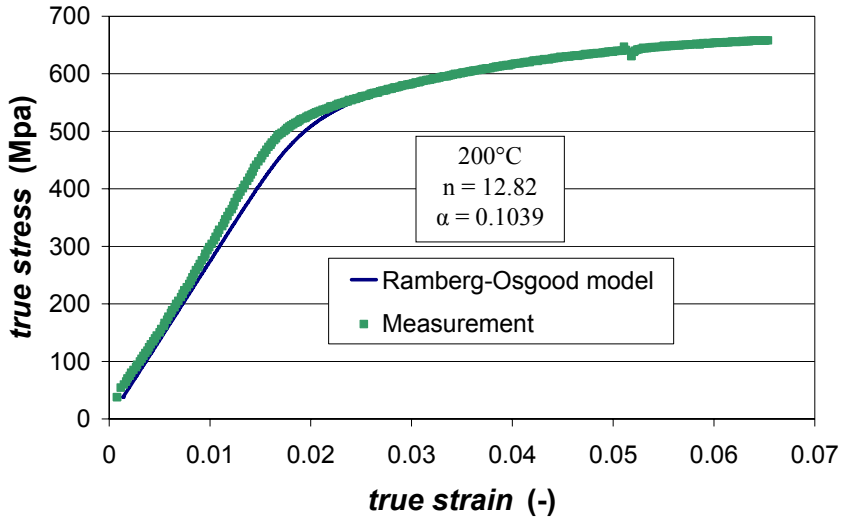

Figure 3.7: true stress-true strain curves of Ramberg-Osgood modal and measurements of tensile tests of T91 steel in air.

After the determination of α and n, σ^*, the coefficient of plasticity of the hardening function, can be determined:

$$\sigma^* = \frac{\sigma_0}{(\alpha \cdot \varepsilon_0)^{\frac{1}{n}}} \quad \textbf{(3.21)}$$

Where σ_0 is the yield strength and $\varepsilon_0 = \sigma_0 / E$ [139].

3.1.3.2.3.2 Ω*: the constraint factor

Ω^* is the mechanical constraint factor and depends on the type of specimen and the type of constraint. The values of this factor range between 0.2678 for plane stress to 0.3638 for plane strain. Ω^* may be evaluated, based on the following equations [139]:

$$P_{N0} = \frac{P_0}{G(b/W)} \quad \textbf{(3.22)}$$

$$\Omega^* = \frac{P_{N0}}{\sigma_0} \quad \textbf{(3.23)}$$

3.1.3.2.3.3 C and m: the G function parameters

m is the exponent of the geometry function and equals 2.2360 for compact tension specimens [141]. C is the coefficient of the geometry function and equals 1.553 [141]. C is considered as a constant, although C may be dependent on m and on the ligament size b/W for compact specimens. The way the parameters C and m were determined, can be found in [140].

3.1.3.2.3.4 Application of the Donoso and Landes method

Using the proposed crack growth law (Equation 3.16) and the last data point (v_f, P_f) of the test, a list of l_0 can be calculated for l_1 ranging from 1.5 to 2.5. For the application of the crack growth law, the plastic term of the displacement is needed. v_{pl} is calculated as follows:

$$v = C_{el} P + v_{pl} \quad \textbf{(3.24)}$$

$$C_{el} = \left(\frac{A(1-\nu^2)}{BE} \right) \left(\frac{b}{W} \right)^{-\mu} \quad \textbf{(3.25)}$$

Where $A = 7.6055$ and $\mu = 2.283$ [142].

Starting from a tentative list of v_{pl}, the plastic displacement, the values of the force P are calculated using the Common Format Equation (Equation 3.17) for each of the values of v_{pl} in the list.

Next, the value of l_1, which gives the best match between the experimental curve and the model *P*-*v* curve, calculated by Equation 3.17, is selected. Figure 3.8 shows an example of this fit, with the selected values of l_0 and l_1 for the selected test.

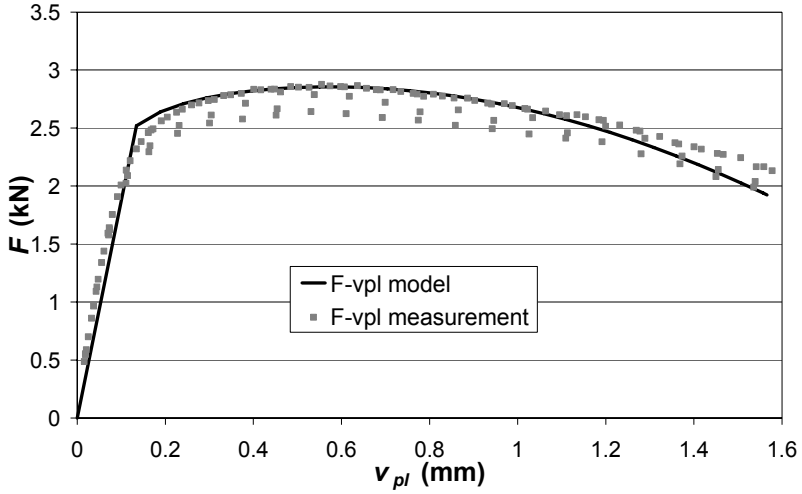

Figure 3.8: Comparison of *P-v* curve measured during the test and calculated using the CFE.

Once the values for l_0 and l_1 for the test are known, Δa is calculated for each of the values in the v_{pl} list using the crack growth law with the selected values of l_0 and l_1.

Finally the elastic and plastic components of the *J*-integral are calculated using equations for J_{el} en J_{pl} [139]:

$$J_{el} = \frac{1}{2}\mu\frac{E}{\left(1-\nu^2\right)}C^*W\left(\frac{b}{W}\right)^{(\mu-1)}\left(\frac{v_{el}}{W}\right)^2 \qquad \textbf{(3.26)}$$

$$J_{pl} = m\Omega^*\sigma^*CW\left(\frac{n}{n+1}\right)\left(\frac{b_0}{W}\right)^{(m-1)}\left(1-\frac{\Delta a}{b_0}\right)^{(m-1)}\left(\frac{1}{l_0}\frac{\Delta a}{W}\right)^{\frac{1}{l_1}\left(1+\frac{1}{n}\right)} \qquad \textbf{(3.27)}$$

3.1.3.2.3.5 General remarks to the applied methods

One of the conditions for the application of the NDR method, is the limitation of the crack length to 4 mm or 15% of the initial uncracked ligament, whichever is less. When using subsize DCT specimens as used in this work, 15% of the uncracked ligament is about 0.7 mm. During the tests, it is very difficult to estimate the actual crack length to such high accuracy. Therefore, the crack length condition was not met. To validate applicability of the NDR method, test data in air will need to be analyzed by the UC, PD and NDR methods to verify the correspondence between the normalisation methods and the online measurement techniques for every condition.

As a single value to characterize the fracture toughness, the J_Q value was calculated for each of the normalization methods according to ASTM E1820. The calculated J_Q value is not valid as J_{Ic} value, which characterizes the toughness of a material near the onset of crack extension from a pre-existing fatigue crack, because the requirements

$$B > 25\frac{J_Q}{\sigma_y} \quad \textbf{(3.28)}$$

$$b_0 > 25\frac{J_Q}{\sigma_y} \quad \textbf{(3.29)}$$

are not met. Although the specimen does not meet al the requirements necessary to be able to calculate J_{Ic}, the J_Q value can give a good indication of the fracture toughness under the applied testing conditions.

However, since the specimens were precracked in air at room temperature, there is no LBE present in the precrack prior to testing. Although the LBE was always introduced while the specimen was under stress, there was no certainty that the LBE would fully penetrate the precrack to the crack tip. To avoid the presence of air bubbles in the crack after the specimen was submerged in LBE, we mechanically tapped the LBE reservoir when testing in oxygen saturated conditions. When testing under controlled oxygen conditions in Limets 1, the gas bubbling provided the necessary vibrations in the liquid metal.

Furthermore, the normalisation methods discussed above are only applicable to ductile tearing conditions. This is in sharp contrast with our envisaged goal of quantifying the embrittlement of the structural steel by the liquid metal environment. However, as long as the macroscopic behaviour of the tested structural material remains sufficiently tough, these methods can be applied. For this reason, one needs to verify the possible applicability of the normalisation methods to every system and for all the tested conditions. Furthermore, analysis of the fracture surfaces is needed to assess the possible brittle nature of the fracture surface.

In Chapter 5, we will discuss the applicability of the normalisation methods to the fracture toughness tests of T91, 316L and the high silicon steels and where possible compare the obtained fracture toughness values in LBE with those in air.
The fracture toughness assessment presented in Chapter 5 should also not be regarded as a conclusive study. Far more data will be needed due to the relatively large scatter of the results. However, this was not possible within the timeframe of this PhD.

3.2 HOT CELL 12

The test set up built inside hot cell 12 at LHMA was initially built for material testing within the Fusion programme. Specimens irradiated in PWR water conditions were tested in LLE environment. To perform these tests, the cell only needed to be licensed as β, γ cell. Cell 12 was licensed as β, γ cell on 27th of November 2006 [109].

In a second phase, the cell was converted to use liquid LBE environment for the MYRRHA and GEN IV programmes in stead of LLE. This complicated matters since the hot cell needed to be able to receive polonium contaminated and thus α-contaminated samples from TWIN ASTIR (see Chapter 4).
Furthermore, the gas conditioning system is very important when using LBE whereas gas conditioning is not relevant when using LLE due to the reducing and chemically active nature of lithium. In the following sections, the hot cell will be described with emphasis on some of the modifications that needed to be made to allow testing Po contaminated material in liquid LBE environment.

Cell 12 was temporarily licensed as an α-cell, allowed to handle polonium contaminated material to test capsule A of the TWIN ASTIR experiment on the 21st of April 2008 [110].
The exploitation permit however forbids transport of any Po contaminated material out of cell 12 and furthermore forbids the use of organic solvents to remove the LBE from the samples. It is therefore impossible to examine the fracture surfaces of irradiated samples, tested in Limets 2, under the terms of the current exploitation permit.

3.2.1 General

The concept and modifications of the cell itself were made in the frame of a new safety approach for polonium contaminated hot cells, which was based on 5 points:

- Leak tightness of the α-box;
- Proper ventilation and filtering;
- Temperature control of the hot cell and Limets 2;
- Decrease of the amount of Po by using its natural decay;
- Shielded storage of Po contaminated PbBi and samples inside the hot cell.

These 5 points of the applied safety approach are further explained in the following sections.

3.2.1.1 Leak tightness

Special precautions have been taken during the construction of the α-box to ensure a leaking rate below 0.6 Vol% per hour, according to class 3 [111], which allows testing of α-contaminated samples.

3.2.1.2 Ventilation and Filters

The main concern for potential safety hazard was the formation of volatile polonium compounds forming α-radioactive aerosols and gaseous compounds. Literature or industrial information on polonium filters to capture these compounds is extremely scarce. Available literature [112]-[114] confirms that significant amounts of polonium aerosols were formed and were both captured in filters and adsorbed to surfaces.
Since aerosol particles in the μm range and beyond can be captured with HEPA filters, the total ventilation chain of cell 12 was equipped with 3 stages of HEPA filters and was tested in the most penetrating particle size range to assure tightness of the filter containment system.

Polonium is known however to possibly form polonium hydride when in contact with water. This PoH_2 has been reported to be 1000x more volatile then Po and PoPb [126]. The formation of PoH_2 in cell 12 was kept small by avoiding the use of water inside the cell. Water was only needed as coolant for the saw since ethanol was not allowed.
For the MEGAPIE experiment, the most important aspect of enclosure was this of polonium [115]. To keep the polonium contained, they did not only use aerosol filters but added active carbon filters as well. Furthermore, it is recognised in the document that the estimated values of polonium release can only be used as an indication because of the uncertainty in the physico-chemical data.

A HEPA filter can only capture particles, so assuming that part of the polonium would have formed volatile gaseous compounds, an activated carbon filter has to be used to decrease the amount of Po that could be released.
The total filter chain of cell 12 thus comprises of 3 HEPA filters and 1 active carbon filter:

1. A Camfil HEPA filter inside the α-box;
2. A Camfil activated carbon filter inside the α-box;
3. A Vokes HEPA filter on top of the cell

4. A large HEPA filter in the filter house of LHMA at the end of the filter chain.

3.2.1.3 Temperature control

The temperature inside the hot cell is considered to be a safety issue and therefore the following actions were foreseen:

1. High temperature alarm on the autoclave temperature;
2. High temperature alarm in the hot cell, visual and audio warnings at 45°C;
3. High temperature alarm inside the hot cell at 55°C followed by automatic shut down of all heating devices inside.

Since the cell is a closed metal box, the heaters of the testing autoclave and dumptank were insulated as good as possible. Furthermore, it was proven necessary to install an air conditioning system on the air inlet to lower the temperature inside the cell.

3.2.1.4 Natural decay of Po

The half life time of polonium is 138 days. So by simply waiting, the polonium activity will be reduced significantly. Initially a cooling down period of 3 months was foreseen before transporting the capsule A of TWIN ASTIR from BR2 to cell 12. However, due to extended discussions regarding the licensing of cell 12 as this was the first of its kind at SCK•CEN, this cooling down period ended up to be 11 months.

3.2.1.5 Storage of Po contaminated waste

All Po contaminated waste is stored inside the hot cell for a sufficient amount of time to allow the natural decay of the polonium. The storage consists of small containers that are placed in cylindrical shaped spaces, submerged in the cell floor. These spaces are surrounded by lead blocks and are covered by lead plugs to shield the radiation.

3.2.2 LIMETS II

The LIMETS 2 facility is the modified version of the LIMETS 1 facility. It is also based on the three vessel concept but since the melting tank is only used to fill the system in the beginning of operation, the melting tank was designed so that it could

be place on top of cell 12 during filling and be detached and removed afterwards. This decreased the total amount of waste for the cell significantly.

The oxygen control system of LIMETS 2 is more flexible than this of LIMETS 1 since each vessel can be bubbled, purged or evacuated separately. The OCS can serve both the dumptank and testing autoclave at the same time. This increased flexibility also significantly decreased the risks of clogging gas pipes which was relatively often encountered when using LIMETS 1.

Further modifications were made to improve the ergonomics for the hot cell operators. This implies the use of magnetic valves, fixed clamping system etc.

A schematic of the LIMETS 2 system is depicted in Figure 3.9.

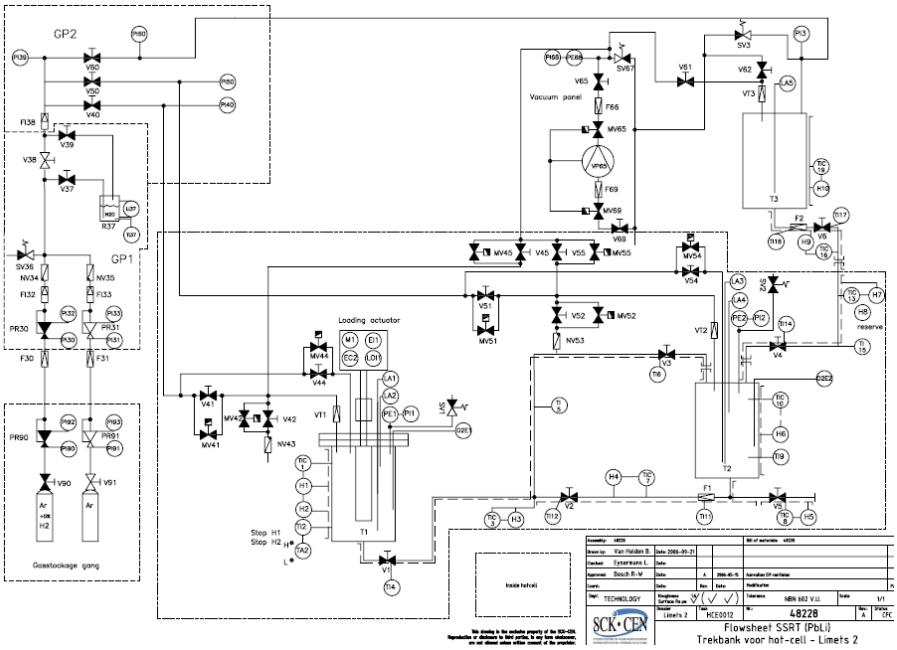

Figure 3.9: Flow sheet LIMETS 2

3.2.3 Saw

A solution for opening the irradiated, lead-bismuth filled capsule had to be found, keeping in mind a minimum of waste creation and a minimal spread of waste inside the cell. Several options were considered but finally a low speed circular saw was made in house. The saw comprised of a three phase separated electrical engine allowing flexible control of the cutting speed, a counterweight and a clamping system for firmly attaching the capsule during sawing. Furthermore, the saw needed

to be mobile inside the cell due to the restricted space. This problem was solved by adding metal ball wheels to the base of the saw. A picture of the saw, while cutting capsule A of TWIN ASTIR (Chapter 4) is shown in Figure 3.10

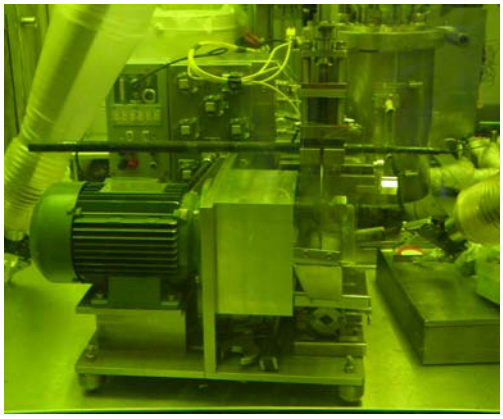

Figure 3.10: picture of the saw in cell 12.

3.2.4 Dismantling installation

A dismantling installation was designed in the frame of a graduation thesis by H. Dekien [116]. However, upon practical realisation of the proposed design, it was clear that it was too heavy and impractical to handle with manipulators. The entire dismantling concept was abandoned. A much more simplified concept was built and tested. The dismantling installation is fully described in the user manual of cell 12 [111] and is depicted in Figure 3.11.

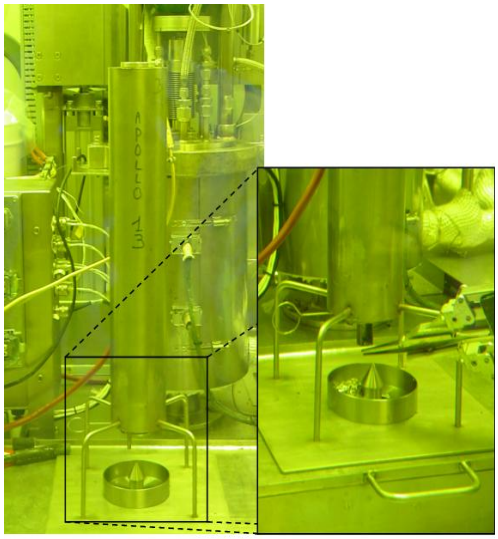

Figure 3.11: dismantling installation in cell 12.

3.2.5 Polonium issue

During irradiation of TWIN ASTIR (Chapter 4) in BR2, polonium was formed due to neutron irradiation of lead-bismuth according to the following nuclear reactions [117]:

$$^{209}Bi + n \rightarrow {}^{210}Bi \underset{t_{1/2}=5d}{\overset{\beta-}{\rightarrow}} {}^{210}Po \underset{t_{1/2}=138d}{\overset{\alpha}{\rightarrow}} {}^{206}Pb \qquad \textbf{(3.30)}$$

$$^{208}Pb + n \rightarrow {}^{209}Pb \underset{t_{1/2}=3.25h}{\overset{\beta-}{\rightarrow}} {}^{209}Bi + n \rightarrow {}^{210}Bi \underset{t_{1/2}=5d}{\overset{\beta-}{\rightarrow}} {}^{210}Po \underset{t_{1/2}=138d}{\overset{\alpha}{\rightarrow}} {}^{206}Pb \qquad \textbf{(3.31)}$$

Polonium has atomic number 84. It is a rare and highly radioactive metalloid, chemically similar to tellurium and bismuth. Polonium does exist in a natural environment as it is the last step in the natural decay of U-238. Since ^{210}Po is a pure α-emitter, the health risks are related to inhalation or swallowing. Several relevant properties of polonium are summarized in Table 3.2.

Table 3.2: Specifications ^{210}Po [118].

Radioactivity	$166.2.10^{12}$ Bq/gr *
Half life time	138.376 days
Atomic number	84
Atomic mass	210 gr/mol
Max. allowed concentration in air	0.2 Bq/m^3 **
Max. allowed concentration in water	0.83 Bq/l
Density	9.398 gr/cm^{-3}
Melting point	254°C
Boiling point	962°C
Appearance	Silvery metallic
Lethal radiation dose thru inhalation	100 MBq (<1µgr)

* Typical value for ^{241}Pu is $3.81.10^{12}$ Bq/gr and for ^{222}Rn is 5689.10^{12} Bq/gr.
** The average value for Radon (^{222}Rn) in Flanders is 35 Bq/m^3 and 70 Bq/m^3 in Wallonie. The EC guidelines for houses are to keep it lower then 200-400 Bq/m^3. The activity yield from ^{222}Rn mainly comes from ^{218}Po and ^{214}Po as Radon is a noble gas which will not stay in the body [118].

Based on MCNP neutronics calculations, the amount of polonium created in capsule A of TWIN ASTIR would have been 2.9 mg [119].

Polonium could have been set free in cell 12 in three different ways [118]:

1. During cutting of the capsules, the gas plenum above the lead bismuth is opened;
2. During melting of the lead bismuth to remove the samples from the capsule;
3. During testing in the Limets 2 test facility.

Po release due to cutting

The gas plenum above the lead bismuth level contained a certain amount of Po, based on the saturation vapour pressure of Po. This amount of Po can be estimated when the saturation vapour pressure of all volatile components are known. R.W. Bosch [118] followed the same approach as V. Sobolev [117] and considered Po and PbPo as volatile components. Since no saturation vapour pressure data were available at room temperature, the used formulas were extrapolated from high temperature (368-850°C) data. The calculated activity release at 20°C is found to be 8.9E-7 Bq and at 30°C, 3.53E-6 Bq.
These values did not pose any problem for the hot cells.

Po release due to melting

When PbBi is in the liquid phase, Po can evaporate directly. Furthermore, when in contact with hydrogen and/or water, the volatile polonium hydride compound can be formed.
J. Neuhausen investigated the polonium release due to evaporation under conditions where liquid LBE is purged with Ar + 7% H_2 or purged with water saturated Ar [120]. He found that the polonium release is very small at temperatures below 625°C when the LBE is heated up for periods of 1 hour and increases very rapidly with temperature. Long term polonium evaporation experiments of up to 25 days, yield the first measurable release at a temperature of 594°C.

At temperatures around 200°C, which was the foreseen dismantling temperature, the Po release is very small [118]. Even at 350°C, which was the actual dismantling temperature, the Po release is calculated to be very small.

Po release due to testing in Limets 2

To preserve the surface conditions as much as possible, the tensile samples that were irradiated in contact with LBE, were not cleaned before testing. This means a small layer of polonium contaminated LBE stuck to the sample and this LBE was dissolved into the LBE of the Limets 2 facility.

During tests, the liquid LBE was purged with a gas mixture of argon and 5% hydrogen. These testing conditions favour the evaporation of polonium and since the gas exhaust of the autoclave and dumptank are inside the hot cell, testing very probably created an additional polonium release. Calculations by R.W. Bosch on the worst case scenario, where all samples would be tested in Limets 2 at once, immediately after irradiation, showed very low releases of Po.

Measuring Po activity in cell 12

Due to the extremely low limits of Po in gas exhaust or waste, the safety authorities demanded monitoring of the Po activity inside cell 12. Therefore an α-probe with a PIPS detector was installed inside the cell. A measuring scheme was proposed using filters inside the cell to monitor the air inside the cell and with a defined reference surface on the inside wall to monitor Po contamination of the surfaces.

However, the very high γ activity of the irradiated capsule itself, which was not allowed to be removed from the cell due to polonium contamination up to now, caused the detectors α measurement to go out of range due to the small cross over between α and γ measurements. Since the expected and calculated quantities of polonium release were very small and the capsule was left to cool down for 11 months after irradiation (2.4 half life times of Po) before being dismantled, we have not been able to measure any polonium activity inside the cell. Draconian safety measures are however still demanded from the safety authorities since we can not prove there is no polonium present.

To solve this problem, in accordance with BEL V and SCK•CEN's IDPBW, all waste was temporarily removed from the cell into an alpha qualified container dedicated to cell 12 and alpha measurements were repeated. Unfortunately, the gamma background of dust and especially of the contaminated manipulator grips prevented any reliable measurement.

In a final attempt, a schedule is being negotiated with SCK•CEN's IDPBW (after approval by BEL V) to take dry and/or wet samples from the cell wall by rubbing and to measure these outside the hot cell in a fume hood.

4 IRRADIATION EXPERIMENT: TWIN ASTIR

The only way to discover the limits of the possible is to try the impossible.
Arthur C. Clark
(1917 - …)

When faced without a challenge, make one.
Dr. Peter Safar
(1942 – 2003)

Chapter 4 discribes the irradiation experiment TWIN ASTIR. This experiment, where capsules filled with samples in contact with LBE were placed in a critical reactor (BR2 at SCK•CEN), was the first of its kind in the West.

The experiment consists of six capsules containing mainly mini tensile samples and one capsule containing mini DCT's (Disc shaped Compact Tension specimens). Three of the tensile containing capsules and half of the DCT containing capsule were filled each with approximately 20 ml of low oxygen (10^{-6} wt%) LBE.

To complete the filling of these capsules with LBE under controlled conditions a dedicated filling installation was constructed at SCK•CEN.

The other three tensile containing capsules are subjected to PWR water conditions, in order to discriminate the effect of PbBi under irradiation from the effect of the irradiation itself.

To extract the effect of the PbBi corrosion itself on the material properties, one of the capsules was exposed to the thermal cycles of the BR2 reactor without being subjected to irradiation.

This resulted in a matrix of three irradiation doses in LBE (0, 1,5 and 2,5 dpa) and two environments (PbBi and PWR water conditions).

The irradiation experiment called TWIN ASTIR, which stands for ADS Steel T91 Irradiation up to two doses (hence Twin) is the first of its kind and started receiving neutron irradiation during the second cycle, 2006 of BR2 in April 2006. The knowledge and expertise that was built up in the MEGAPIE initiative, which received its first proton beam on target only a few months later, was of great importance and facilitated the licensing and realisation of Twin Astir.

The Twin Astir experiment had the purpose to distinguish and quantify the most important influencing parameters on the liquid metal corrosion and/or embrittlement in LBE and to examine possible synergistic effects of these parameters.
In this chapter the concept and realisation of the TWIN ASTIR irradiation project will be explained as well as the licensing issues that influenced the design.
Although initially foreseen to be irradiated and tested fully within the frame of this PhD, the suffered delays in the preparation of the experiment made it impossible to include the highest irradiation dose in this work. Despite the absence of testing results on the highest dose in this PhD, we decided to describe the complete experiment in this chapter.

4.1 CONCEPT AND PURPOSE

The concept of the TWIN ASTIR experiment is a parameterisation study of the most important degradation phenomena of the structural material for the future accelerator driven system at 350°C. The future ADS is expected to have a window of operational temperature (core inlet – outlet) between 300 and 550°C. The lower boundary of the heavy liquid metal coolant core inlet temperature under operation is a very important input for the design. However, this lower core inlet temperature has led to discussion among material scientists due to the known irradiation hardening problems at 300°C [108]. For this reason the irradiation temperature of the TWIN ASTIR programme was chosen to be on the lower temperature boundary for operation.

The parameters that are thought to be dominating in the material degradation process are irradiation hardening (accumulated dose), liquid metal corrosion, liquid metal wetting and liquid metal embrittlement. These will be assessed by performing corrosion examinations and tensile tests, crack growth tests both in inert environment as in liquid lead bismuth eutectic environment.

Thus it is expected to gain a better idea of the key influencing factors and possible synergies between these factors on the material degradation in a liquid lead bismuth environment under irradiation. This may allow us to focus on replacing or inhibiting the weakest link in the chain of materials degradation and therefore possibly increasing the operation lifetime of the accelerator driven system (ADS) facility.

4.2 SAFETY

The irradiations were initially to be performed at 300°C up to a fluence of 1.2 and 2.5 dpa. A large part of the desired irradiation conditions were compatible with what the PWR loop in BR2 (CALLISTO) could provide. Therefore it was decided to perform the irradiations of TWIN ASTIR inside this loop.

The samples were inserted in open tubes if they were to be irradiated under PWR conditions and in closed tubes if they were to be irradiated in lead bismuth eutectic. As we will explain in detail further on however, the necessity to use double walled capsules out of safety considerations for the irradiation in contact with LBE increased the irradiation temperature by 50°C. This temperature increase is caused by the gamma heating of the samples and the capsule itself and the subsequent temperature gradient over the gap between the inner and outer tube of the capsule. Because the PWR water temperature in CALLISTO could not be lowered due to other experiments running at the same time, the overall irradiation temperature for both open (PWR conditions) and closed (LBE filled) tubes of the Twin Astir experiment was set to be 350°C.

The IPS2 of CALLISTO gives an accumulated dose of 0.25 dpa per cycle, or 1.25 dpa/year which resulted in an irradiation period of one year for the low dose and two years for the higher irradiation dose. Furthermore, it was desired that the dose difference between the samples in the experiment would not exceed 15%. For this reason the length of the stack of samples needed to be restricted to a maximum length of 300 mm. The limited neutron dose difference across the length of the capsule and relatively small length of the capsules also result in a negligible temperature difference across the stack off samples.

The issue remained however that LBE and especially its activation product polonium were/are not well known materials. This is particularly true for the Po^{210}, which is difficult – and dangerous – to handle and is not available in quantities suitable for the accurate determination of its properties [122]. Therefore, the conditional tense is widely used in what follows.
Likewise, PbBi is not a usual reactor coolant. Before it gained a renewed interest for ADS-related studies, the only practical experience came from the Russian nuclear submarines programmes and therefore references are scarce in the open literature. Basically, in terms of the licensing of the experiment there were three major concerns being the corrosion of steels, the volume change of the LBE after solidification and the activation of Bi^{209} into Po^{210}.

Concerning the corrosion it is well known that the LBE preferentially dissolves the nickel in stainless steels. However the dissolution kinetics are slow below 600°C and the native oxide layer of the steels should be able to protect them during irradiation.

The volume change of LBE however was considered to possibly pose a problem in terms of the structural stability of the irradiation capsule as the capsule loaded with LBE needed to undergo freezing-defreezing cycles with the BR2 operating cycles. This volume change of the LBE upon cooling has been studied quite extensively [123]-[125] and depends on the solidification and cooling profile. The faster the cooling, the more pronounced the expansion. To experimentally verify the risk posed by this volume change of the LBE several freezing-defreezing cycles were performed on a mock-up capsule. Additionally another installation similar in volume and shape to the capsules to be used in the irradiation was left idle for two months to allow the possible problem to develop. No permanent deformation or crack of the PbBi container was ever noticed.

The integrity of the irradiation capsules was considered crucial by the licensing authorities due to the presence of Po^{210} after irradiation. This pure alpha-emitter could pose a very serious health hazard in case the capsule would be breached. Polonium is supposed to be volatile. However, research conducted in the frame of the ADS programmes found that, in PbBi, Polonium forms Lead Polonide that remains in solution in the bulk and is not released until a temperature of about 600°C is reached [126]. Above 600°C, all the stored Po would be released abruptly, but this is not a situation which could have occurred in CALLISTO.

However regarding the possibility of volume expansion causing cracking of the capsule and resulting in a possible Po contamination, the capsule needed to have a double wall. In the worse case scenario, that is the failure of both tubes of a capsule the Po would come into contact with the PWR water of the CALLISTO loop.
In presence of water, the Po is expected to form the volatile and unstable PoH_2 [126]. At the process temperature, PbBi is liquid and Po should be mobile within the liquid metal. There is the possibility that PoH_2 would have formed at the interface between a droplet of PbBi/PoPb and CALLISTO water. The PoH_2 would then have been taken away in the water stream, where it could decompose further away. After decomposition, Po could be adsorbed on walls, or integrated in crud, or could reform another PoH_2. Ultimately, Po could have been transported everywhere, including to the Surge Tank where the hydrogen gas bubbling would have likely extracted the volatile PoH_2 from the water and mixed it with the air stream of the non-recyclable

ventilation. So there was a possibility that the contamination would be spread across the whole building ventilation and outside, in the environment. As Po is a pure alpha emitter, there is little way to detect it specifically at an early stage and prevent the spreading, e.g. by isolation of the Surge Tank.

The thermochemical properties of Po are however not sufficiently known to assess its chemical behaviour with a reasonable degree of certainty [127]-[130]. Furthermore, there is no such thing as stable Po which could be used to perform measurements or tests. Therefore, it was not possible to predict the behaviour of the Po contamination of liquid PbBi in presence of water and it was not possible to exclude the scenario described in the above paragraph [131].
Hence, it was difficult to predict which proportion of Po could be released in the water. This is why we opted for the double-wall solution.

The double wall – with monitoring of the pressure of the intermediate space - allowed a permanent control of the integrity of the capsule. A leak – be it on the inner or the outer capsule – could have been detected and adequate action could be taken in time, that is before the second barrier might have failed.
If any permanent deformations of the capsule walls would be induced by the cooling of the LBE, the expansion could have possibly modified the temperature control of the capsule by reducing the gap thickness but the influence would have been limited to the decrease of the irradiation temperature by a few degrees.
By using double wall capsules, the release of Polonium in CALLISTO water – and further - was ruled out as design basis accident.

4.3 DESIGN

The experiment consists of six capsules containing mainly mini tensile samples and one capsule containing mini DCT's. Three of the tensile containing capsules and half of the DCT containing capsule are double walled and filled each with approximately 20 ml of low oxygen (10^{-6} wt%) LBE. The final concentration of oxygen in the capsule however, can differ from 10^{-6} wt%, as it depends on when a thermodynamic stability of the system was reached. There will have been a thermodynamic balance or equilibrium between the dissolution of oxygen in the LBE and the reduction or oxidation of the oxide film on the stainless steel surfaces. Moreover, the solubility of oxygen and other chemical elements in the LBE is not constant during the irradiation experiment due to the fluctuations in temperature of the LBE caused by the cycles of the BR2 reactor. The final oxygen concentration is therefore difficult to predict.

To complete the filling of these capsules with LBE under controlled conditions a dedicated filling installation was constructed. The other three tensile containing capsules were foreseen with holes to allow the PWR water to enter and flow thru. Thus these capsules were subjected to PWR water conditions, in order to discriminate the effect of PbBi under irradiation from the effect of the irradiation itself. To extract the effect of the PbBi corrosion itself on the material properties, one of the capsules was subjected to the thermal cycles of the BR2 reactor without being subjected to irradiation.

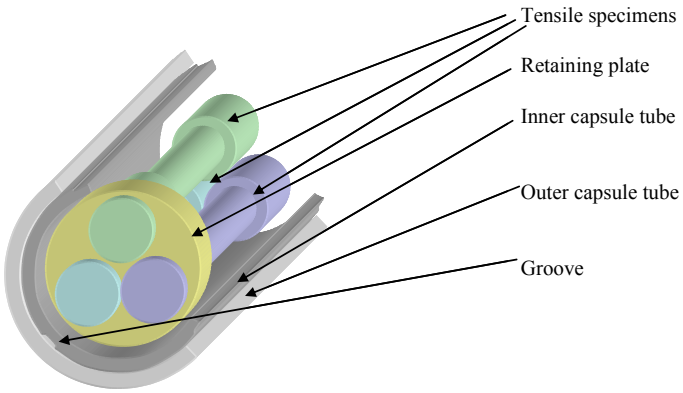

Figure 4.1: Schematic representation of tensile samples and retaining plate inside double walled capsule.

The tensile filled capsules were designed to contain mostly tensile specimens which were screwed in a retaining plate in an arrangement of three specimens per stage. One stage is schematically represented in Figure 4.1, showing the three tensile specimens screwed in their retaining plate inside the double walled capsule.

The drawing of the capsules is illustrated in Figure 4.2 showing both types of tensile capsules (middle and lower capsule) as well as the CT filled capsule (upper capsule). The tube containing the corrosion plates is being magnified in Figure 4.2.

Due to the vertical position of the capsule in the reactor, the corrosion plates would have been pressed together by the buoyancy forces preventing adequate liquid metal contact. To ensure contact with the LBE, spacers (rings provided with an opening) were placed in between the plates.

The CT filled capsule consists of two parts. Half of the capsule containing CT's is in contact with PWR water, the other half, also containing the same amount of CT's is closed, filled with LBE and foreseen of a double wall. Because the PbBi filled

capsules are submitted to a strong external pressure of the PWR water, they were pressurized at room temperature by 50 bar of helium. The pressure control of the LBE filled capsules will be discussed more in detail further on.

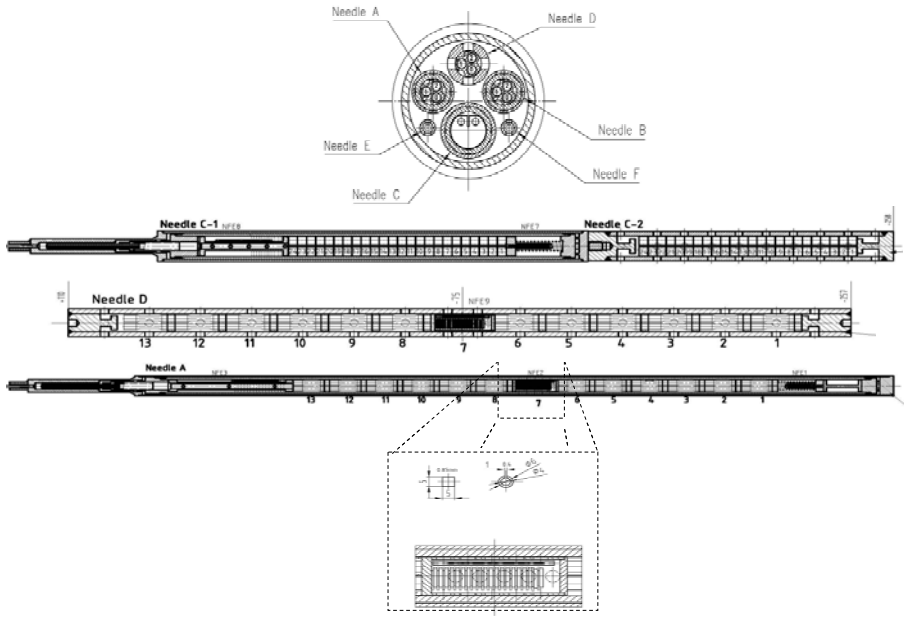

Figure 4.2: Design drawings of the capsules of Twin Astir. Cross section showing the position of each capsule (above); Capsule with CT specimens (upper capsule). PbBi filled section on the left and open section in contact with PWR water on the right; Capsule for tensiles open to PWR water (middle capsule); Capsule for tensiles in contact with PbBi (bottom capsule).

4.4 NEUTRONICS

MCNP calculations of the detailed axial distributions of the neutron fluxes and gamma heating were made based on the design of the needles of TWIN ASTIR located in the IPS2 channel of CALLISTO and the dpa rates, production of Po^{210} and the reactivity effect were evaluated. The calculations were performed for the full scale 3D heterogeneous MCNP & ORIGEN-S model of BR2 with detailed 3D fuel depletion distribution in the fuel elements.

The calculated accumulated dpa for each of the capsules based on 10 operating cycles of BR2 are given in Table 4.1.

Table 4.1: calculated accumulated dpa in the needles of Twin Astir based on 10 BR2 operating cycles. Values for the regions around the mid plane of the reactor core given in dpa.

Needle A	Needle B	Needle D	Needle C1
2.68 ± 2.3%	2.67 ± 2.3%	2.82 ± 2.2%	2.46 ± 1.6%

Note that needle A was removed after only 6 cycles (5 cycles were initially foreseen). The production of Po^{210} in these needles after 10 cycles of irradiation was estimated to be around 0.01g using MCNP. This amount of Po corresponds to a total activity of $1,66.10^{12}$ Bq or, given a total PbBi volume of $67cm^3$, the volumic activity is $2,48.10^{10}$ Bq/cm^3. The axial distribution of the fast and the thermal neutron flux for Needle A as well as the axial distribution of the gamma flux for each needle are depicted in Figure 4.3.

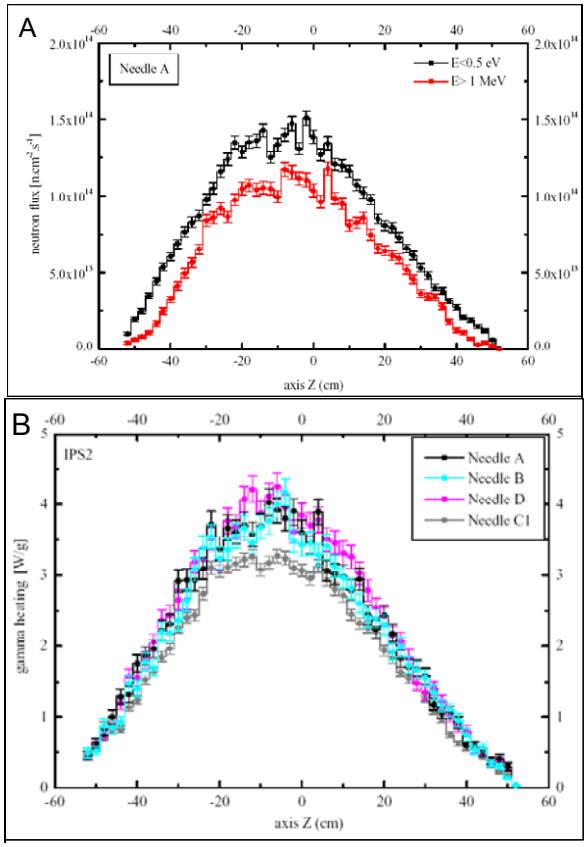

Figure 4.3: Axial distribution of neutronics; A: Axial distribution of the fast and thermal neutron flux (shown for needle A – other needles are comparable); B: Axial distribution of the gamma flux.

4.5 TEMPERATURE AND PRESSURE CONTROL

Having to change to a double wall concept, there was an additional resistance to heat transfer that needed to be taken into account. The high gamma heating, in the range of 4 W/g for IPS 2, did not make things easy. Hence, the tubes were matched as close as possible, coming possibly into contact at several spots. Four grooves, 0.25 mm deep were machined in the inner tube to facilitate the control of the gap. Even if the capsule tubes were machined in order to get a close fit, the tolerances leave a thin gap between the tubes (see Table 4.2 and Table 4.3).

According to the tolerance range, the gap thickness varied between 0.01 and 0.05 mm. Due to further circularity and cylindricity errors, the gap could close at some locations. Hence, the temperature gradients across the capsule tubes were calculated to vary according to the gap thickness, as indicated below in Table 4.2. In addition, there was a gradient at the interface tube / CALLISTO water (forced convection in CALLISTO water) and another 5°C temperature gradient within the capsule (gamma heating of the materials contained by the inner tube). The results of the heat transfer calculations are summarized in Table 4.2 for the tensile containing capsule and in Table 4.3 for the CT containing capsule.

Table 4.2: Calculation of the temperature gradient across the tensile loaded capsule tube based on the gap thickness.

Temperature gradients across the capsule		Hot plane			
Tensile-loaded capsule		Contact	Minimum	Average	Maximum
Geometry data			gap	gap	gap
Inner tube inner diameter	mm	10	10	10	10
inner tube thickness	mm	2	1,89	1,88	1,88
Inner tube outer diameter	mm	14	13,78	13,77	13,76
Gap thickness	mm	0,000	0,110	0,125	0,140
Outer tube inner diameter	mm	14	14	14,02	14,04
Outer tube thickness	mm	1	1	0,99	0,98
Outer tube outer diameter	mm	16	16	16	16
Tubes Δt					
Inner volume Δt	°C	10,3	10,3	10,3	10,3
Inner tube Δt	°C	11,1	10,4	10,3	10,3
Gap Δt	*°C*	*0,0*	*32,0*	*36,9*	*41,8*
Outer tube Δt	°C	4,1	4,1	4,1	4,0
Δt convection	°C	1,9	1,9	1,9	1,9
Tubes Δt	°C	**17,1**	**48,4**	**53,2**	**58,0**
Total Δt		**27,4**	**58,7**	**63,5**	**68,3**

Table 4.3: Calculation of the temperature gradient across the CT loaded capsule tube based on the gap thickness.

Temperature gradients across the capsule		Hot plane			
CT-loaded capsule		Contact	Minimum gap	Average gap	Maximum gap
Geometry data					
Inner tube inner diameter	mm	14	14	14	14
inner tube thickness	mm	2	1,99	1,98	1,97
Inner tube outer diameter	mm	18	17,98	17,96	17,94
Gap thickness	mm	0,000	0,010	0,030	0,050
Outer tube inner diameter	mm	18	18	18,02	18,04
Outer tube thickness	mm	1,5	1,5	1,49	1,48
Outer tube outer diameter	mm	21	21	21	21
Tubes Δt					
CT Δt	°C	18,70	18,70	18,70	18,70
Inner tube Δt	°C	13,3	13,3	13,2	13,1
Gap Δt	*°C*	*0,0*	*5,7*	*17,0*	*28,2*
Outer tube Δt	°C	12,5	12,4	12,3	12,2
ΔT convection	°C	2,38	2,37	2,36	2,36
Total Δt in capsule tubes	**°C**	**25,8**	**31,4**	**42,5**	**53,5**
Total Δt with Δt in CT specimens	**°C**	**46,9**	**52,4**	**63,6**	**74,6**

As the capsules temperature control did not rely on the fluid heat conductivity for heat transfer, the "closed gap" technology made the system insensitive to the fluid used for the intermediate room control. Therefore the control fluid could be gas, despite its low thermal conductivity.
In this case, the integrity control was performed based on the pressure in the intermediate room between the inner and the outer capsule tube. Three pressure sensors (one per capsule) were installed in the instrumentation head to monitor the capsule integrity.

When heating a given volume of gas from 20°C to 310°C, the pressure increases by a factor 2 as calculated in Equation 4.1 (the volume remains almost constant):

$$\frac{p_1}{T_1} = \frac{p_2}{T_2} \text{ , thus, } p_2 = p_1 \cdot \frac{273{,}15 + 310}{273{,}15 + 20} \cong 2 \cdot p_1 \quad \textbf{(4.1)}$$

The inner PbBi capsules could be pressurised to 2.5 MPa (cold condition), resulting in a pressure of 5 MPa in hot condition whereas the intermediate room is inflated to 5 MPa, becoming 10 MPa in hot condition. This inner pressure is sufficient to counter the external pressure applied to the outer tube by CALLISTO (0 to 1 MPa in cold condition and 15.5 MPa in hot condition).

In order to get an efficient leak detection, i.e. a significant pressure change in case of leak, the intermediate volume should be small compared to the inner volume (half the volume would be nice). In practice, the control volume should be built as close as possible to the PbBi capsule.
In case of a leak of the inner tube, considering a volume V1, filled at P1 = 5 MPa, in communication with a volume V2 = 0.5.V1, filled at 10 MPa, the pressure at equilibrium is +/- 6.6 MPa. As the helium molecule is very thin, it should be able to find the leak path even in the 'closed' gap. The pressure change could however be very gradual.
A leak of the outer tube would obviously increase the pressure to 15.5 MPa, which is unmistakable.

4.6 LBE FILLING

For the filling of the capsules with PbBi a dedicated filling installation was designed and built at SCK•CEN. Since oxygen content is the key parameter for corrosion control in PbBi systems, particular emphasis was put on this aspect during the filling procedure.

The filling installation is schematically represented in Figure 4.4 along with a picture of the actual installation. The installation is composed of a PbBi conditioning tank in which the PbBi is melted and its chemistry set to the required O_2 concentration (10^{-6} wt%), a vacuum pump, a set of heaters, which have to keep the whole installation at or above 150°C, to prevent the freezing of PbBi during the filling process, and a filling connection, connecting the tank, the capsule to fill and the vacuum pump.

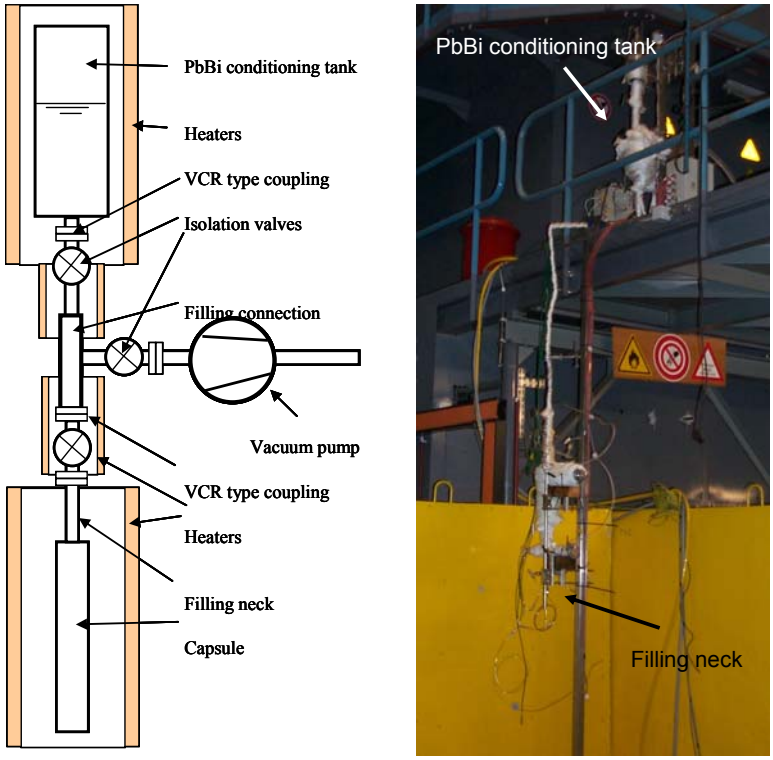

Figure 4.4: Filling system for the TWIN ASTIR capsules.
Right: Schematic; Left: Picture.

The filling connection itself is schematically represented in Figure 4.5. The purpose of this system was to allow the evacuation of the capsule, its bakeout, and its filling without opening to the atmosphere and contamination of the PbBi by air.

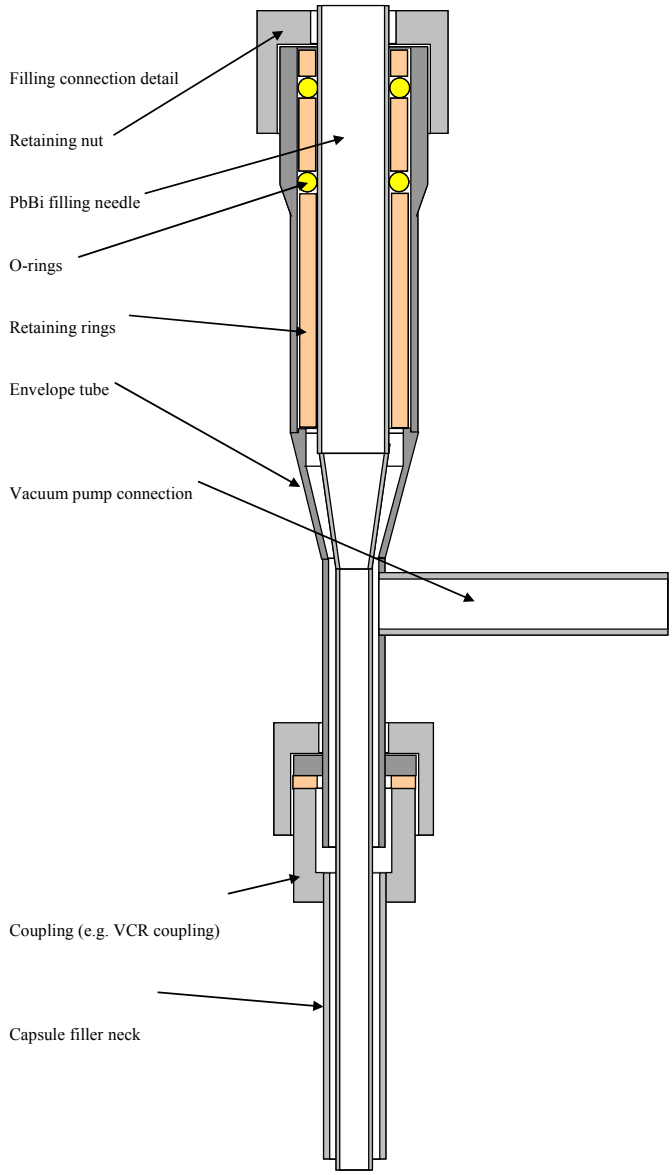

Figure 4.5: Schematic representation of the filling connection (detail of Figure 4.4).

The filling needle is inserted in the filler neck of the capsule to avoid any risk of contamination of the latter by the PbBi, which would prevent the execution of a tight sealing weld. The filling needle is withdrawn after filling. With adequate isolation valves, as shown on Figure 4.4, the conditioning and PbBi filling could be performed in air without contamination of the PbBi melt. The capsule would then be disconnected from the conditioning tank and the vacuum pump and brought into a

glove box where it is pressurised and seal welded. The chemical composition of the LBE used in the Twin Astir programme is given in Table 4.4.

Table 4.4: Chemical composition of LBE for filling of TWIN ASTIR capsules (in µg/g).

Bi (wt%)	Pb (wt%)	Cu	Ag	Sn	Ti	Na
54.3	45.7	4.1	13	4.25	2.25	<50
Ca	Cr	Fe	Ni	Mo	Cd	Th
<250	<10	<100	<5	<1	<1	<0.5

4.7 0 DPA CAPSULE

The online temperature and pressure measurements of the BR2 reactor are all stored in a database system called Bidasse. We exported the water temperature data (1 data point per minute) of the IPS2 channel of CALLISTO from the Bidasse database and made the temperature correction according to the calculated gamma heating as mentioned before in Table 4.2 for the points corresponding to the reactor in operation. It was impossible to use the actual temperature since the TWIN ASTIR experiment did not have any thermocouple inside the capsule.

Using these modified temperature data, we could have a capsule, identical to the capsule A under irradiation, following the thermal profile of the irradiated capsule. Apart from 2 erroneous data points which led to sharp temperature increases, the non irradiated capsule (0 dpa capsule) followed the thermal profile of the BR2 irradiation very well.
Both the temperature profile of the irradiated capsule and the non-irradiated capsule are represented in Figure 4.6.

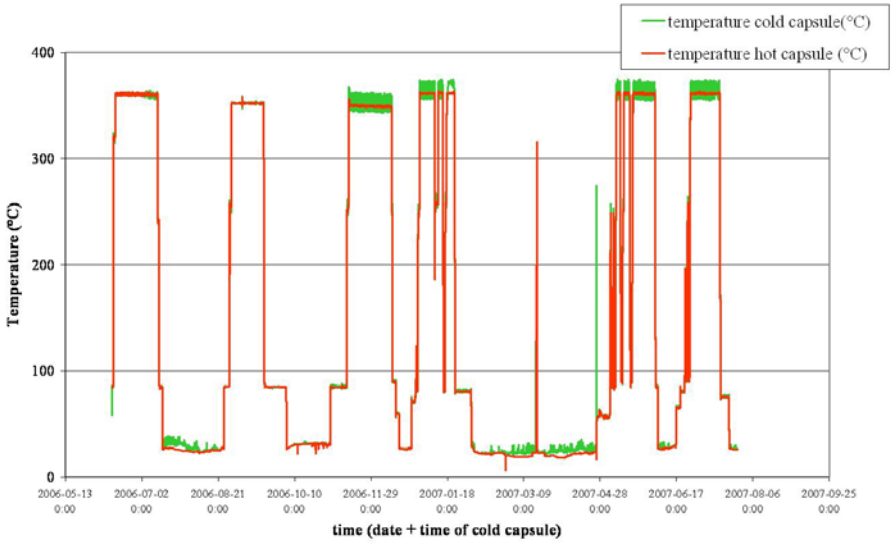

Figure 4.6: Thermal profile of the in-pile (capsule A) and out of pile capsule (0 dpa capsule).

The use of a 0 dpa capsule allows discriminating the effect of the thermal cycling and thermal exposure from the effect of the neutron irradiation. This is important, since, as described above, PbBi is known to have the tendency to expand after solidification depending on the cooling parameters. Furthermore, the comparison of corrosion in LBE after thermal cycling can be compared to the corrosion under thermal cycling and irradiation in LBE. Due to licensing issues, it was however not possible to examine irradiated specimens in the SEM. Therefore, the corrosion issue will not be discussed further.

5 COMPATIBILITY OF "AS RECEIVED" STRUCTURAL MATERIALS WITH LIQUID METALS

The test of all knowledge is experiment.
Richard P. Feynman
(1918 – 1988)

In Chapter 5 we discuss the mechanical tests performed on the materials in the as received condition. No prior exposure to liquid metals, no surface treatments, abnormal heat treatments or cold work were applied prior to testing.
First, we will discuss the results of the SSRT testing of 316L, T91 and the silicon enriched steels in liquid lead bismuth eutectic and compare the results to tests performed in inert environment. These tensile tests are to be considered as a screening method for liquid metal embrittlement.
Second, we will discuss the plane strain fracture toughness assessment of both 316L and T91 in liquid lead bismuth eutectic. These tests could not be done using the traditional testing method. The problems in respect to the traditional methods will be explained and the applied method which allows plane strain fracture toughness testing in LBE will be discussed. These fracture toughness tests are a means of quantifying the embrittling effect of the LBE and are very important regarding the safety of the future nuclear systems. Unfortunately however, they could not be applied to the elevated silicon steels due to the nature of the fracture toughness testing method.

5.1 SSRT TESTS

All SSRT tests of as received materials were carried out using Liquid Metal Embrittlement Testing Station 1 (LIMETS 1) which was especially designed for testing in liquid lead bismuth environment and which was described in Section 3.1. For validation of comparison between non active and active tests on irradiated samples (see Chapter 7), a few tests were performed in the LIMETS 2 facility. These tests were also used as verification of the operation of LIMETS 2 prior to the conversion of the hot cell from β, γ-cell to α-cell as described in Chapter 3.

Small size cylindrical tensile samples were used with a total length of 24 mm, a gauge length of 12 mm and a diameter of 2.4 mm. These samples were manufactured in L orientation (rolling direction) with a lathe machine and did not undergo any other surface treatment. Prior to testing, the samples were degreased by ultrasonic cleaning in methanol and dried in air. The samples were measured using a digital profile projector (type Mutitoyo PJ300).

5.1.1 SSRT tests of 316L

Compared to SSRT testing of T91 steel, considerably less attention has been focussed on the possible liquid metal embrittlement of the austenitic stainless steel 316L in liquid lead alloys. This is not because the austenitic steel 316L would be less important or because it would not be in intimate contact with the LBE in the future envisaged liquid metal cooled facilities. Since no embrittlement due to LBE has been found in tensile tests after long term exposure [51] nor in low cycle fatigue tests [52], the international community has simply stated that the mechanical behaviour of 316L in contact with LBE will not be a life limiting factor in the context of its envisaged use [137]. Furthermore, tensile tests in LBE at 200°C on neutron irradiated 316L steel have not shown any evidence of embrittlement in comparison with tests in air under similar conditions [72].

However, since no experience is openly available on the behaviour of 316L under the simultaneous influence of both neutron irradiation and liquid metal contact, we should not neglect the importance of materials testing on 316L under relevant conditions.
Here, we will discuss the reference tests, performed on the as received 316L as function of strain rate in contact with LBE at 350°C. For comparison, tests have been performed in argon and hydrogen gas mixture, using the same testing machine, LIMETS 1.

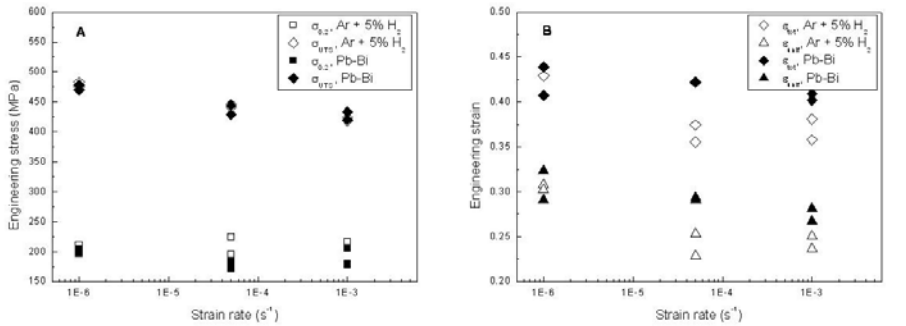

Figure 5.1: Tensile results of 316L as function of strain rate (temperature 350°C). Full symbols for tests performed in LBE, empty symbols for reference data on the same batch of 316L, tested in Ar + 5% H_2. A: Influence of the strain rate on the yield stress, ultimate tensile strength in LBE at 350°C; B: Influence of the strain rate on the uniform elongation and total elongation in LBE at 350°C.

Figure 5.1 shows the tensile properties of 316L at 350°C as function of the strain rate between 1.10^{-6} s^{-1} and 1.10^{-3} s^{-1}. The full symbols in the figure represent tests performed in LBE, the hollow ones represent tests performed in gas atmosphere.
In Figure 5.1A, the yield stress and ultimate tensile strength are depicted. Although the scatter is larger on the yield stress values, the figure shows that the yield stress remains around a value of 200 MPa for all conditions whereas the ultimate tensile strength decreases slightly with increasing strain rate. In terms of strength parameters, the environment seems to have no influence at all since the values for both testing environments coincide rather well.

In Figure 5.1B, the uniform elongation and total elongation of 316L at 350°C are depicted as function of the applied strain rate. As seen in section 1.3.1 of Chapter 1, when LME occurs, the total elongation should decrease significantly compared to this in inert environment. However, in the results presented in Figure 5.1, the total elongation of the tests performed in LBE is nearly always higher than this in inert environment. This suggests there was no embrittling effect of the LBE.

Fracture surface examination of the least ductile 316L specimen (1.10^{-6} s^{-1}, 350°C, LBE) revealed a fully dimpled and thus ductile fracture surface.
These results confirm that 316L is not prone to liquid metal embrittlement under these conditions.

5.1.2 SSRT tests of T91

In the frame of this PhD, two batches of T91 were tested. Initially we performed tensile tests on the T91 batch which was the reference steel in the SPIRE project [21]. Later, all the work was focussed on the T91 batch which was the reference steel within DEMETRA EUROTRANS project. Mechanical properties of both batches of the same type of steel in air are compared in section 2.1.2.4.2 of Chapter 2.

In order to find the ductility trough (discussed in section 1.3.1 "temperature" and "strain rate") for T91 in LBE, we performed tensile tests as function of temperature at a strain rate of 5.10^{-5} s^{-1} and tensile tests as function of strain rate at 245°C (T91, SPIRE), 350°C (T91 DEMETRA) and 450°C (T91 SPIRE).

To examine the effect of temperature on the susceptibility of T91 to liquid metal embrittlement, a constant strain rate of 5.10^{-5} s^{-1} was applied. This strain rate was chosen as an optimum between practical and physical considerations. For physical reasons it was best to have a slow strain rate to obtain wetting of fresh metal surface that appears by breaking the oxide layer on the sample surface and allowing the penetration of LBE. On the other hand, from a practical point of view it was desirable to have a strain rate which results in the optimal use of the testing setup under controlled conditions. Taking into account the time needed for attaching the sample, heating, liquid metal transfer, settling of temperature, testing and cooling a strain rate of 5.10^{-5} s^{-1} made it possible to perform tests under well defined and controlled conditions.

The tensile tests were performed in lead bismuth eutectic at temperatures between 150°C and 450°C. To assess the possible occurrence of LME, the results of the tests in LBE are compared with previous tensile tests performed in gas environment by different labs [132]-[136]. These tests were done within the European FP5 programme SPIRE and were all on the same batch of T91 as the one we tested in LBE. To verify the fitted curves, four tests were performed at temperatures between 100 and 350°C in argon with 5% hydrogen gas environment using the same machine as for the tests in LBE. To have an idea on the scatter of the mechanical properties between two batches of the same type of steel, we added two tests on the T91 DEMETRA in Ar + 5%H_2 at 350°C also at a strain rate of 5.10^{-5} s^{-1} (indicated in red in Figure 5.2).

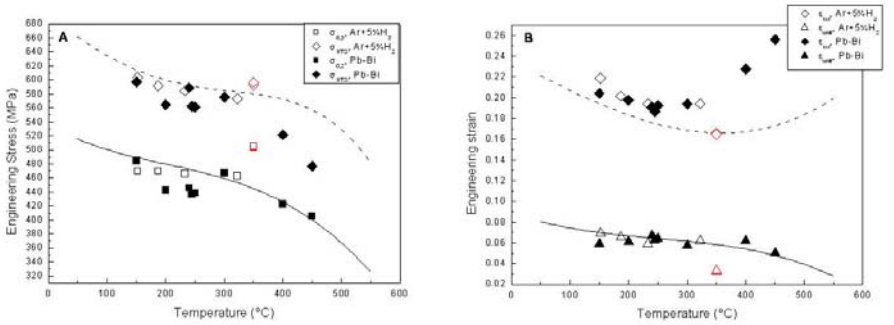

Figure 5.2: Tensile results as function of temperature (strain rate: $5.10^{-5}s^{-1}$). Full symbols for tests performed in LBE, empty symbols for tests performed in controlled gas atmosphere. The lines are obtained from fitting to tensile data from tests in gas environment performed within the Spire project. T91 DEMETRA data in red. A: Influence of temperature on the yield strength and tensile strength; B: Total and uniform elongation as a function of temperature.

Figure 5.2 shows the strength and ductility properties of the T91 material tested in liquid LBE and in hydrogen and argon gas mixture environments compared to the fitted curves from previous tests in gas environment as a function of temperature using a constant strain rate of $5.10^{-5}s^{-1}$. The full symbols in the curves represent data obtained from tensile testing in liquid LBE whereas the empty ones are of the tests performed in the controlled gas environment. The red data points represent tests of the T91 DEMETRA batch.

The yield strength, $\sigma_{0.2}$ and the ultimate tensile strength, σ_{UTS} are plotted in Figure 5.2A as function of temperature. At temperatures between 100 and 320°C the strength properties of the material are slightly dependent on the test temperature. Above 320°C both yield stress and tensile strength decrease. The yield stress of the T91 tested in liquid lead bismuth environment follows the same trend as the reference data. The tensile strength of the T91 tested in LBE above 350°C however decreases considerably faster than the reference curve indicates. This might be due to the fact that at temperatures above 300°C reference data is scarce and the statistical population for the fitting was insufficiently large.

The results shown in Figure 5.2A are compatible with the data of Dai et al. [57] obtained using similar slow strain rate tensile tests performed at 300°C and at 375°C using 5 mm x 1,5 mm x 0,75 mm rectangular specimens that were electro polished to avoid the presence of sharp microcracks and consequently mechanically polished.

The influence of temperature on the ductility properties plotted in Figure 5.2B shows that the uniform elongation decreases monotonically with temperature in the interval of 115°C to 450°C with values between 7% and 5%. The environment does

not affect the uniform elongation under these conditions and both results from testing in LBE and in gas environments follow the same trend. At temperatures up to 245°C, the total elongation in both environments decreases with the temperature, reaching a minimum value in liquid metal at 245°C. The minimum total elongation in the reference curve is at 350°C. At temperatures above 245°C the total elongation in gas environment remains about constant up to 450°C, whereas in LBE it steadily increases reaching a maximum value at 450°C. Although Di Gabriele *et al.* [53] confirm the increased ductility of T91 in LBE at elevated temperatures (500°C), more data is needed to confirm this trend. As mentioned before, according to us, the difference at elevated temperature is due to experimental spread and the insufficiently large statistical population of the reference data. Although the faster self healing of the oxide layer at elevated temperatures may be important in preventing the occurrence of LME at elevated temperatures, we believe it is very unlikely that the self healing of the oxide layer would increase the ductility of the material in comparison to tests performed in air, as was suggested by Di Gabriele *et al.* [53].

In case of LME, one would expect a minimum in the ductility properties at temperatures close to the melting point of lead bismuth eutectic. However, our obtained data clearly demonstrates there is no decrease in mechanical properties of cylindrical specimens of T91 when the native oxide layer of the steel has not been removed and the surface does not contain cracks prior to testing.

The influence of the strain rate on the mechanical properties of the material was tested using different strain rates at a constant temperature. The testing temperatures were 245°C and 450°C for the T91 SPIRE material due to the minimum in the total elongation shown in Figure 5.2B and the fact that the strength properties of T91 decrease above 320°C. The T91 DEMETRA was tested at different strain rates at 350°C due to the minimum in the reference curve in Figure 5.2 and the fact that the irradiation temperature of TWIN ASTIR was envisaged to be 350°C.

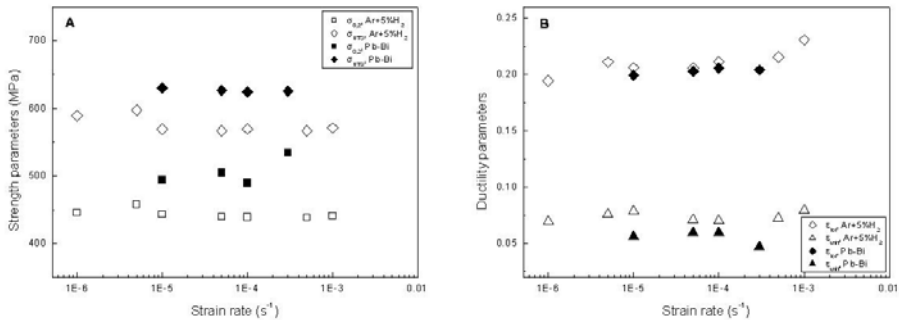

Figure 5.3: Tensile results as function of strain rate (temperature: 245°C). Full symbols for tests performed in LBE, empty symbols for tests performed in controlled gas atmosphere.
A: influence of the strain rate on the yield stress, ultimate tensile strength at 245°C; B: Influence of the strain rate on the uniform elongation and total elongation at 245°C.

Figure 5.3A shows the strength properties of T91 as function of the strain rate at 245°C whereas Figure 5.3B shows the total elongation and uniform elongation obtained under the same conditions. The full symbols represent data points obtained from tensile tests in liquid metal environment and the empty points represent the results of tests in argon and hydrogen gas environment. The strength properties are independent of the strain rate both in liquid metal and in gas environment however the values of yield stress and tensile strength are higher in liquid metal environment than in gas when tested at the same strain rate. The ductility properties both in gas and in liquid metal environment are barely influenced by the strain rate at 245°C. The elongations remain close to the same value although the elongations in the liquid metal environment are little smaller than those in gas environment.

At 450°C, the tensile tests were only performed in lead bismuth eutectic using strain rates between 1.10^{-6} s^{-1} and 1.10^{-3} s^{-1}.

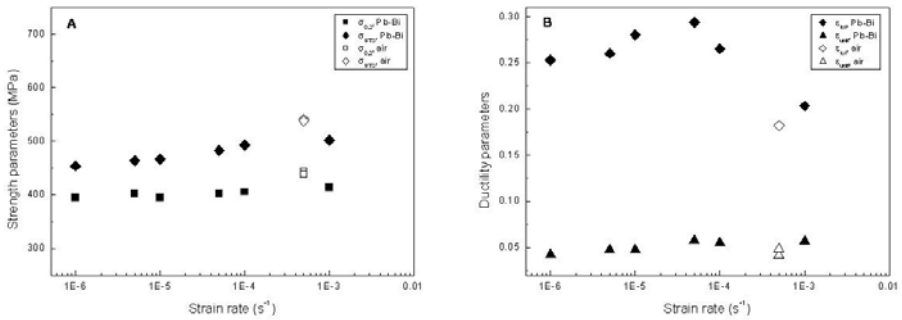

Figure 5.4: Tensile results as function of strain rate (temperature 450°C). Full symbols for tests performed in LBE, empty symbols for reference data on the same batch of T91 tested in air. A: Influence of the strain rate on the yield stress, ultimate tensile strength in LBE at 450°C; B: Influence of the strain rate on the uniform elongation and total elongation in LBE at 450°C.

Figure 5.4A displays the strength properties of the T91 material tested in LBE at 450°C together with reference data obtained from testing in air at 450°C [132]. Yield stress and ultimate tensile strength are plotted as a function of strain rate.

The yield stress remains constant within the observed range of strain rates. However, ultimate tensile strength increases with increasing strain rate. The yield strength and tensile strength of the reference tests performed in air are little higher than those obtained from testing in LBE. Figure 5.4B shows the total and uniform elongations from the tests in LBE and the total and uniform elongations from the reference tests in air as a function of strain rate. The uniform elongation is not influenced by the strain rate at 450°C and remains around 0.05 in all strain conditions. The total elongation exhibits a slight dependence on the strain rate with a maximum between 1.10^{-4} and 1.10^{-5}. No decrease in ductility due to LBE was observed under these test conditions.

At 350°C, tensile tests were performed on T91 DEMETRA using strain rates ranging between 1.10^{-7} s^{-1} and 1.10^{-3} s^{-1}. The results are depicted in Figure 5.5. Again here, full symbols represent tests performed in LBE and hollow symbols represent tests performed in a gas mixture of argon and hydrogen.

The yield stress remains constant at 350°C within the tested range of strain rates. The ultimate tensile strength however slightly decreases with increasing strain rate in contrast with its behaviour at 450°C.

The ductility parameters, shown in Figure 5.5B, slightly decrease with increasing strain rate at 350°C.
Although the uniform elongation is independent of the environment since all data points are nicely aligned, there is a clear outlier in the total elongation of one of the tests at 1.10^{-6} s^{-1} (indicated by the red arrow in Figure 5.5). To verify these results, the stress-strain curves of all four tests performed at 1.10^{-6} s^{-1} are shown in Figure 5.6.

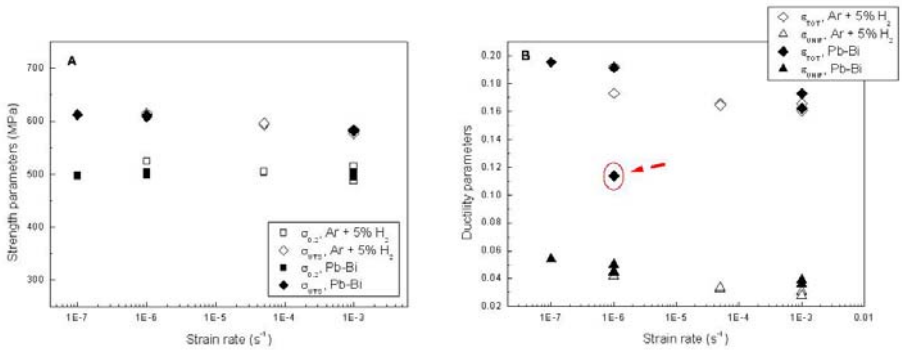

Figure 5.5: Tensile results of T91 DEMETRA as function of strain rate (temperature 350°C). Full symbols for tests performed in LBE, empty symbols for reference data on the same batch of T91 tested in air. A: Influence of the strain rate on the yield stress, ultimate tensile strength in LBE at 350°C; B: Influence of the strain rate on the uniform elongation and total elongation in LBE at 350°C.

Figure 5.6 clearly shows that one of the tests in LBE has significantly reduced total elongation while yield stress and ultimate tensile strength are the same for all four tests. This is typically the mechanical behaviour linked with liquid metal embrittlement of T91 in LBE as reported by other research groups [53],[55],[57]. However, the large difference in mechanical behaviour between both tests in LBE, under the same testing conditions, underlines the problem of reproducibility of liquid metal embrittlement tests of T91. This is a well known problem often attributed to a lack of wetting in tests which do not show any effect and has led numerous researchers to resort to wetting and/or embrittlement favouring techniques as discussed in section 1.3.3.2 of Chapter 1.

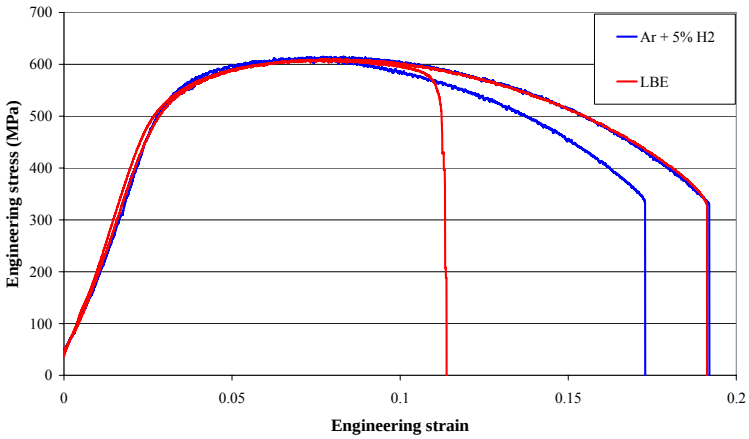

Figure 5.6: Stress-strain curves of T91 Demetra at 350°C, 1.10^{-6} s^{-1}; Tests in LBE in red, tests in Ar + 5% H_2 in blue.

In Figure 5.7, we show the fracture surfaces of both T91 samples tested in LBE at 350°C at a strain rate of 1.10^{-6} s^{-1}. The embrittled specimen shows several initiation sites at the surface which formed semi-circular fracture patterns. While the fracture surface at the centre of the embrittled specimen is fully dimpled, typical of ductile fracture surfaces, the semi-circular fracture patterns, which initiated at the surface, do not have dimples. The brittle fracture surface does not show clear evidence of intergranular fracture, nor of clear cleavage fracture.
We attribute this complex fracture morphology to the complex nature of the T91 ferritic-martensitic microstructure.

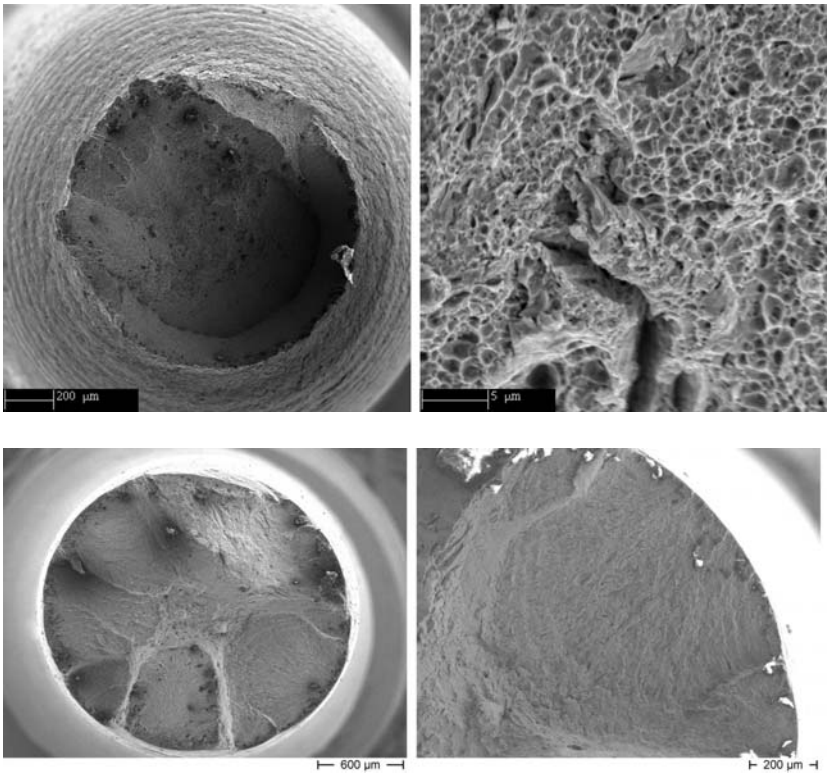

Figure 5.7: SEM fracture surface images of T91 specimens tested in LBE at 350°C, 1.10^{-6} s^{-1}; (above) T91 specimen not showing embrittlement when compared to results in Ar + 5%H_2; (below) T91 specimen showing several initiation sites of liquid metal embrittlement.

The fracture surface of the specimen which was not embrittled, shows a nearly fully dimpled fracture surface, having the well known cup and cone shape. However, in the upper left side of the overview SEM picture, one can distinguish two relatively small initiation sites having the same embrittled fracture pattern as those in the embrittled specimen. One can also see the disturbance in the traditional ductile cup and cone shape on this side of the sample. The embrittlement was apparently very

little since macroscopically, no difference was seen in the reference curve and the tensile curve of this specimen.

The apparent contradiction between the test results under the same conditions might be explained by two possibilities: either there was insufficient wetting during the non embrittled tests and/ or the absence of localised corrosion or cracks at our specimen surfaces. It might be due to the fact that the test duration is relatively short and the samples were not pre-treated to remove the native oxide layer.

Regarding the wetting, as the oxide layer is much harder and thus less ductile than the underlying base metal, it was assumed that the oxide layer at the surface breaks under the applied stress so revealing the underlying metal and allowing intimate contact between the liquid lead bismuth and the base metal. So, local wetting of bare surface of the tested steel was indeed possible, unless T91 (high Cr steel) would have the necessary time to re-passivate in an oxide poor environment. This means that the bare base metal uses oxides present in the liquid metal environment to form a new oxide layer on its surface. Due to this repassivation of the surface, high chromium steels are said to have a self healing oxide layer. These two surface mechanisms of breaking under stress and repassivation are clearly competing and the relative speed of the two determines the degree of wetting. As we have no data on the actual kinetics of these two phenomena, it is difficult to state if the material was partially wetted or not.

Based on the tensile results discussed in section 1.3.3.2 of Chapter 1, we believe that the environmental embrittlement of T91 due to the presence of LBE is possible only in the case of the presence of an initial crack, wetted at the atomic scale and having a critical stress level at its tip. It is therefore reasonable that we did not see LME in the vast majority of our "as received" experiments due to the fact that there was no surface defect or local corrosion attack during the tests that would allow the initiation of the above described crack. The use of cylindrical tensile specimens also prevents stress concentrations at the surface of the specimens which is in sharp contrast with the stress concentrations obtained at the corners of rectangular shaped specimens as used in mechanical properties studies by Dai and Bin [57],[64]. Further, it might be considered that the self healing mechanism of the material was also fast enough to re-passivate the oxide layer under the tested conditions.

Both the effect of local corrosion by pre-exposure and the effect of surface stress concentrators will be further discussed in Chapter 6.

5.1.3 SSRT tests of Si enriched steels

As mentioned in section 2.1.4 of Chapter 2, the addition of silicon has been proven to significantly increase the corrosion resistance of steels in flowing liquid LBE [80]-[83]. It is clear that steels with increased corrosion resistance would be of great importance for all liquid metal cooled systems and therefore form an interesting subject within the frame of this study.

Their mechanical properties in liquid LBE environment were studied by performing SSRT tests in the Limets 1 facility. Unfortunately, the limited amount of available material limited the possible amount of testing conditions. We could therefore not perform tests as function of strain rate or as function of temperature for all the elevated Si steels.
The mechanical properties of the ferritic/bainitic/martensitic and the austenitic elevated Si steels are discussed in the following two sections.

5.1.3.1 SSRT tests of ferritic/bainitic/martensitic Si enriched steels

The ferritic/bainitic/martensitic steels we studied are the T91-Si, 2439, 2440 and 2441 steels.

T91-Si steel

The T91-Si which is very similar in microstructure to the conventional T91 as discussed in section 2.1.4.3 of Chapter 2, has an addition of Si which alters its mechanical properties. The silicon has a solid solution strengthening effect which increases the yield strength and the ultimate tensile strength.
The tensile properties of T91-Si were examined at 350°C at a strain rate of 5.10^{-6} s^{-1} both in mixed hydrogen and argon gas environment and in liquid LBE environment. The tensile curves are presented in Figure 5.8. To compare the tensile properties of the T91-Si with the conventional T91 steel, the tensile results of T91 in argon and hydrogen gas have been added.

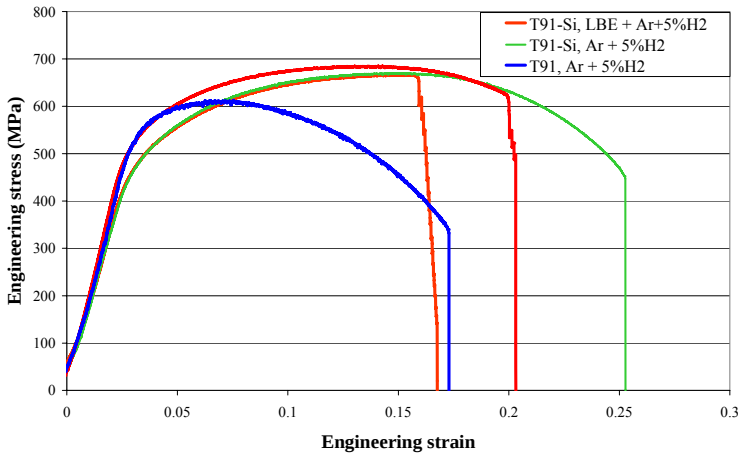

Figure 5.8: Tensile curves of T91-Si (red, green) in comparison with the conventional T91 steel (blue). Curves in red are resulting from tests of T91-Si in LBE. All tests were performed at 350°C, using a strain rate of 5.10^{-6} s^{-1}.

Figure 5.8 clearly shows that when the material is in contact with the liquid metal environment, the total elongation of the T91-Si is significantly reduced while the yield stress and tensile strength remain the same. This is in agreement with the observations of the liquid metal embrittlement of conventional T91 by Dai *et al* [57]. Although the embrittled T91-Si steel still has as much total elongation as the conventional T91 steel in inert environment, it should be noted that the tests of T91-Si are very well reproducible. This was not the case for the traditional T91 steel as discussed in section 5.1.2 above.
The tensile curves also show a stepwise fracture progression. As can be seen in Figure 5.8, the load of the red curves being T91-Si in LBE does not drop to zero immediately. The advancing crack is stopped each time.

SEM examination of the fracture surfaces was performed to verify this fracture behaviour. Figure 5.9 shows the SEM pictures of the fracture surfaces of the T91-Si steel samples tested both in gas and in liquid metal environment. Picture A shows an overview of the sample tested in gas. The sample shows significant necking and the typical cup and cone shape, characteristic for ductile tearing of cylindrical tensile specimens. The detail presented in picture B shows that the fracture surface of the T91-Si tested in gas was fully dimpled, having some precipitates in the centre of the larger dimples. This fracture surface is typical for ductile fracture.

Pictures C to H in Figure 5.9 show the fracture surfaces of the T91-Si steel samples tested in LBE. The overview of the most embrittled sample (least total elongation in Figure 5.8) of T91-Si shows a fully embrittled fracture surface on a sample which

had no necking. The detailed pictures reveal the initiation site at the surface of the sample (picture D) and the crack arrest sites (picture E) where the advancing LME was temporarily halted. The cause of the crack arrest is difficult to assess and attributing it to a lack of liquid metal at the crack tip would be rather speculative. It is however clear that this extent of embrittlement, showing a fully brittle fracture surface has not been encountered so far in any tensile test of as received T91.

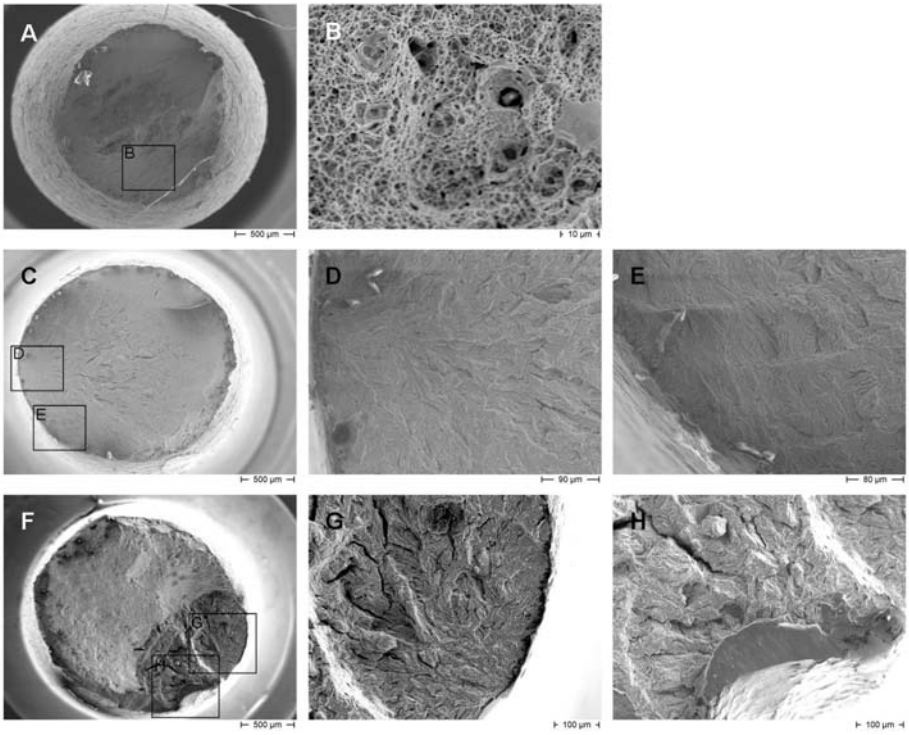

Figure 5.9: SEM examination of fracture surfaces of T91-Si tested in Ar + 5%H_2 and LBE at 350°C, using a strain rate of 5.10^{-6} s^{-1}. A: Overview of T91-Si tested in Ar + 5%H_2; B: Detail of fully ductile fracture surface showing dimples with precipitates in some of the larger dimples; C: Overview of T91-Si tested in LBE showing a fully brittle fracture surface; D: detail of the initiation site at the surface of the sample spreading to the inside; E: Detail of crack arrest sites showing consecutive crack fronts; F: Overview of T91-Si tested in LBE showing a partially brittle and partially ductile fracture surface; G: Detail of fully brittle initiation site; H: Detail of fully brittle initiation site.

The other T91-Si sample tested at 350°C in LBE is shown in picture F-H of Figure 5.9. In contrast with the previously discussed specimen of T91-Si, this one is only partially fractured in a brittle manner. The fracture surface overview in picture F shows a relatively small amount of necking has preceded fracture and at least three brittle fracture initiation sites can be distinguished (two lower right, represented in picture G and H; one upper left). The majority of the fracture surface of this sample is however dimpled and does not show any signs of embrittlement.

2439 steel (11.58 wt% Cr; 0.48 wt% Ni; 2.75 wt% Si)

The bainitic 2439 steel is relatively close in chemical composition to the conventional T91. However, it has 2.75 wt% Si and about 11 wt% Cr instead of the 9 wt% Cr in T91 steel. Its bainitic microstructure comprises of small grains as shown in section 2.1.4 of Chapter 2. The tensile properties of 2439 steel were tested at 350°C at a strain rate of 5.10^{-6} s^{-1}, both in Ar + 5% H_2 and in liquid LBE environment. The tensile curves are depicted in Figure 5.10.

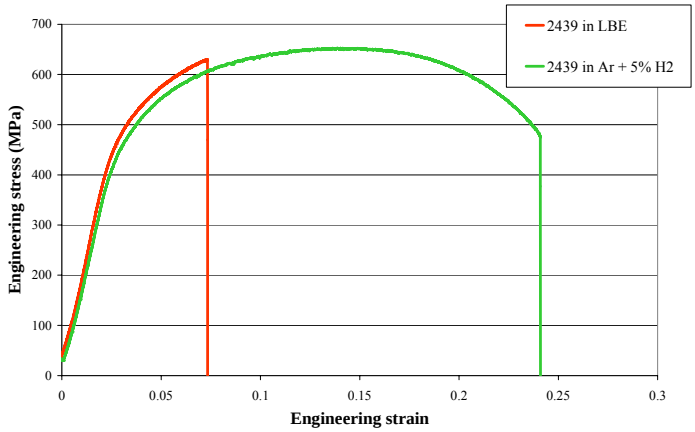

Figure 5.10: Tensile curves of 2439 steel tested at 350°C, 5.10^{-6} s^{-1} in Ar + 5% H_2 (green) and in LBE purged with Ar + 5% H_2 (red).

In Figure 5.10, the green curve represents the tensile test performed in argon and hydrogen gas mixture and the red curve represents the test in liquid LBE environment. The amount of total elongation is very strongly reduced when tested in liquid metal environment and although the yield strength is still the same as in gas environment, the tensile strength is not reached for the sample tested in liquid LBE. Despite a relatively small deviation within experimental scatter, it seems that both tensile curves coincide up to the moment of fracture. In contrast to the stepwise drop of the load in the fracture of T91-Si in LBE, the specimen of 2439 steel in LBE completely breaks without crack arrest showing a sudden drop to zero in the tensile curve.

The fracture surfaces of both the 2439 steel tested in gas and the 2439 tested in LBE were examined by SEM. The SEM pictures are shown and compared in Figure 5.11.

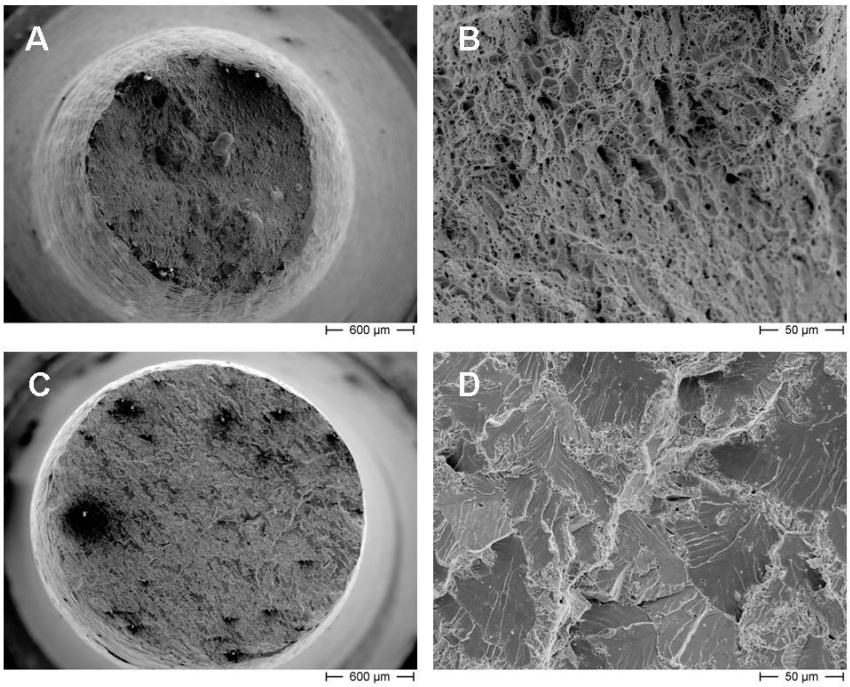

Figure 5.11: SEM examination of fracture surfaces of 2439 steel, tested in Ar + 5%H_2 and LBE at 350°C, using a strain rate of 5.10^{-6} s^{-1}. A: Overview of 2439 tested in Ar + 5% H_2 showing significant necking; B: Detail of fracture surface depicted in A, showing a fully dimpled surface indicating ductile fracture; C: Overview of 2439 steel tested in LBE purged with Ar + 5% H_2 showing no necking at all; D: Detail of fracture surface depicted in C, revealing brittle fractured grains showing river patterns and a small fraction of dimples on certain grain boundary areas.

Picture A of Figure 5.11 shows an overview of the 2439 steel sample tested in gas. The sample shows significant necking and somewhat the cup and cone shape typical for ductile fracture of cylindrical tensile specimens. The detail shown in picture B acknowledges the ductile nature of the fracture, showing a fully dimpled fracture surface.

In Picture C of Figure 5.11 the overview of the 2439 steel sample tested in liquid LBE is shown. The sample does not show any necking nor does it show any obvious fracture initiation sites. The nature of the fracture surface is shown more in detail in picture D of Figure 5.11. The fracture surface seems to consist of brittle fractured grains showing clear river patterns indicating cleavage type fracture. A relatively small amount of dimpled area is still found on what appears to have been prior austenite grain boundaries. Note that the scale of pictures B and C is identical. The liquid metal environment has completely altered the fracture behaviour of the 2439 under these conditions.

Since the liquid metal embrittlement effect was so obvious for the 2439 steel at 350°C, the test matrix was expanded to examine the LME effect of 2439 steel as function of temperature. All tensile tests as function of temperature were performed at a strain rate of 5.10^{-6} s^{-1}. The total and uniform elongation of the 2439 steel as function of temperature are given in Figure 5.12. The red curves with full symbols are resulting from tests in liquid LBE whereas the green curves with hollow symbols are from tests in Ar + 5% H_2.

The red curve of the total elongation has a similar shape to the ductility trough presented for leaded steels in section 1.3.3 of Chapter 1. The total elongation of the tested specimens strongly decreases between 250 and 375°C. Although the total elongation below 250°C is still less in liquid metal environment compared to this in gas, the embrittlement is not as pronounced as between 250 and 375°C. Above 375°C the LME effect disappears entirely.

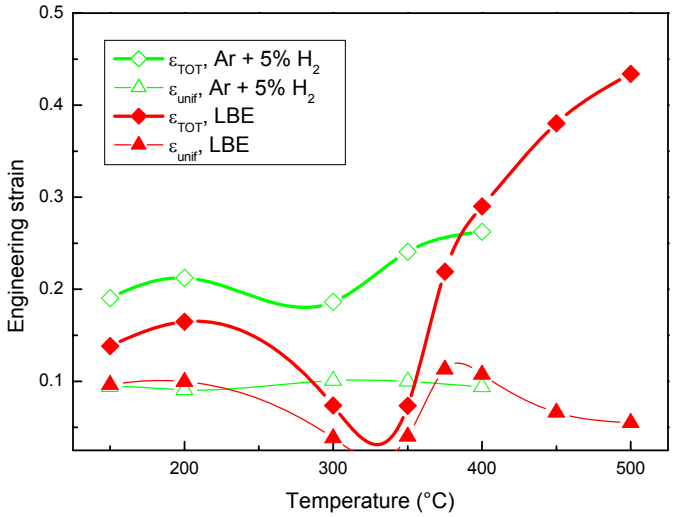

Figure 5.12: Tensile results of 2439 steel as function of temperature (strain rate: $5.10^{-5}s^{-1}$). Full, red symbols for tests performed in LBE, empty, green symbols for tests performed in controlled gas atmosphere (Ar + 5% H_2).

To verify the observations made based on the total and uniform elongation, presented in Figure 5.12 above, we examined the fracture surfaces of the 2439 steel samples tested in liquid LBE environment. Figure 5.13 shows the fracture surfaces of the 2439 steel samples tested between 300 and 400°C. The sample tested in LBE at 300°C shows very little to no necking and a fully brittle fracture surface. At 350°C, there is no necking at all and the fracture surface is nearly entirely brittle. However, small amounts of dimpled area can be seen on what appears to have been

the prior austenite grain boundaries as mentioned above. By gradually further increasing the temperature of the liquid LBE environment, the amount of plastic deformation prior to fracture is increased. The amount of necking of the sample increases and the fracture surface shows an increased amount of dimples. Above 400°C, the fracture behaviour returns to a fully ductile behaviour with cup and cone shaped broken specimens and fully dimpled fracture surfaces. The fracture properties of the 2439 steel above 400°C are very similar for both gas and liquid metal environment and show the same type of fracture surface.

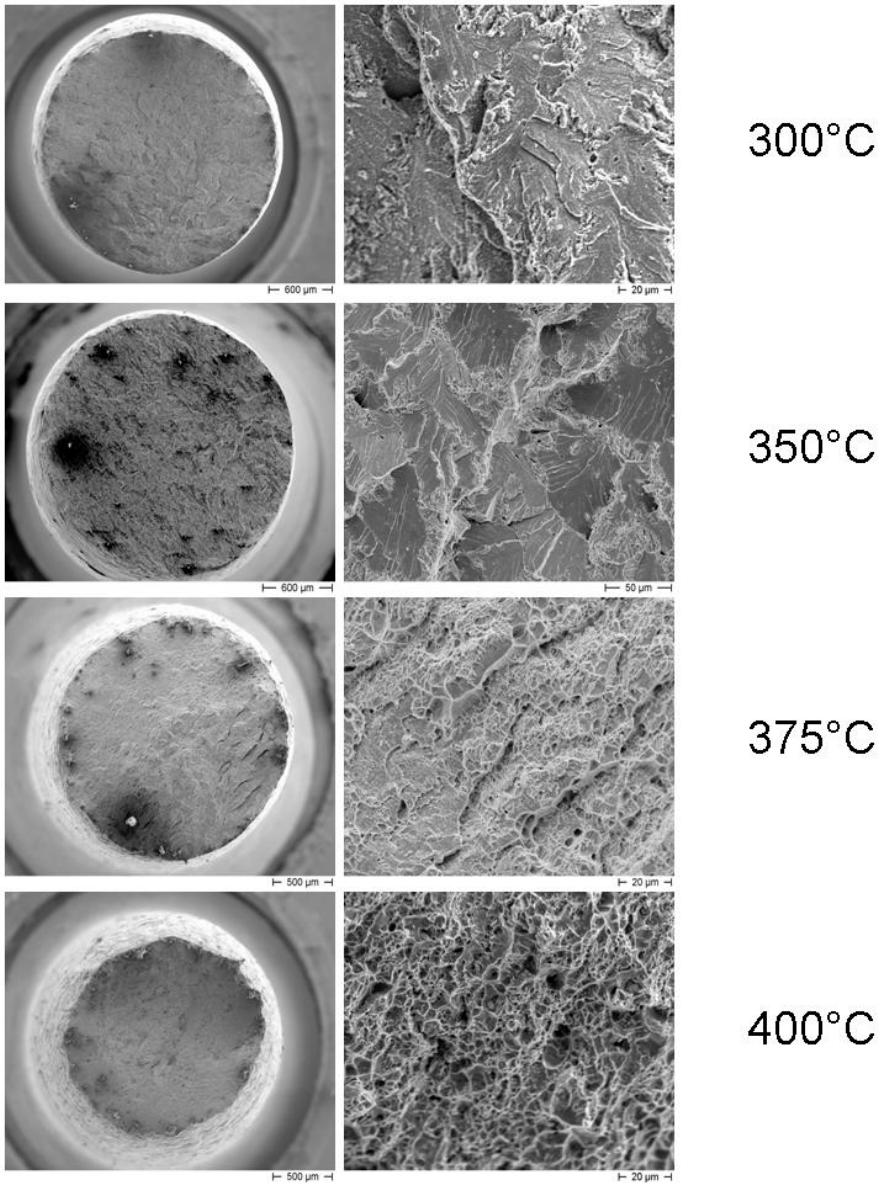

Figure 5.13: SEM examination of fracture surfaces of 2439 steel tested in liquid LBE environment as function of temperature.

2440 steel (13.52 wt% Cr; 0.51 wt% Ni; 4.8 wt% Si)

Unlike the bainitic 2439 steel, the 2440 steel has a ferritic microstructure due to the lowered M_s temperature. The 2440's ferritic microstructure consists of large grains as shown in Figure 2.24, typical for high silicon steels. Since the grain size was mentioned in section 1.3.1 of chapter 1 as one of the metallurgical parameters influencing LME, the behaviour of the 2440 steel in LBE and in gas was tested under identical conditions as this of the 2439 steel.
The tensile properties were examined at 350°C in both argon and hydrogen gas mixture and in liquid LBE environment. The applied strain rate was 5.10^{-6} s^{-1} as for the 2439 steel specimens. The resulting tensile curves are represented in Figure 5.14.

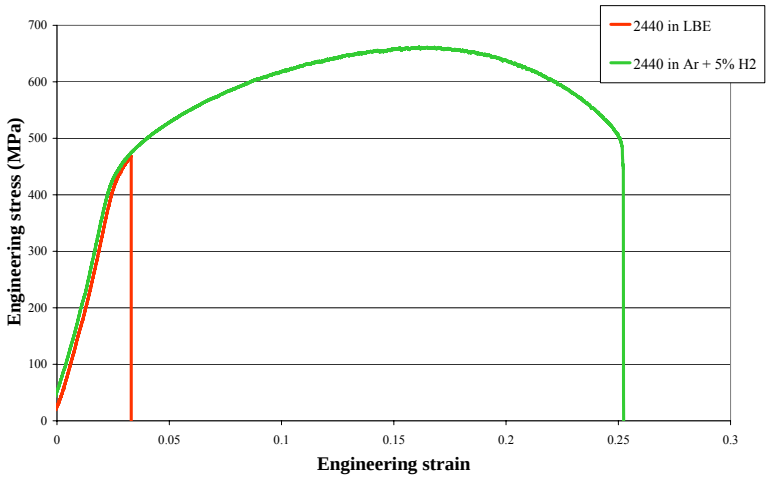

Figure 5.14: Tensile curves of 2440 steel tested at 350°C, 5.10^{-6} s^{-1} in Ar + 5% H_2 (green) and in LBE purged with Ar + 5% H_2 (red).

The green curve in Figure 5.14 is the result of the test in Ar + 5% H_2 environment whereas the red curve is the result of the test on 2440 under the same conditions of temperature and strain rate in liquid LBE. Although both curves coincide perfectly up to the moment of fracture, it is very obvious that the fracture behaviour is severely altered.
The yield stress remains the same for the 2440 steel tested in LBE, however after nearly any plastic deformation, the specimen suddenly breaks. Based on the tensile curve, the specimen did not show any necking nor does the curve show any signs of crack arrest.

The SEM examination of both specimens acknowledged the very large difference in fracture behaviour between the 2440 steel in both environments. The SEM images are depicted in Figure 5.15. Picture A shows the overview of the sample tested in Ar + 5% H_2 at 350°C. Although the sample shows a large amount of necking, the

plastic deformation is clearly non isotropic and the sample does not have the expected cup and cone shape. It has rather been broken in shear since the fracture surface is about at an angle of 45° to the tensile load. Nevertheless, the detail of its fracture surface shown in picture B of Figure 5.15 is fully dimpled with some precipitates in the bottom of the dimples.

The overview of the sample tested in liquid LBE (picture C) however does not show any necking and the fracture surface is perpendicular to the direction of the load. The upper part as well as the lower part of the fracture surface shown in picture C of Figure 5.15 are nearly entirely flat whereas the middle section of the fracture surface seems like it has some building blocks sticking out. This area was magnified and is shown in picture D. The small amount of dimples found in this area indicates there was some plastic deformation prior to fracture in this area. The sharp angled block like structures sticking out however indicate a cleavage type final fracture.

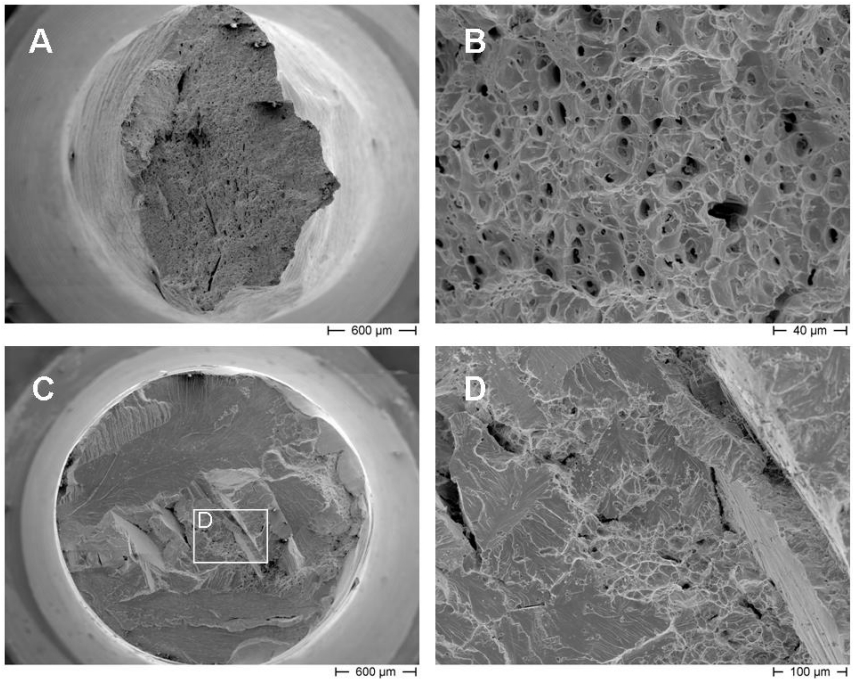

Figure 5.15: SEM examination of fracture surfaces of 2440 steel, tested in Ar + 5%H_2 and LBE at 350°C, using a strain rate of 5.10^{-6} s^{-1}. A: Overview of 2440 tested in Ar + 5% H_2 showing significant necking; B: Detail of fracture surface depicted in A, showing a fully dimpled surface indicating ductile fracture; C: Overview of 2440 steel tested in LBE purged with Ar + 5% H_2 showing no necking at all; D: Detail of the middle of the fracture surface depicted in C, showing some dimples on a surface which appears to have broken in cleavage mode.

It is clear from the previous observations that the embrittlement of the 2440 steel in liquid LBE environment is worse than this of steel 2439 under identical conditions. It would however be too simple to conclude that this is an effect of grain size. The chemical composition of the two steels is too different to attribute the difference in embrittlement to the difference in grain size.

Unfortunately we did not have sufficient material of the 2440 steel to perform the evaluation of the temperature dependence on the liquid metal embrittlement process. However, we were able to perform a constant load test on one single specimen.

As discussed in section 1.3.1 of Chapter 1, the constant load test has been used in previous work to examine the stress or deformation based principle of the LME phenomenon. As stated in Chapter 1, these LME studies found delayed failure of the material without any signs of penetration of the liquid metal into the bulk nor dissolution of the solid into the liquid metal.

Because of the limited amount of material, we decided to perform a constant load test above the stress level which initiated rapid fracture in LBE during the SSRT test. Since a constant load test can be regarded as an SSRT test with a very low strain rate, we assume that if there is any critical stress level below which LME does not occur, it will be the same for the SSRT test and the constant load test.

Therefore, the constant load test was started in Ar + 5% H_2 gas mixture and the desired load level (2750 N) was slowly applied. After the sample had been subjected to the constant load of 2750 N for approximately 2 days (45 hours), the LBE was introduced into the autoclave of the Limets 1 facility at a constant temperature of 350°C under controlled atmosphere. The introduction of the LBE caused a small fluctuation in the elongation of the specimen as indicated in Figure 5.16 above. After 17 hours at a load of 2750 N in LBE at 350°C the sample broke. The time – load curve of the last 4 minutes of the test are depicted in Figure 5.16 below.

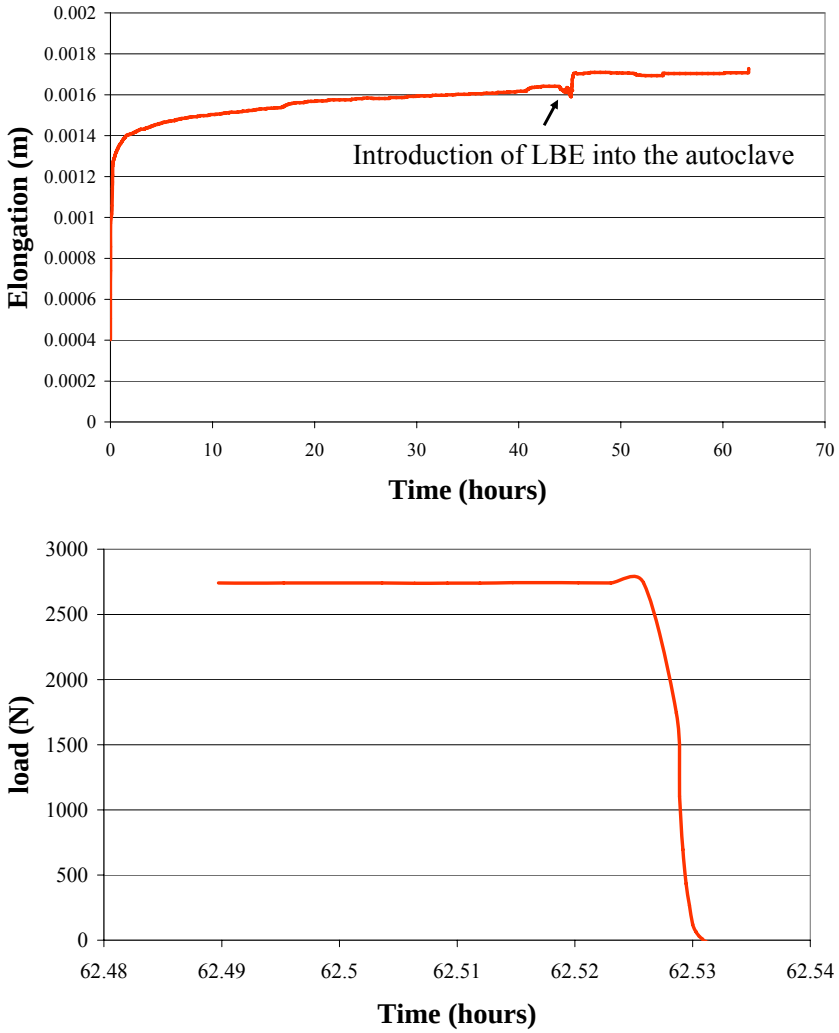

Figure 5.16: Constant load test of 2440 steel in LBE.
The specimen of 2440 steel was subjected to a load of 2750 N in Ar + 5% H_2 atmosphere at 350°C for approximately 48 hours prior to introducing the LBE into the autoclave. The LBE was introduced at a constant temperature of 350°C. (Above) Elongation as function of time with the indication of the introduction of the LBE; (Below) The load as function of time for the last 4 minutes of the test.

It is clear that even though the sample was loaded at a stress above the critical stress which led to sudden fracture in the SSRT test at a strain rate of 5.10^{-6} s^{-1} at 350°C, it took about 17 hours for the sample to break after it was submerged in the LBE as indicated by Figure 5.16 above. Furthermore, the fracture was not sudden as in the SSRT test but the load dropped gradually as can be seen in the lower curve of Figure 5.16 which displays the load during the last 4 minutes of the test.

This constant load test does not allow a simple conclusion as to whether the LME phenomenon in the high silicon 2440 steel is purely related to a threshold stress level rather than to a certain amount of plastic deformation. It is however clear that the reported delayed fracture as mentioned in Chapter 1 corresponds to the results we observed on the 2440 steel in LBE.

To further examine the LME effect which manifested as delayed fracture during the constant load test, we examined the fracture surface of the 2440 steel sample by SEM.

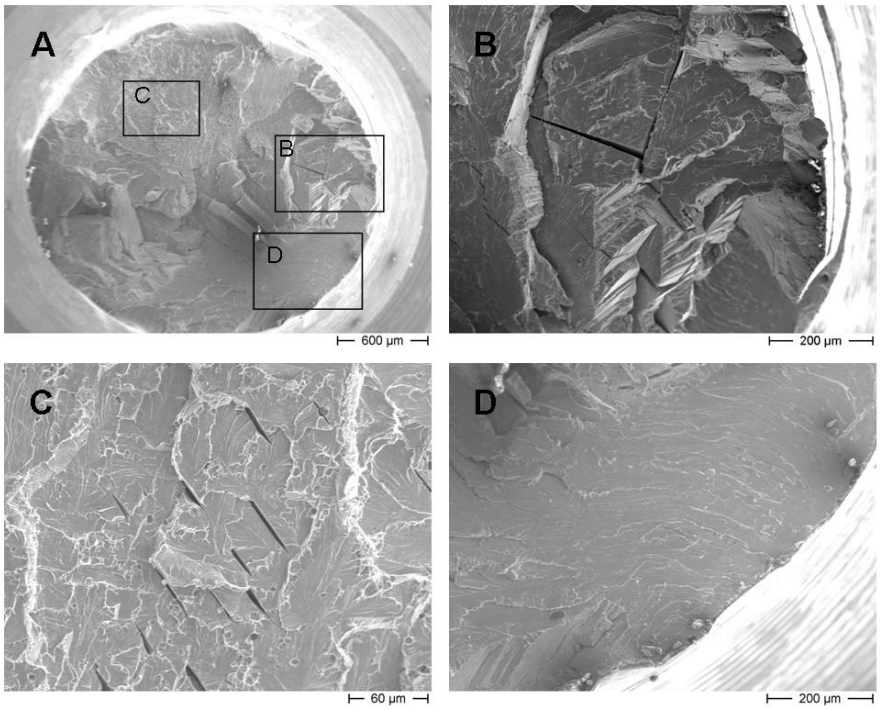

Figure 5.17: SEM examination of 2440 steel fractured after constant load (2750 N) test in LBE at 350°C. A: Overview of the fracture surface; B: Cleavage fracture in perpendicular directions, perpendicular to the fracture surface; C: Parallel oriented cleavage initiations perpendicular to the fracture surface; D: Surface initiation site (in the middle at the bottom).

The fracture surface overview (Figure 5.17A) shows several different features which support brittle failure by cleavage. However, strangely the cleavage fracture is not simply perpendicular to the tensile load as one might expect.
The fracture surface has some similarities with the fracture surface of the 2440 sample tested at 350°C as presented in Figure 5.15. For instance, the middle of the sample also shows the "building block" feature as seen in picture D of Figure 5.15

while the upper and lower areas of the fracture surface are more or less perpendicular to the tensile load and show a clear brittle fracture pattern with the typical river patterns.

In contrast to the SSRT tested sample however, the 2440 which cracked under constant load shows some very obvious cleavage cracks along certain crystallographic planes. Although these planes were not identified, it is clear that the perfect perpendicular nature of the cleavage cracks as shown in Figure 5.17B can not be coincidence. The same could be said about the parallel cleavage initiations in Figure 5.17C. These cleavage cracks are transgranular and at first sight nearly "atomically flat".
The complex nature of the fracture surface does however not allow drawing simple conclusions about the nature of the embrittlement process.

2441 steel (18.35 wt% Cr; 0.51 wt% Ni; 5.2 wt% Si)

The 2441 steel has a microstructure which at first sight very much resembles this of the 2440 steel. Both steels have a large grained ferritic microstructure as shown in section 2.1.4.3 of Chapter 2. The 2441 steel has a higher Si content (5.3 wt%) and a higher Cr content than the 2440 steel. Despite these higher alloying element concentrations, the hardness of the 2441 seems to be slightly lower than this of the 2440 steel as discussed in Chapter 2.

Also for the 2441 steel, the tensile properties were examined at 350°C in both argon and hydrogen gas mixture and in liquid LBE environment at a strain rate of 5.10^{-6} s^{-1}. The resulting tensile curves are depicted in Figure 5.18. The green curve was obtained by tensile testing in Ar + 5% H_2 environment while the red curve was obtained by tensile testing in liquid LBE environment.

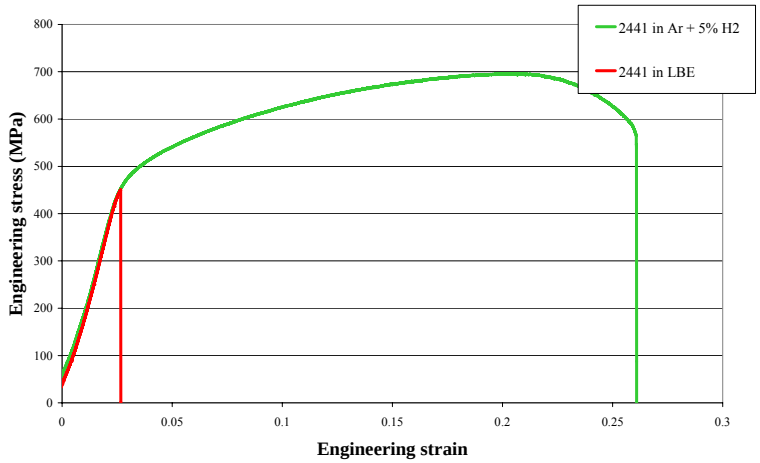

Figure 5.18: Tensile curves of 2441 steel tested at 350°C, 5.10^{-6} s^{-1} in Ar + 5% H_2 (green) and in LBE purged with Ar + 5% H_2 (red).

It is obvious from Figure 5.18 that the liquid metal environment has a very strong influence on the fracture behaviour of the 2441 steel. In the elastic region the two curves perfectly coincide however at about the yield point, the 2441 steel suddenly breaks in LBE. Since the macroscopic yielding criterion of 0.2% of plastic deformation does not say anything about the effective local plastic deformation in the material, it is difficult to state based on the tensile curves whether there was any plastic deformation of the material prior to fracture. It can be seen in the tensile curve of the test in liquid LBE environment that the fracture was sudden and without any crack arrest process taking place. Compared to the other high Si steels tested in LBE, it is clear that the 2441 steel is the most severely embrittled.

The fracture surfaces of both samples were examined using SEM. The pictures are shown in Figure 5.19. In picture A, an overview is shown of the fracture surface of the sample tested in gas environment. The sample shows significant necking but similar to the deformation of the 2440 steel tested in gas environment (Figure 5.15), the shape of the sample is not the conventional cup and cone shape but has an inclination of about 45° to the tensile load. This points to plastic deformation in shear mode. The detailed image of picture B shows the fracture surface is fully dimpled and thus the fracture was fully ductile.

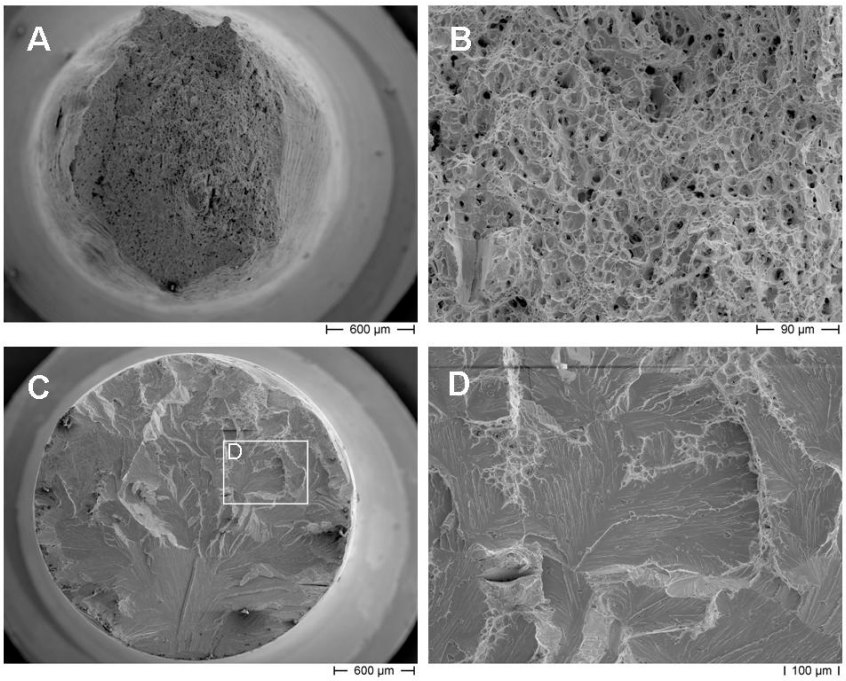

Figure 5.19: SEM examination of fracture surfaces of 2441 steel, tested in Ar + 5%H_2 and LBE at 350°C, using a strain rate of 5.10^{-6} s^{-1}. A: Overview of 2441 tested in Ar + 5% H_2 showing significant necking; B: Detail of fracture surface depicted in A, showing a fully dimpled surface indicating ductile fracture; C: Overview of 2441 steel tested in LBE purged with Ar + 5% H_2 showing no necking at all; D: Detail of the fracture surface depicted in C, showing some dimples on a surface which appears to have broken in cleavage mode, showing significant river patterns.

Image C in Figure 5.19 is the overview of the 2441 steel sample tested in liquid LBE environment. The sample does not show any necking and the fracture surface is perpendicular to the tensile load. The brittle fracture initiation site seems to have been at the surface of the sample at the very bottom of Figure 5.19C because the river patterns seem to fan out from there. The fracture surface does not have any dimples on the lower part of the sample, near the initiation site. Picture D is a detail of the upper side of the fracture surface shown in picture C and does have a relatively small amount of dimples. The vast amount of the surface is however fully brittle showing the characteristic river patterns.

5.1.3.2 SSRT tests of austenitic Si enriched steels

The austenitic Si enriched steels we studied are the 2442 steel provided by Los Alamos National Laboratory and the L413 steel and A078 steel, provided by LISm, Ghent University.

2442 steel (18.25 wt% Cr; 14.16 wt% Ni; 5.2 wt% Si)

Due to its high nickel content, the 2442 steel has an austenitic microstructure. This experimental steel grade was produced in the frame of a corrosion improvement study at LANL but due to budget cut backs in their LBE programme, this particular grade was never tested for its corrosion resistance in LBE. Nevertheless, its tensile properties were tested at 350°C in both gas environment (Ar + 5% H_2) and in liquid LBE purged with Ar + 5% H_2 gas at a strain rate of 5.10^{-6} s^{-1}. The tensile curves are presented in Figure 5.20.

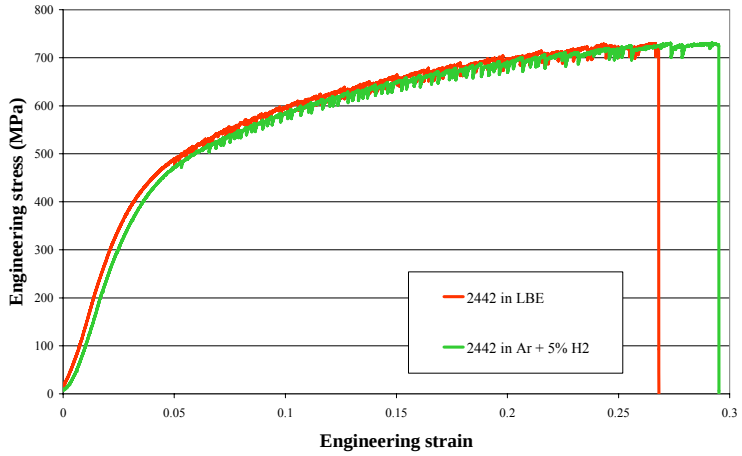

Figure 5.20: Tensile curves of 2442 steel tested at 350°C, 5.10^{-6} s^{-1} in Ar + 5% H_2 (green) and in LBE purged with Ar + 5% H_2 (red).

In contrast with the ferritic Si enriched steels, discussed in section 5.1.3.1 above, the fracture behaviour of the austenitic 2442 steel is not drastically altered by the liquid LBE environment. Both tensile curves coincide up to the point of fracture. The 2442 material shows a significant amount of work hardening but no necking.

The shape of the tensile curve with its sharp, relatively small, fluctuations points to the creation of small cracks and voids in the material during deformation long before the final point of fracture. These fluctuations in the curve start already just after the yield stress.

Despite the difference in total elongation between the sample tested in gas environment and the one tested in LBE, this relatively small difference might be within the experimental scatter for this particular material. More data would be needed to make any conclusions on the effect of the liquid metal environment.

The fracture surfaces of both specimens were examined using SEM and the resulting images are depicted in Figure 5.21. Picture A and picture C in Figure 5.21 show the overview of the sample of 2442 steel tested in respectively gas and liquid metal environment. Both specimens have no necking as expected from the tensile curves in Figure 5.20. The fracture surfaces of both specimens are perpendicular to the loading direction and relatively geographically flat. No initiation sites can be distinguished.

The details of the fracture morphology shown in pictures B and D reveal what appear to be dimples. However, these dimples are rather cornered and the fracture morphology has a strong resemblance to what is called micro-brittleness. This is in agreement with the shape of the tensile curves showing small, sharp stress fluctuations and no necking.

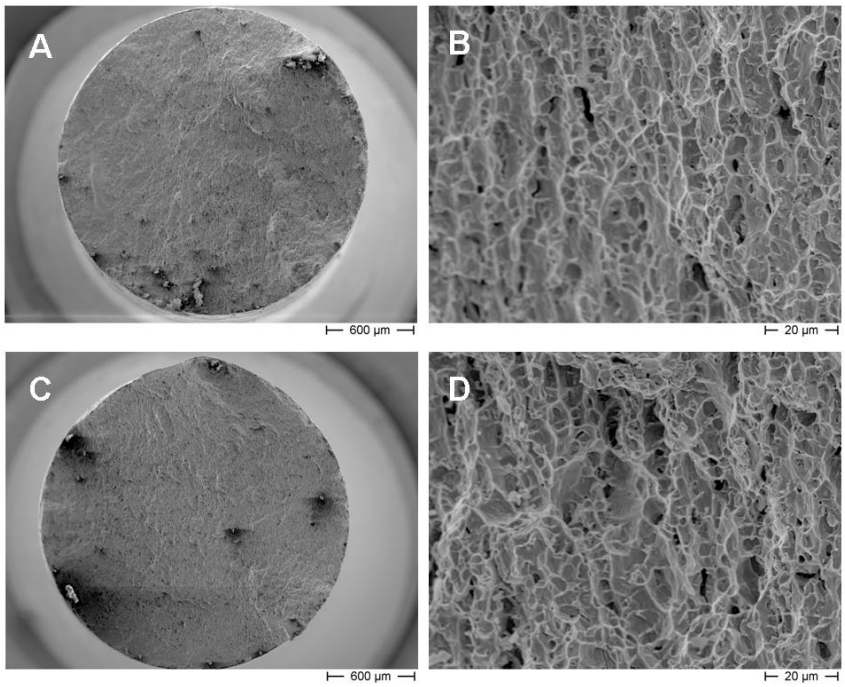

Figure 5.21: SEM examination of fracture surfaces of 2442 steel, tested in Ar + 5%H_2 and LBE at 350°C, using a strain rate of 5.10^{-6} s^{-1}. A: Overview of 2442 tested in Ar + 5% H_2, showing no necking; B: Detail of fracture surface depicted in A; C: Overview of 2442 steel tested in LBE purged with Ar + 5% H_2 showing no necking; D: Detail of the fracture surface depicted in C. The seemingly cornered dimples on a sample which did not show any necking indicates the material failed by micro-brittleness in both environmental conditions.

L413 steel (18.4 wt% Cr; 8.5 wt% Ni; 1.0 wt% Si)

Unlike the previously discussed high silicon steels, the experimental L413 steel, which is a variation of the 304 stainless steel having an addition of Si, was not developed to examine its corrosion resistance in flowing LBE. This particular steel was developed in the frame of the PhD of Xiaoqiang Li to examine the influence of the stacking fault energy (SFE) on the deformation of steel after irradiation. The L413 steel is the reference low SFE steel in his work. This means that dislocations in this steel can easily form partial dislocations and cross slip to other slip planes to avoid pinning by microstructural defects such as precipitates. We will not go too much into detail in this work however it is important to note that the ability of a material to easily form partial dislocations and cross slip to avoid pinning promotes ductility and strongly lowers the material's tendency to cleavage.

The L413 steel was examined by tensile testing at a strain rate of 5.10^{-6} s^{-1} at 350°C in both liquid LBE and argon gas. The tensile curves are depicted in Figure 5.22. The L413 steel did not undergo any influence of the environment since both tensile curves perfectly coincide.

The fracture surfaces of both samples also look very much alike. The specimens show a significant amount of necking but broke in shear since the fracture surface does not have the cup and cone shape but is inclined at an angle of about 45°C to the loading direction. Both fracture surfaces are fully dimpled as can be seen in the detail images, depicted in Figure 5.23.

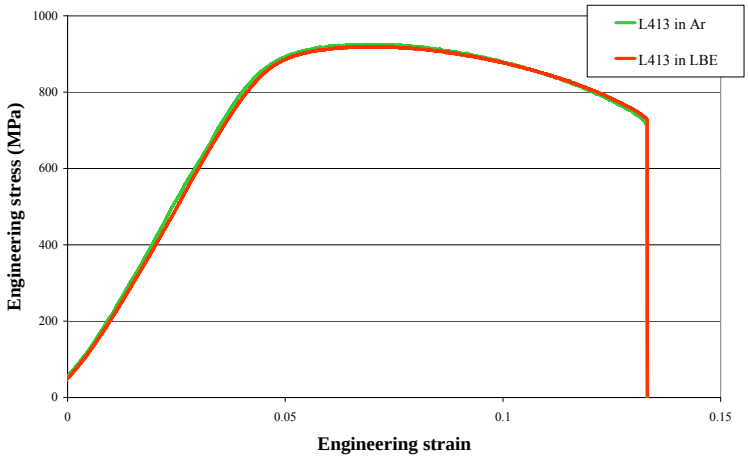

Figure 5.22: Tensile curves of L413 steel tested at 350°C, 5.10^{-6} s^{-1} in Ar (green) and in LBE purged with Ar (red).

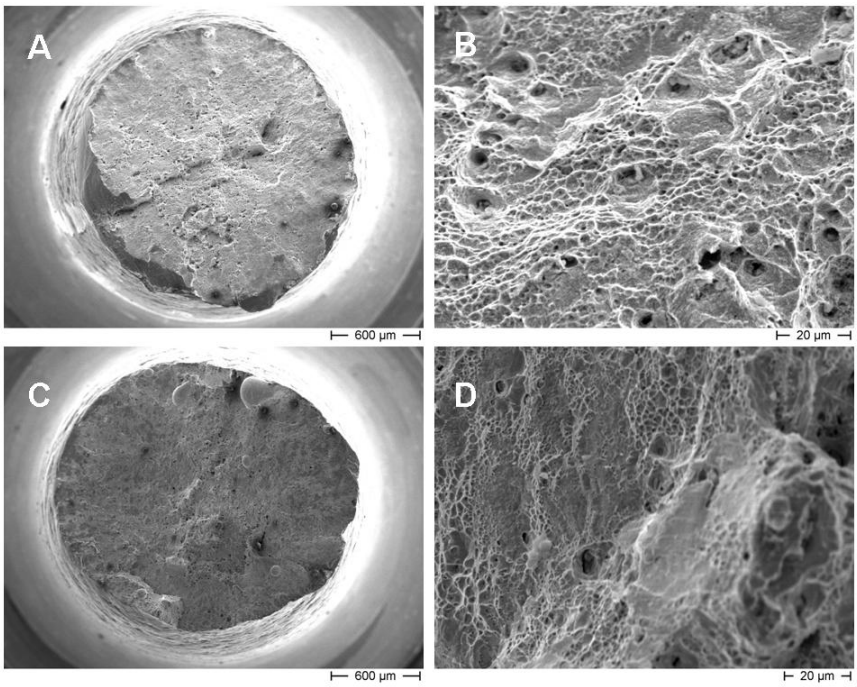

Figure 5.23: SEM examination of fracture surfaces of L413 steel, tested in Ar and LBE at 350°C, using a strain rate of 5.10^{-6} s^{-1}. A: Overview of L413 tested in Ar; B: Detail of fracture surface depicted in A; C: Overview of L413 steel tested in LBE purged with Ar; D: Detail of the fracture surface depicted in C.

A078 steel (19.7 wt% Cr; 9.98 wt% Ni; 4.85 wt% Si)

Although the A078 steel very probably does have an increased corrosion resistance to flowing LBE due to its high Cr and Si content, this steel was not developed for this purpose. The A078 steel was used in the frame an irradiation assisted stress corrosion cracking (IASCC) in water study. The high chromium and high silicon content made it interesting to include this material in our study. Furthermore, the tendency to hydrogen embrittlement of the A078 steel made it possible to compare two different types of environmental assisted cracking in the same steel.

The tensile curves resulting from tests at 350°C at a strain rate of 5.10^{-6} s^{-1} in various environments are depicted in Figure 5.24.

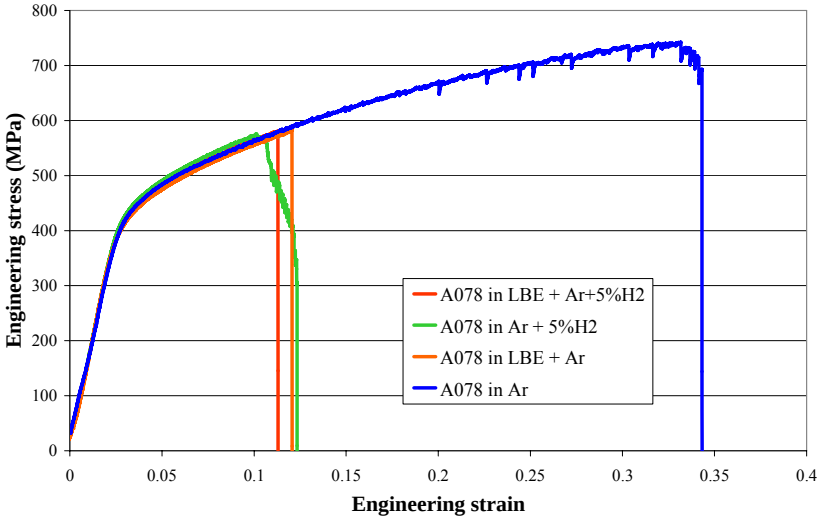

Figure 5.24: Tensile curves of A078 steel tested at 350°C, 5.10^{-6} s^{-1} in Ar (blue), in Ar + 5% H_2 (green), in LBE purged with Ar + 5% H_2 (red) and in LBE purged with Ar (orange).

For the A078 steel, the blue curve in Figure 5.24 should be taken as the reference curve since this steel is prone to hydrogen embrittlement. The green curve resulting from tensile testing A078 steel in a gas mixture of argon and hydrogen shows significant embrittlement compared to the blue curve which resulted from testing in pure argon.

None of the testing conditions show a significant amount of necking. However, it is clear from Figure 5.24 that the environment has a very strong influence on the fracture behaviour of A078 steel. The environment does not seem to change the bulk properties of the steel since all curves nicely coincide but it does strongly influence the amount of total elongation.

The embrittlement due to the hydrogen gas environment and the liquid metal environment seems to have a very similar effect since the specimens break after approximately the same amount of deformation or at the same stress level. The fracture process itself seems slightly different based on the tensile curves.
The green curve resulting from testing in argon and hydrogen gas mixture does not immediately show a steep drop in load but gradually affects the material. This could be due to the fact that the adsorption of hydrogen at the surface is the rate determining step.
In LBE purged with argon gas, there is a crack arrest based on the tensile curve although it is only very limited.

The strongest embrittlement takes place in the combined embrittling environment of liquid LBE purged with Ar + 5% H_2 gas. Which type of embrittlement is more predominant is difficult to say based on the tensile curves alone.

Therefore, the fracture surfaces of the specimens tested in the four different environments were examined by SEM. The results are depicted in Figure 5.25.

The sample tested in argon gas environment does not show any necking but as the detailed image in Figure 5.25 shows, the fracture surface is dimpled. Moreover, the fracture surface of the sample tested in argon gas strongly resembles the fracture surface of the 2442 steel samples.

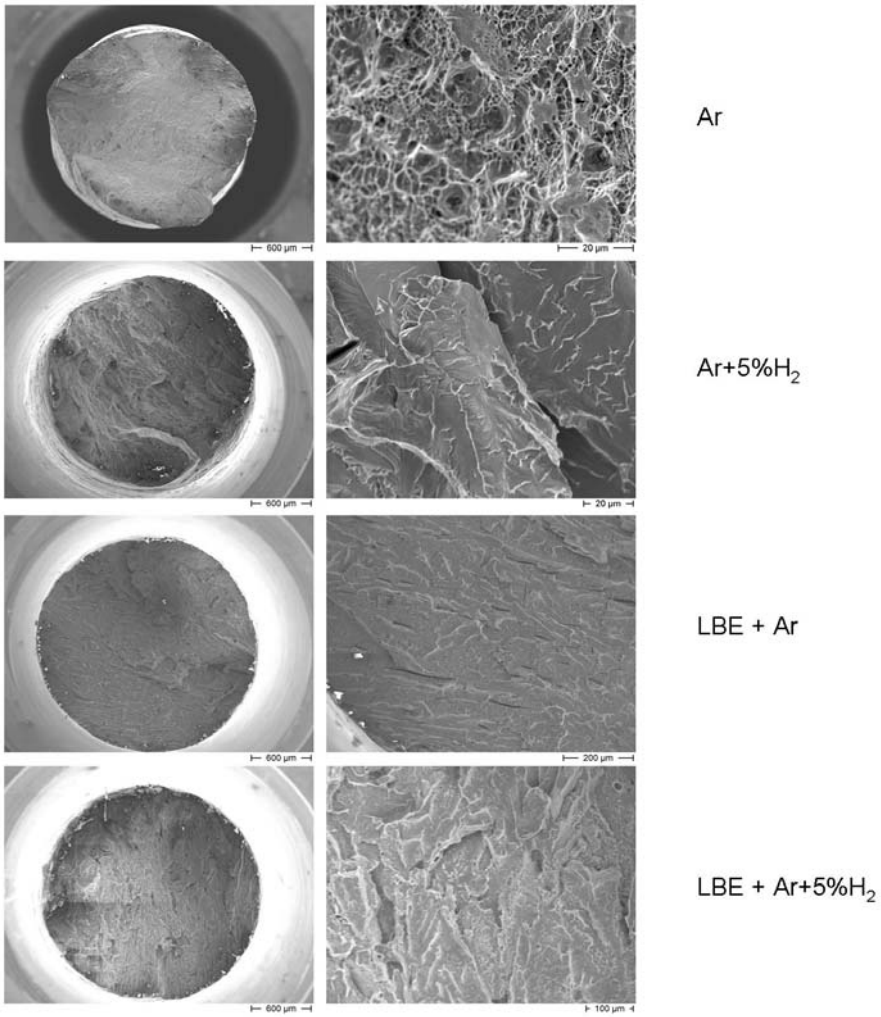

Figure 5.25: SEM examination of the fracture surfaces of A078 steel tested in various environments at 350°C, 5.10^{-6} s^{-1}.

The samples of A078 tested in argon and hydrogen gas mixture, in LBE purged with argon and in LBE purged with a mixture of argon and hydrogen are all three fully brittle without any necking. The fracture surfaces do not show any obvious initiation sites and the detailed morphology of the surfaces look very much the same.

Although no observations have been made of lead or bismuth penetrating the bulk of any of the studied materials while penetration of hydrogen into the bulk has been often reported in hydrogen embrittlement studies, the fracture surfaces are very similar.
The available data is too limited to make any strong conclusions but both environmental cracking phenomena seem to have strong similarities in their influence on the fracture behaviour.

5.2 PLANE STRAIN FRACTURE TOUGHNESS TESTS

As indicated before, the tensile tests should be considered as exploratory tests to examine the susceptibility to liquid metal embrittlement. However, once the susceptibility to LME has been established, it is needed to quantify the embrittlement. For this reason, we needed to examine the possibility of performing plane strain fracture toughness measurements in LBE and compare them to tests performed in air.

To assess the fracture toughness of the austenitic 316L steel and the T91 ferritic-martensitic steel in air and in LBE, we applied elastic-plastic fracture mechanics (EPFM) tests because of the significant amount of plastic deformation during testing at elevated temperatures. For the determination of fracture toughness values, J_{Ic} tests were executed.

The specimens used for the J_{Ic} tests, are disc-shaped compact tension specimens (DCT). The dimensions of the specimen are displayed in Figure 5.26. The specimens are smaller than recommended by the standard ASTM E-1820, but these small dimensions were necessary for future verification of irradiated specimen results. The actual testing of the irradiated DCT specimens will be performed in the future.

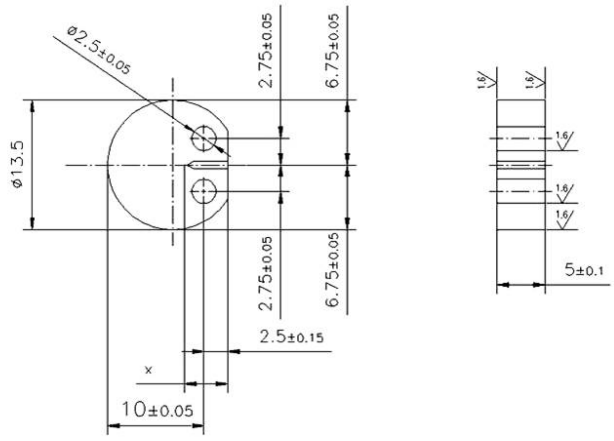

Figure 5.26: Dimensions (mm) of disc shaped compact in tension specimen (DCT).

After polishing and measuring, the specimens were pre-cracked by fatigue to a crack length between $a = W/2$ and $a = W/2 - 0.5mm$. After precracking, the specimens were side grooved, using a fraise with a radius of 0.1 mm and an angle of 60°. The side grooves were milled 0.5 mm deep, resulting in a thickness reduction of

0.20 *B*, which is recommended by ASTM E1820. The root of the side groove is located along the specimen centreline.

The difficulty in measuring the plane strain fracture toughness in LBE was that none of the conventional online methods to measure the crack advancement could be used. For accurate application of the unloading compliance method in LBE, a clip gauge was needed. However, the glue holding the strain gauge would dissolve in LBE. Furthermore, the conducting nature of the LBE disturbed the signal. The potential drop method proved impossible to apply because the conductivity difference between the LBE in an advancing crack tip and the conductivity of a massive specimen was insufficiently large. Therefore, new or alternative methods for measuring plane strain fracture toughness had to be developed. These methods were discussed section 3.1.3.2 of Chapter 3.

5.2.1 Fracture toughness of T91

Fracture toughness tests of T91 steel were performed at 200 and at 300°C. These temperatures were chosen because 200°C is foreseen to be the stand-by maintenance temperature of the MYRRHA facility and 300°C would be the lower limit of the operational temperature of MYRRHA. Furthermore, based on findings of liquid metal embrittlement, discussed in section 1.3.1 on the influence of temperature, the LME effect is expected to be most severe at the lower temperatures.

In literature on LME in LBE, embrittlement has been seen in tensile tests at 300°C [53],[57] but results at 200°C are scarce and do not show embrittlement [21]. The majority of the tests were performed using a displacement rate of 0.25 mm/min. A few tests were performed at 2.5 mm/min and at 0.025 mm/min.
For a clear overview of the performed tests, the test matrix for fracture toughness testing of T91 is presented in Table 5.1.

Table 5.1: Test matrix of performed J_{Ic} tests on T91 steel

	0.025 mm/min		0.25 mm/min		2.5 mm/min	
	200°C	300°C	200°C	300°C	200°C	300°C
Air	-	-	5	5	-	-
LBE, oxygen saturated	2	2	5	5	2	2
LBE, controlled oxygen (10^{-6}-10^{-7} wt%)	-	-	5	5	-	-

5.2.1.1 Fracture toughness tests of T91 in air

As mentioned before, tests were performed at 200 and at 300°C. For tests in air, there was no problem to use a clip gauge for UC nor to apply the PD technique for fracture toughness analysis. This allowed validating the possible application of the proposed normalisation methods by comparison between the traditional methods based on the online measurement of crack advancement and the normalisation methods based on initial and final crack length and the force-displacement data.

The load-CMOD curves recorded during the tests of T91 in air are shown in Figure 5.27. On the top, the curves resulting from the tests at 200°C are represented, whereas the load-CMOD curves obtained at 300°C are depicted on the bottom in Figure 5.27. The used specimen numbers are indicated in the legend of the figure.

The "T" in the specimen numbering refers to T91 and the 11-4-xx refers to the position of the tested material in the original hot rolled plate.

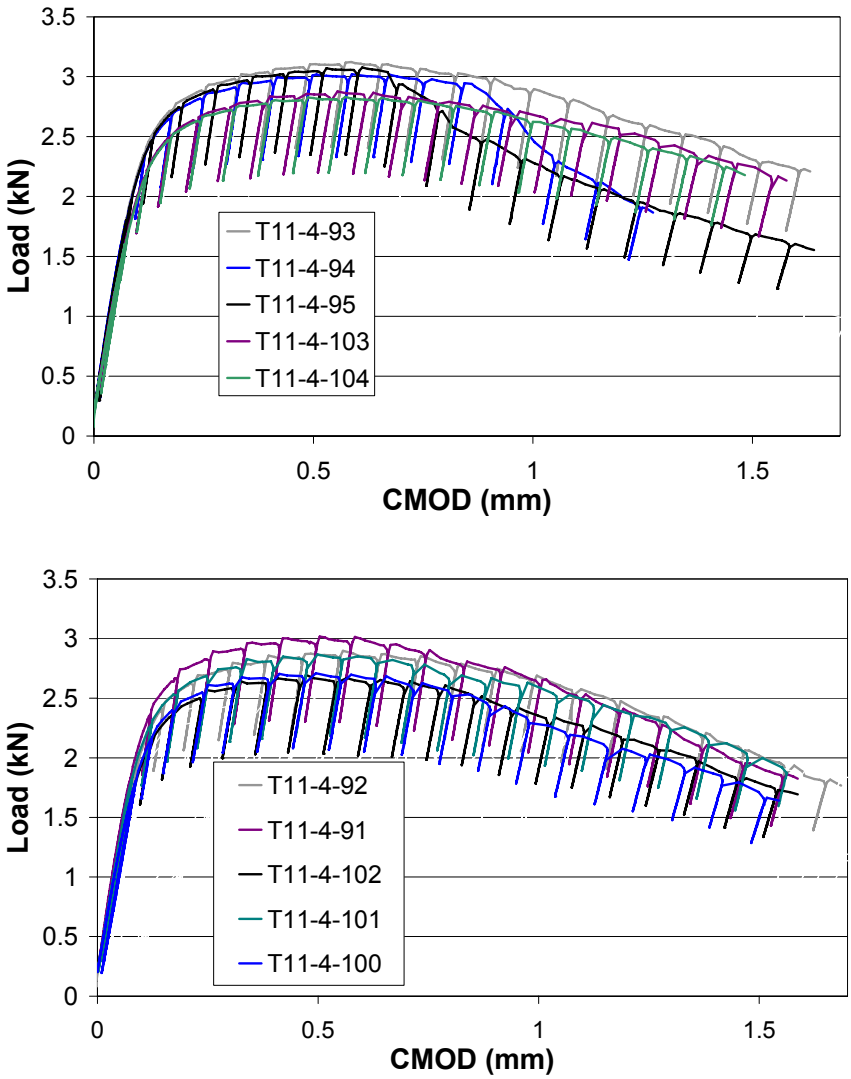

Figure 5.27: Load-CMOD curves of J_{Ic} tests of T91 in air; Above: 200°C, 0.25 mm/min; Below: 300°C, 0.25 mm/min.

For specimen T11-4-94 and T11-4-95, tested at 200°C, there is a visibly steeper decrease in the load-CMOD curve in comparison with the other curves. This is attributed to local plastic instability or local cleavage fracture. SEM examination of these two samples revealed local brittle fracture areas. The fracture appearance indicates local brittle failure however no clear cause of the local brittleness could be

found. The SEM pictures of sample T11-4-95 are depicted in Figure 5.28 along with the digital overview picture.
Since it was unclear what caused the local brittle fracture of these two specimens, it was decided not to include them in the determination of the average fracture toughness of T91 steel at 200°C. They will also not be included in the comparison of the fracture toughness of T91 steel in air and in LBE. By doing so, we might over estimate the fracture toughness of T91 in air at 200°C, resulting in a conservative conclusion on the possible LBE embrittlement effect.

In contrast with the observed local brittle behaviour at 200°C, there is no faster decrease in load when comparing all load-CMOD curves at 300°C, as can be seen on the right in Figure 5.27.

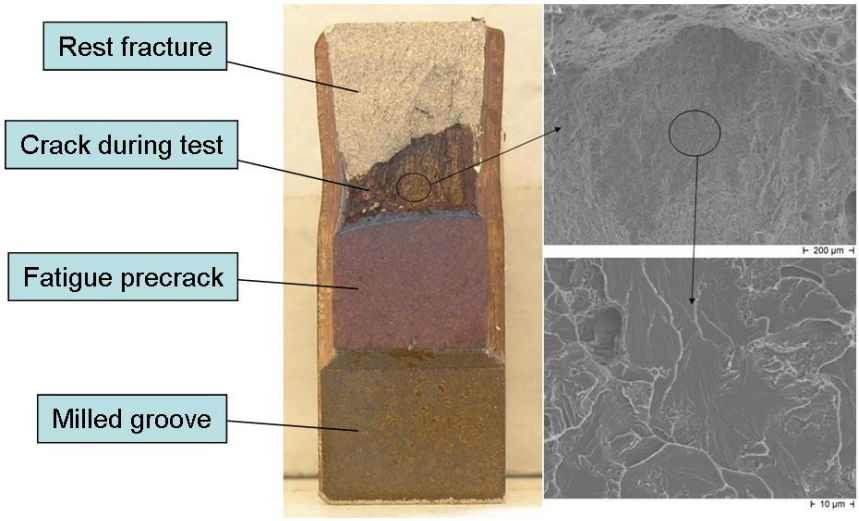

Figure 5.28: Digital and SEM pictures of the crack surface of specimen T11-4-95, tested in air at 200°C, 0.25 mm/min.

Using the load-CMOD data of the tests performed at 200°C, presented in Figure 5.27 on the left, in combination with the digital pictures of the cracked specimens after testing in air, we could calculate the *J-R* curve using all the suggested analysis methods. The resulting *J-R* curves for specimen T41-4-103 are depicted in Figure 5.29. It is clear that all analysis methods fall inside the expected ± 15% scatter of fracture toughness test analysis. The same appeared to be the case when all methods were applied to the tests performed at 300°C. This showed that the proposed normalisation methods are in good agreement with the conventionally used methods based on online crack advancement monitoring when testing T91 in air at 200 and 300°C.

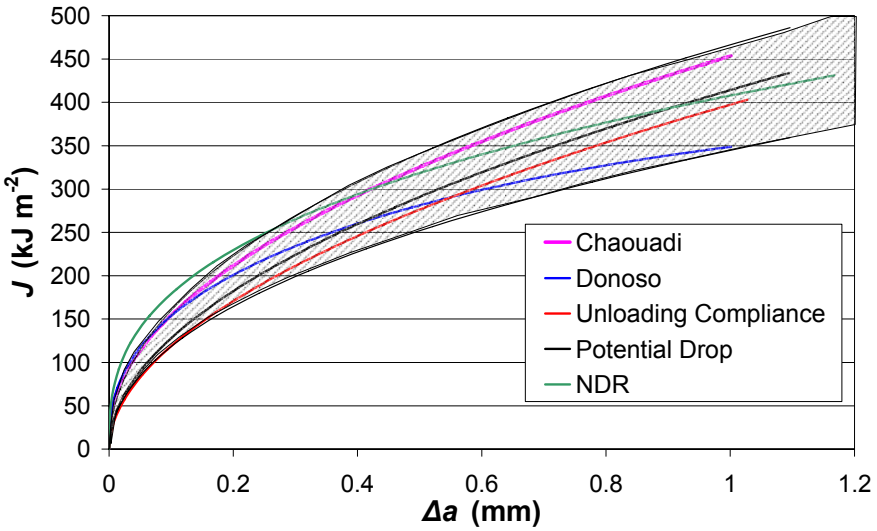

Figure 5.29: *J-R* curves of T91 specimen T41-4-103, tested at 200°C, calculated by potential drop (black), unloading compliance (red), NDR (green), Chaouadi (magenta) and Donoso (Blue) methods.

For comparison of the obtained results for all tested T91 specimens at 200°C in air, we present the calculated J_Q values in Table 5.2. The same is done for the tests on T91 performed at 300°C in Table 5.3.

Table 5.2: J_Q values of T91 specimens tested in air at 200°C, calculated by unloading compliance (UC), potential drop (PD), NDR, Chaouadi and Donoso methods.

Specimen code	UC	PD	NDR	Chaouadi	Donoso
	J_Q (kJ/m²)	J_Q (kJ/m²)	J_Q (kJ/m²)	J_Q (kJ/m²)	J_Q (kJ/m²)
93	260.5	237.6	272.2	266.5	230.1
103	253.7	273.4	313.4	278.8	244.8
104	205.8	235.2	219.1	251.9	215.8
average	**240.0**	**248.7**	**268.2**	**265.7**	**230.2**
σ	18.86%	13.53%	29.90%	8.52%	9.17%
average UC and PD		244.4			
	+15%	281.0			
	-15%	207.7			

Table 5.3: J_Q values of T91 specimens tested in air at 300°C, calculated by unloading compliance (UC), potential drop (PD), NDR, Chaouadi and Donoso methods.

Specimen code	UC	PD	NDR	Chaouadi	Donoso
	J_Q (kJ/m²)	J_Q (kJ/m²)	J_Q (kJ/m²)	J_Q (kJ/m²)	J_Q (kJ/m²)
91	229.3	213.8	234.1	221.8	237.8
92	293.6	227.6	267.9	231.5	227.7
100	201.9	185.7	188.4	199.6	196.1
101	209.9	209.9	242.0	234.1	213.0
102	220.6	219.6	221.5	225.6	205.9
average	**215.4**	**207.3**	**221.5**	**220.3**	**213.2**
σ	9.30%	11.55%	18.30%	11.42%	13.79%
average UC and PD		211.3			
	+15%	243.0			
	-15%	179.6			

Specimen T41-4-92 resulted in erroneous values after correct application of the UC and PD analysis methods. This is often observed in fracture toughness analysis. For this reason specimen code 92, presented in Table 5.3 should not be regarded to compare the traditional methods to the normalisation methods.

It should however be noted that for the calculation of the normalisation methods presented above, we used the CMOD data recorded by the clip gauge. However, as mentioned before, it was not possible to use a clip gauge during tests in liquid metal environment. The above presented results show good correlation with the conventional methods but do not prove that the suggested methods are applicable without clip gauge or in liquid metal environment.

For fracture toughness measurements in liquid metal environment we had to resort to the use of the test bench stroke signal. This is the displacement as recorded by the machine's LVDT sensor. In contrast with the clip gauge's CMOD signal, which measures only the displacement of the specimen, the stroke signal comprises the compliance of the entire load train.
To compensate for this compliance error, we used a linear compliance correction model. The compliance correction model is actually a mathematical correction to have the elastic part of the curve based on the CMOD (compliance of the specimen) coincide with the elastic part of the curve based on the stroke signal of the test bench (compliance of the entire load train).

During the tests in air, both the displacement from the machine and CMOD from the clip gauge were monitored. By calculating x and y in the following equation:

$$(Displacement - CMOD) \cdot x + y = Load \quad \textbf{(5.1)}$$

a linear model for the tested specimen is created. By doing so for each of the specimens tested at a given temperature and then calculating the average of the calculated x and y values, a linear compliance correction model was determined.

The displacement recorded during the tests in LBE, at the same temperature, can now be used to indirectly calculate the CMOD (by approximation).

Table 5.4 shows the values calculated for the specimens at 200°C. Figure 5.30 compares the load-displacement (stroke data) curve, the load-CMOD curve and the curve calculated by the compliance correction model for 200°C. As can be seen in the figure, the approximation of the CMOD by the model is quite good. Similar correspondence was observed when applying the compliance correction model at 300°C, using the compliance correction parameters determined for the tests at 300°C.

Table 5.4: Values for the compliance correction model at 200°C

specimen	x (kN/mm)	y (kN)
93	10.879	-0.4405
103	9.3978	0.1874
104	9.403	-0.3
Average	**9.893**	**-0.138**

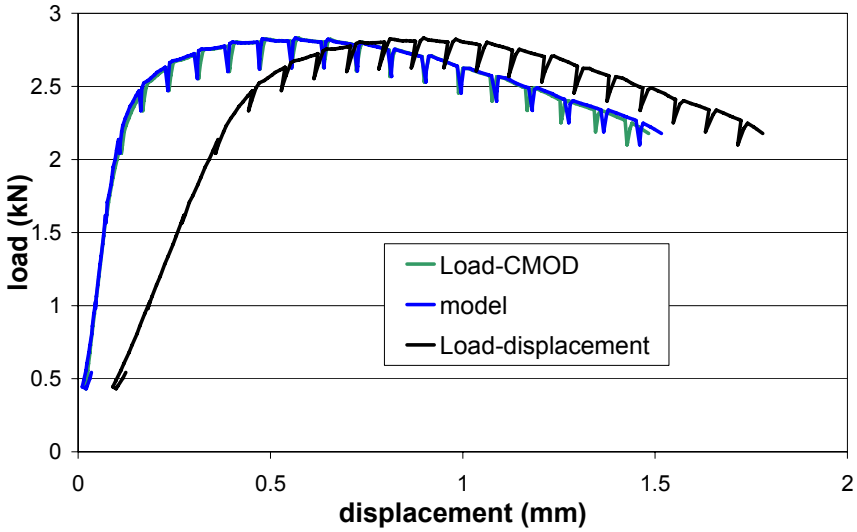

Figure 5.30: Comparison between load-CMOD curve, load-displacement curve and curve corrected by compliance correction model at 200°C.

In [143] NDR analysis was performed on PCCv specimens (precracked charpy V-notch specimens) using both CMOD and stroke as displacement signal. It was concluded that it is feasible to avoid the use of a clip gauge when using the NDR technique on PCCv specimens.

The Chaouadi method and Donoso method were applied to both stroke and compliance correction model. When compared to the results received by the use of the CMOD data, the effect of using stroke or compliance correction model could be determined. The results are summarised in Table 5.5 for the Chaouadi method and in Table 5.6 for the Donoso method.

Table 5.5: Comparison of Chaouadi method results using CMOD, stroke and compliance correction model at 300°C.

Specimen code	Chaouadi method (CMOD)			Chaouadi method (stroke)			Chaouadi method (model)		
	J_Q (kJ/m²)	K_{JQ} (MPa√m)	T_M (MPa)	J_Q (kJ/m²)	K_{JQ} (MPa√m)	T_M (MPa)	J_Q (kJ/m²)	K_{JQ} (MPa√m)	T_M (MPa)
91	221.84	217.30	289.59	242.39	227.14	319.40	226.92	219.78	294.98
92	231.46	221.96	306.45	244.39	228.08	319.26	229.71	221.12	297.70
100	199.55	206.10	272.20	232.78	222.60	306.18	212.36	212.61	292.34
101	234.13	223.24	306.89	262.75	236.49	340.33	243.71	227.76	321.22
102	225.61	219.14	288.35	259.36	234.96	332.05	245.25	228.48	310.62
average	222.52	217.55	292.70	248.33	229.85	323.44	231.59	221.95	303.37
σ	12.27%	6.09%	12.96%	11.16%	5.16%	11.76%	12.07%	5.82%	10.91%

As a result of using stroke instead of CMOD in the Chaouadi method, the average value of J_Q is increased by about 12%. When comparing CMOD and compliance

corrected results in Table 5.5, the differences are rather small. The model results remain slightly higher than the CMOD based results however the error is much smaller than without compliance correction. This is also visible when looking at the *J-R* curves, shown in Figure 5.31.

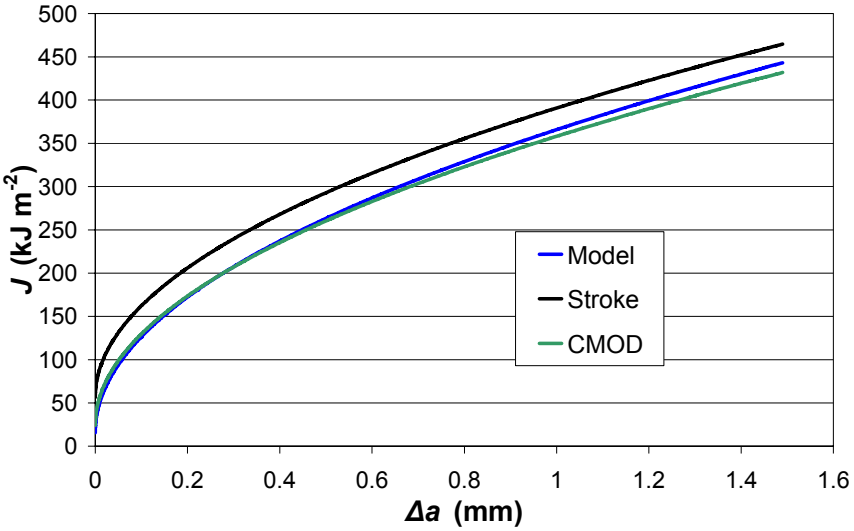

Figure 5.31: Comparison of the J-R curves resulting from the Chaouadi method using CMOD, stroke and model data.

Table 5.6: Comparison of Donoso method results using CMOD, stroke and compliance correction model at 300°C.

Specimen code	Donoso method (CMOD)			Donoso method (stroke)			Donoso method (model)		
	J_Q (kJ/m²)	K_{JQ} (MPa√m)	T_M (MPa)	J_Q (kJ/m²)	K_{JQ} (MPa√m)	T_M (MPa)	J_Q (kJ/m²)	K_{JQ} (MPa√m)	T_M (MPa)
91	237.80	224.98	171.88	265.08	237.54	235.40	222.61	217.68	208.24
92	227.72	220.16	207.88	252.62	231.89	230.04	226.45	219.55	207.18
100	196.11	204.31	191.21	257.16	233.96	231.09	214.20	213.53	199.73
101	213.00	212.93	215.73	267.74	238.73	254.09	226.27	219.46	219.34
102	205.88	209.34	198.65	266.97	238.38	248.00	230.41	221.46	222.05
average	216.10	214.35	197.07	261.91	236.10	239.72	223.99	218.34	211.31
σ	14.96%	7.41%	15.08%	5.98%	2.70%	9.61%	5.48%	2.69%	8.25%

When using stroke data as input for the Donoso method, the average J_Q value is 21% higher than the value resulting from the use of CMOD data (Table 5.6). When using the compliance correction model however, the overestimation of the J_Q value is much smaller.

It can be concluded that when the Donoso method is used with stroke data as input, the compliance correction model should be applied to obtain valuable results. This is

a logical conclusion when looking at the Donoso method. The measured force-CMOD curve has to be fitted to the calculated curve, using the common format equations (see 3.1.3.2.3). When the stroke data is used, the initial slope of the measured curve is much flatter than the one of the calculated curve, so a good fit is not possible (Figure 5.32).

Based on the previous findings, we could apply the proposed normalisation methods to fracture toughness tests of T91 in LBE under the assumption that sufficient toughness would be present to macroscopically assume ductile tearing. This will be discussed in the following two sections.

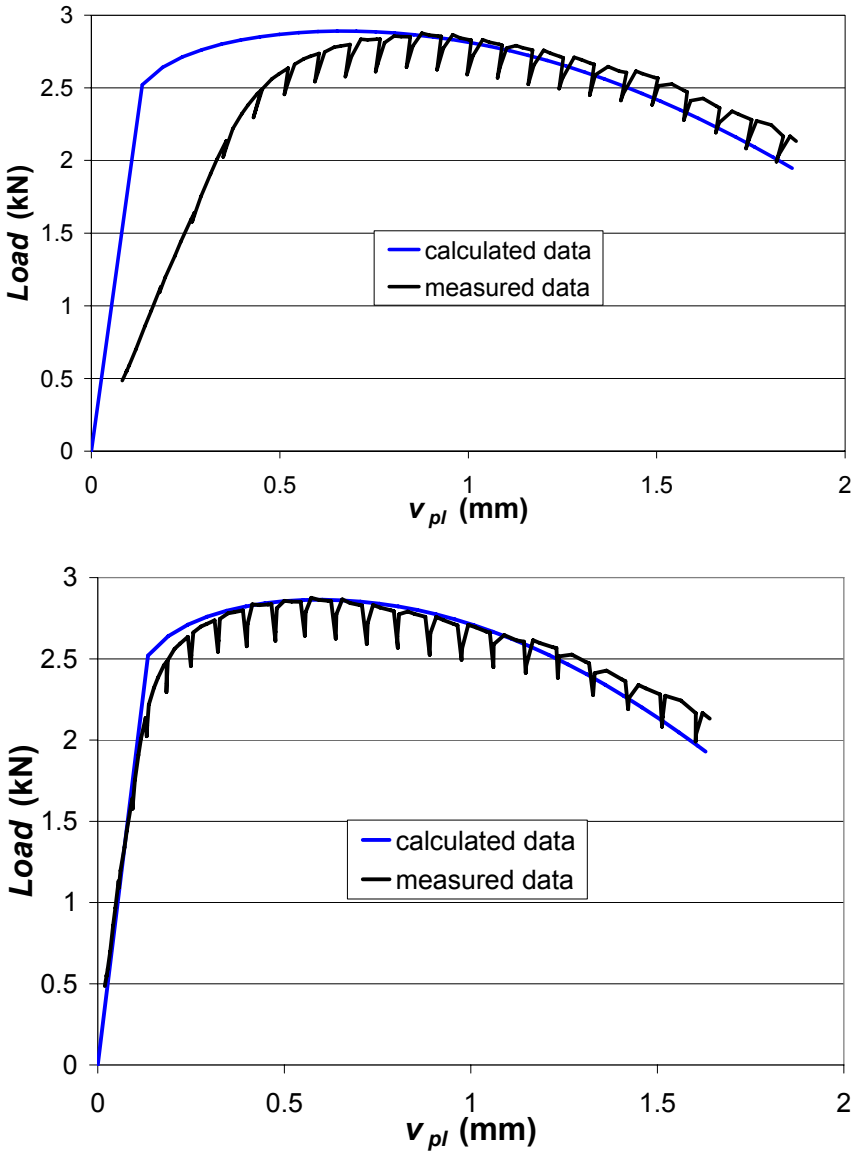

Figure 5.32: Comparison of calculated (blue) and measured data (black) for the application of the Donoso method (above) using stroke data; (below) using CMOD data.

5.2.1.2 Fracture toughness tests of T91 in oxygen saturated LBE

The fracture toughness tests in oxygen saturated condition were performed by submerging the DCT sample in an open LBE reservoir which was mounted onto the load line inside a furnace. The set up is depicted in Figure 5.33. The DCT sample

was mounted and the set up was heated to a minimum of 150°C. Once the reservoir and sample reached a temperature above 150°C, the LBE which was molten in a separate container was poured into the reservoir and the temperature was left to settle at the desired testing temperature. The test was started after the temperature remained constant, within ± 2°C, for 20 minutes.

Figure 5.33: picture of the LBE reservoir mounted onto the load line inside the furnace.

The load-displacement curves of the tests performed at 200°C under oxygen saturated condition are depicted in Figure 5.34. In contrast to the load-CMOD curves presented in Figure 5.27, the displacement on the X axis in Figure 5.34 is the displacement measured by the LVDT sensor of the test bench or stroke signal since these tests were performed without using a clip gauge.
It is clear from Figure 5.34 that samples T11-4-89 and T11-4-90 show a significantly sharper decrease in load in comparison with the other samples.

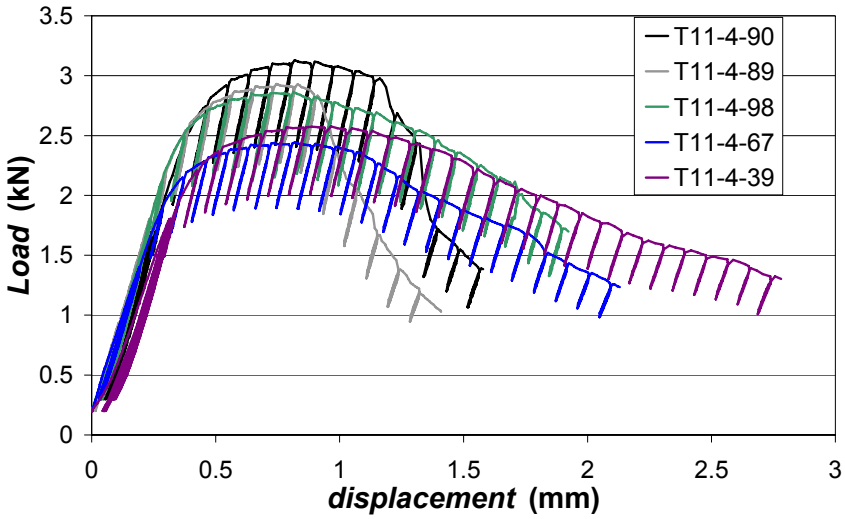

Figure 5.34: load-displacement curves of tests in oxygen saturated LBE at 200°C, 0.25 mm/min.

Table 5.7 shows the J_Q values calculated from the *J-R* curves determined by the normalization methods for the tests performed in LBE (saturated oxygen) at 200°C. For the application of the Chaouadi and Donoso method, the compliance correction model was applied (see 5.2.1.1). The Donoso method for specimen 39 gave an unreliable result because the final crack length was too large to accurately apply this method.

J_Q values calculated for specimens 89 and 90 are significantly lower than the other values, as was expected when examining their load displacement curves (see Figure 5.34).

Table 5.7: J_Q values calculated by normalization methods for specimens tested at 200°C in LBE (saturated oxygen). The NDR method did not give reliable results for specimens 39 and 89.

Specimen code	NDR	Chaouadi	Donoso
	J_Q (kJ/m²)	J_Q (kJ/m²)	J_Q (kJ/m²)
39	49.7	304.0	342.1
67	262.0	274.7	248.9
89	206.6	120.5	147.8
90	168.8	171.3	176.9
98	172.3	233.6	225.5

SEM investigation of the crack surfaces of both specimen T11-4-89 and specimen T11-4-90, tested in LBE under oxygen saturated condition, showed clear signs of embrittlement. This indicates there was wetting between the liquid lead bismuth and the T91 steel at the advancing crack tip. For the other samples, the fracture surface appeared fully dimpled indicating fully ductile tearing comparable to the tests performed in air.

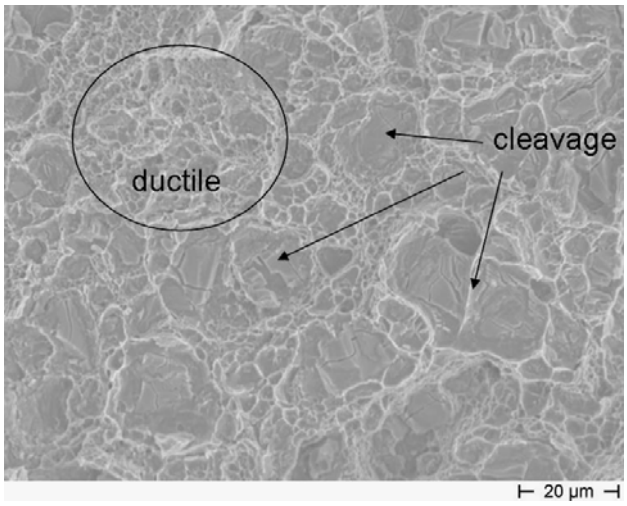

Figure 5.35: SEM of the mixed ductile-brittle fracture surface of sample T11-4-89. Several grains which cracked in cleavage mode are indicated by arrows. Note that many more cleaved grains can be seen in the picture. A region with a relatively high fraction of dimples was circled. More detailed investigation of this area also reveals small areas cracked in cleavage mode.

The surface of sample T11-4-89 exhibits mixed ductile and brittle fracture characteristics across the entire fracture surface. A detail of the fracture surface is shown in Figure 5.35. It seems that individual grains were fractured in cleavage mode whereas other grains fractured in ductile mode. Several grains which cracked in cleavage mode are indicated by arrows in Figure 5.35. It is however clear that many more grains which cracked in cleavage can be found in the picture.
An area which shows a relatively high fraction of dimples has been circled in Figure 5.35. When examining this area more in detail however, one can still find small regions which cracked in cleavage fracture mode. This difference in fracture mode is probably due to the orientation of the grains in respect to the crack surface plane and the related tendency to cleavage in these orientations.

The surface of sample T11-4-90 exhibits a few local fully brittle fracture sites combined with mixed ductile and brittle fracture characteristics across the majority of the sample's fracture surface. Picture A in Figure 5.36 shows a fully brittle crack initiation site which is located at the notch of the side groove on the side of the

sample. This indicates that the crack advancement was not solely initiated at the precrack which is the case for fracture toughness tests in air. Picture B in Figure 5.36 shows a detail of the middle of the sample's fracture surface. I the middle of Figure 5.36B one can see a grain which fully cracked in cleavage, surrounded by mixed ductile-brittle fracture area. The mixed ductile-brittle fracture surface reveals very similar characteristics to the fracture type shown in Figure 5.35.

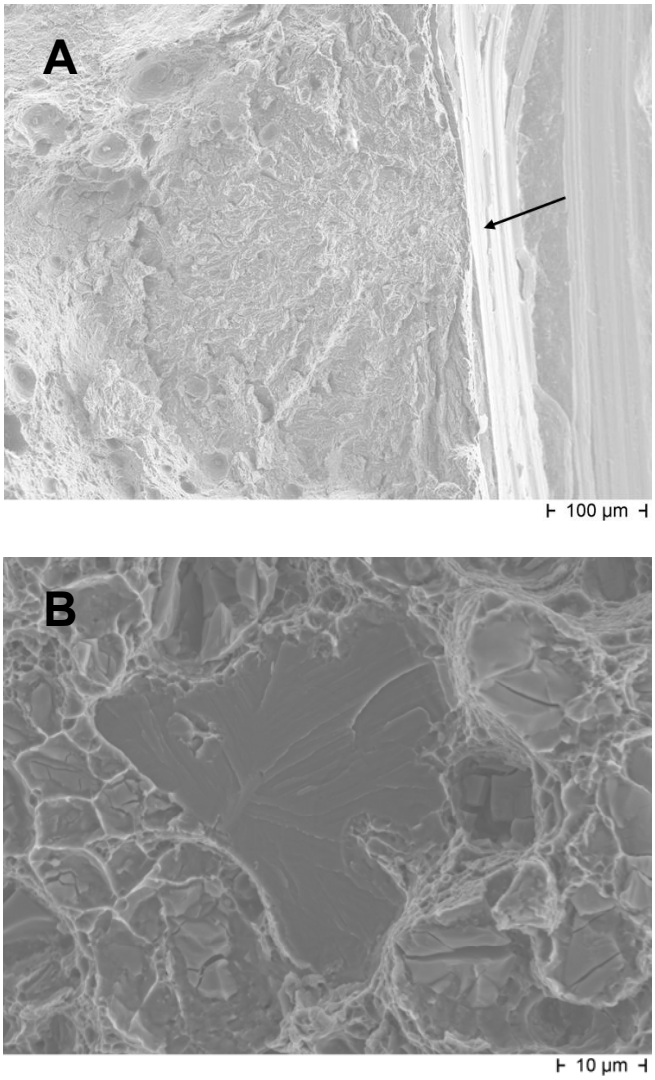

Figure 5.36: SEM of fracture surface of sample 2: (a) pseudo-cleavage fracture initiation site in the notch of the side groove on the side of the sample; (b) detail of local brittle fractured grain surrounded by mixed ductile-brittle fracture areas in the middle of the sample's fracture surface.

To compare the fracture toughness values of T91 steel in air and in LBE, we have selected the best result from tests in air at 200°C, being this of sample T11-4-103 (*J-R* curves resulting from different normalization methods in Figure 5.29) and compared it to the results of the most embrittled specimen in LBE at 200°C, being sample T11-4-89. For clarity, we have calculated the average *J-R* curve based on the applied analysis methods and taken the ± 15% uncertainty rule in consideration. The results are depicted in Figure 5.37.

Based on these results, the decrease in fracture toughness of T91 steel in LBE at 200°C is maximum 30%. This is in agreement with the work of Long *et al.* [64] who used 3 point bending tests in LBE to characterize the fracture toughness of T91 in LBE.

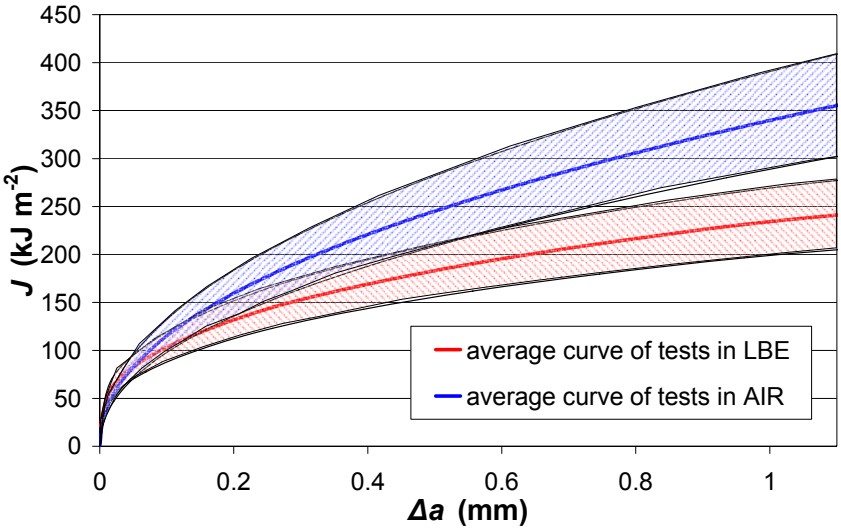

Figure 5.37: Comparison of *J-R* curves in air (blue) and LBE (red); Experimental uncertainty of ± 15% indicated by dashed lines.

The test results of T91 in LBE under oxygen saturated conditions at 300°C were quite different from those at 200°C. Unlike the load-displacement curves resulting from tests at 200°C, those of T91 in LBE at 300°C did not show any sharp decrease in load with increasing displacement. The load-displacement curves of T91 in LBE at 300°C are depicted in Figure 5.38. Small signs of possible embrittlement are visible in the load-displacement curves of sample T11-4-69 (at a displacement of 1.2 mm) and sample T11-4-96 (at a displacement of about 1.5 mm). For sample T11-4-64, the maximum load is noticeably lower in comparison with the other specimens. This is due to the precrack of specimen T11-4-64 which had a crack length of 5.53 mm (where the max. crack length in precracking was 5 mm) because the precracking procedure was not stopped in time.

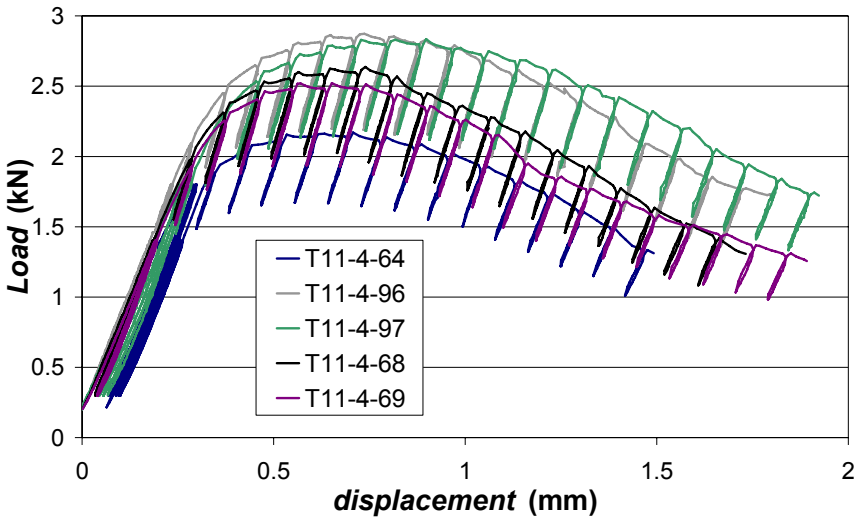

Figure 5.38: Load-displacement curves of tests in LBE (saturated oxygen) at 300°C and 0.25 mm/min.

Table 5.8 shows the J_Q values calculated from the *J-R* curves determined by the normalization methods for the tests performed in LBE (saturated oxygen) at 300°C. The NDR method did not give as good results as the other methods. Furthermore, J_Q values for specimen 64 seem rather small. This could be because the final crack length after precracking was too large. However, SEM examination of the fracture surface reveals brittle fracture properties on both sides of the sample as shown in Figure 5.39. The brittle fracture behaviour due to LME has been initiated in the side groove on both sides of the sample whereas the onset of cracking nearest to the precrack is dimpled and therefore ductile. Furthermore, the middle of the fracture surface is fully dimpled.

Sample T11-4-97 also revealed brittle fracture aspects on the sides of the DCT sample with initiation in the side groove. The embrittlement was far less than in sample T11-4-64 however.

Table 5.8: J_Q values calculated by normalization methods for specimens tested at 300°C in LBE (saturated oxygen)

Specimen code	NDR	Chaouadi	Donoso
	J_Q (kJ/m²)	J_Q (kJ/m²)	J_Q (kJ/m²)
64		133.3	124.6
68	156.5	179.9	179.6
69	160.0	193.9	201.6
96	140.0	216.7	201.5
97	105.0	222.6	202.4

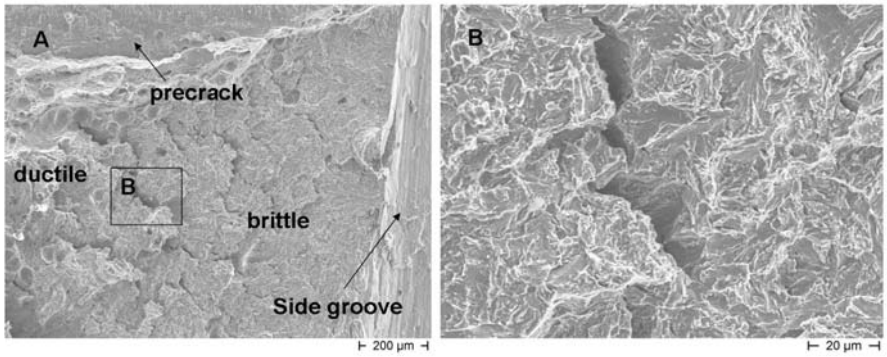

Figure 5.39: fracture surface of T11-4-64. A: overview showing the precrack and side groove. Brittle fracture on the side of the DCT specimen initiated in the side groove; ductile fracture in the middle of the specimen and at the onset of cracking nearest to the precrack; B: magnification of brittle fracture surface.

5.2.1.3 Fracture toughness tests of T91 in oxygen depleted LBE (10^{-6}-10^{-7} wt%)

The fracture toughness tests in oxygen controlled condition were performed in the autoclave of the Limets 1 facility, described in section 3.1. This test set up allowed controlling both temperature and oxygen content of the liquid metal environment. Tests were performed at a displacement rate of 0.25 mm/min in depleted oxygen conditions with an oxygen concentration between 10^{-6} and 10^{-7} wt% in the LBE at both 200 and 300°C.

The Limets 1 loading rig did not allow accurate loading unloading compliance measurements due to the current design of the lower sample holder and the limitations of the loading actuator software. Since the loading unloading compliance is not strictly needed to analyse the fracture toughness of the steels in LBE, the test set up was not altered.

The load-displacement curves of the tests performed on T91 at 200 and 300°C in oxygen depleted conditions are depicted in Figure 5.40.

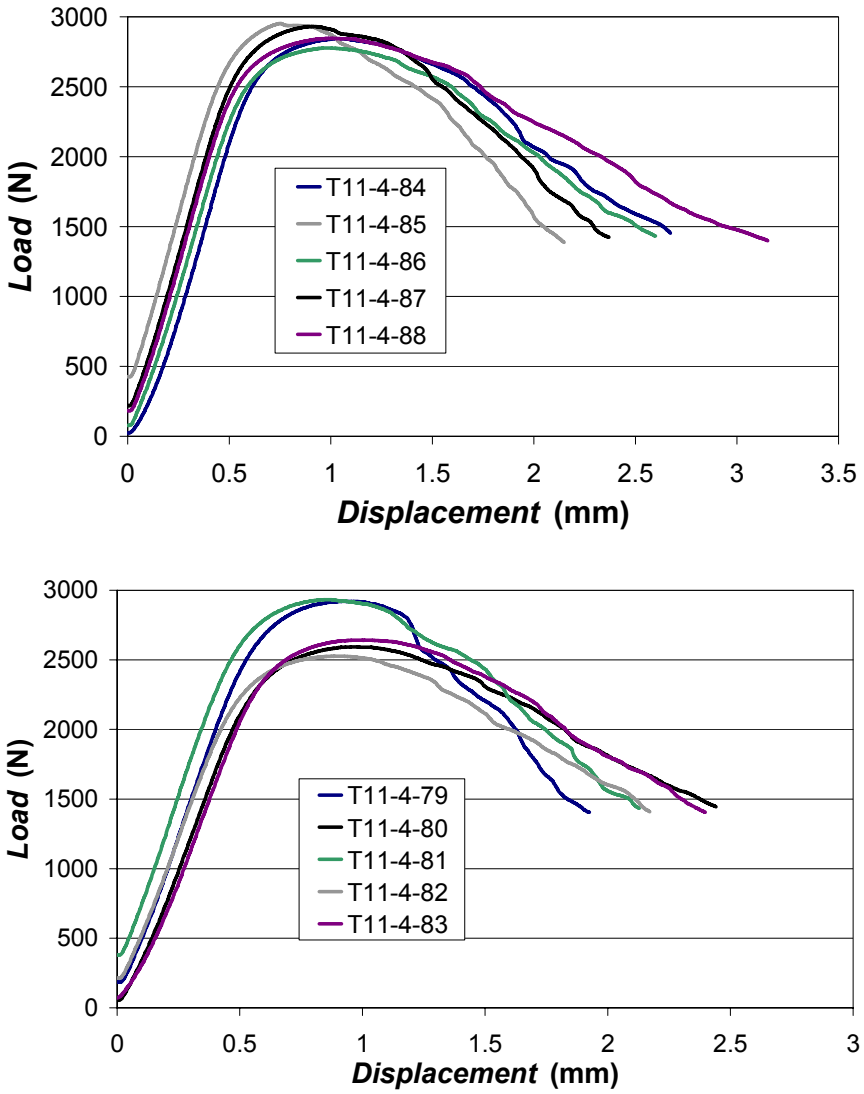

Figure 5.40: Load-displacement curves of tests in LBE (10^{-6}-10^{-7} wt% O_2) at 200°C (above) and 300°C (below) at a displacement rate of 0.25 mm/min.

For the tests performed in LBE environment (10^{-6}-10^{-7} wt% O_2), no compliance correction was determined since there was no possibility to compare the stroke data of Limets 1 with CMOD data at elevated temperature. As a result, the obtained *J-R* curves will still be within the normal scatter range expected in fracture toughness test analysis, however, they will give a slight overestimation of the values (see 5.2.1.1). The determination of a compliance correction model in the future is

desirable. This would require modification of a clip gauge to allow measurement of CMOD inside the autoclave of Limets 1 at elevated temperatures and has not been done due to time restrictions. Furthermore, the software of the Limets 1 actuator would need to be adapted to correlate the CMOD measurement to the corresponding stroke signal.

Table 5.9 shows the J_Q values corresponding to the tests performed in LBE (10^{-6}-10^{-7} wt% O_2) at 200°C. Looking at these results and comparing them with the force-displacement curves (Figure 5.40), it is clear that specimen 85 shows the most signs of embrittlement.

Table 5.9: J_Q values calculated by normalization methods for specimens tested at 200°C in LBE (10^{-6}-10^{-7} wt% O_2)

Specimen code	NDR	Chaouadi	Donoso
	J_Q (kJ/m²)	J_Q (kJ/m²)	J_Q (kJ/m²)
84	169.4	244.2	299.5
85	212.3	209.0	180.9
86	252.2	233.2	302.6
87	212.8	223.2	282.5
88	246.7	321.1	348.9

Figure 5.41 shows a SEM picture of the crack surface of specimen 85. The crack surface exhibits a mixed brittle and ductile fracture surface. This shows that load-displacement curves, fracture toughness values and SEM pictures all point to an embrittling effect of the liquid metal environment at 200°C under oxygen depleted conditions.

When taking into account the overall average value of J_Q at 200°C, we obtain an average value of 250.56 kJ/m^2 for tests in air and 249.23 kJ/m^2 for tests in oxygen depleted LBE. Keeping in mind the fact that we used the stroke data without compliance correction and therefore slightly overestimate the fracture toughness, this shows that although the liquid metal environment has an influence on the fracture behaviour of the T91 steel as shown from SEM images, the influence on the fracture toughness is rather small.

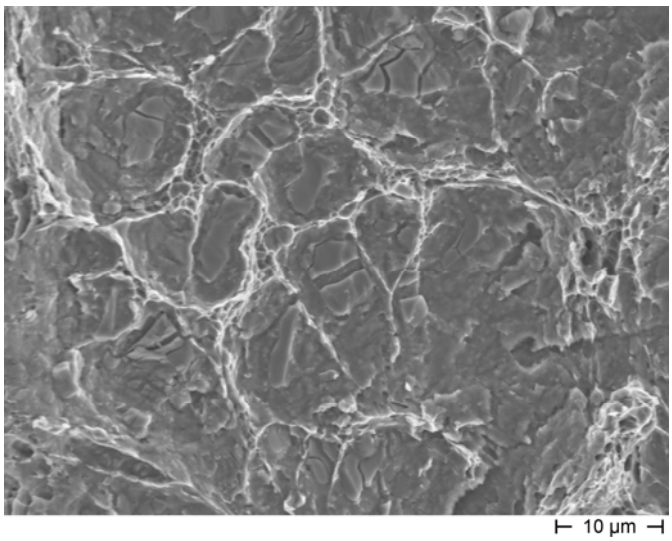

Figure 5.41: SEM picture of mixed brittle and ductile crack surface of specimen 85.

Table 5.10 shows the results of the fracture toughness tests performed in LBE (10^{-6}-10^{-7} wt% O_2) at 300°C. Both force-displacement curves (Figure 5.40) as J_Q values point out that that LBE had the most effect on specimen 79.

Table 5.10: J_Q values calculated by normalization methods for specimens tested at 300°C in LBE (controlled oxygen)

Specimen code	NDR	Chaouadi	Donoso
	J_Q (kJ/m²)	J_Q (kJ/m²)	J_Q (kJ/m²)
79	224.6	175.3	215.9
80	248.3	223.7	214.3
81	264.3	203.9	247.4
82	239.0	194.0	237.3
83	231.0	215.0	275.4

Figure 5.42 shows a SEM picture of a part of the fracture surface at the side of specimen 79 exhibiting pseudo cleavage fracture initiated in the side groove. Figure 5.43 shows the middle of the sample crack surface which exhibits a mixed brittle and ductile crack surface.

Although the calculated J_Q values of tests performed in Limets 1 give a slight overestimation due to the use of stroke data instead of CMOD data, the results indicate there is a decrease of the fracture toughness of T91 both at 200 and at 300°C.

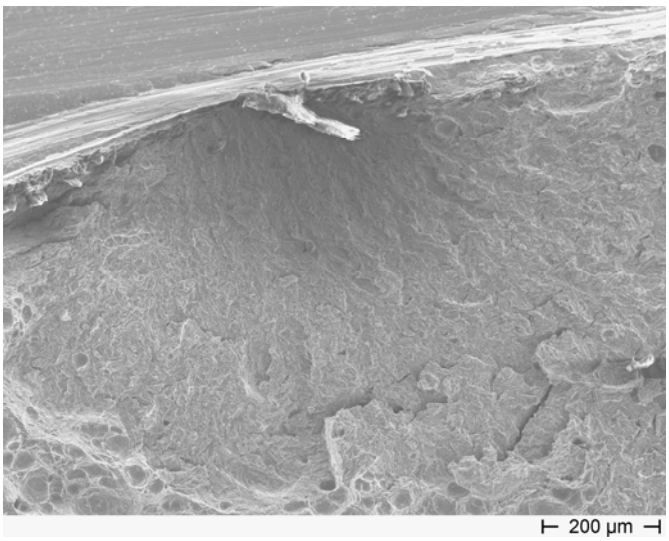

Figure 5.42: SEM picture of specimen 79 showing pseudo cleavage fracture at the side of the specimen.

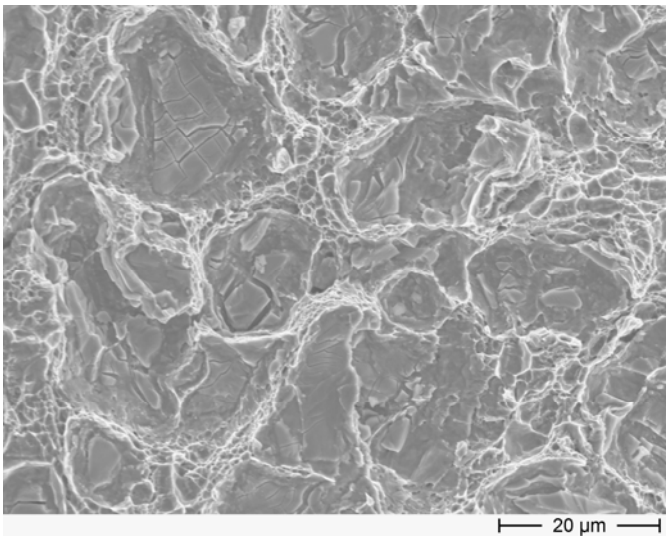

Figure 5.43: SEM picture of the mixed brittle and ductile crack surface of specimen 79.

5.2.2 Fracture toughness of 316L

As for T91, the plane strain fracture toughness of 316L was determined at 200 and 300°C in both air and oxygen saturated LBE. No fracture toughness tests were performed on 316L in oxygen controlled conditions.

The same sample geometry was applied and the applied displacement rate for fracture toughness testing was 0.25 mm/min as was the case for T91 discussed above.

5.2.2.1 Fracture toughness tests of 316L in air

To determine the reference value of fracture toughness of 316L at 200 and 300°C tests were performed in air. Furthermore these tests allowed one to examine whether the normalisation methods discussed in section 3.1.3.2 could be successfully applied to 316L steel.

Six tests were performed at 200°C and six tests at 300°C. The load CMOD curves are depicted in Figure 5.44. The tests performed at 200°C are depicted on the top, those performed at 300°C are depicted on the bottom. The sample numbers are indicated in the legend of the figure. The "L" stands for 316L steel. The 631 indicates the piece of the original hot rolled plate where these samples were taken and the last number is the sample number to identify each sample.

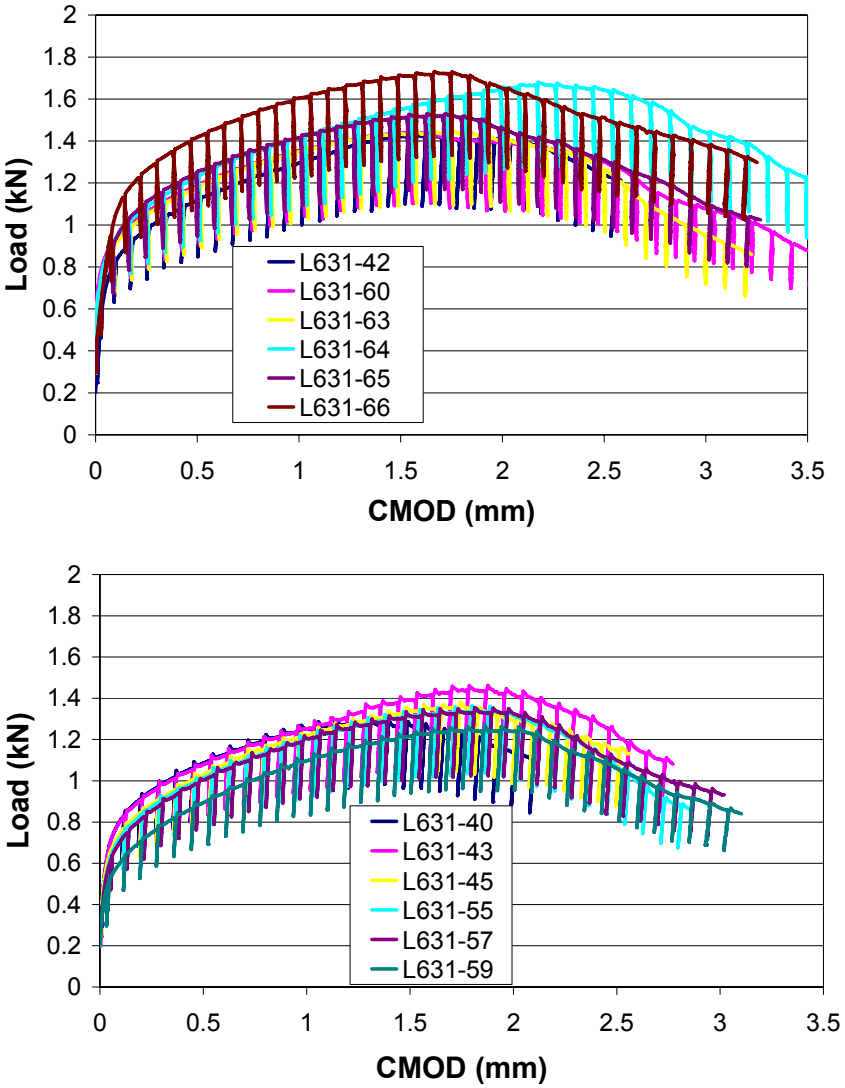

Figure 5.44: Load-CMOD curves of J_{Ic} tests of 316L in air; Above: 200°C, 0.25 mm/min ; Below: 300°C, 0.25 mm/min.

Since tests in air can be performed using the conventional fracture toughness testing methods as well as the normalisation methods discussed above in section 3.1.3.2, the tests in air allow one to examine the applicability of the normalisation methods to the specific steel. For 316L, the Donoso method seemed to result in slightly more deviating results in comparison with the NDR and Chaouadi methods which both give very good agreement with UC. However, as can be seen in Figure 5.45, all three normalisation methods can be used for fracture toughness analysis of 316L steel.

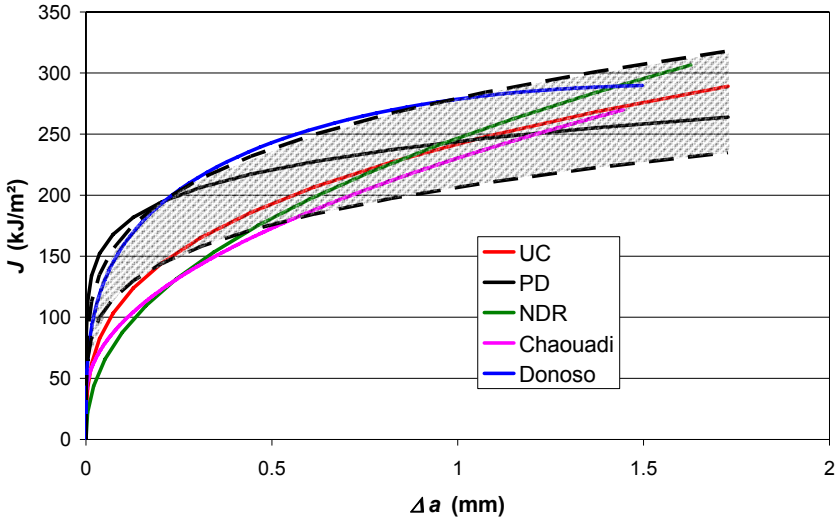

Figure 5.45: *J-R* curves of 316L specimen L631-45, tested at 300°C, calculated by potential drop (black), unloading compliance (red), NDR (green), Chaouadi (magenta) and Donoso (Blue) methods.

The values for J_Q calculated by UC, PD, NDR, Chaouadi and Donoso methods are summarized in Table 5.11 for tests of 316L in air performed at 200°C and in Table 5.12 for tests of 316L performed in air at 300°C.

Table 5.11: J_Q values of 316L specimens tested in air at 200°C, calculated by unloading compliance (UC), potential drop (PD), NDR, Chaouadi and Donoso methods.

Specimen code	UC	PD	NDR	Chaouadi	Donoso
	J_Q (kJ/m²)	J_Q (kJ/m²)	J_Q (kJ/m²)	J_Q (kJ/m²)	J_Q (kJ/m²)
42	280.2	284.1	249.8	179.3	212.6
60	261.6	258.8	305.0	258.7	258.7
63	265.8	265.8	242.0	232.4	270.3
64	292.5	292.5	267.2	242.0	258.6
65	276.2	276.2	251.8	244.6	221.9
average	**275.3**	**275.5**	**263.2**	**231.4**	**244.4**
average UC and PD		275.4			
	+15%	316.7			
	-15%	234.0			

Table 5.12: J_Q values of 316L specimens tested in air at 300°C, calculated by unloading compliance (UC), potential drop (PD), NDR, Chaouadi and Donoso methods.

Specimen code	UC	PD	NDR	Chaouadi	Donoso
	J_Q (kJ/m²)	J_Q (kJ/m²)	J_Q (kJ/m²)	J_Q (kJ/m²)	J_Q (kJ/m²)
40	173.1	192.8	155.9	127.4	116.0
43	274.2	287.1	267	166.7	214.2
45	191.2	222.9	174.4	142.6	180.3
55	233	245.4	193.1	121.4	185.8
57	245.1	245.7	238.0	146.7	211.9
59	235.4	235.4	215.1	134.0	202.0
average	**225.3**	**238.2**	**207.2**	**139.8**	**185.0**
average UC and PD		231.7			
	+15%	266.4			
	-15%	196.9			

5.2.2.2 Fracture toughness tests of 316L in oxygen saturated LBE

Tests of 316L in oxygen saturated conditions were performed in the same open reservoir which was attached to the load line as for the tests performed on T91. To allow analysis without the use of a clip gauge we needed to apply a compliance correction similar to the compliance correction applied for the tests on T91 steel. The load-displacement curves for both the tests performed at 200°C and at 300°C are depicted in Figure 5.46.

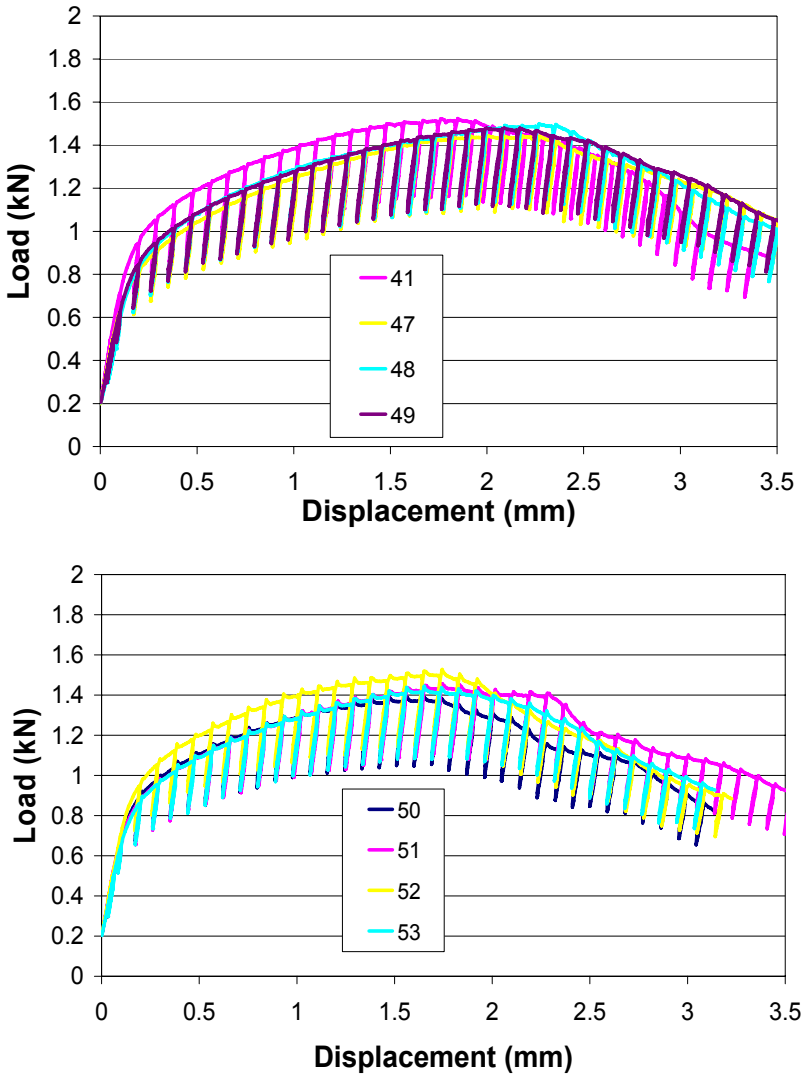

Figure 5.46: Load-displacement curves of J_{Ic} tests of 316L in LBE; Above: 200°C, 0.25 mm/min; Below: 300°C, 0.25 mm/min.

At 200°C, the load displacement curves of 316L in LBE do not have any remarkable sharp decreases in load with increasing displacement. However, the load-displacement curves of some 316L specimens in LBE under saturated oxygen conditions at 300°C do show some sharp decreases in load with increasing displacement. This can be seen in Figure 5.46 on the right for specimen L631-51. Despite this sharp decrease in load for some specimens, all examined crack surfaces of 316L were fully dimpled and no special features were observed.

The fracture toughness values calculated by NDR, Chaouadi en Donoso methods are summarized in Table 5.13 for tests performed in LBE at 200°C and in Table 5.14 for tests performed in LBE at 300°C.

Table 5.13: J_Q values of 316L specimens tested in LBE at 200°C, calculated by NDR, Chaouadi and Donoso methods.

Specimen code	NDR	Chaouadi	Donoso
	J_Q (kJ/m²)	J_Q (kJ/m²)	J_Q (kJ/m²)
41	254.3	156.5	222.0
47	236.5	191.7	258.6
48	281.0	176.3	270.3
49	276.7	182.2	275.1

Table 5.14: J_Q values of 316L specimens tested in LBE at 300°C, calculated by NDR, Chaouadi and Donoso methods.

Specimen code	NDR	Chaouadi	Donoso
	J_Q (kJ/m²)	J_Q (kJ/m²)	J_Q (kJ/m²)
50	209.4	135.9	184.9
51	182.5	148.8	192.2
52	138.8	113.2	156.4
53	261.9	163.9	210.8

Although the average J_Q value of tests performed on 316L in LBE is about 10% lower than the average J_Q for tests performed on 316L in air, the cracked surfaces were all fully ductile. This means that the fracture toughness of 316L in LBE might be slightly influenced by the LBE environment however more tests would be needed to make sound conclusions.

5.2.3 Fracture toughness of Si enriched steels

Due to the severe embrittlement of the high silicon steels in LBE, the normalisation methods which are based on ductile tearing could not be applied.

A possible approach to still quantify the embrittlement of these high Si steels in LBE would be to perform K_{Ic} tests in LBE at elevated temperature and compare them to an extrapolation to elevated temperature of K_{Ic} tests performed on the high Si steels at low temperature.
Furthermore, Maugis [144] states that the ratio of K_{Ic} in air and in LBE at the same temperature and crack velocity would be equal to the ratio of the surface energies and the ratio of the strain energy release rates in both environments according to the following equation:

$$\frac{\gamma_1}{\gamma_2} = \frac{G_1}{G_2} = \frac{K_{1c}^2}{K_{2c}^2} \qquad \textbf{(5.2)}$$

Unfortunately, due to a lack of material, time and surface energy data for the elevated Si steels this interesting path could not be pursued any further.

6 COMPATIBILITY OF "TREATED" STRUCTURAL MATERIALS WITH LIQUID METALS

A million experiments can't prove me right, but one experiment can prove me wrong.
Albert Einstein
(1879 – 1955)

In Chapter 6 we discuss the tensile tests performed on the materials in a "treated" condition. This means several possible conditions (except irradiation) which could have an influence on the material's susceptibility to LME.

By performing tensile tests on the steels in these treated conditions in both liquid LBE and gas environment we can obtain a first impression of the possible detrimental effect of some service conditions on the material's susceptibility to LME.

Firstly, we discuss the effect of hardening the material. For T91 this hardening consisted of a modified heat treatment whereas for 316L the hardening effect was obtained by cold work.

Secondly, the effect of surface stress concentrators is discussed. These surface stress concentrators can be obtained by either using notched specimens or by local corrosion due to pre-exposure under low oxygen LBE condition.

The pre-exposure under low oxygen conditions itself is discussed in a third point. Pre-exposure under low oxygen LBE conditions which is also assumed to benefit wetting was performed continuously at 450°C and by thermal cycling.

As a combination of exposure and hardening the compatibility of TIG and EB welds of the T91 and 316L structural materials will also be discussed in this last section.

6.1 COMPATIBILITY OF HARDENED STRUCTURAL MATERIALS WITH LIQUID METALS

As discussed in section 1.3.1 of Chapter 1 on the general phenomena occurring in contact with liquid metals, the hardness and strength of a material seems to influence its susceptibility to LME in the sense that harder or stronger materials are often more embrittled.

Therefore, we wanted to verify the effect of hardness and strength of the studied T91 and 316L steels on their susceptibility to LME. This will be discussed more in detail in the following sections.

Furthermore, the hardness profile across welds as shown in section 2.2.2 and 2.2.3 of Chapter 2 makes that every welded connection in practise consists of material having a different hardness and thus might be differently susceptible to LME. The examination of the susceptibility of the welds to LME will be discussed more in detail in section 6.3.2 of this chapter.

6.1.1 SSRT tests of thermally hardened T91

Thermal hardening of a ferritic-martensitic steel by tempering at a lower temperature is used as pretence to create a harder material without the need of irradiation experiments. Although the microscopic defects determining the bulk hardening effect are different, the macroscopic change (hardness increase) is the same. Of course, for a phenomenon like LME of which the mechanism is unknown and which is known to be influenced by many different metallurgical parameters, the question remains whether simple thermal treatment hardening effects can be used to extract knowledge about LME of structural materials under irradiation.

We thermally hardened T91 by re-austenitisation at 1050°C for one hour followed by a water quench and subsequent tempering at 500°C for one hour followed by air cooling.
The resulting T91 steel had a Vickers hardness of 388 H_{V5} compared to a Vickers hardness of 225 H_{V5} for the conventional T91 which was tempered at 770°C.

The thermally hardened T91 steel was tensile tested at 350°C in both gas and liquid metal environment at a strain rate of 1.10^{-6} s^{-1} or at a strain rate of 1.10^{-3} s^{-1}. The resulting tensile curves are shown in Figure 6.1.

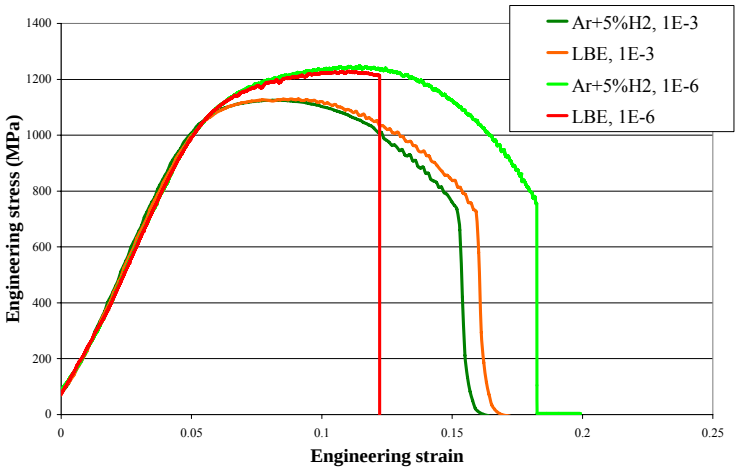

Figure 6.1: Tensile curves of thermally hardened T91 at 350°C in Ar + 5% H_2 and LBE at different strain rates. Test in Ar + 5%H_2 at a strain rate of 1.10^{-6} s^{-1} (bright green); Test in LBE at a strain rate of 1.10^{-6} s^{-1} (red); Test in Ar + 5%H_2 at a strain rate of 1.10^{-3} s^{-1} (dark green); Test in LBE at a strain rate of 1.10^{-3} s^{-1} (orange);

As can be seen in Figure 6.1, the mechanical properties of the thermally hardened T91 depend on the applied strain rate. This was not the case for the conventional T91 tested as function of strain rate at 350°C (see section 5.1.2).
At a strain rate of 1.10^{-3} s^{-1} the curves nicely coincide and the difference in total elongation is within the experimental scatter. However at a strain rate of 1.10^{-6} s^{-1} the specimen tested in LBE breaks near its ultimate tensile strength. Careful examination of the tensile curve shows that the fracture is not immediately all the way thru the sample.

When examining the fracture surfaces of these samples, that of the specimen tested in LBE with an oxygen concentration of 10^{-6} – 10^{-7} wt% at a strain rate of 1.10^{-6} s^{-1}, shows a large area of LME fracture which was initiated at the surface. The initiation site is indicated by a red arrow in Figure 6.2. The other three thermally hardened samples tested in either gas or LBE were fully ductile. Broken halves had the typical cup and cone shape and the fracture surface was fully dimpled. The detailed examination of the sample affected by LME showed no dimples in the semi circular LME fractured area. Furthermore, this single initiation site LME area comprised the largest fraction of the fracture surface area encountered in T91 within this study. It remains unclear why the progression of the LME fracture was stopped.

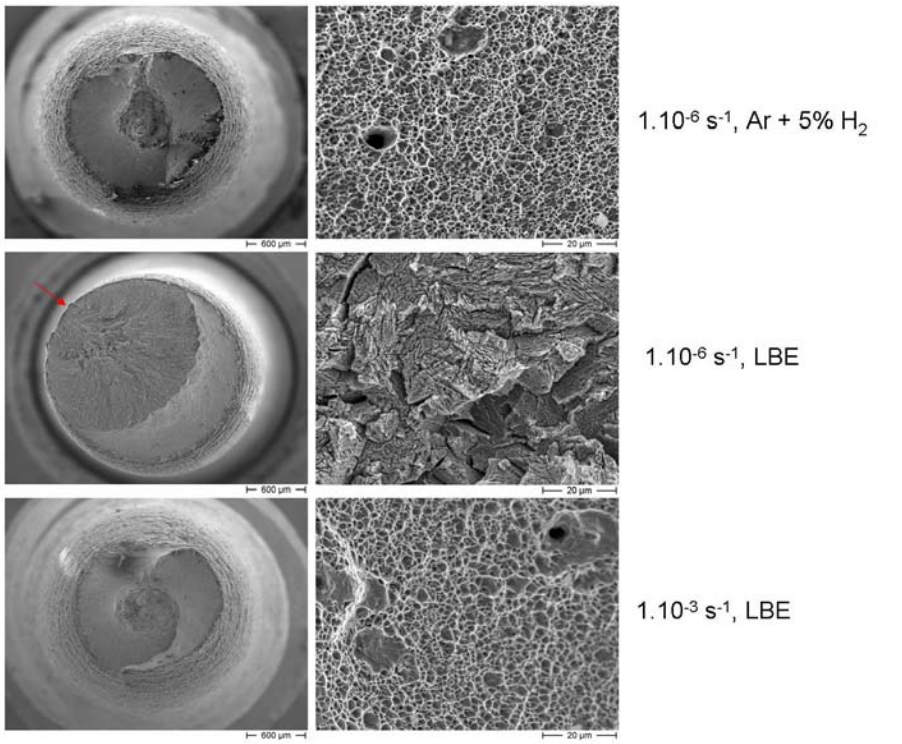

Figure 6.2: Fracture surfaces of thermally hardened T91 tested at 350°C.
(Above) thermally hardened T91 tested in a gas mixture of Ar and 5% H_2 at a strain rate of 1.10^{-6} s^{-1}. The broken sample has the typical cup and cone shape and a fully dimpled, ductile fracture surface;
(Middle) thermally hardened T91 tested in LBE at a strain rate of 1.10^{-6} s^{-1}. The sample shows very little necking and the fracture surface is dominated by a large area of LME fracture initiated in the upper left of the picture, indicated by the red arrow. Detailed fracture surface examination reveals no dimples in the LME fractured area;
(Below) thermally hardened T91 tested in LBE at a strain rate of 1.10^{-3} s^{-1}. The broken sample has the typical cup and cone shape and the fracture surface is fully dimpled.

The SSRT tests on thermally hardened T91 by Long *et al.* [58] were performed on EDM cut rectangular specimens at a strain rate of 1.10^{-5} s^{-1}. The absence of embrittlement of our thermally hardened T91 at a strain rate of 1.10^{-3} s^{-1} might be an indication that above a certain strain rate the LME phenomenon is no longer found. However, the difference in embrittlement may also be due to the absence of stress concentrators in cylindrical specimens since small punch tests, which have a rather high local strain rate, on thermally hardened T91 at 300°C did show embrittlement as discussed in section 1.3.3.2.

From these results we can acknowledge that thermal hardening increases the susceptibility of T91 to LME. However, it does not cause LME to occur under all conditions.

6.1.2 SSRT tests of cold worked 316L

Since 316L austenitic stainless steel is fabricated using a solution annealing heat treatment followed by rapid cooling, it is impossible to heat treat the material to obtain a higher hardness. The only way to increase the hardness of the material is by work hardening. Therefore, we used 40% cold worked 316L steel. The initial thickness of the plate was reduced by 40% by cold rolling. The plastic deformation needed to achieve this thickness reduction produces a high density of dislocations in the material. These dislocations interact creating jogs, kinks and dislocation forests which hinder the movement of dislocations in the material. Furthermore, the cold rolling results in a microstructure of long stretched grains in the rolling direction.

Since the grain size was found to influence a material's susceptibility to LME as discussed in section 1.3.1 of Chapter 1, we tested the 40% cold worked 316L steel both in L (rolling direction) and in T direction (perpendicular to the rolling direction in the rolling plane). Tensile tests were performed in Limets 1 at 350°C, using a strain rate of either 1.10^{-6} s^{-1} or 1.10^{-3} s^{-1} in both argon and hydrogen gas mixture and in liquid LBE. The tensile curves of 316L 40%CW tested at a strain rate of 1.10^{-6} s^{-1} are depicted in Figure 6.3. The tensile curves of 316L 40%CW tested at a strain rate of 1.10^{-3} s^{-1} are depicted in Figure 6.4.

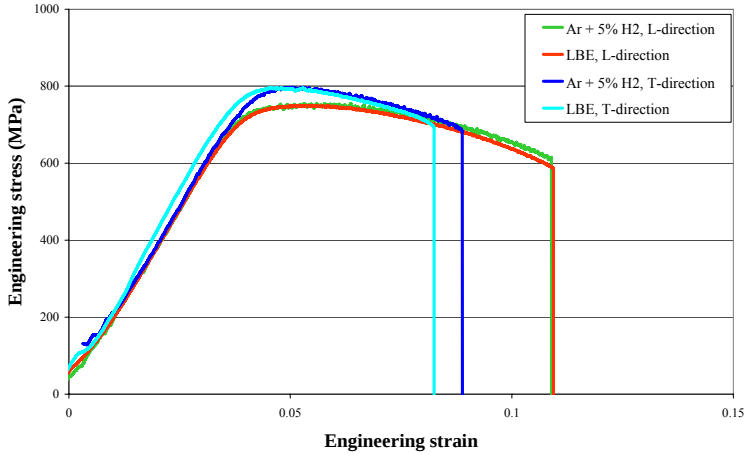

Figure 6.3: Tensile curves of 40%CW 316L at 350°C in Ar + 5% H_2 and LBE at 1.10^{-6} s^{-1}.
40%CW 316L tested in L direction in Ar + 5%H_2 (green); 40%CW 316L tested in L direction in LBE (red); 40%CW 316L tested in T direction in Ar + 5%H_2 (dark blue); 40%CR 316L tested in T direction in LBE (light blue).

Figure 6.3 and Figure 6.4 show that due to the cold work the yield stress of the 316L has significantly increased from an average value of 200 MPa at 350°C for the solution annealed condition to an average value (across both sample orientations) of

720 MPa at 350°C for the 40% cold worked 316L material. On the other hand, the average total elongation has decreased from about 40% for the solution annealed 316L to about 10% for the 40% cold worked 316L.

Despite the significant hardening increase none of the tested condition shows a significant decrease in total elongation due to the liquid metal environment. In fact, all curves nicely coincide except for the 40%CW 316L tested in T direction at a strain rate of 1.10^{-6} s^{-1}. This small decrease in total elongation is however within the experimental scatter. Furthermore, SEM examination of the fracture surfaces revealed fully dimpled, ductile fracture surfaces.

These results show that cold rolling or prior plastic deformation of austenitic 316L steel does not increase its susceptibility to LME in liquid lead bismuth eutectic under the tested conditions.

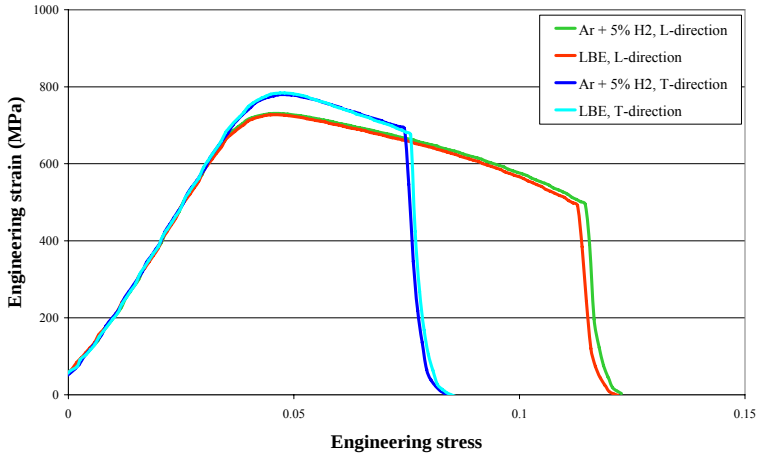

Figure 6.4: Tensile curves of 40%CW 316L at 350°C in Ar + 5% H_2 and LBE at 1.10^{-3} s^{-1}.
40%CW 316L tested in L direction in Ar + 5%H_2 (green); 40%CW 316L tested in L direction in LBE (red); 40%CW 316L tested in T direction in Ar + 5%H_2 (dark blue); 40%CR 316L tested in T direction in LBE (light blue).

6.2 COMPATIBILITY OF NOTCHED STRUCTURAL MATERIALS WITH LIQUID METALS

The results of Dai *et al.* [57] and Long *et al.* [58] on rectangular EDM cut specimens have shown that the presence of surface cracks and increased hardness strongly increase the susceptibility of T91 steel to liquid metal embrittlement. However examination of their fracture surfaces show that the initiation of brittle LME fracture often occurs at the corners of the rectangular specimens where they have stress concentrations.

To verify whether stress concentrators and sharp edges do influence the occurrence of LME, we used notched cylindrical specimens. The notch had a depth of 0.1 mm with an opening angle of 60° and a maximum radius at the tip of 0.20. The notch was mechanically applied using a lathe machine and was positioned in the middle of the gauge.

6.2.1 SSRT tests of notched T91

Two different batches of T91 were tested to assess the effect of a notch on the material's susceptibility to LME. Initially, a notched T91 sample of the T91 SPIRE batch was tested at 200°C at a strain rate of 5.10^{-5} s^{-1} in LBE environment containing 10^{-6}-10^{-7} wt% oxygen. For this particular notched T91 specimen, the total elongation was significantly reduced in LBE when compared to a reference test on the same T91 batch in argon and hydrogen mixture [21]. However when the examination was extended to a survey of notched T91 as function of temperature using T91 DEMETRA material and applying the same strain rate of 5.10^{-5} s^{-1} and LBE oxygen concentration, the results became less obvious.

The tensile results of the study as function of temperature are depicted in Figure 6.5. Tests in LBE are represented by full symbols whereas tests in gas are represented by empty symbols. For every temperature one test was performed in gas environment and two in liquid LBE environment. The latter to slightly improve the statistical uncertainty of the data. The initial test results on notched T91 from SPIRE are represented in red. A significant difference in total elongation was found for this specimen, as can be seen in Figure 6.5B, while the yield and tensile strength remained the same.

The LME effect was also found in the tests of notched T91 at 250°C although the effect was not as pronounced. The fracture surface had brittle fracture aspects at the rim of the specimen.

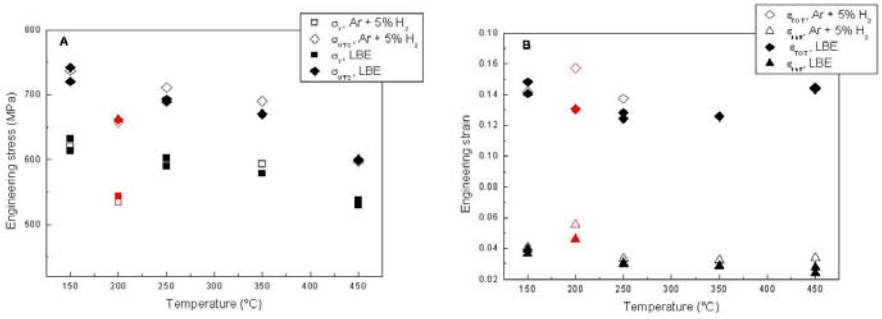

Figure 6.5: Tensile results of notched T91 as function of temperature (strain rate: $5.10^{-5}s^{-1}$). Full symbols for tests performed in LBE, empty symbols for tests performed in controlled gas atmosphere. T91 SPIRE data in red [21]. A: Influence of temperature on the yield strength and tensile strength; B: Total and uniform elongation as a function of temperature.

SEM observation of the fracture surface of the notched T91 SPIRE sample tested in LBE is shown in Figure 6.6. Figure 6.6A shows the overview of the fracture surface. The majority of the surface was ductile clearly showing dimples. On the edge of the fracture surface however, areas that were not fully ductile, showing some faces could be distinguished as can be seen in Figure 6.6.

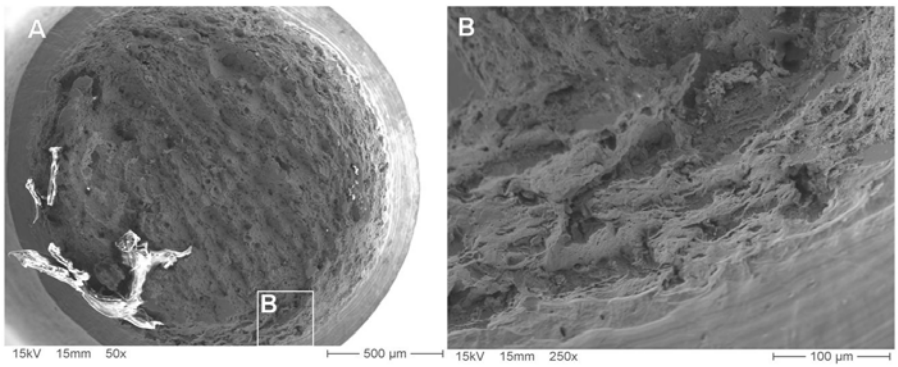

Figure 6.6: SEM observation of the fracture surface of the notched T91 SPIRE sample tested in LBE at 200°C. A: overview of the entire fracture surface. The brighter parts in the picture are pieces of LBE that were not removed by the cleaning of the sample; B: Close up of the edge of the sample showing the rim of the machined notch. The edge of the sample shows a partly brittle fracture surface [21].

Despite the fact that LME was not found for all the examined temperatures, it could still be said that surface stress concentrators increase the T91 steel's susceptibility to LME. We believe this is due to the creation of cracks at the surface in the notch

which are initiators for LME. As discussed in section 5.2.1 on fracture toughness of T91 in LBE, this type of LME initiation sites were also seen in the notch of the side grooves on the side of several DCT samples of T91 tested in LBE. However, as in other tensile tests on cylindrical specimens of T91 showing a certain degree of LME, the embrittlement is not very severe since the middle of the specimen remains fractured in a ductile manner.

6.2.2 SSRT tests of notched 316L

As for T91, notched specimens of 316L were tested as function of temperature in both LBE and in argon and hydrogen gas mixture. The applied strain rate was 5.10^{-5} s^{-1}. The results are depicted in Figure 6.7. Only one test in LBE per temperature was performed since no embrittlement of 316L in LBE had been seen before.

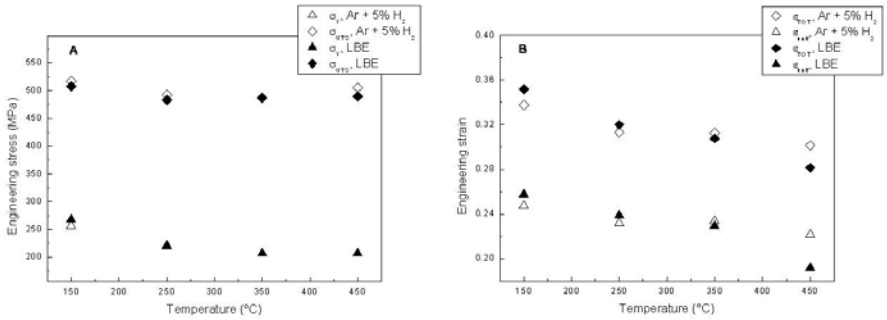

Figure 6.7: Tensile results of notched 316L as function of temperature (strain rate: $5.10^{-5}s^{-1}$). Full symbols for tests performed in LBE, empty symbols for tests performed in controlled gas atmosphere.
A: Influence of temperature on the yield strength and tensile strength; B: Total and uniform elongation as a function of temperature.

The tensile results of the notched 316L nicely coincide for all temperatures except for the tests performed at 450°C. However when examining the fracture surfaces of the specimens tested at 450°C no signs of embrittlement were found. The fracture surfaces of both the test in gas and the test in LBE were fully dimpled.

The difference in elongation between the test in LBE and the one in gas is assumed to be due to an actual temperature difference. This is confirmed by the difference in the yield strength results at 450°C of Figure 6.7A (±200 MPa) and these summarized in Table 2.4 in section 2.1.3.4.2 on the tensile properties of 316L (±150 MPa). Due to the lower thermal conductivity of the argon and hydrogen gas mixture compared to the LBE, one needs to increase the temperature of the controller of Limets 1 to achieve the same temperature on the sample. This was very probably overseen.

We therefore conclude that notched 316L specimens do not show an increased susceptibility to LME due to the presence of stress concentrators.

6.3 COMPATIBILITY OF PRE-EXPOSED STRUCTURAL MATERIALS AND THEIR WELDS WITH LIQUID METALS

Pre-exposure in low oxygen LBE is probably the most realistic and therefore relevant pre-treatment one can use. Since liquid metal wetting and LME are part of a dynamic process in which corrosion, passivation and possible liquid metal penetration play an important role. Unfortunately pre-exposure can be very time consuming and the outcome is not always straight forward or fully reproducible.

Although pre-exposure in flowing low oxygen LBE might be preferable to avoid the setting of an equilibrium saturation condition of soluble steel elements, all pre-exposure studies we performed were based on pre-exposure in stagnant LBE. We performed a continuous pre-exposure of T91 and 316L in stagnant LBE, continuously purged with Ar + 5% H_2 gas mixture at 450°C for 4000 hours and a thermal cycling exposure which took a little over one year. The thermal cycling exposure was performed in a capsule identical to the ones in the irradiation experiment and followed the thermal cycles of the BR2 reactor corrected with the "initially" (see Chapter 7) calculated gamma heating correction. This thermally exposed capsule was called the 0 dpa capsule since it was subjected to the same temperatures without any irradiation and was discussed in section 4.7 of Chapter 4. The tests resulting from these pre-exposure experiments will be discussed in the following sections.

6.3.1 SSRT tests of structural materials pre-exposed in low oxygen LBE at 450°C

Tensile samples of untreated T91 were pre-exposed for 4000 hours in an LBE container at 450°C which was continuously purged with Ar + 5% H_2. Although the oxygen concentration was not measured during the exposure, the continuous gas bubbling ensured a low oxygen concentration at 450°C.

After exposure the samples were tested at a strain rate of 5.10^{-5} s^{-1} at temperatures of 300°C and 450°C. The tensile curves were compared to ones obtained from testing non-exposed T91 material under the same conditions.
The resulting tensile curves are shown in Figure 6.8. The T91 showed a decrease in total elongation while yield strength and tensile strength remained constant when tested in lead bismuth environment at 450°C. However, the sample tested in LBE at 300°C did not show any significant sign of decrease in tensile properties after being

pre-exposed for 4000 hours at 450°C under the same conditions as the sample tested at 450°C.

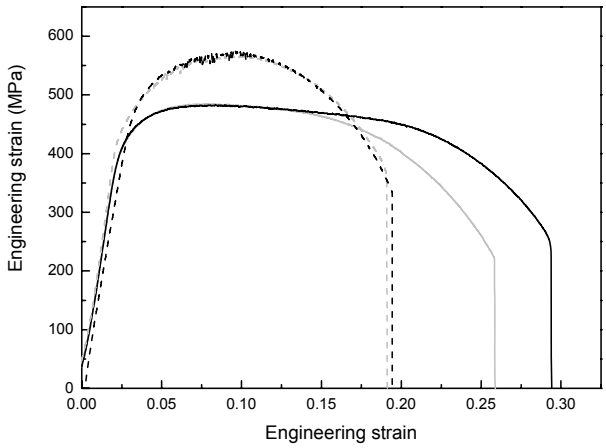

Figure 6.8: Tensile curves from tests at 300°C (dashed) and 450°C (solid) for samples of T91 that were pre-exposed to Pb-Bi at 450°C for 4000 hours (gray curves). The black curves result from tensile testing T91 without pre-exposure to Pb-Bi under the same conditions.

SEM observations of the corrosion at the surface of the samples determined that the sample tested at 300°C still had an almost uniform oxide layer on its surface whereas the sample tested at 450°C showed small local penetrations of the LBE as can be seen in Figure 6.9.

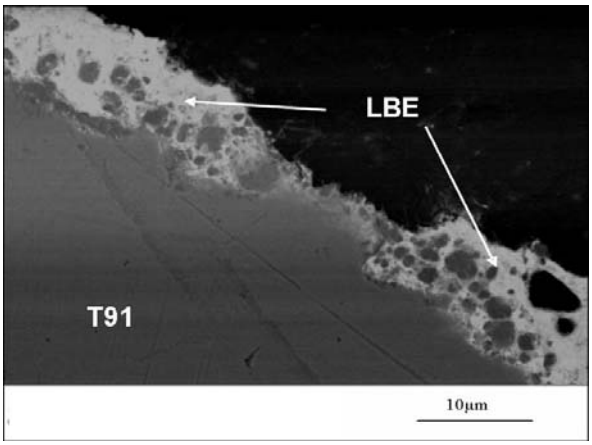

Figure 6.9: SEM observation of the surface layer of the T91 sample, tested at 450°C after 4000 hours of exposure in oxygen poor LBE. Locally the oxide layer can no longer be clearly distinguished and shows penetration of LBE.

The fracture surface of the pre-exposed sample tested at 450°C is shown in Figure 6.10 and consists of two different types of fracture surface. The majority of the fracture surface is dimpled (Figure 6.10A) but on one side it has a more brittle appearance (Figure 6.10B). Based on the fracture surface of the sample tested at 450°C and the observations of its corroded surface, it is thought that the penetration of LBE created a surface defect similar to a crack. When the stress reaches a value above the tensile strength, preferential deformation will occur at the section of the surface defect provided that the defect or crack is sufficiently large. As the liquid metal is known to lower the surface tension of the newly formed fracture surface, its presence is likely to increase the propagation speed of the fracture thus lowering total elongations. The embrittlement of T91 is however limited since the "normal" ductile tearing mechanism which initiates by microvoid coalesence in the middle of the specimen section is still predominant.

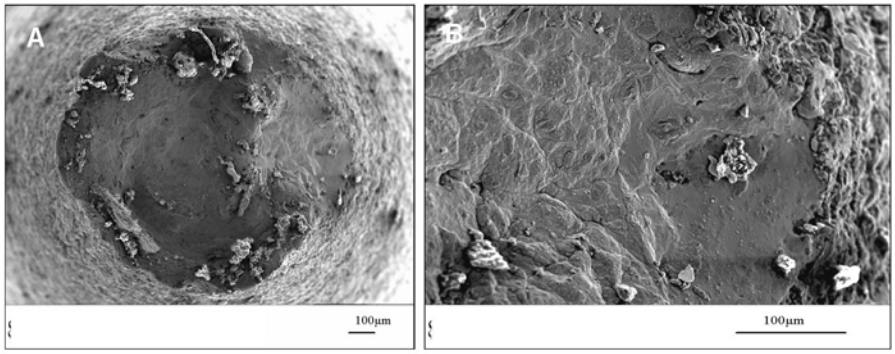

Figure 6.10: SEM observation of the fracture surface of the pre-exposed T91 sample tested at 450°C. A: overview of the entire fracture surface showing two different types of roughness; B: The brittle part of the fracture showing steps due to the actuator of the step motor.

Some samples of 316L stainless steel were submerged in the same exposure pot as the T91 specimens discussed above. Therefore, they were also exposed to low oxygen LBE at 450°C for 4000 hours. However, no difference was found between the pre-exposed 316L and the non exposed 316L steels samples.

6.3.2 SSRT tests of structural materials pre-exposed in low oxygen LBE under thermal cycling (0 dpa capsule TWIN ASTIR)

The pre-exposure under thermal cycling was performed on a capsule filled with samples of the same materials and placed inside the capsule in the identical stacking order as was the case for the samples in the LBE filled capsules which were irradiated in the TWIN ASTIR irradiation (see Chapter 4).
The thermal profile of this identical but not irradiated capsule was to be the same as for the capsules under irradiation. To achieve this, we used a PID temperature controller which had the temperature of the CALLISTO water on a minute by minute basis as an input. To compensate for the gamma heating caused by the neutron irradiation which was known to internally heat the capsule, we corrected the temperatures of the CALLISTO water environment by adding the "initially" (see Chapter 7) calculated ΔT for the capsule. The thermal exposure of this 0 dpa capsule was discussed in section 4.7 at the end of Chapter 4. The thermal cycling exposure was done to expose the material to LBE under the same thermal conditions as for the irradiated material but without irradiation to distinguish the thermal and corrosion effects from the irradiation effects.
Furthermore, the capsule was filled along with the capsules to be irradiated and thus contained LBE with the same oxygen concentration.

In contrast to the exposure of materials in oxygen depleted LBE at 450°C, the pre-exposure in low oxygen LBE under thermal cycling was performed without continuous purging with a reducing gas mixture of argon and hydrogen.

In the following sections we will discuss the results of the SSRT tests of the 316L, T91 and Si-enriched samples pre-exposed in oxygen depleted LBE under thermal cycling in the 0 dpa capsule. Since nearly all tests on the pre-exposed samples were performed in liquid metal environment, the results will be compared to the reference tests in both inert gas and liquid metal environment without prior treatment which were discussed already in Chapter 5.

The tests performed in liquid LBE on sections of the TIG and EB welds will be compared to reference tests performed in argon and gas mixture on samples fabricated from similar areas of the weld but which were not exposed to LBE prior to testing.

Since the active tests which will be discussed in Chapter 7 had to be performed in the LIMETS 2 test facility inside the hot cell and all prior non active tests, discussed in Chapter 5, had been performed in LIMETS 1, some of the samples from the 0 dpa capsule were tested in Limets 1 and some in Limets 2. This allowed us to verify whether comparison between tests performed in these two facilities would be allowed.

6.3.2.1 SSRT tests of pre-exposed 316L

The SSRT tests on pre-exposed 316L samples from the 0 dpa capsule were performed at 350°C, using three different strain rates. At the highest strain rate (1.10^{-3} s^{-1}) and at the lowest strain rate (1.10^{-6} s^{-1}) used, we also performed a test on a cleaned sample in gas environment.
These samples were cleaned using a mixture of acetic acid, ethanol and hydrogen peroxide in a 1:1:1 ratio similar to the cleaning process used to remove the LBE from the fracture surface for SEM investigation. This cleaning method removes the adherent LBE without corroding the steel.
By testing a cleaned specimen in gas environment we could determine whether any deterioration in mechanical properties would be due to a change in bulk properties or severe dissolution corrosion or due to the presence of liquid metal at the surface.

The tensile curves of the pre-exposed 316L specimens from the 0 dpa capsule tested at 350°C are depicted in Figure 6.11. On the left are the curves of the material tested at 1.10^{-3} s^{-1}. The tests at a strain rate of 5.10^{-5} s^{-1} and 1.10^{-6} s^{-1} are respectively in the middle and on the right in Figure 6.11. No apparent embrittlement can be seen in the tensile curves.

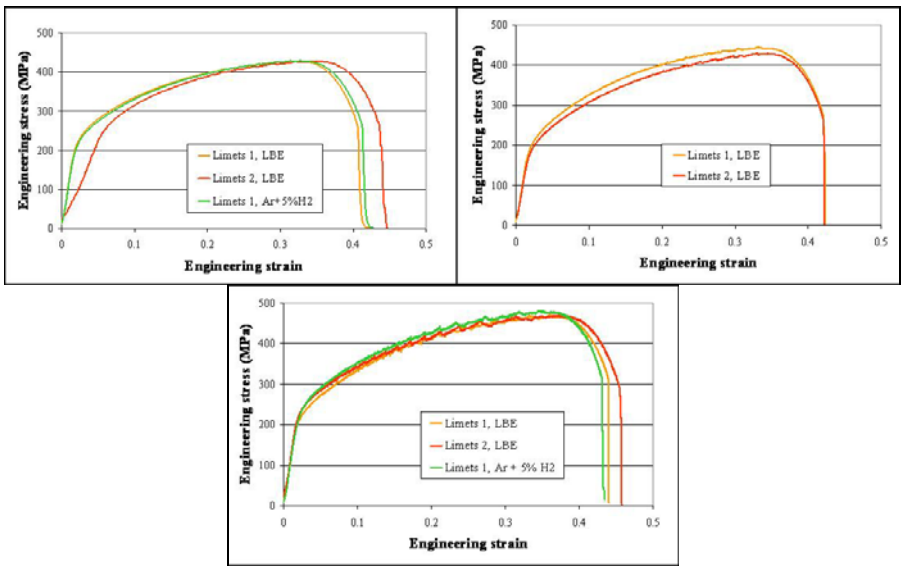

Figure 6.11: Tensile curves of 316L pre-exposed to LBE under thermal cycling (from 0 dpa capsule) tested at 350°C. Upper left: strain rate 1.10^{-3} s^{-1}; Upper right: strain rate 5.10^{-5} s^{-1}; Below: strain rate 1.10^{-6} s^{-1}.

Furthermore, there is no difference between test results from Limets 1 and from Limets 2. When the tensile properties are compared with the reference tests prior to exposure as discussed in Chapter 5, it can be seen in that they coincide very well. As before, no effect of the liquid metal environment has been found on the mechanical properties of 316L stainless steel.

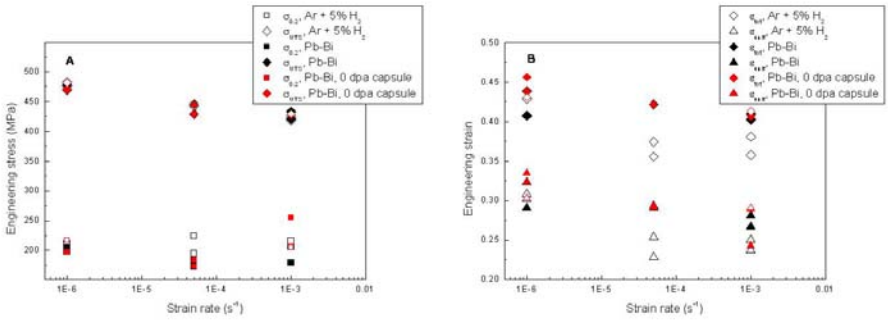

Figure 6.12: Tensile results of 316L as function of strain rate (temperature 350°C). Full symbols for tests performed in LBE, empty symbols for reference data on the same batch of 316L, tested in Ar + 5% H_2. Symbols in red for 316L specimens from the 0 dpa capsule exposed to thermal cycling prior to testing. A: Influence of the strain rate on the yield stress, ultimate tensile strength in LBE at 350°C; B: Influence of the strain rate on the uniform elongation and total elongation in LBE at 350°C.

6.3.2.2 SSRT tests of pre-exposed T91

Similar to the tests performed on the pre-exposed samples of 316L, the SSRT tests on pre-exposed T91 samples from the 0 dpa capsule were performed at 350°C, using three different strain rates. At the highest strain rate (1.10^{-3} s^{-1}) and at the lowest strain rate (1.10^{-6} s^{-1}), we also performed a test on a cleaned sample in gas environment. The tensile curves are depicted in Figure 6.13.

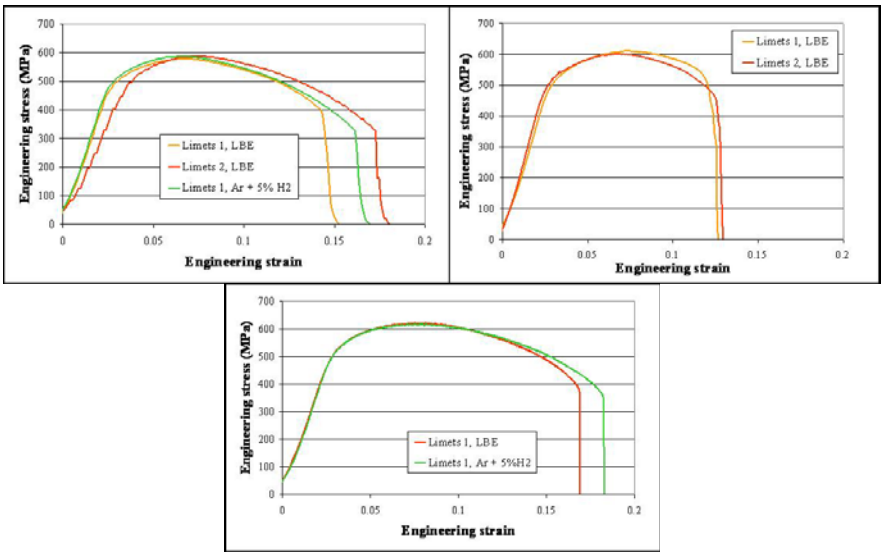

Figure 6.13: Tensile curves of T91 pre-exposed to LBE under thermal cycling (from 0 dpa capsule) tested at 350°C. Upper left: strain rate 1.10^{-3} s^{-1}; Upper right: strain rate 5.10^{-5} s^{-1}; Below: strain rate 1.10^{-6} s^{-1}.

On the left are the curves of the material tested at 1.10^{-3} s^{-1}. The tests at a strain rate of 5.10^{-5} s^{-1} and 1.10^{-6} s^{-1} are respectively in the middle and on the right in Figure 6.13. Although both curves nicely coincide, one can see that the T91 tested in LBE at 350°C at a strain rate of 5.10^{-5} s^{-1} has considerably less total elongation than the ones tested at higher and at lower strain rate. In general, the shape of the tensile curve is different and this is an indication these samples suffered from LME.

The tests at a strain rate of 1.10^{-3} s^{-1} show a relatively large amount of scatter in total elongation. The red curve resulting from a test in LBE has more total elongation than the green curve resulting from the test on the cleaned sample. The light orange curve does however show less total elongation which could be due to LME.
At a strain rate of 1.10^{-6} s^{-1} the red curve resulting from the test in liquid LBE also has less total elongation than the green curve of the cleaned sample tested in gas. However, the tensile curves presented in Figure 6.13 are not sufficient proof of the occurrence or absence of LME under these conditions. More extensive data

comparison would be beneficial and furthermore analysis of the fracture surface is needed.

In Figure 6.14 we compare the tensile results from the samples that were pre-exposed in the 0 dpa capsule to the reference tests and tests performed in LBE without prior treatment as discussed in Chapter 5. The red symbols represent test results from the 0 dpa capsule pre-exposure.
It is obvious that even after pre-exposure during an extended time period, the testing environment does not affect the strength properties of the T91 steel.

Based on Figure 6.14, one can assume that the decrease in total elongation when tested in LBE in comparison with the cleaned sample tested in argon and hydrogen gas at a strain rate of 1.10^{-6} s^{-1} can not be attributed to LME. The tests performed in LBE at a strain rate of 5.10^{-5} s^{-1} after pre-exposure in the 0 dpa capsule are however most likely cases of LME. The test performed in LBE at a strain rate of 1.10^{-3} s^{-1} which had the least total elongation might be suffering from LME however the difference is too small to draw any conclusion without looking at the fracture surface.

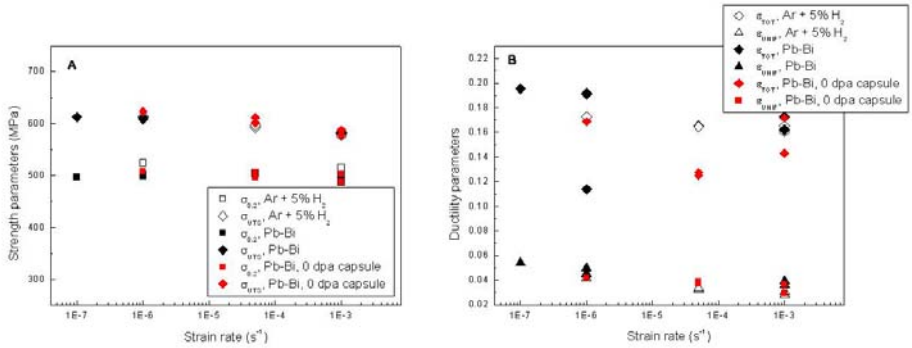

Figure 6.14: Tensile results of T91 as function of strain rate (temperature 350°C). Full symbols for tests performed in LBE, empty symbols for reference data on the same batch of T91 tested in air. Red symbols for results from pre-exposed T91 after thermal cycling (0 dpa capsule) A: Influence of the strain rate on the yield stress, ultimate tensile strength in LBE at 350°C; B: Influence of the strain rate on the uniform elongation and total elongation in LBE at 350°C.

To clarify the possible presence of LME the fracture surfaces were all examined by SEM. Both pre-exposed samples tested in liquid LBE at 350°C at strain rate of 5.10^{-5} s^{-1} did indeed show significant signs of LME and several initiation sites could be distinguished at the surface. These are all indicated by red arrows in Figure 6.15. The sample tested at a strain rate of 1.10^{-3} s^{-1} showing the least total elongation as shown in Figure 6.14 above, also had two sites of LME fracture. These were however much smaller. All other samples were fully ductile.

It can be said that pre-exposure of T91 in contact with low oxygen LBE increases the occurrence of LME however the magnitude of embrittlement cannot be quantified reliably based on these results.

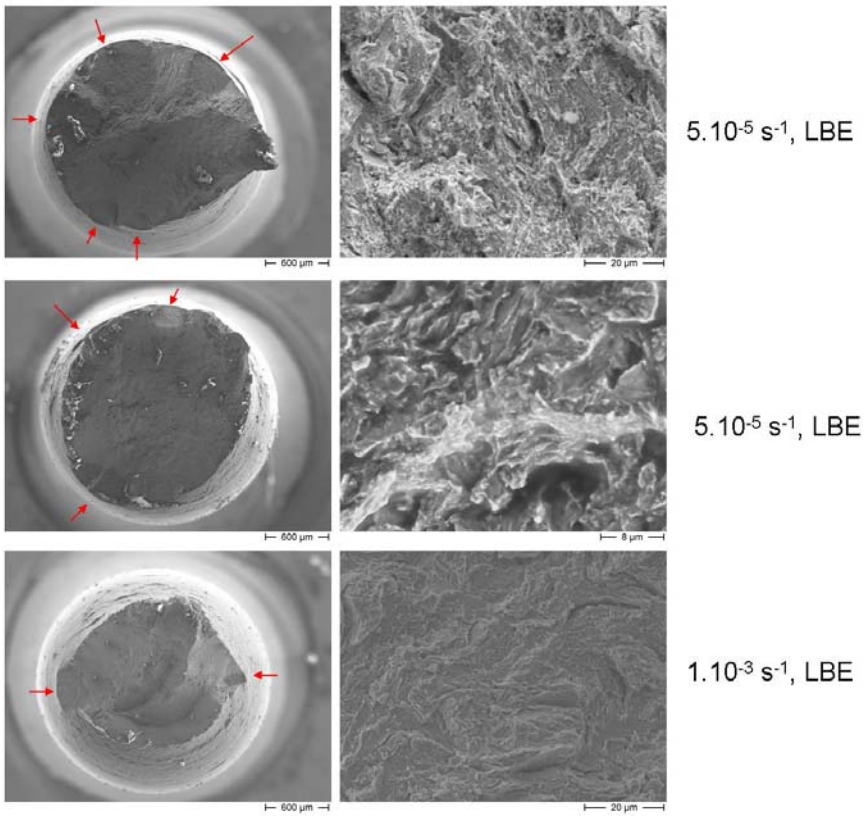

Figure 6.15: Fracture surface examination of T91 tested in LBE at 350°C after pre-exposure in the 0 dpa capsule. LME initiation sites are indicated by red arrows. (Above & Middle) pre-exposed T91 tested in liquid LBE at a strain rate of 5.10^{-5} s^{-1}. (Below) pre-exposed T91 tested in liquid LBE at a strain rate of 1.10^{-3} s^{-1}.

6.3.2.3 SSRT tests of pre-exposed Si enriched steels

The pre-exposure under thermal cycling performed using the so called 0 dpa capsule only contained a limited amount of material. The 2439, 2440, 2441 and 2442 silicon enriched experimental steels were included in this pre-exposure. At the time the exposure started, we did not have the other elevated Si materials to our disposal.
Here, we will compare the results after exposure to the reference tests in both air and LBE which were already discussed in Chapter 5.

2439 steel (11.58 wt% Cr; 0.48 wt% Ni; 2.75 wt% Si)

The 2439 Si enriched steel was tested in liquid LBE purged with a gas mixture of argon and 5% hydrogen at 350°C, using a strain rate of 5.10^{-6} s^{-1} after pre-exposure in low oxygen LBE under thermal cycling as described in section 4.7 of Chapter 4. The resulting tensile curve is compared to the tensile curve obtained in gas environment and the tensile curve obtained by testing in liquid LBE without any prior treatment as discussed in Chapter 5. These tensile curves are depicted in Figure 6.16.

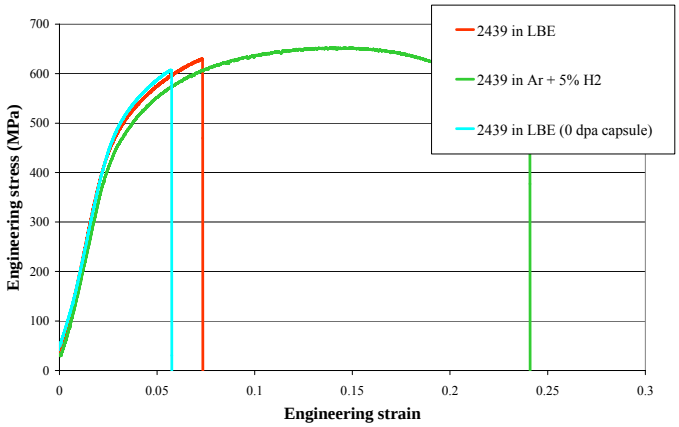

Figure 6.16: Tensile curves of 2439 steel tested at 350°C, 5.10^{-6} s^{-1} in Ar + 5% H_2 (green), in LBE purged with Ar + 5% H_2 (red) and in LBE after pre-exposure under thermal cycling in the 0 dpa capsule (turquoise).

After exposure in low oxygen LBE under thermal cycling the amount of total elongation is further decreased and the ultimate tensile strength is clearly not reached. The mechanical behaviour of the 2439 steel prior to sudden and instant fracture remains however the same as prior to exposure. This indicates the bulk properties of the material have not been affected under prolonged contact with liquid LBE.

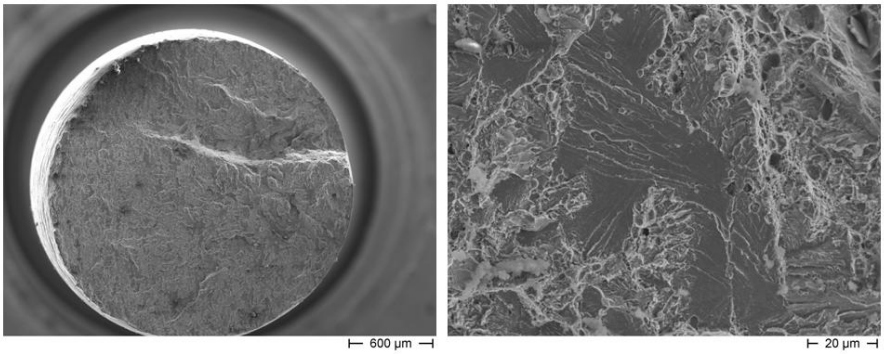

Figure 6.17: Fracture surface of 2439 steel tested in liquid LBE at 350°C, using a strain rate of 5.10^{-6} s^{-1} after pre-exposure in the 0 dpa capsule.

The sample showed no necking and the fracture is nearly perpendicular to the loading direction. The fracture surface, depicted in Figure 6.17 is affected by LME over its entire surface. The detailed image, shown on the right in Figure 6.17, shows very similar aspects to those of the semi circular LME fracture areas of T91 shown above. Here, the majority of the small bainitic grains seem to be fractured in cleavage mode as indicated by the river patterns. However, still a significant amount of dimples can be found.
In contrast with the semi circular areas of LME in T91, it is very difficult to identify the initiation site or sites on the fracture surface of the 2439 steel sample pre-exposed in the 0 dpa capsule.

2440 steel (13.52 wt% Cr; 0.51 wt% Ni; 4.8 wt% Si)

After pre-exposure in the 0 dpa capsule, the 2440 steel was tested in liquid LBE purged with argon and hydrogen gas at 350°C using a strain rate of 5.10^{-5} s^{-1}. These conditions are identical to those used for the tests discussed in Chapter 5 on the as received 2440 steel. The resulting tensile curve from the test after pre-exposure is compared to the obtained curves of the as received 2440 steel in Figure 6.18.

Similar to the behaviour of the 2439 steel after pre-exposure, the 2440 steel suffers from a further decrease in total elongation when tested in liquid LBE after pre-exposure. Nearly no plasticity is left as the 2440 steel sample suddenly and completely breaks near its yield stress. The elastic behaviour of the pre-exposed sample is identical to this of the as received material. It is very clear that despite its very high corrosion resistance in LBE, the mechanical behaviour of the 2440 steel is very severely affected by the liquid metal environment.

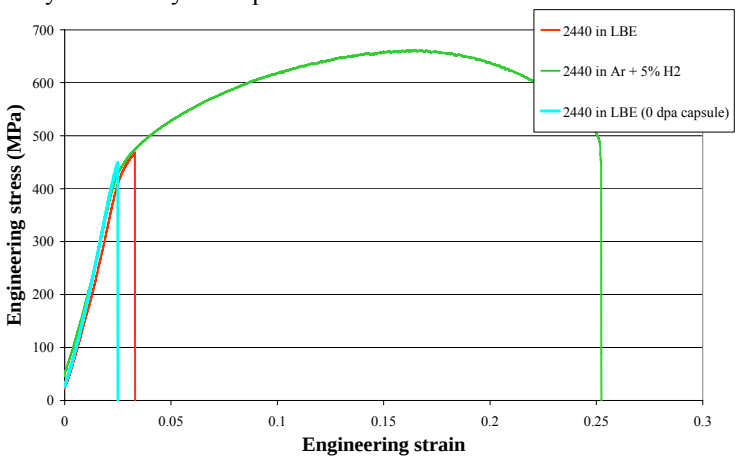

Figure 6.18: Tensile curves of 2440 steel tested at 350°C, 5.10^{-6} s^{-1} in Ar + 5% H_2 (green), in LBE purged with Ar + 5% H_2 (red) and in LBE after pre-exposure under thermal cycling in the 0 dpa capsule (turquoise).

Examination of the fracture surface confirms the expected brittle LME fracture without any necking. The SEM pictures presented in Figure 6.19 show no dimples and when examining the detailed fracture surface image it is clear that the fracture type is pure cleavage.

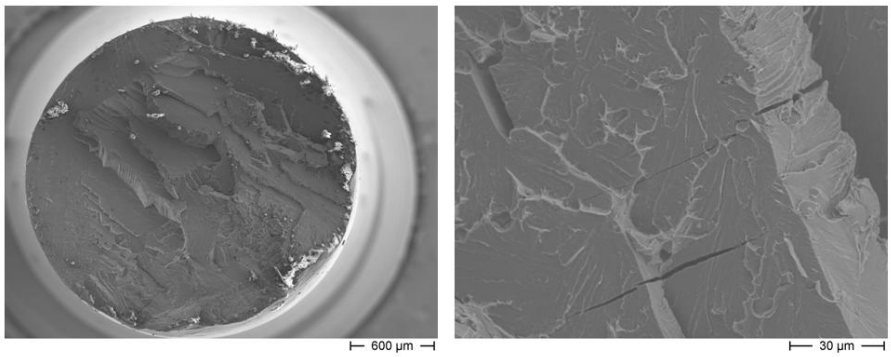

Figure 6.19: Fracture surface of 2440 steel tested in liquid LBE at 350°C, using a strain rate of 5.10^{-6} s^{-1} after pre-exposure in the 0 dpa capsule.

The straight crack lines are all perpendicular and the fracture surface is made up of areas having sharp corners. These are indications that the cleavage fracture is along certain crystallographic orientations. Unfortunately, it is very difficult to identify the initiation site or sites of the LME induced fracture.

2441 steel (18.35 wt% Cr; 0.51 wt% Ni; 5.2 wt% Si)

As for the 2439 and 2440 steels, the 2441 steel was tested at 350°C, 5.10^{-5} s^{-1} after pre-exposure in the 0 dpa capsule. The resulting tensile curve is depicted in Figure 6.20 where it is compared to the reference tests discussed in Chapter 5.
Unlike the 2439 and 2440 steels, the 2441 steel is not more severely embrittled in the liquid metal environment after pre-exposure in the 0 dpa capsule. The 2441 steel breaks suddenly and completely near its yield stress as it already did when tested in the as received condition in liquid LBE prior to exposure. This could be considered as an indication that this is the worst possible liquid metal embrittlement for this steel under these conditions. The elastic behaviour of the 2441 steel remains unchanged.

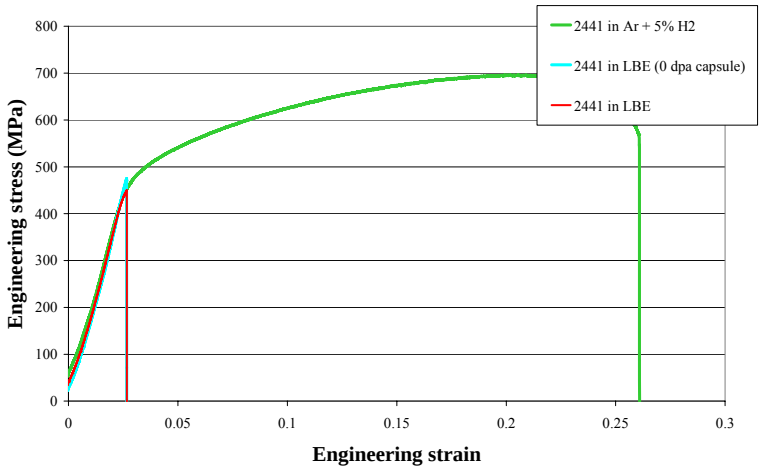

Figure 6.20: Tensile curves of 2441 steel tested at 350°C, 5.10^{-6} s^{-1} in Ar + 5% H_2 (green), in LBE purged with Ar + 5% H_2 (red) and in LBE after pre-exposure under thermal cycling in the 0 dpa capsule (turquoise).

Examination of the fracture surface of the pre-exposed 2441 steel sample revealed a 100% brittle fracture image. As shown in Figure 6.21, the fracture surface shows no dimples and fracture aspects are very flat surfaces at sharp corners of about 90° in respect to each other.

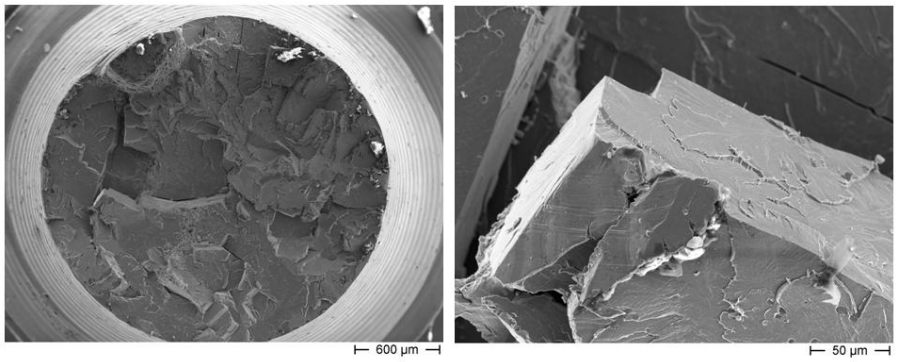

Figure 6.21: Fracture surface of 2441 steel tested in liquid LBE at 350°C, using a strain rate of 5.10^{-6} s^{-1} after pre-exposure in the 0 dpa capsule.

While the 2441 steel tested in LBE at 350°C without any pre-exposure showed some dimples and the initiation of the LME fracture was probably at the bottom of picture C in Figure 5.19, there were no dimples seen on this fracture surface and the initiation site or sites cannot be identified.

2442 steel (18.25 wt% Cr; 14.16 wt% Ni; 5.2 wt% Si)

The only austenitic silicon enriched steel available to us at the onset of the pre-exposure was the 2442 steel. The material was tested after pre-exposure under the same condition as the previously discussed ferritic/bainitic/martensitic elevated silicon steels. This means the test was performed at 350°C in liquid LBE purged with a gas mixture of argon and 5% hydrogen and at a strain rate of 5.10^{-5} s^{-1}. The resulting tensile curve is compared to the reference tests in both gas and liquid metal environment in Figure 6.22.

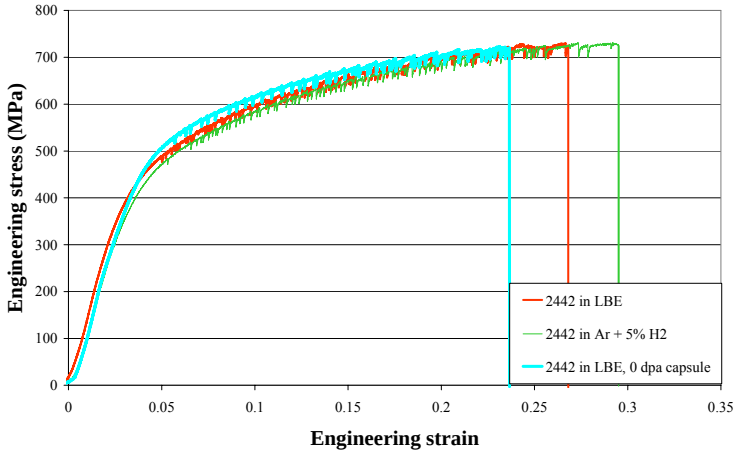

Figure 6.22: Tensile curves of 2442 steel tested at 350°C, 5.10^{-6} s^{-1} in Ar + 5% H_2 (green), in LBE purged with Ar + 5% H_2 (red) and in LBE after pre-exposure under thermal cycling in the 0 dpa capsule (turquoise).

The 2442 steel shows the same deformation behaviour after pre-exposure as that of the as received 2442 steel. The fanciful shape of the tensile curve prior to sudden fracture without any necking is typical for the so called micro-brittleness. This means small cracks are formed in the material under deformation until the material suddenly completely breaks.

It is remarkable however that the point at which the 2442 steel finally breaks is shifted to smaller elongations due to the liquid metal environment. This decrease in total elongation was observed after testing the as received 2442 steel in liquid LBE but since there was only one test this premature failure could have been due to experimental scatter. The further decrease in total elongation after pre-exposure in liquid LBE under thermal cycling does confirm there could be a certain liquid metal embrittlement effect present in this austenitic 2442 steel. However, the micro-brittleness fracture type might lead to large scatter in total elongation values and the amount of experimental data is still very small.

Since the fracture surface of the 2442 steel tested in liquid LBE after pre-exposure in the 0 dpa capsule looks very similar to the fracture surfaces of the as received samples tested in gas and LBE, no firm conclusions can be made on the effect of the liquid LBE on the fracture properties of the 2442 steel.

6.3.2.4 SSRT tests of pre-exposed T91/T91 welds

To examine the mechanical behaviour of the T91/T91 welds in liquid LBE, cylindrical tensile specimens with a total length of 24 mm, a gauge length of 12 mm and a diameter of 2.4 mm had to be taken out of the weld so that a maximum of information could be extracted out of a minimum of weld material. In principle, tensile tests on this geometry of specimen are not optimal to examine the behaviour of welds. However, in the frame of the TWIN ASTIR irradiation experiment, the used samples had to be compatible with the geometry of the irradiated samples.

The T91/T91 TIG weld was too large to have a single specimen contain the HAZ of both sides as well as the weld deposit in its gauge section. It was therefore decided to manufacture specimens out of the deposited weld metal in the length of the welded seem, across the TIG weld having the deposited weld metal in the middle of the gauge and across the weld having the HAZ in the middle of the gauge.

For the EB weld however, the very narrow weld seem allowed all specimens to be manufacture across the weld having the entire weld as well as both HAZ in their gauge section.

In the following two sections, the mechanical properties of the T91/T91 welds in liquid LBE will be further described.

6.3.2.4.1 SSRT tests of pre-exposed T91/T91 TIG weld

The T91/T91 TIG weld was tested in the welded and heat treated condition prior to exposure in oxygen depleted LBE in the 0 dpa capsule. As described in section 2.2.2 of Chapter 2, the T91/T91 TIG weld had very good mechanical properties and fully behaved as expected from a high quality T91/T91 TIG weld.

Due to the reproducibility difficulties encountered in tensile testing of T91 base material in liquid LBE and the inherent difficulties in the interpretation of tensile tests of welds, no tests were performed in liquid metal environment prior to exposure. After pre-exposure to oxygen depleted LBE in the 0 dpa capsule, the T91/T91 TIG weld was tested and compared with similar T91/T91 TIG weld

samples tested in argon and hydrogen gas mixture without any prior surface treatment. The resulting tensile curves are depicted in Figure 6.23.

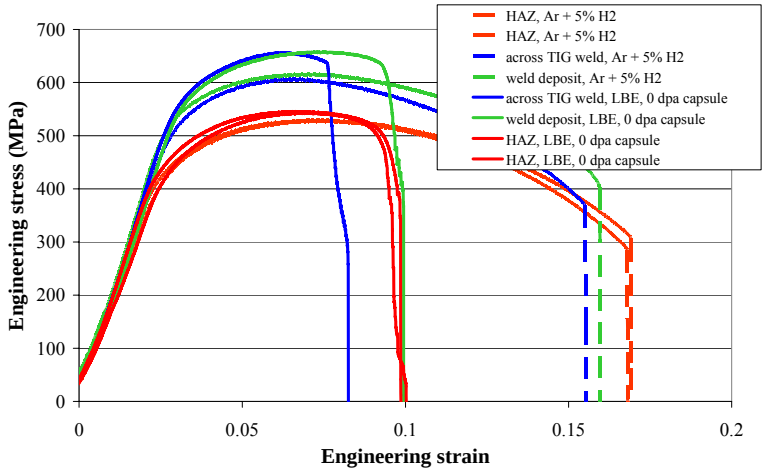

Figure 6.23: Tensile curves of T91/T91 TIG weld tested at 350°C, 5.10^{-6} s^{-1} in different orientations in both Ar + 5% H_2 and in liquid LBE after pre-exposure in oxygen depleted LBE under thermal cycling (0 dpa capsule). Full curves result from tests in LBE after pre-exposure, dashed curves result from tests in Ar and H_2 gas mixture. (Blue) specimen across TIG weld, having weld deposit of the centre of the gauge; (Green) specimen fully inside the weld deposit along the length of the welded seem; (Red) specimen taken across the TIG weld, having the HAZ in the middle of the gauge length.

The dashed curves in Figure 6.23 are resulting from the reference tests performed in argon and hydrogen gas mixture whereas the full curves are resulting from tests in liquid LBE after pre-exposure in the 0 dpa capsule.

Specimens taken across the T91/T91 TIG weld, having the weld deposit in the middle of the gauge are depicted in blue in Figure 6.23. Specimens taken inside the weld deposit, along the length of the weld seem are depicted in green and specimens taken across the T91/T91 TIG weld having the HAZ in the middle of their gauge are depicted in red.

It can immediately be seen in Figure 6.23 that all specimens tested in liquid LBE after pre-exposure in the 0 dpa capsule show significantly less total elongation than the similarly oriented specimens tested in gas environment. In general, the fracture behaviour of the T91/T91 TIG welded material has been changed when tested in liquid LBE environment.

The tested T91/T91 TIG weld is completely comprised of T91 material however the weld deposit is slightly over alloyed as could be seen in the chemical analysis profile across the weld presented in Figure 2.43 in section 2.2.2.
In contrast to the reproducibility problem we encountered with the T91 base material, all tested specimens from the TIG weld show similar behaviour when tested in liquid LBE. All specimens show reduced total elongation while other tensile properties remain approximately the same.

The fracture behaviour is not suddenly resulting in complete failure as was the case for the elevated silicon steels but fracture seems to be faster with less plastic work than when tested in gas environment.

The fracture surface analysis confirmed the presence of LME since all fracture surfaces clearly showed brittle fracture initiation sites at the surface. This can be seen very well in Figure 6.24 where an overview is presented of the fracture surfaces of three T91/T91 TIG samples tested in LBE after pre-exposure in the 0 dpa capsule. The LME effect can be clearly recognised by the semi circular crack patterns which initiated at the surface. None of the samples was fully fractured in a brittle LME fashion.

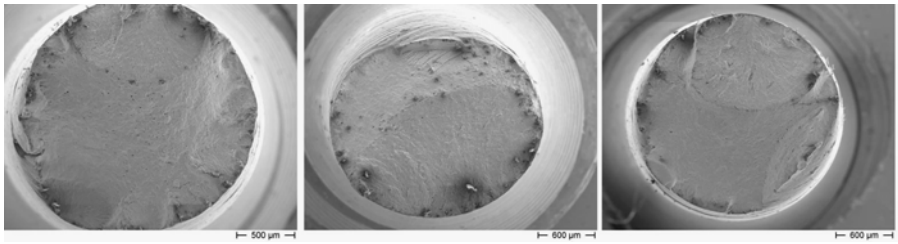

Figure 6.24: Fracture surfaces of T91/T91 TIG weld samples. (Left) sample taken across the weld, having the HAZ in the middle of the gauge; (Middle) sample taken across the weld, having the weld deposit in the middle of the gauge; (Right) sample taken in the weld deposit along the length of the weld seem.

It is especially difficult to identify where exactly in the welded connection the fracture took place. All three specimen orientations show the same tendency to break in liquid metal environment and the fracture is always approximately in the centre of the gauge length. Furthermore, due to the small differences in chemical composition along the weld, the position of the fracture is difficult to determine. What is very obvious is that the T91/T91 TIG welded connection is much more prone to LME than the T91 base material.

6.3.2.4.2 SSRT tests of pre-exposed T91/T91 EB weld

The SSRT tests of the T91/T91 EB weld discussed here were all performed on specimens taken across the EB weld, having the weld itself in the middle of their gauge. As mentioned before, since the EB weld is so narrow the specimen gauge contains both HAZ and weld zone as well as a significant portion of base material.

All T91/T91 EB specimens were given a proper PWHT according to the thermal treatment proposed in Chapter 2.

The tensile curves resulting from tensile testing of the T91/T91 EB weld specimens are depicted in Figure 6.25. For comparison a tensile curve of the T91 base material tested in gas environment was added to the figure.

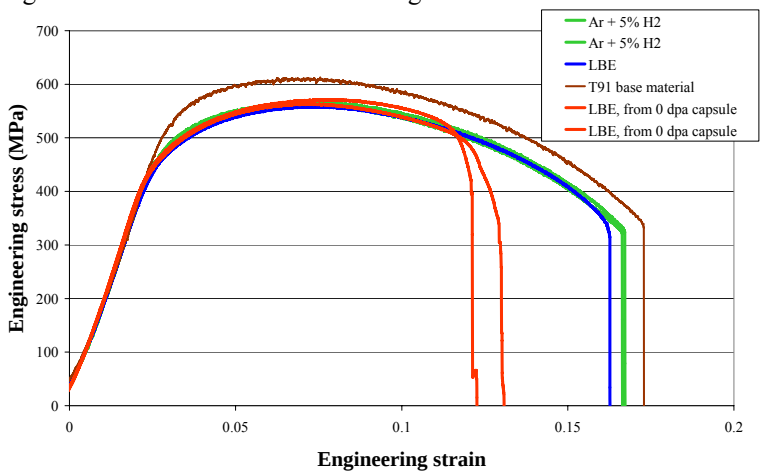

Figure 6.25: Tensile curves of T91/T91 EB weld tested at 350°C, 5.10^{-6} s^{-1} in Ar + 5% H_2 and in liquid LBE purged with Ar + 5% H_2. (Green) T91/T91 EB weld tested in Ar + 5% H_2; (Blue) T91/T91 EB weld tested in liquid LBE without pre-exposure; (Red) T91/T91 EB weld tested in liquid LBE after pre-exposure in the 0 dpa capsule; (Brown) T91 base material.

The yield stress and ultimate tensile strength of the T91/T91 EB weld are slightly lower than the values for the T91 base material when tested under the same conditions. At first sight this would lead to the expectation that the T91/T91 EB weld would be less prone to LME since it is weaker as discussed in Chapter 1. However, the hardness profile across the EB weld discussed in section 2.2.2.2.2.1 of Chapter 2 showed a sharp increase in hardness in the welded zone. Due to the very narrow EB weld seem, this area of increased hardness has very little influence on the tensile behaviour in gas environment.

Although the T91/T91 EB weld does not show any LME effect when tested in liquid LBE without any pre-exposure as depicted by the blue curve in Figure 6.25, both specimens of the T91/T91 EB weld have significantly less total elongation when tested in liquid LBE after pre-exposure in the 0 dpa capsule (red curves in Figure 6.25). Similar to the fracture behaviour of the T91/T91 TIG weld specimens discussed in the previous section, the fracture is not instantaneous and occurs after a significant amount of plastic deformation.
Prior to the onset of cracking, the mechanical behaviour of the material tested in liquid LBE is completely the same as the mechanical behaviour of the material tested in gas environment.

The fracture surfaces of the two T91/T91 EB welded specimens which were tested in liquid LBE after pre-exposure in the 0 dpa capsule were studied by SEM and the resulting pictures are given in Figure 6.26.

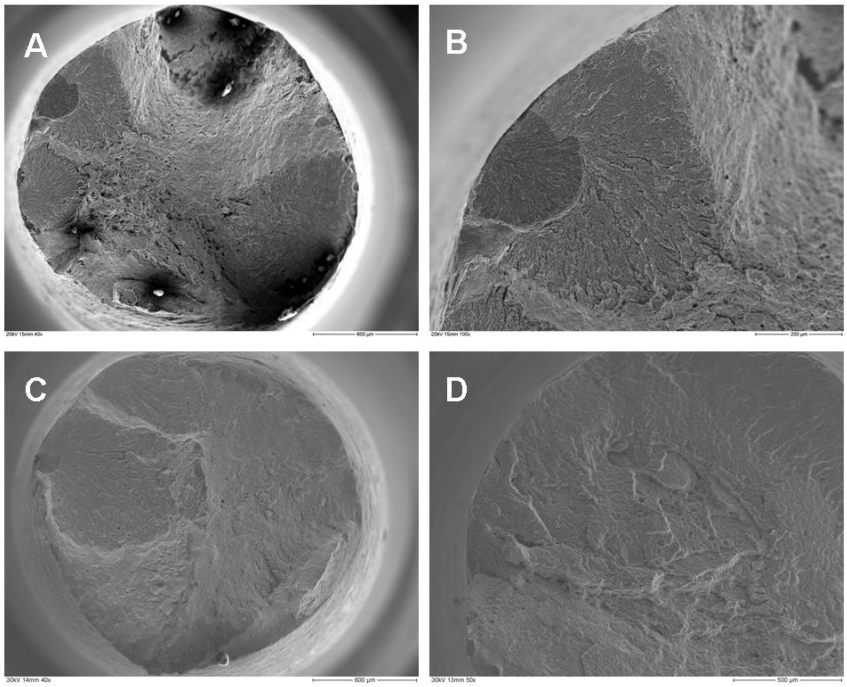

Figure 6.26: SEM examination of fracture surfaces of T91/T91 EB welded specimens, tested in LBE at 350°C, using a strain rate of 5.10^{-6} s^{-1}. A, C: Overview of T91/T91 EB welded specimens showing some necking and several semi circular LME fracture areas; B, D: Details of fracture surfaces depicted in A and C respectively, showing the flowering pattern initiated at the surface typical for LME fracture.

The overview images of the fracture surfaces (Figure 6.26A & C) both show several LME initiation sites which progressed into the bulk leaving a semi circular "flowering pattern" in the fracture surface. Similar to all the previously studied

affected fracture surfaces of T91 steel, the fracture surfaces are not fully brittle but show a majority of ductile fracture surface.
The fracture occurred in the centre of the specimens gauge but due to the very narrow nature of the EB weld it is not possible to say whether the fracture occurred in the HAZ near the welded zone or in the welded zone itself.
The obvious presence of LME in T91/T91 EB welded specimens compared to the sporadic occurrence in the T91 base material does lead us to believe that the increased hardness of the welded zone which is known to increase the susceptibility to LME has led to the LME fracture of the tested T91/T91 EB welded specimens.

6.3.2.5 SSRT tests of pre-exposed T91/316L welds

The complex nature of the dissimilar T91/316L weld makes it very difficult to assess the mechanical properties of this welded connection in contact with liquid LBE. Furthermore, in the case of the T91/316L weld the weld in fact comprises of four different materials and could not be fully included in the gauge of a simple small tensile specimen. Therefore, we fabricated tensile specimens along different orientations. Samples were taken across the weld with either the HAZ on the T91 side or the HAZ on the 316L side in the middle of the gauge and inside the 316L weld material.
For the T91/316L EB weld, the narrow weld made it possible to fully include the HAZ on both sides of the weld as well as the weld deposit itself in the gauge of the sample. Therefore, all T91/316L EB weld specimens were taken across the weld, having the weld deposit in the middle of the gauge.

In the following two sections we will further discuss the mechanical properties of the T91/316L mixed TIG and EB welds in contact with liquid LBE after pre-exposure in oxygen depleted LBE under thermal cycling in the 0 dpa capsule.

6.3.2.5.1 SSRT tests of pre-exposed T91/316L TIG weld

Tensile tests were performed in three different orientations as mentioned above. The stress-strain curves are depicted in Figure 6.27, along with a schematic representation of the orientation of the sample. The schematic representation of the T91/316L TIG weld was already discussed more in detail in section 2.2.3.1 of Chapter 2.

The tests were performed both in a gas mixture of argon and 5% hydrogen as well as in liquid LBE. The samples tested in gas environment did not undergo any treatment or exposure prior to testing. The samples tested in LBE were pre-exposed in low oxygen LBE in the 0 dpa capsule, following the thermal cycling pattern identical to

the samples in the Twin Astir irradiation experiment which will be discussed in the next chapter. This thermal cycling means 6 periods of approximately 1 month each at about 360°C separated by periods of about 1 month at room temperature.

As shown in Figure 6.27, the sample taken with the HAZ on the 316L side in the middle of the gauge did not undergo any liquid metal embrittlement. The sample inside the 316L weld deposit did however suffer from liquid metal embrittlement since its total elongation is significantly reduced. This effect is comparable with the embrittlement found in ferritic/martensitic steels after exposure in low oxygen lead alloys and does not represent a dramatic problem since sufficient ductility is still present. The sample with the HAZ on the T91 side in the middle of the gauge however, broke in a fully brittle manner displaying very little elongation and no necking at all. It can be seen from the picture of the broken sample in Figure 6.27, that the specimen was broken at the interface of the T91 with the 309 steel. This severity of liquid metal embrittlement is probably due to the increased hardness at this location of the weld as was depicted in the hardness profile of the T91/316L TIG weld discussed in section 2.2.3.1.2.1.

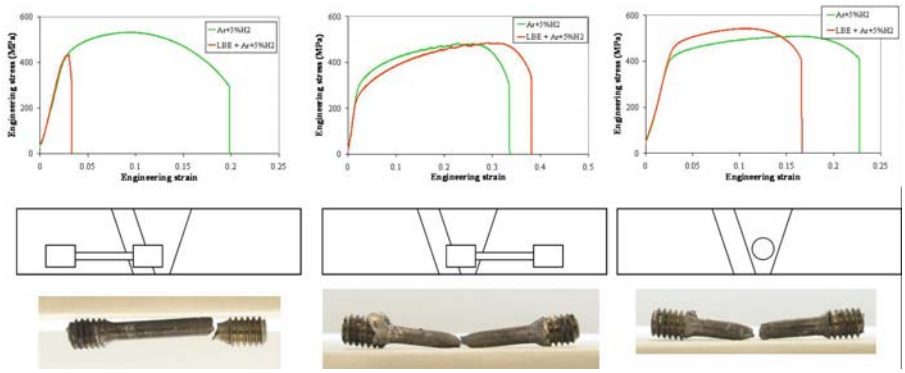

Figure 6.27: Tensile results of T91/316L TIG weld tested in Ar + 5% H_2 and LBE. Schematic representation of sample orientation indicated below the stress strain curves. Picture of the broken sample after testing in LBE depicted below the schematic representation of sample orientation.

The fracture surface of the most embrittled sample, being the one having the HAZ on the T91 side in the middle of the gauge is depicted in Figure 6.28. The fracture is entirely brittle except for rather small areas showing dimples. The detailed picture in Figure 6.28 shows what appears to be an initiation site at the edge of the sample. However, in contrast to previous samples where the LME effect was characterized by a semi circular pattern, the initiation on this area seems to have been all along the edge.

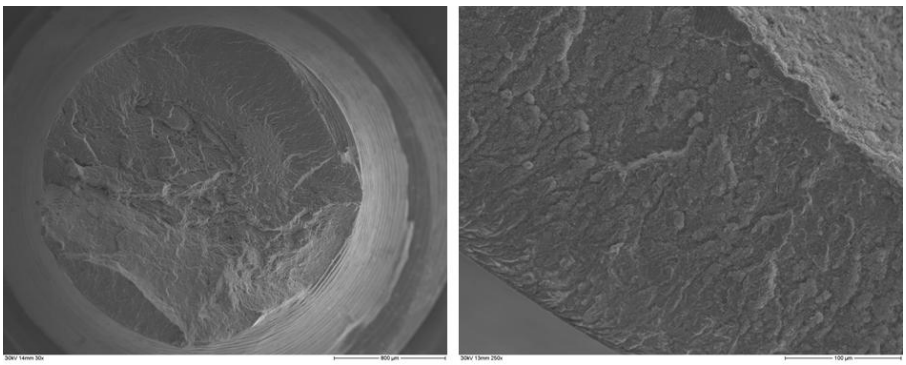

Figure 6.28: SEM fracture surface analysis of the T91/316L TIG weld sample having the HAZ on the T91 side in the middle of the gauge.

The embrittlement of the buttering area in liquid LBE should be considered problematic. The T91/316L TIG weld was fabricated by a certified welding company using one of two available conventional techniques. The other conventionally available technique uses a nickel alloy for buttering between the ferritic-martensitic T91 and the austenitic 316L steel. However, as mentioned before, this buttering material can not be used due to the very high solubility of nickel in liquid LBE. If both T91 and 316L will be used in any liquid LBE handling facility, the welding procedures will need to be examined thoroughly and alternatives have to be found to replace the conventional TIG welding process.

6.3.2.5.2 SSRT tests of pre-exposed T91/316L EB weld

All T91/316L EB welded specimens discussed here were given the heat treatment proposed in Chapter 2 to relieve the welding stresses as much as possible without softening the 316L side too much.
Because we only needed to test one orientation, it allowed us to perform two tests per condition. The results of the tensile tests are depicted in Figure 6.29. It can be seen that the shape of the stress-strain curve of the T91/316L EB weld is similar to this of 316L but has more limited elongation. This was to be expected since the yield and tensile strength of 316L are lower than this of T91.

Tests in Ar + 5% H_2 showed good mechanical properties. When the EB weld is tested in LBE without pre-exposure however, the specimen was broken in the weld without any necking of the sample. The fracture surface has aspects of both brittle and ductile behaviour. As depicted in the SEM picture on the lower right in Figure 6.29, some initiation sites of liquid metal embrittlement can clearly be distinguished.

After pre-exposure under thermal cycling in the 0 dpa capsule, the embrittlement is much worse and the sample breaks in the weld after very little plastic deformation.

The fracture surface is predominantly brittle. Again here, the increased susceptibility to LME in the weld is attributed to the locally increased hardness of the weld.

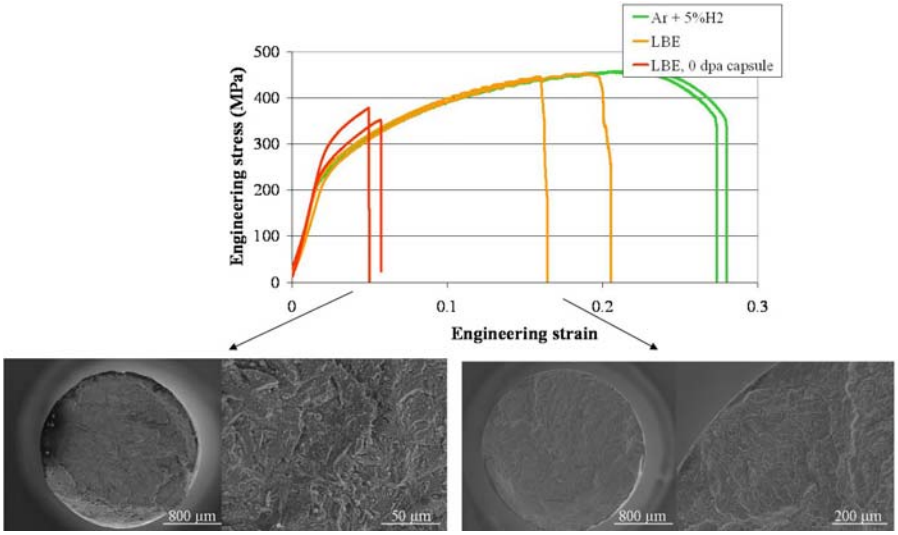

Figure 6.29: Tensile results of T91/316L EB weld tested in Ar + 5%H_2 and LBE without pre-exposure and after thermal cycling in low oxygen LBE in the 0 dpa capsule.
SEM fracture surface images show mixed fracture surface when tested in LBE without pre-exposure and fully brittle fracture after thermal cycling in low oxygen LBE.

In contrast to the T91/316L TIG weld, the T91/316L EB welds do not have buttering and the T91 is directly fused onto the 316L. This leads to very sudden changes in the chemical composition across the weld as shown in the chemical profile across the weld discussed in section 2.2.3.2 of Chapter 2. Furthermore, it was shown that the T91/316L EB weld is embrittled by LBE and that the embrittlement becomes worse after thermal cycling in contact with LBE.

7 COMPATIBILITY OF STRUCTURAL MATERIALS WITH LIQUID METALS IN NEUTRON IRRADIATION ENVIRONMENT

The most exciting phrase to hear in science, the one that heralds the most discoveries, is not "Eureka!" (I found it!) but "That's funny..."
Isaac Asimov
(1920-1992)

Experience: that most brutal of teachers. But you learn, my God do you learn.
C.S. Lewis
(1898-1963)

Chapter 7 discribes the test results of the low irradiation dose capsule of the TWIN ASTIR irradiation which was descibed in Chapter 4.
Due to safety and licensing rules, none of the polonium contaminated material could be cleaned or transported to other hot cells for possible further examination. Therefore, fracture surface examination was impossible up to now.
In this Chapter, we will first discuss the SSRT tensile curves of the T91 steel, the 316L steel, the silicium enriched steels and the TIG and EB welds of T91 and 316L after irradiation in contact with LBE.
Based on the obtained tensile results, we found a discrepancy between the measured irradiation hardening and the expected irradiation hardening for an irradiation damage of 1.5 dpa at 350°C.
After thorough investigation we found that the actual irradiation temperature was between 450 and 500°C. The cause and the scientific implications of this higher temperature irradiation will be discussed in a second point.

7.1 SSRT TESTS OF MATERIAL IRRADIATED IN CONTACT WITH LBE

The lead-bismuth eutectic filled "capsule A" of TWIN ASTIR (see Chapter 4) was retrieved from the BR2 reactor after 6 reactor cycles which resulted in an accumulated irradiation damage of about 1.5 dpa. The capsule was then stored in the BR2 deep pool to allow cooling of the capsule by natural decay. For safety reasons, the capsule was stored inside a pressure monitored container. After 11 months, the

capsule was transported to LHMA and dismantled inside hot cell 12 (see Chapter 3) and the tensile samples, irradiated in contact with liquid LBE, were tested in liquid LBE under controlled oxygen conditions in Limets 2, inside hot cell 12 (see Chapter 3).

Unfortunately, strict regulations regarding the possible Po^{210} contamination of other facilities made it impossible up to now to examine the fracture surfaces of the tested material or to examine the corrosive interaction of the LBE with the solid structural steels after irradiation in contact with LBE. To validate the obtained test results after irradiation in contact with LBE, we will compare the SSRT test results to those discussed in Chapters 5 and 6 and to the tensile results of T91 and 316L tested in LBE after irradiation in water.

In the following sections we will discuss the SSRT results of the T91 steel, 316L steel, the Si enriched steels and the T91 and 316L welds after irradiation in contact with LBE up to 1.5 dpa in the low dose capsule of the TWIN ASTIR experiment.

7.1.1 SSRT tests of T91 irradiated in contact with LBE

Tensile tests were performed on the samples irradiated in contact with LBE in liquid LBE environment at 200 and 350°C. At 350°C because this was the intended irradiation temperature and because non irradiated T91 was found to be prone to LME to a certain extent in this temperature range. Furthermore, the effect of thermal hardening by reducing the tempering temperature strongly increased the susceptibility of T91 steel to LME. Neutron irradiation at 350°C would cause a significant amount of hardening and might also increase the susceptibility of the irradiated material to LME. Furthermore, the irradiation in contact with LBE was assumed to benefit wetting and therefore also increase the material's susceptibility to LME.

Tests of T91 steel at 350°C in liquid LBE environment were performed at a strain rate of 1.10^{-3} s^{-1} and 1.10^{-6} s^{-1}. The choice for these two strain rates was based on the embrittlement of the as received T91 steel in LBE at a strain rate of 1.10^{-6} s^{-1} as shown in Figure 5.6 in Chapter 5 and the fact that the thermally hardened T91 did suffer embrittlement at a strain rate of 1.10^{-6} s^{-1} but did not at a strain rate of 1.10^{-3} s^{-1}.

The tensile curve of T91 steel tested in liquid LBE at 350°C, 1.10^{-3} s^{-1} after neutron irradiation in contact with liquid LBE up to 1.5 dpa is depicted in red in Figure 7.1. The green curves in Figure 7.1 resulted from tests on the as received T91 in gas environment. The blue and orange curves resulted from testing T91 at 350°C, 1.10^{-3} s^{-1} in LBE respectively without and with prior exposure to LBE in the 0 dpa capsule.

Contrary to our expectations, the irradiated T91 steel did not show any hardening but was softened by the neutron irradiation in contact with liquid LBE. The total elongation was comparable to one of the results of the T91 pre-exposed in the 0 dpa capsule and tested in LBE.

The absence of hardening and more precisely the softening of the T91 steel were regarded as very suspicious and it was considered to be impossible that the bulk irradiation effects could be altered by the liquid metal contact. This result caused us to re-examine the entire dismantling procedure and the test procedure. Since no abnormalities were discovered, tests were also performed at 350°C and a strain rate of 1.10^{-6} s^{-1}.

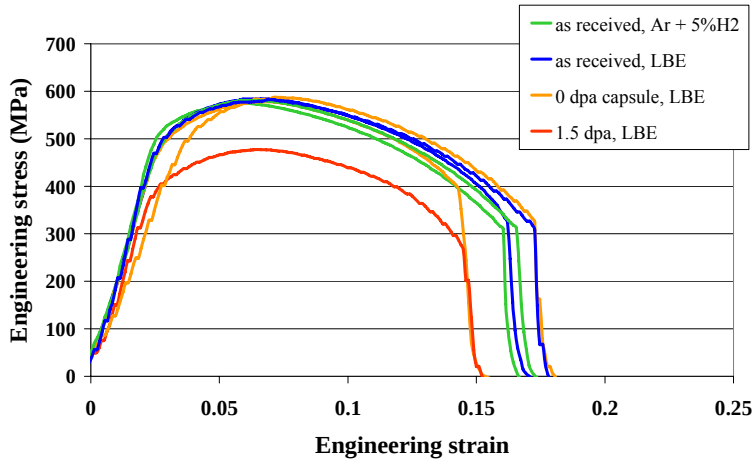

Figure 7.1: Tensile curves of T91 steel tested at 350°C, 1.10^{-3} s^{-1} in liquid LBE after neutron irradiation up to 1.5 dpa in contact with LBE (red) compared with T91 tested under the same conditions of temperature and strain rate in contact with Ar + 5% H_2 (green), in contact with LBE (blue) and in contact with LBE after pre-exposure under thermal cycling in contact with LBE in the 0 dpa capsule (orange).

The tensile curves of T91 steel tested in liquid LBE at 350°C, 1.10^{-6} s^{-1} after neutron irradiation up to 1.5 dpa in contact with LBE are depicted in red in Figure 7.2. To allow comparison with results previously discussed in Chapter 5 and Chapter 6, we have added the most important tensile curves that resulted from tests of T91 in LBE after several treatments. The reference tests performed on as received T91 steel in gas environment are depicted in green while the as received T91 tested in LBE are

depicted in blue. The orange curve was the tensile curve of T91 tested in LBE at 350°C, 1.10^{-6} s^{-1} after pre-exposure in LBE in the 0 dpa capsule.

As for the test of the irradiated T91 at a strain rate of 1.10^{-3} s^{-1}, the first test performed at a strain rate of 1.10^{-6} s^{-1} had a lower yield stress and a lower ultimate tensile strength than the other tests performed on non irradiated T91 under the same circumstances. Furthermore, the total elongation for the T91 irradiated in contact with LBE and tested in LBE was less than that of the embrittled T91 specimen discussed in Figure 5.6 and Figure 5.7 of Chapter 5. To confirm this result, the test was repeated and as can be seen in Figure 7.2, although the yield and ultimate tensile strength of the two samples vary, the LME effect is rather similar.

Although the irradiated T91 did not harden but moreover softened due to irradiation, the embrittlement due to the liquid metal environment was worse and more reproducible than prior to irradiation. Unfortunately we were unable to examine the fracture surfaces due to reasons of licensing and regulations as mentioned before.

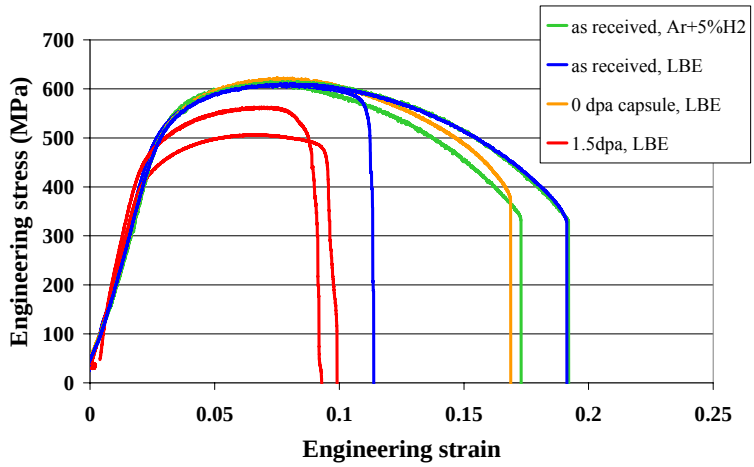

Figure 7.2: Tensile curves of T91 steel tested at 350°C, 1.10^{-6} s^{-1} in liquid LBE after neutron irradiation up to 1.5 dpa in contact with LBE (red) compared with T91 tested under the same conditions of temperature and strain rate in contact with Ar + 5% H_2 (green), in contact with LBE (blue) and in contact with LBE after pre-exposure under thermal cycling in contact with LBE in the 0 dpa capsule (orange).

It was very clear that when studying a phenomenon as complex as LME which is influenced by such a variety of metallurgical parameters, we needed to know the exact history of our material to be able to draw any conclusions. Especially since we were unable to perform any other type of examination on the irradiated material and because the softening of the bulk parameters was still considered extremely suspicious.

Apart from the tests at 350°C, tests needed to be performed at 200°C to compare with results of T91 tested in LBE after irradiation in water at a strain rate of 5.10^{-6} s^{-1} [108]. The specimens of T91 irradiated in water were irradiated at 200°C up to a displacement damage dose of almost 5 dpa. The tensile curves are compared in Figure 7.3. As in the previous two figures, the tensile curve of T91 after irradiation in contact with LBE up to 1.5 dpa is depicted in red.

Although the T91 samples were irradiated in different environments, the difference in irradiation temperature between irradiation at 200°C and at 350°C should not result in completely different mechanical behaviour. The results shown in Figure 7.3 along with the softening seen in figures 7.1 and 7.2 confirmed that somewhere along the line the irradiated T91 material was annealed above stage V for a considerable amount of time to allow annealing out of the irradiation defects.

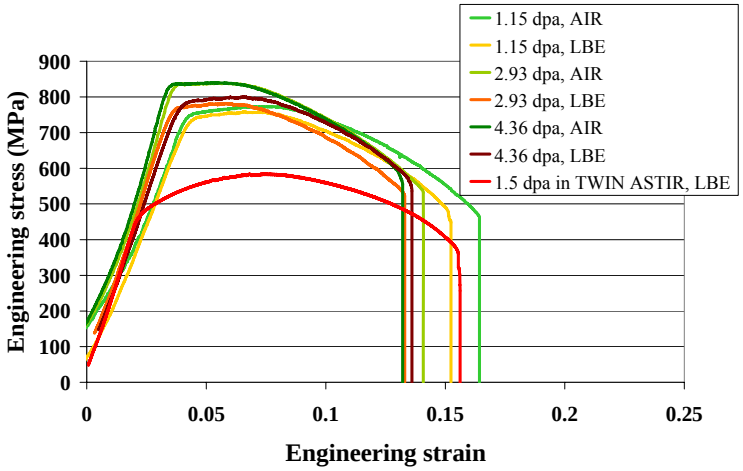

Figure 7.3: Tensile results of T91 irradiated up to 1.5 dpa in contact with liquid LBE (red) compared with tensile results of T91 irradiated in water at 200°C up to about 5 dpa.

Questioning everything we did to the material and re-examination of the entire history of the samples and the irradiation experiment led us to the discovery that the gamma heating of the liquid lead bismuth during irradiation was strongly underestimated. This caused the irradiation temperature inside the lead bismuth filled capsule to be increased to a temperature between 460 and 490°C instead of the initially envisioned 350°C. The temperature issue and its scientific implications will be further discussed in section 7.2.

The practical implication was that the envisioned TWIN ASTIR test matrix in the frame of this work was limited. However, tests at 350°C and 200°C in liquid LBE environment were still considered useful to allow comparison with previous results.

Since the TWIN ASTIR irradiation was at 460-490°C in contact with LBE, an SSRT test was performed on T91 from capsule A in contact with LBE at 450°C. This is foreseen to be the upper limit temperature of the future MYRRHA facility and furthermore no significant difference in possible LME effect was to be expected between tests performed at 450°C and at 460-490°C.
In Figure 7.4, a comparison is made between the tensile curves obtained from SSRT tests of T91 steel before and after irradiation. Both tests were performed in liquid LBE environment at 450°C using a strain rate of 5.10^{-5} s^{-1}. The green curve in Figure 7.4 was obtained by testing T91 from the SPIRE batch in LBE without any prior surface treatment. This particular experiment was included in the study on the effect of temperature on the occurrence of LME discussed in section 5.1.2 of Chapter 5. The red curve in Figure 7.4 was obtained by testing T91 from the DEMETRA batch after neutron irradiation in contact with LBE in capsule A of TWIN ASTIR. As can be seen, the yield stress and ultimate tensile strength of the irradiated T91 steel are slightly lower than those of the T91 SPIRE which is in contrast with the initial yield and tensile strength of these two batches of T91 (see Figure 2.17 in Chapter 2). However, for both tensile tests, no LME effect can be observed under these conditions. Furthermore, since both specimens show very similar ductility, the results obtained after irradiation confirm the deviating, increased ductility of the non irradiated sample (see Figure 5.2 in Chapter 5). Despite confirmation of the high ductility of T91 in LBE at 450°C caution is needed when comparing with the reference line of Figure 5.2 for tests in inert environment since data was scarce above 350°C (see discussion Figure 5.2).

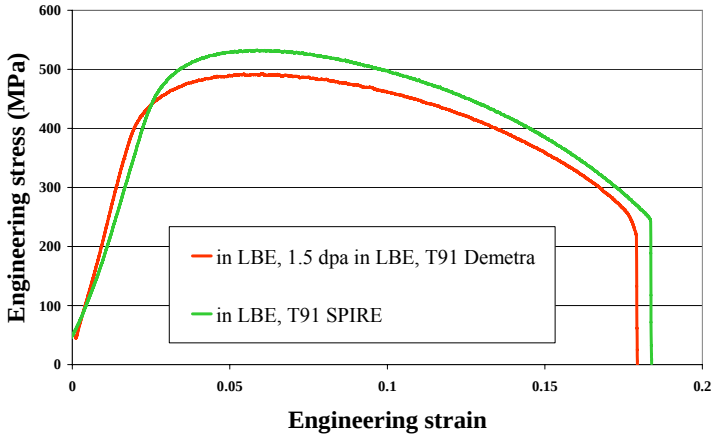

Figure 7.4: T91 steel tested in LBE at 450°C before and after irradiation in contact with LBE using a strain rate of 5.10^{-5} s^{-1}. (red) T91 DEMETRA after neutron irradiation in capsule A of TWIN ASTIR up to 1.5 dpa in contact with liquid LBE; (green) T91 SPIRE tested in liquid LBE at 450°C.

7.1.2 SSRT tests of 316L irradiated in contact with LBE

To examine the possible effect of LME on 316L stainless steel hardened by neutron irradiation in contact with LBE tests were foreseen at 350°C and at 200°C in liquid LBE. The tests at 350°C were performed at a strain rate of 1.10^{-6} s^{-1} and 1.10^{-3} s^{-1}. However, due to the unexpected increased irradiation temperature the 316L did not show any hardening and was softened due to the irradiation. At the temperature of 450-500°C the liquid metal corrosion plays an important role and may promote degradation of the material properties. However, this degradation is still too small to influence the tensile behaviour of the 316L steel samples. As before, no embrittlement of 316L due to the liquid metal environment could be found.

The tensile curves for the tests of 316L at both strain rates after neutron irradiation in contact with LBE are depicted in Figure 7.5. The increase in strain rate causes a decrease in ultimate tensile strength as was discussed in section 5.1.1 of Chapter 5. Furthermore, the irradiated 316L has a lower ultimate tensile strength and a lower total elongation than the material pre-exposed in the 0 dpa capsule. This decrease in strength accompanied by the decrease in elongation is attributed to the high temperature irradiation. Fracture surface examination should be performed to exclude any liquid metal effects but as mentioned before this could not be performed due to licensing restrictions.

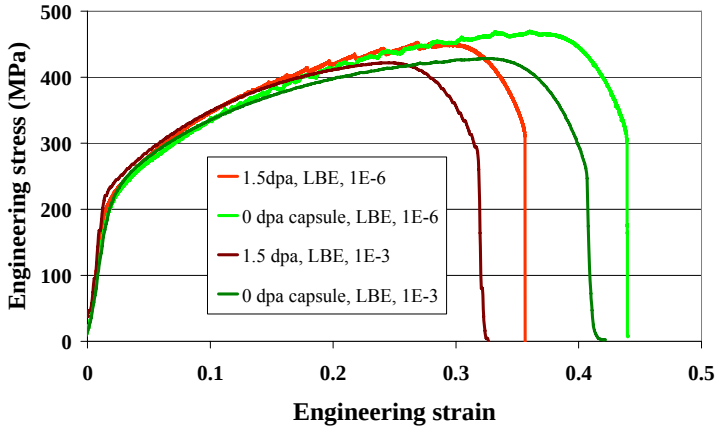

Figure 7.5: Tensile curves of 316L steel tested in liquid LBE at 350°C after different pre-treatments. 316L tested at a strain rate of 1.10^{-6} s^{-1} after irradiation in contact with LBE (bright red); 316L tested at a strain rate of 1.10^{-6} s^{-1} after pre-exposure in the 0 dpa capsule (bright green); 316L tested at a strain rate of 1.10^{-3} s^{-1} after irradiation in contact with LBE (dark red); 316L tested at a strain rate of 1.10^{-3} s^{-1} after pre-exposure in the 0 dpa capsule (dark green).

To compare with previous tests performed on active 316L steel in liquid LBE, we have depicted the test results of the 316L steel tested in LBE at 200°C at a strain rate of 1.10^{-6} s^{-1} after neutron irradiation in contact with LBE together with the results of 316L steel tested in liquid LBE at 200°C at a strain rate of 5.10^{-6} s^{-1} after neutron irradiation in contact with water at 200°C. The tensile curves are represented in Figure 7.6.

Although all tests were performed on 316L steel irradiated up to a displacement damage dose of around 1.5 dpa, it is clear that the irradiation temperature completely determines the mechanical behaviour of the steel. After irradiation between 450 and 500°C the 316L steel keeps excellent work hardening capabilities which is in sharp contrast with the mechanical behaviour after irradiation at 200°C. The 316L irradiated in water shows significant hardening but did not undergo any effect of the liquid metal environment [108]. It should however be noticed that the aqueous irradiation environment formed a thick oxide layer on the steel during irradiation. Low temperature irradiation in contact with LBE would be needed to fully exclude any LME effect on 316L steel after irradiation up to 1.5 dpa and higher.

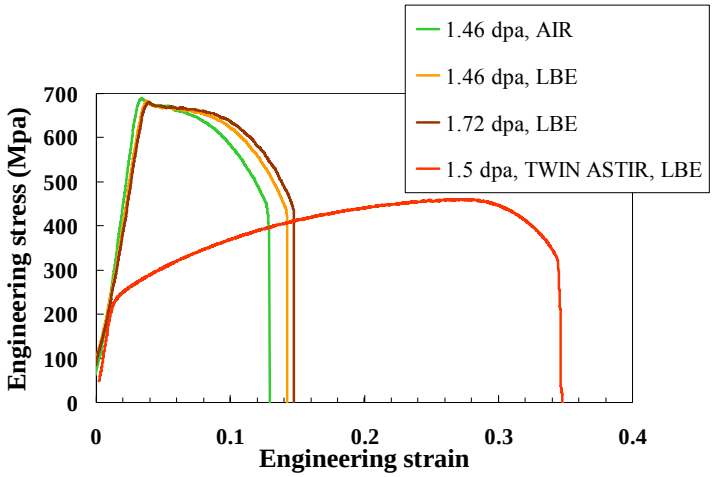

Figure 7.6: Tensile curves of 316L steel tested at 200°C in air (green) or liquid LBE after neutron irradiation in water (green, yellow, brown) at 200°C or after neutron irradiation in LBE at 450-500°C (red).

7.1.3 SSRT tests of Si enriched steels irradiated in contact with LBE

As for the pre-exposure in the 0 dpa capsule discussed in section 6.3.2.3 of Chapter 6, only the ferritic/martensitic/bainitic 2439, 2440 and 2441 steels as well as the austenitic 2442 steel were included in the TWIN ASTIR irradiation experiment. For each of these materials, one tensile specimen was tested in liquid LBE at 350°C after irradiation in contact with LBE at 450-500°C. The applied strain rate was 5.10^{-6} s^{-1} for all the tests on the Si enriched steels. To validate the obtained results after irradiation, we will compare the obtained tensile curves with those already discussed in section 5.1.3 of Chapter 5 and in section 6.3.2.3 of Chapter 6.

2439 steel (11.58 wt% Cr; 0.48 wt% Ni; 2.75 wt% Si)

The tensile curve of the bainitic 2439 steel tested in liquid LBE environment at 350°C after neutron irradiation in contact with LBE at 450-500°C is depicted in blue in Figure 7.7. In contrast to the mechanical behaviour of the T91 steel and the 316L, the 2439 steel has hardened due to the irradiation at 450-500°C. This is most probably due to radiation induced segregation and precipitation which caused extra barriers for dislocation movement. However, without thorough examination of the microstructure after irradiation this can not be firmly concluded. The irradiation hardening can be seen in the further increase of the elastic area in the tensile curve.

Figure 7.7 does show that the LME of the 2439 steel in contact with liquid LBE has further increased after irradiation in contact with LBE in comparison with the previously discussed tensile results after pre-exposure. Based on the tensile curves presented in Figure 7.7 and the previously examined fracture surfaces, it can be expected that the 2439 was fractured in cleavage mode. Unfortunately these could not be examined.

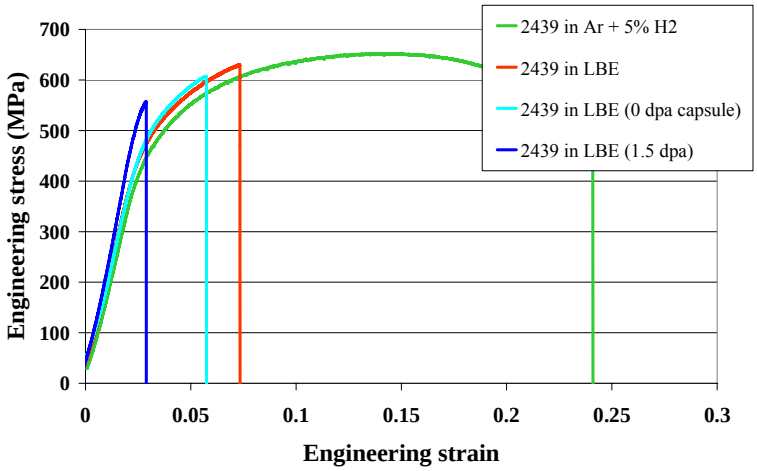

Figure 7.7: Tensile curves of 2439 steel tested at 350°C, 5.10^{-6} s^{-1} in Ar + 5% H_2 (green), in LBE purged with Ar + 5% H_2 (red), in LBE after pre-exposure under thermal cycling in the 0 dpa capsule (turquoise) and in LBE after neutron irradiation in contact with LBE at 450-500°C in the TWIN ASTIR experiment (blue).

2440 steel (13.52 wt% Cr; 0.51 wt% Ni; 4.83 wt% Si)

The tensile curves obtained from SSRT testing of the 2440 steel are depicted in Figure 7.8. The SSRT curve obtained from testing in liquid LBE after neutron irradiation in contact with liquid LBE at 450-500°C in the TWIN ASTIR experiment is depicted in blue in the figure. As for the 2439 steel, the 2440 steel seems to be hardened due to the irradiation since the slope of its elastic behaviour deviates from the previously discussed test results. It is however difficult to determine with certainty since the LME is so pronounced that the 2440 steel breaks very early in the test. The blue tensile in Figure 7.8 does not reveal any plastic behaviour and the resulting total elongation is even slightly less than this of the sample pre-exposed in the 0 dpa capsule. It is clear that the embrittlement has increased but without thorough examination of the sample it is difficult to conclude whether this is due to irradiation hardening, liquid metal corrosion or a combination of both.

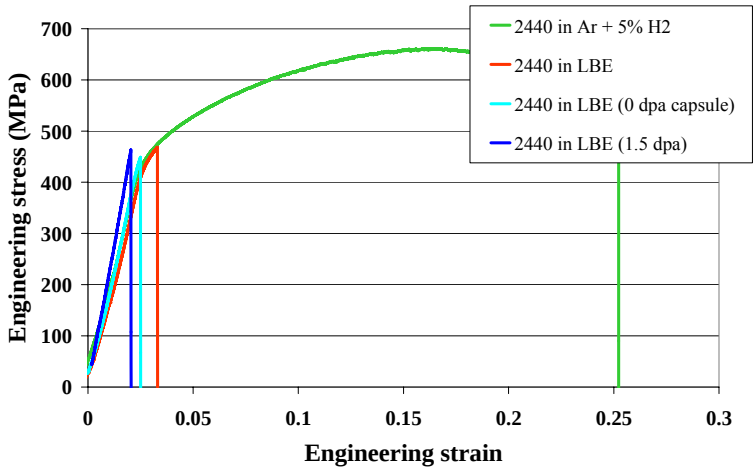

Figure 7.8: Tensile curves of 2440 steel tested at 350°C, 5.10^{-6} s^{-1} in Ar + 5% H_2 (green), in LBE purged with Ar + 5% H_2 (red), in LBE after pre-exposure under thermal cycling in the 0 dpa capsule (turquoise) and in LBE after neutron irradiation in contact with LBE at 450-500°C in the TWIN ASTIR experiment (blue).

2441 steel (18.35 wt% Cr; 0.51 wt% Ni; 5.2 wt% Si)

The 2441 steel was tested twice in contact with LBE at 350°C after neutron irradiation in contact with LBE at 450-500°C. The reason for this was that the first sample broke very early into the test and resulted in a very strange looking tensile curve. Visual inspection of the first tested sample showed that the sample had broken in the screw thread. The second attempt resulted in the blue tensile curve depicted below in Figure 7.9. However, visual inspection of the tested sample again revealed that the sample was broken in the screw thread. This resulted in the fact that the tensile curve does not sharply drop to zero stress upon fracture. The sample broke in the screw thread and the remaining part was pulled thru the sample holder resulting in a few extra small fractures. It is clear that the irradiation in contact with LBE has severely increased the LME effect. Even to the point that the material no longer reaches its yield stress.

Unfortunately fracture surface examination was not possible but it is clear that the sample has broken in a totally brittle, cleavage mode having the screw thread serve as a notch effect to facilitate cleavage fracture even though the stress was lower than in the gauge of the sample.

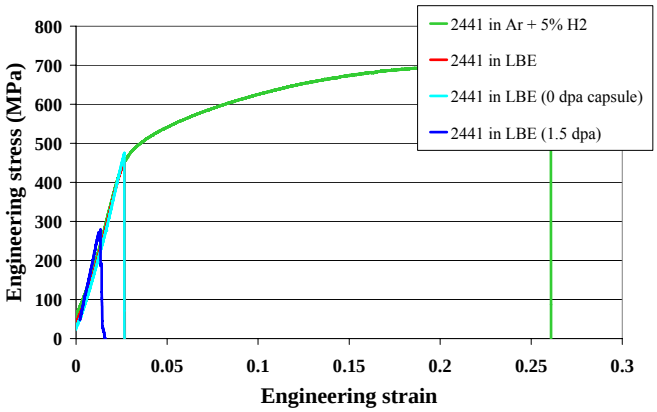

Figure 7.9: Tensile curves of 2441 steel tested at 350°C, 5.10^{-6} s^{-1} in Ar + 5% H_2 (green), in LBE purged with Ar + 5% H_2 (red), in LBE after pre-exposure under thermal cycling in the 0 dpa capsule (turquoise) and in LBE after neutron irradiation in contact with LBE at 450-500°C in the TWIN ASTIR experiment (blue).

2442 steel (18.25 wt% Cr; 14.16 wt% Ni; 5.2 wt% Si)

In contrast with the ferritic/bainitic/martensitic elevated Si steels, the austenitic 2442 steel did not show any change in its fracture behaviour based on the fracture surface examination in the non irradiated specimens. The total elongation of the 2442 steel did consistently decrease when tested respectively in LBE and in LBE after pre-exposure in the 0 dpa capsule but the fanciful shape of the tensile curve and the fracture surface remained similar.

The tensile curve of the 2442 steel tested in LBE at 350°C after neutron irradiation in contact with LBE at 450-500°C in the TWIN ASTIR experiment is depicted in Figure 7.10.

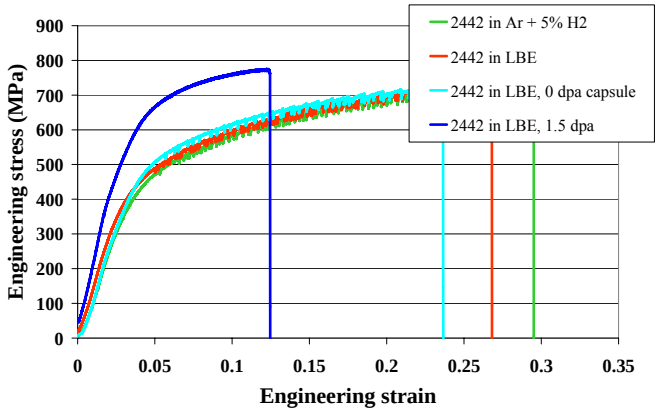

Figure 7.10: Tensile curves of 2442 steel tested at 350°C, 5.10^{-6} s^{-1} in Ar + 5% H_2 (green), in LBE purged with Ar + 5% H_2 (red), in LBE after pre-exposure under thermal cycling in the 0 dpa capsule (turquoise) and in LBE after neutron irradiation in contact with LBE at 450-500°C in the TWIN ASTIR experiment (blue).

It is clear based on the blue tensile curve of Figure 7.10 that the 2442 steel has hardened due to neutron irradiation at 450-500°C since its yield stress and ultimate tensile strength have significantly increased. However, it should be noted that the shape of the tensile curve has changed as well.
The tensile curve of the 2442 steel after irradiation is much smoother than those before and therefore no longer points to micro brittleness. Despite the increased smoothness of the tensile curve, the material's total elongation has significantly decreased when tested in LBE after neutron irradiation.

For the 2442 steel it is especially unfortunate that we were not able to perform fracture surface examination since the shape of the tensile might be an indication that the fracture mode changed from micro brittleness to cleavage. Without detailed fracture surface examination we can however only state that the material has hardened and that the ductility has decreased strongly.

7.1.4 SSRT tests of T91/T91 welds irradiated in contact with LBE

The specimens of the welds which were irradiated in contact with LBE in TWIN ASTIR were taken out of the welds in the same orientations as those discussed in section 6.3.2.4 of Chapter 6. Therefore, to validate the obtained tensile results, they will be compared to the results after pre-exposure in the 0 dpa capsule.
It needs to be mentioned that due to the unexpected increase in irradiation temperature the thermal history of the irradiated specimens is different from those pre-exposed in the 0 dpa capsule. This difference in thermal history is translated in a different stress relaxation and different mobility of certain constituents in the weld microstructure. This makes comparison between the irradiated and pre-exposed weld specimens rather difficult, especially since no detailed microstructural examination was possible.

In the following two sections, the mechanical behaviour of the T91/T91 TIG and EB welds after neutron irradiation in contact with LBE will be discussed on the basis of the obtained tensile curves.

7.1.4.1 SSRT tests of T91/T91 TIG weld irradiated in contact with LBE

Figure 7.11 shows the comparison of the tensile curves obtained by testing in liquid LBE at 350°C after pre-exposure in the 0 dpa capsule and after irradiation in contact with LBE at 450-500°C. In general the tensile curves of the irradiated specimen show a slight decrease in yield and tensile strength and a slightly lower total elongation. The largest difference is for the samples taken out of the weld deposit itself (bright green vs. dark green curves). The softening due to the high temperature irradiation is more pronounced for the specimen taken out of the weld deposit. Furthermore, the decrease in total elongation is more pronounced as well.

The softening of the weld deposit can be explained by the effect of the annealing at 450-500°C which releases the stresses from welding as a PWHT does. The decrease in total elongation is presumably due to LME but without fracture surface analysis this is difficult to state. However, when comparing the results of the irradiated weld samples to these of the 0 dpa capsule which were embrittled by LBE as discussed in section 6.3.2.4.1 of Chapter 6 it can be said that the conditions of the irradiation experiment increased the LME susceptibility of the T91/T91 TIG weld.

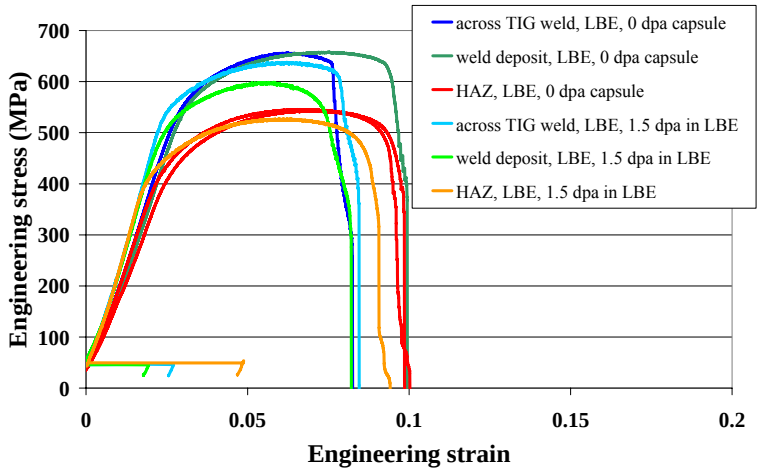

Figure 7.11: Tensile curves of T91/T91 TIG weld tested at 350°C, 5.10^{-6} s^{-1} in different orientations in liquid LBE after pre-exposure in oxygen depleted LBE under thermal cycling (0 dpa capsule) and after neutron irradiation up to 1.5 dpa in contact with LBE. (Blue) specimen across TIG weld, having weld deposit of the centre of the gauge; (Green) specimen fully inside the weld deposit along the length of the welded seam; (Red) specimen taken across the TIG weld, having the HAZ in the middle of the gauge length.

7.1.4.2 SSRT tests of T91/T91 EB weld irradiated in contact with LBE

One single test in liquid LBE at 350°C was performed on the T91/T91 EB weld after neutron irradiation in contact with LBE. The obtained tensile curve is depicted in red in Figure 7.12. Also for the T91/T91 EB weld the tensile curve shows softening and a further decrease in total elongation compared to the T91/T91 EB welded specimens pre-exposed in the 0 dpa capsule and tested in LBE.

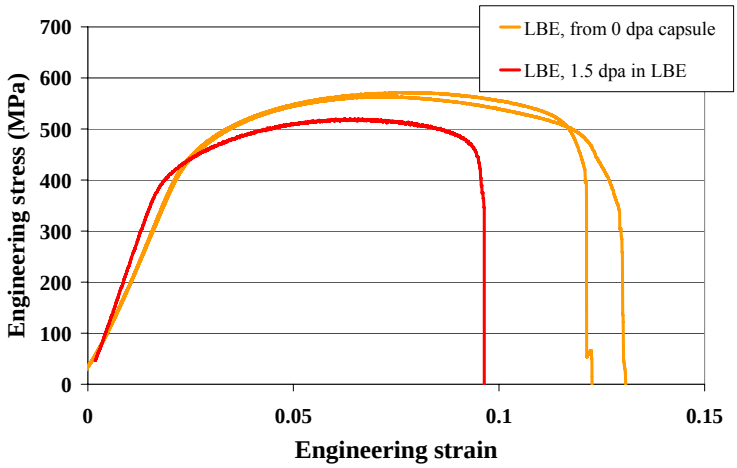

Figure 7.12: Tensile curves of T91/T91 EB weld tested at 350°C, 5.10^{-6} s^{-1} in liquid LBE purged with Ar + 5% H_2. (Orange) T91/T91 EB weld tested in liquid LBE after pre-exposure in the 0 dpa capsule; (Red) T91/T91 EB weld tested in liquid LBE after neutron irradiation up to 1.5 dpa in contact with LBE.

In section 6.3.2.4.2 of Chapter 6, we showed that the T91/T91 EB weld suffered significant LME after pre-exposure in the 0 dpa capsule. This LME effect has become pronounced after irradiation in contact with LBE at 450-500°C.

7.1.5 SSRT tests of T91/316L welds irradiated in contact with LBE

As discussed in section 2.2.1.2.3 of Chapter 2, the carbon content of the materials on both sides of the dissimilar weld plays a very important role in the welding and mechanical properties of a dissimilar weld. Since the increased irradiation temperature was at 450-500°C and carbon is already mobile at these temperatures while other important constituents such as chromium are not, it has become very difficult to interpret the mechanical properties of the T91/316L welds solely on the basis of tensile curves. Detailed microstructural examination of the different areas of

the welds would be needed to really understand the causes of the macroscopic behaviour of the weld. Since this was not possible, we need to rely on comparison between the previously discussed results and the tensile curves obtained after irradiation in contact with LBE. It is clear that only general tendencies and qualitative interpretation can be possible at this stage.

In the following two sections we will examine the tensile curves obtained after neutron irradiation of the dissimilar welds in contact with LBE.

7.1.5.1 SSRT tests of T91/316L TIG weld irradiated in contact with LBE

The complex structure of the T91/316L TIG weld comprises of four different areas as discussed before in section 2.2.3.1 of Chapter 2. Tensile specimens were taken in three different orientations in respect to the weld. The orientations are schematically represented below the obtained tensile curves in Figure 7.13 for each of the respective specimen orientations.

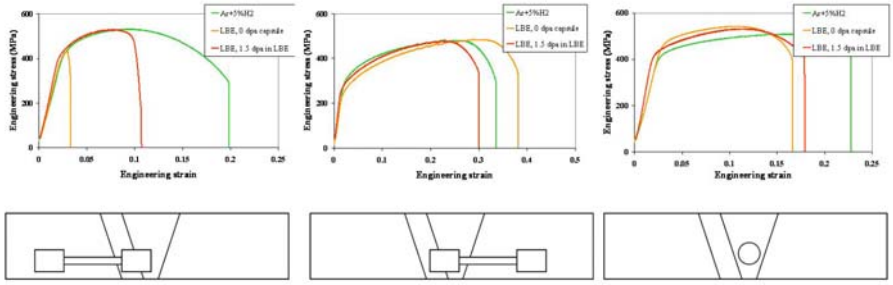

Figure 7.13: Tensile results of T91/316L TIG weld tested in Ar + 5% H_2 (green), LBE after pre-exposure in the 0 dpa capsule (orange) and LBE after neutron irradiation in contact with LBE in TWIN ASTIR (red). Schematic representation of sample orientation indicated below the stress strain curves.

The tensile curves on the left in Figure 7.13 show that the LME effect has decreased after irradiation in contact with LBE at 450-500°C. This is very probably due to the stress relaxation of the welded connection on that side. As discussed in section 2.2.3.1.2.1, the hardness profile of the T91/316L TIG weld has a peak at the T91 side because the tempering is in fact rather short to relieve the stresses from welding in the martensitic steel. The irradiation at 450-500°C has had a tempering effect on the weld in this location resulting in a decrease of hardness and therefore also a decrease in the susceptibility to LME at this location. Despite the observed decrease in LME effect after irradiation, the mechanical behaviour of the weld is still troubling.

For the specimen taken on the side of the 316L steel in the T91/316L weld, we can observe a decrease in tensile strength and total elongation. Without observation of the fracture surface it is however impossible to say whether this is attributed to LME or simply the result of the irradiation softening of the 316L steel.

The mechanical properties in liquid LBE of the weld deposit material did not seem to be affected after neutron irradiation in contact with LBE since the red tensile in Figure 7.13 does not deviate much from the one obtained after pre-exposure in the 0 dpa capsule.

7.1.5.2 SSRT tests of T91/316L EB weld irradiated in contact with LBE

In the electron beam weld both materials are fused together without the addition of any weld deposit material. Furthermore, the weld seam is very narrow. At temperatures of 450-500°C diffusion of carbon is activated as mentioned before. This means the EB weld could be prone to sensitisation or other diffusion and segregation related phenomena. However we could only examine the T91/316L EB weld by tensile test of a sample taken across the weld.

The tensile obtained after irradiation at 450-500°C in contact with liquid LBE is depicted in purple in Figure 7.14. The weld sample has very little plastic deformation left. Based on visual inspection of the broken sample, it seems to have broken in the middle of the gauge which would indicate fracture in the weld.

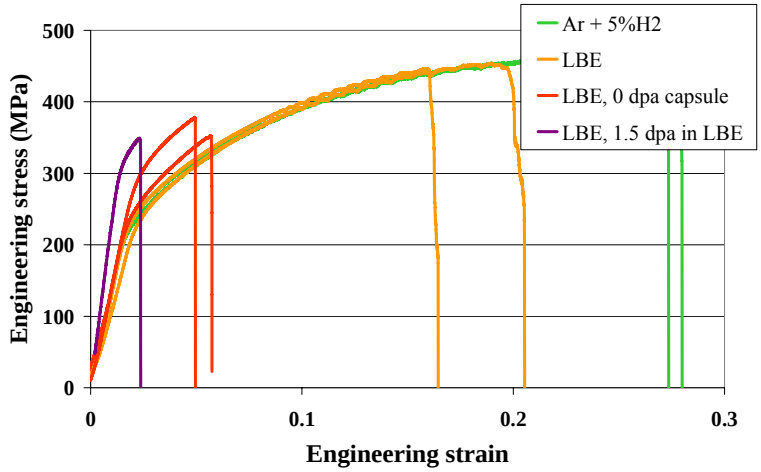

Figure 7.14: Tensile results of T91/316L EB weld tested in Ar + 5%H_2 (green), LBE (orange), LBE after thermal cycling in low oxygen LBE in the 0 dpa capsule (red) and LBE after neutron irradiation in contact with LBE in TWIN ASTIR (purple).

Figure 7.14 obviously shows that the T91/316L EB weld would not be applicable for the construction of any LBE cooled facility since its mechanical properties strongly deteriorate with exposure and irradiation. As mentioned before, detailed microstructural examination or even a relatively simple chemical profile across the weld would be very interesting. This was however not possible.

7.2 IRRADIATION TEMPERATURE TWIN ASTIR & ITS IMPLICATIONS

As was seen in the tensile results discussed above, the irradiation temperature of the TWIN ASTIR experiment was higher than foreseen resulting in the absence of irradiation hardening. In the following two sections we will elaborate on the cause of this unexpected overshoot in temperature and its scientific implications in the frame of this PhD work.

7.2.1 Irradiation temperature TWIN ASTIR

An irradiation experiment such as TWIN ASTIR which was the first of its kind in Western Europe is obviously not realised by a PhD student alone. Many people contribute in the realisation of an innovative irradiation experiment. Furthermore, to achieve the test result of a seemingly simple tensile curve as those presented above many handling operations had to be performed.

When the first tensile tests of T91 irradiated in LBE were produced it was immediately noticed that we did not have any irradiation hardening. Since the material was radioactive there was no doubt that it had been irradiated. However post irradiation annealing is known to alleviate the hardness increase resulting from irradiation damage as was discussed in section 1.4.2 of Chapter 1.
The irradiated capsule had been stored for 11 months in the storage of BR2 after irradiation to allow natural decay. The capsule was dismantled in the hot cell which needed heating of the capsule to remove the LBE inside. The capsule itself was a double wall capsule and the size of the gap between the inner and outer tube was known to have a severe influence on the temperature inside.
A large amount of factors could have caused annealing of the irradiated material and finding this cause was not only important in the frame of this PhD work but also for the continuation of the LBE programmes at SCK•CEN.

Extrapolation of the available data on yield stress of 9% Cr martensitic steels and 316 austenitic stainless steels after neutron irradiation to about 1.5 dpa as function of temperature presented in section 1.4 led to the conclusion that the irradiation temperature had to have been between 450 and 550°C. This extrapolation had a rather large uncertainty because there was no data of T91 or 316L under the exact same conditions available.

Careful examination of the complete history of capsule A of TWIN ASTIR and the communications and reports in the preparation of the irradiation experiment brought to light an unfortunate communication error between one of the nuclear physicists of BR2 and the project engineer of TWIN ASTIR. The gamma heating in the experiment was calculated using MCNPX neutron calculation software. The gamma heating in the samples was calculated to be of the order of 4 Watt per gram. The project engineer used the 4 W/gr as the heating power for the entire experiment and used this value to calculate the temperatures in the TWIN ASTIR experiment. These temperature results were summarized in Table 4.2 of Chapter 4 for the tensile filled capsule A.

However, unlike in other irradiation experiments, the gamma heating of the LBE in the capsule was of the order 11 Watt per gram. This much higher heat deposition had not been taken into account nor was the influence of the delayed gammas and caused the increase in the irradiation temperature. Since safety regulations had not allowed for a thermocouple to be inserted into the capsule for reasons of possible leaks, the increased temperature had not been discovered until after the low dose capsule was opened, dismantled and tested.

Post irradiation detailed recalculation of the gamma heating values revealed the following results:

Table 7.1: Actual gamma heating values for capsule A of TWIN ASTIR (in W/gr).

T91 sample	Inner SS tube	Outer SS tube	LBE
5.59	5.60	5.64	11.77

This detailed calculation led to an irradiation temperature of the samples between 465 and 495°C instead of 350°C (327-368°C).
Moreover, since the gamma heating is significantly different in the structural materials compared to in the liquid LBE and the tensile samples were screwed into a retainer plate on one side only, the temperature varied over the sample. This is depicted in Figure 7.15 which gives the temperature profile along the length of a sample in capsule A under irradiation. It should be noted however that the gamma heating values given in Table 7.1 are calculated for the middle of the gauge length and can not be strictly applied to the entire geometry. The temperature profile across the sample will in actuality be slightly more evened out compared to the profile presented in Figure 7.15.

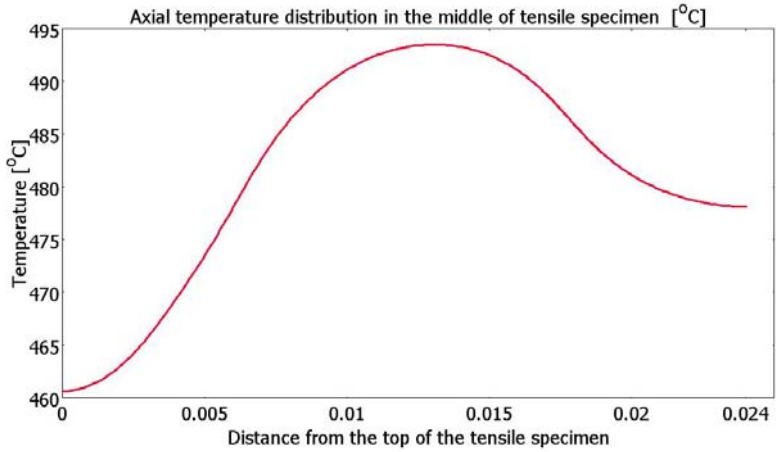

Figure 7.15: Axial temperature distribution in the middle of a tensile specimen under irradiation in contact with liquid LBE inside capsule A of TWIN ASTIR (Distance in meters).

The radial temperature distribution in the middle of the gauge of the tensile specimens for a single stage of three tensile samples screwed into their retaining plate is depicted in Figure 7.16. These calculated temperatures are now considered to have been the actual temperature distribution under irradiation.

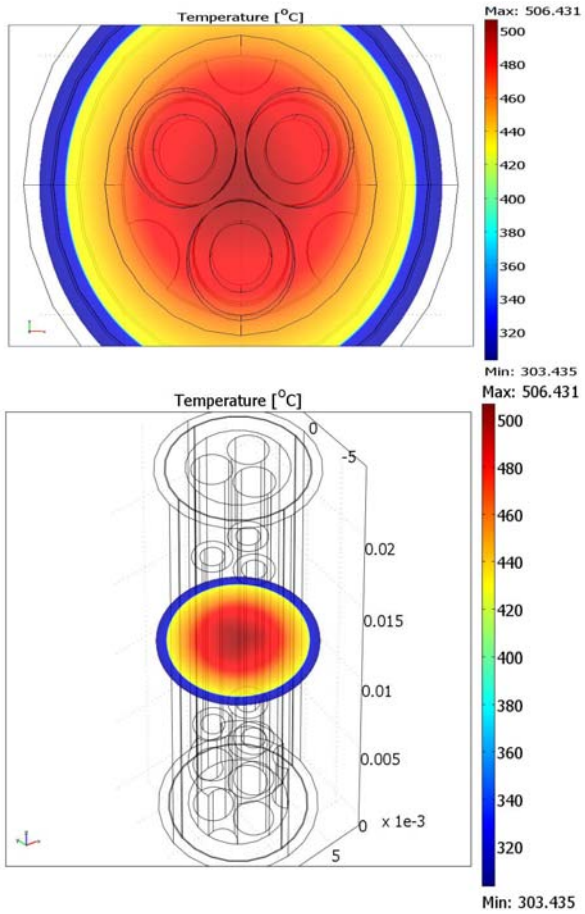

Figure 7.16: Radial temperature distribution under irradiation in contact with LBE in the middle of the gauge of a stage of three tensile samples screwed into their retaining plate.

7.2.2 Scientific implications of irradiation temperature at 450-500°C

Clearly the experimental results produced by the TWIN ASTIR irradiation are still of great importance in the frame of the licensing and engineering of a future LBE cooled nuclear facility. However in the frame of this PhD, the one-on-one parameterisation study which was the initial goal of the TWIN ASTIR experiment is lost due to the unexpected temperature increase.

The 0 dpa capsule, which was to allow assessment of the thermal ageing and corrosion part in the mechanical degradation of the structural steels, was

programmed based on the initial ΔT temperature calculations. Since the actual irradiation experiment was at 450-500°C in stead of at 350°C, the thermal corrosion will have been greater in the irradiated capsule than this in the 0 dpa capsule. This makes it impossible to distinguish the irradiation effect on corrosion from the thermal corrosion effect. Repeating the thermal exposure of a new 0 dpa capsule using the correct temperatures would take more than a year to complete and could therefore not be included in this PhD.

Another scientific implication of the increased irradiation temperature is the absence of irradiation hardening. The intention was to compare SSRT results of tests performed in LBE on thermally hardened material (see section 6.1.1 of Chapter 6) to SSRT test results of tests performed on irradiation hardened material in LBE. Due to the absence of irradiation hardening at 450-500°C, 1.5 dpa this was not possible and the question remains whether irradiation hardening increases the material's susceptibility to LME like thermal hardening does.

8 GENERAL DISCUSSION AND CONCLUSIONS

Experiments are never wrong; it is our judgement/interpretation that is wrong.
Leonardo Da Vinci
(1452-1519)

I forgot my USB stick but if you have any questions…..
Georg Mueller
(1961 - …)

Sometimes I'm confused by what I think is really obvious. But what I think is really obvious obviously isn't obvious...
Michael Stipe
(1960-…)

In Chapter 8, we evaluate, interpret and discuss the results presented in chapters 5, 6 and 7 and place them in the frame of the available literature presented in chapter 1. Furthermore, based on the available scientific arguments, we draw the conclusions on liquid metal embrittlement and compatibility of the examined structural materials in contact with liquid lead bismuth eutectic in general.

Firstly, we will discuss the validity of the produced tensile and fracture toughness results by evaluating the testing method and comparison of our results with results found in literature.

Secondly, we will extract the metallurgical parameters influencing LME and compatibility of structural materials with liquid metals based on our results and correlate our results with those discribed in literature.

Thirdly, the available liquid metal embrittlement models will be critically reviewed in the frame of our results.

In a last section, the most important conclusions of this work will be summarised.

8.1 VALIDITY OF PRODUCED EXPERIMENTAL RESULTS

The absence of any standard on mechanical testing in liquid metal environment makes it sometimes difficult to confidently compare results. No recommendations or requirements are set on the chemistry control of the applied liquid metal, the used quantity of liquid metal or on the surface conditions of the solid metal. This leads to a wide variety in applied methods and apparent contradictions in results.

To add to the problem many authors do not mention the detailed testing conditions in their publications and therefore make it very difficult to reliably extract influencing parameters from available literature.
Many of the used test benches in liquid metal testing are modified or specifically constructed to allow liquid metal environment testing and are therefore often not certified or officially calibrated machines. Both the Limets 1 and Limets 2 facilities were designed and constructed at SCK•CEN especially for the purpose of liquid metal testing.
For all these reasons, critical evaluation of the validity of produced experimental results is not at all a trivial issue.

In the following two sections we will critically discuss the validity of the performed mechanical tests and make recommendations for future standardisation of liquid metal testing.

8.1.1 Validity of tensile results

All tensile tests reported in chapters 5, 6 and 7 were performed in either Limets 1 or Limets 2. These testing facilities were designed and used to comply with ASTM standard E 8M on tensile testing of metallic materials. This standard does however not include any liquid metal environment testing. When comparing the tensile results of T91 and 316L steel in gas environment as function of temperature (see Figure 5.1 to Figure 5.5) to the values described in the materials standard for both steels (T91: ASTM A 387-Ed99; 316L: ASTM A 240 Ed02), the values correspond very well.
Once the liquid metal environment is introduced however, no standard is available leading to a wide variety of applied conditions.

The liquid metal used in Limets 1 and Limets 2 was delivered to us by Hetzel Metalle GmbH, Germany with a composition of 55.2 wt% Bi and 44.8 wt% Pb with an impurity level of 2 mg/g Cr and less than 1 mg/g Ni. The vessel was filled with almost 4 litres of liquid metal of which 2 litres is transferred to the autoclave for testing each time.
The advantage of the Limets set up is the reliable oxygen control system and the relatively large quantity of LBE surrounding the sample during testing. The disadvantage is that with time, the LBE saturates with impurities coming from corrosion of the autoclave walls and ducts since the same liquid metal is re-used for all tests without any purification regarding the impurities. Since certain impurities such as Zn, Sn and Sb are known to favour embrittlement and others such as Ni and

Cr are known to be preferentially dissolved from the solid, standardisation of liquid metal testing should incorporate maximum impurity levels. Furthermore, since quantity and pressure of liquid metal are known to play a role in the susceptibility to LME as discussed in section 1.3.1 of Chapter 1, standards should include liquid metal testing depth and volumetric quantity boundaries.

The most discussed item in the validity of liquid metal testing however is the solid metal surface condition.
Although obvious cases of LME such as the Si enriched steels in LBE (see sections 5.1.3, 6.3.2.3 and 7.1.3) are so severely embrittled by the liquid metal that they will break in a brittle manner every time no matter the surface conditions, it can be seen that the amount of total elongation is still reduced after pre-exposure without penetration of LME into the bulk (see Figure 6.18). This can be solely attributed to the degree of wetting which occurs at the solid metal – liquid metal interface at the initiation of the test.
For the intermediate embrittlement cases such as T91 in LBE where results are often contradictory ([55] vs. [108]) and reproducibility is problematic (see Figure 5.6), the surface condition is of primordial importance to allow comparison of results. Although most authors, like ourselves polish their samples to "mirror shine" prior to testing this is not a certitude for comparable surface roughness. Surface roughness recommendation might improve the scatter in experimental SSRT results. Furthermore, some authors use soldering flux to remove the oxide layer prior to testing in liquid metal environment [63]. Although they present reference tests where they applied flux on a sample tested in gas environment to argument the absence of any influence of the flux on the mechanical properties of the tested material, this flux does introduce certain impurities into the liquid metal and might have a surface roughness increasing effect.

Comparison of tensile results with available literature shows that 316L is not or very little affected by the liquid metal environment. Under none of the examined tensile testing conditions is there a change observed in the fracture behaviour of 316L, nor is there a change in total elongation observed. The tensile results all correspond very well with those measured in gas environment. This is a common conclusion of all work found on 316L tensile tested in LBE [51],[72],[87],[108].

For T91 the reported tensile results are sometimes contradicting. This problem of apparent contradiction in results was also observed within this work resulting in very different total elongation values under the same testing conditions (see Figure 5.6). Based on the available tensile results it can be said that T91 in its standard condition is to a certain extent prone to LME in LBE between 200 and 450°C. The LME

reduces the total elongation while keeping yield stress and tensile strength the same. Fracture surface examination reveals different numbers of LME initiation sites at the surfaces depending on the test however none of the observed fracture surfaces of T91 in its standard condition were fully embrittled by the LBE. Despite the sometimes different surface treatment (fluxing, PVD, surface defects, pre-exposure) when LME is observed, the observed embrittlement of the ferritic-martensitic T91 steel is of approximately the same magnitude. The effect of strain rate on the occurrence of LME is more difficult to assess due to the difficulty in reproducibility.

Unfortunately no other data was found on LME of elevated Si steels. All related studies we found were on the improved corrosion resistance of these types of steels in LBE. However, due to the excellent reproducibility of embrittlement in SSRT tests as reported in section 5.1.3 of chapter 5, section 6.3.2.3 of chapter 6 and section 7.1.3 of chapter 7, we can be very confident about the observed results. It is clear that the increasing amount of Si causes an increasing amount of LME for the ferritic/bainitic/martensitic steels. For the austenitic elevated Si steels, there is no apparent change in fracture behaviour when tested in LBE compared to tests in gas environment for the steels which are not prone to hydrogen embrittlement. It does seem that susceptibility to hydrogen embrittlement and susceptibility to LME are linked. The SSRT results of the 2442 steel after irradiation need fracture surface examination and microstructural observation before any sound conclusion can be made.

All tensile results in this work were presented or interpreted as engineering stress – engineering strain curves and no true stress – true strain analysis was made. Although this did not strictly allow examining the influence of the liquid metal environment on the flow properties of the materials, it did allow maximum interpretation of the embrittlement process. True stress – true strain based on the displacement of the machine is only valid up to the point of necking and the opaque nature of the liquid metal prevents visual measurement of the actual section of the necking sample. Furthermore, the use of true stress – true strain would not allow comparison of the elastic behaviour of the material.

Based on our results presented in Chapter 5, 6 and 7 and compared to the literature data presented in Chapter 1, we can state that we have produced valid and valuable tensile results. However, until the creation of a liquid metal testing standard, data should be accompanied with as much information as possible on the testing facility, liquid metal composition, quantity and the solid metal surface condition.

8.1.2 Validity of fracture toughness results

As for the tensile test, there is no mechanical test standard available which describes the requirements and recommendation for performing fracture toughness tests in liquid metal environment. Furthermore, the conventional analysis methods are often not applicable due to the opaque and conducting nature of the liquid metal environment. This led some authors to resort to different specimen geometries [63] or self developed calibration methods [64]. In our work, as explained in chapter 3, we relied on the NDR normalisation method described in Annex A15 of ASTM standard E 1820 and complimented this analysis method with two other normalisation methods found in literature [138],[139]. To compare the results from our work presented in section 5.2 of chapter 5 with those from SPIRE [146] and the AAA materials handbook [147], we have plotted the available data on the plane strain fracture toughness of T91 together in Figure 8.1.

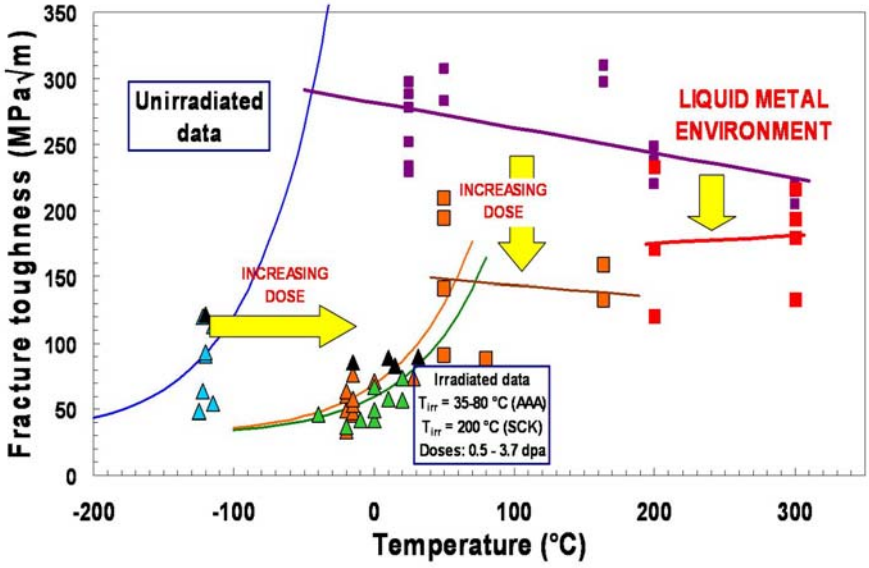

Figure 8.1: Fracture Toughness of T91 before and after irradiation (0.5 – 3.7 dpa) compared with fracture toughness of unirradiated T91 in LBE.
Data at 200 and 300°C from results discussed in chapter 5; Reference data and irradiation data from AAA materials handbook and SCK•CEN results within SPIRE programme.

Our reference tests performed on DCT samples of T91 in air at 200 and 300°C are plotted in purple in Figure 8.1 together with the available fracture toughness values on T91 steel from the AAA materials handbook. Our data is in good agreement with the reference data on T91 from the AAA materials handbook.

The data in red in Figure 8.1 are the values obtained from testing T91 in LBE at 200 and 300°C. The fracture toughness values of non irradiated T91 tested in LBE at 200 and 300°C are comparable to the values obtained from testing the fracture toughness of irradiated T91 in gas. Although there is large scatter as will be discussed further, the values of fracture toughness are considerably lower when tested in LBE compared to the values obtained from testing in air.

Due to the absence of recommendations for liquid metal environment testing, the fracture toughness test suffers from the same uncertainties as encountered in the discussion on the validity of the tensile test discussed above.

The tests performed in liquid LBE which were discussed in section 5.2 of chapter 5 can not be seen as a final quantification of the embrittlement of T91 and 316L in LBE. These tests proved the possibility to use normalisation methods for plane strain fracture toughness assessment in liquid metal environment and gave the first quantitative results for this type of test in LBE.
The test results are still quite scattered and not all samples suffered from LME. This is largely due to the sample geometry and testing orientation which does not fully prevent the possible presence of gas bubbles in the pre-crack. Pre-cracking in LBE could resolve this problem although making the pre-crack in liquid metal embrittlement is not at all a sinecure. Furthermore testing in a vacuum autoclave or changing the orientation of the sample so that the crack is positioned vertically allowing gas bubbles to escape might resolve the encountered problems of absence of liquid metal contact.

Despite the uncertainties and encountered problems in performing plane strain fracture toughness tests in liquid LBE, it is very encouraging that the fracture toughness tests of T91 by 3-point bending in LBE [64] result in the same conclusion of a maximum of about 30% decrease in fracture toughness when testing T91 steel in liquid LBE.
It is clear that the materials database on fracture toughness of the candidate structural materials in liquid lead alloys needs to be extended. It can however be stated at this moment that the first quantitative results in non irradiated condition indicate a decrease in fracture toughness of T91 steel in liquid LBE but acknowledge that sufficient fracture toughness remains for engineering applications.
It must also be stated however that the tensile results of the thermally hardened T91 discussed in section 6.1.1 and in [58] indicate a much stronger decrease in fracture toughness of hardened material in contact with LBE. This underlines the importance of plane strain fracture toughness assessment of the candidate structural materials after neutron irradiation in the low temperature regime.

Due to the scatter in fracture toughness results and the difficulties in reproducibility for intermediately embrittling solid metal – liquid metal couples it is very strongly advised to adopt the strategy of using uni-axial tensile tests as exploratory LME test and using plane strain fracture toughness tests to quantify the embrittlement. Furthermore, the observations of the fracture surfaces obtained by both tensile testing and fracture toughness testing need to be thoroughly examined.

Absence of either one of the above mentioned examinations would result in an incomplete picture of the environmentally influenced mechanical behaviour of structural materials.

8.2 METALLURGICAL PARAMETERS INFLUENCING LME REVIEWED

In this section we will re-examine the features commonly ascribed to LME and the most important influential variables on LME which were already discussed in section 1.3.1 of chapter 1 in relation to the available literature on the LME phenomenon in general. However, here we will focus on the observations made in the frame of this work, possibly complemented by work of others on the compatibility of structural steels in LBE.
In addition to the metallurgical parameters discussed in section 1.3.1, we will discuss the effect of the surface condition and the effect of neutron irradiation while in contact with LBE on the occurrence of LME.

Elastic & plastic behaviour

The elastic domain and the yield stress of the solid were unchanged by the testing environment (gas or LBE) for all tests except for the 2441 steel after irradiation in contact with LBE. This elevated Si steel became so brittle when tested in LBE after irradiation that its yield stress was not reached.
The yield stress and elastic domain of neutron irradiated material can not be compared with the same material before irradiation since the microstructure is altered by the introduction of irradiation defects, radiation induced segregation and precipitation as discussed in chapter 1. Unfortunately, the results of the SSRT tests after irradiation in LBE could not be compared with SSRT tests irradiated in water or gas and tested in gas. However, in all cases reported in chapter 5 and 6, the elastic domain and the yield stress of the tested material remained unchanged when tested in LBE.
In fact, up to the point of fracture, the engineering stress – engineering strain curves of all studied materials obtained by testing in liquid LBE nicely coincided with their respective reference engineering stress – engineering strain curve obtained by testing in gas environment. This was obviously the case for the 316L steel which was not affected but also the severely embrittled ferritic elevated Si steels showed nearly identical elastic and plastic behaviour up to the point of fracture.
These observations confirm the trend in elastic and plastic behaviour postulated by Westwood [18] and Stoloff [29] that until fracture occurs, the stress-strain behaviour of the solid is the same as in the unwetted condition.

Fracture behaviour

The fracture behaviour of the 316L stainless steel remained unchanged under all examined conditions. Although the fracture toughness values found after testing in LBE were about 10% lower than those obtained in gas, all examined fracture surfaces were fully dimpled (see Figure 8.2). Therefore, it cannot be said that the fracture behaviour of 316L is altered by the liquid metal environment.

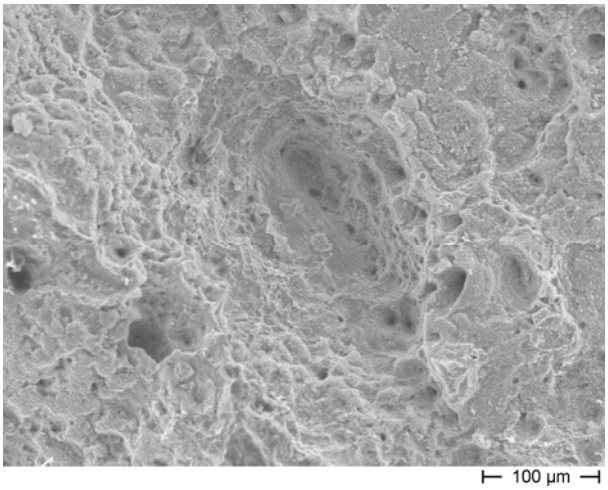

Figure 8.2: Dimpled, ductile fracture surface of 316L tested in LBE.

For the intermediately embrittled T91 steel, the LME did indeed, as mentioned in section 1.3.1, cause a decrease in ductility while leaving other mechanical properties unaffected. Even for the embrittled thermally hardened T91, the UTS was reached (see Figure 6.1), leaving only the total elongation as an affected tensile property when looking at numerical data of the performed tests.
The fracture surface did however give clear indication of embrittlement when it occurred. Fracture appearance of the ferritic-martensitic T91 was obviously changed where LME occurred (see Figure 8.3), leaving the typical semi-circular patterns which flowered out from an initiation point at the sample surface. This fracture appearance is often referred to as "quasi-cleavage" and commonly accepted to be due to the competition of ductile and brittle fracture [149].

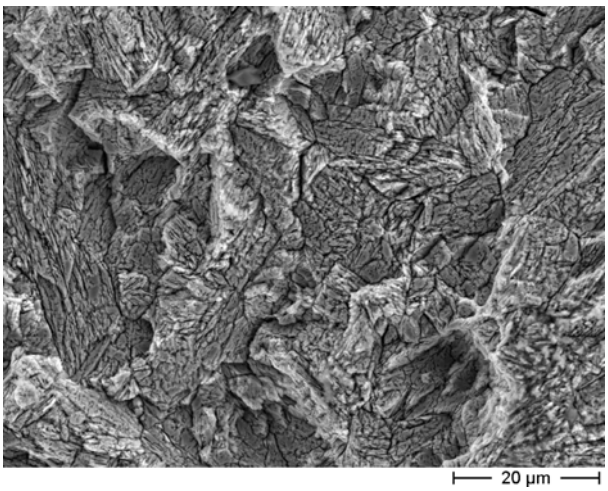

Figure 8.3: Quasi-cleavage fracture surface of T91 tested in LBE.

In the fracture surfaces of the DCT samples of T91 tested in LBE to determine the fracture toughness, several grains were found to be fully fractured in cleavage while the surrounding grains were fractured in quasi-cleavage mode or mixed dimpled and quasi-cleavage. A nice example of this was depicted in Figure 5.36B. This indicates the importance of the crystallographic orientation of the grains with respect to the advancing crack.

The ferritic/bainitic/martensitic elevated Si steels were the most severely embrittled when tested in LBE. Although the as received elevated Si steels tested in LBE still had a very small amount of dimples on the fracture surface, the pre-exposed elevated Si ferritic/bainitic/martensitic steels fractured 100% in cleavage. Several areas in the fracture surfaces even showed a very small amount of river patterns (see Figure 8.4) indicating an almost crystallographic flat fracture surface.
Since the river patterns observed in cleavage fracture are caused by the crack moving through the crystal along a number of parallel planes which form a series of plateaus and connecting ledges, their relative absence in cleavage fracture images is an indication of a very low absorption of energy due to the absence of local deformation.

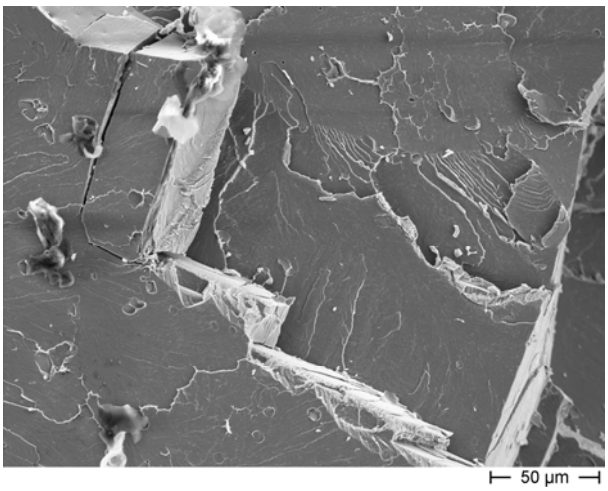

Figure 8.4: Cleavage fracture of elevated Si 2441 steel tested in LBE.

Despite several authors mentioning the predominant fracture type in LME to be intergranular failure as discussed in section 1.3.1, we did not observe any intergranular failure.

The presence of liquid metal at the moving crack tip does appear to be a necessity for LME to occur although the transition from quasi-cleavage fracture to ductile fracture in the examined fracture surfaces of T91 appears to be due to the competition between LME and ductile fracture rather than due to the lack of liquid metal at the advancing crack tip. This will be discussed more in detail in section 8.3.

Temperature

The 316L stainless steel is not or hardly affected by the liquid metal environment. Even if the 10% decrease in fracture toughness in liquid metal environment would turn out to be consistent with other measurements, the observed effect is too small to determine a reliable ductility trough temperature range.

For the ferritic-martensitic steel T91 tested in LBE, the encountered problems in reproducibility prevent the clear experimental determination of the ductility trough. However, it is clear from the tests at a fixed strain rate that do show embrittlement of T91 by LBE that the ductility trough temperature range does exist. Therefore, we summarized the references of papers that report on LME of T91 in LBE in Table 8.1. The mentioned references are not meant to include all available papers on LME of T91 but indicate the temperature range within which the LME phenomenon was encountered. Furthermore, the references stated in Table 8.1 are not only dealing

with T91 in its standard condition but also include thermally as well as surface treated T91 steel results. Furthermore, no distinction was made between different strain rates. The papers dealing with neutron irradiated T91 were not included however.
In Figure 8.5 we depicted the reported cases of LME for T91 in its standard condition only for several sizes of cylindrical specimens and for dog bone shaped specimens. It can be seen that the dog bone shaped specimens are more severely embrittled by the LBE than the cylindrical specimens. This is due to the stress concentrations at the corners of their rectangular section. Despite several test campaigns at 500°C and above, no embrittlement was reported above 450°C.

Based on Table 8.1, we can state that the ductility trough for T91 steel in liquid LBE is between 150 and 450°C. The most severe embrittlement being reported for temperatures between 300 and 450°C. Above 450°C the T91 steel behaves fully ductile and mechanical properties are found to be identical or even superior [53] to those in gas environment.

Table 8.1: Reference overview on LME of T91 steel under all investigated conditions.

150°C	200°C	250°C	300°C	350°C	400°C	450°C
[58]	[21][58][150]	[58]	[53][54][57][58]	[54][56][57][58]	[51][54][57][58]	[21][57][58]

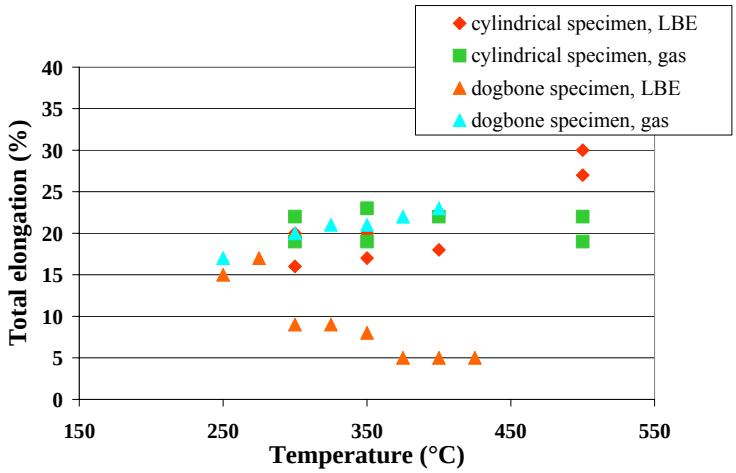

Figure 8.5: Ductility of standard T91 in liquid LBE environment and in gas environment.
Total elongation as function of temperature for several sizes of cylindrical specimens and for dog bone shaped specimens. Only cases reported as LME in literature were represented for results in LBE. References summarized in Table 8.1 above.

The severe LME and therefore well reproducible SSRT tests of the ferritic/bainitic/martensitic elevated Si steels would very well allow determining the ductility trough of all the examined materials. However, due to the very limited quantity of material available to us, we only determined the ductility trough temperature range for the 2439 steel at a strain rate of 5.10^{-6} s^{-1}. As shown in Figure 5.12, the ductility trough for the 2439 steel extends from about 250°C up to 375°C. The total elongation below 250°C is still lower than this in gas environment however the difference between the results in LBE and those in gas environment are not as large as between 250 and 375°C. Above 375°C, the embrittlement effect disappears entirely and the 2439 steel behaves fully ductile in both LBE and gas environment.

Strain rate

Despite our systematic study on the effects of strain rate on LME of T91 at 245, 350 and 450°C, the problems in reproducibility which prevented a reliable determination of the ductility trough, also prevented a reliable determination or verification of the effect of strain rate. In the produced results, no effect of strain rate was found.
However, for the thermally hardened T91 the sample tested in LBE at a strain rate of 1.10^{-6} s^{-1} broke in a brittle manner while the sample tested in LBE at a strain rate of 1.10^{-3} s^{-1} did not. As mentioned in section 1.3.1 of chapter 1, the effect of strain rate is thought to be related to the increase in yield stress of the embrittled solid which is also the case here as shown in Figure 6.1 in chapter 6. However, in contrast to what was mentioned in 1.3.1, the yield and ultimate tensile strength of the thermally hardened T91 increased with decreasing strain rate causing embrittlement at the lower strain rate but not at the high strain rate.

Apart from the possible influence of a strain rate dependent yield and UTS, the subtle influence of strain rate can be due to differences in wetting with time. This is especially hard to determine for the intermediately embrittled cases such as T91 in LBE.
Since the yield and UTS of T91 steel are hardly influenced by the strain rate as discussed in section 5.1.2 of chapter 5, the time dependant effect of wetting is considered to be more important for the study of LME of T91.

Stress

The vast majority of tests performed within the frame of this PhD were SSRT tests. This type of test does not allow straight forward determination of a possible threshold stress for LME. For 316L there is no LME evident and therefore also no threshold stress for LME.
For T91 the difficulties in reproducibility of the SSRT tests implied strong difficulties to determine a reliable threshold stress level for LME. The use of constant load tests for the determination of a possible threshold stress for LME would be more appropriate but since this type of testing is very time consuming, no constant load tests have been performed on the intermediately embrittled T91.

The constant load test performed on the notch sensitive 2440 steel did result in delayed failure. As for the examples mentioned in section 1.3.1 of chapter 1, no penetration of LBE into the 2440 steel was found in this study. This test confirmed that time dependent penetration or dissolution is not the cause of the embrittlement of the ferritic/bainitic/martensitic elevated Si steels.
Further study on the sensitivity of these elevated Si steels to the applied stress level in constant load tests in contact with liquid LBE would be required to make sound conclusions regarding the threshold stress level for LME.

Pressure

Although no systematic study on the influence of liquid metal pressure on LME has been performed in this PhD, it is acknowledged to be an important parameter for future heavy liquid metal applications. Due to the high density of lead alloys, the pressure is strongly increased with depth (about 1 metre of LBE for 1 bar of pressure). The liquid metal pressure will certainly have an influence on the liquid metal penetration into an advancing crack and therefore indisputably have its influence on LME. For this reason, as mentioned before, recommendations and/or limitations should be included on liquid metal testing depth in a future liquid metal testing standard.

Relatively small adaptations to the Limets 1 facility would allow for systematic study on the influence of liquid metal pressure and could be desirable for future licensing and design purposes.

Composition of the liquid metal

No systematic study of the composition of the liquid metal on the LME phenomenon was performed although with time the composition of the used LBE was altered slightly due to the repeated use of the same liquid metal inside the Limets 1 facility. Furthermore, the composition of the liquid metal inside the Limets 2 facility is not identical to this of Limets 1 since Limets 2 had been used for testing in liquid lead lithium eutectic environment prior to its conversion to liquid lead bismuth environment testing. Although as much as possible of the lead lithium was removed and the facility was rinsed with liquid lead bismuth, small quantities of lithium remained. Between 2 and 5 mg/g Li were detected in the LBE at the start-up of the Limets 2 LBE programme.
Despite these differences in chemical composition of the used liquid metal, no differences in occurrence of LME were observed over time in Limets 1 nor were any differences observed between the occurrence of LME in Limets 1 and Limets 2.

As mentioned in section 1.3.1, relatively large amounts of alloying are expected to be needed to alter the embrittlement.

For corrosion and initiation of LME the oxygen content of the liquid lead bismuth plays a very important role. The corrosion mode of the structural material in contact with the liquid metal, being either dissolution or oxidation, is determined by the oxygen content of the liquid metal as shown in section 1.2 of chapter 1. Since a dense oxide layer prevents wetting and therefore also LME initiation, oxygen contents were kept as low as possible during pre-exposures. Oxygen concentrations were however never measured during pre-exposure or during irradiation. Tests in Limets I were all performed at an oxygen concentration of 10^{-6} to 10^{-7} wt% oxygen while tests in Limets II were at oxygen concentrations between 10^{-7} to 10^{-8} wt% oxygen.
These oxygen concentrations are within the desired oxygen concentration range where no lead or bismuth oxides can be formed and the structural material's oxide layer remains stable or is slowly being dissolved [11],[108].

Composition of the solid metal

The remark mentioned in section 1.3.1 of chapter 1 that it is commonly accepted that the effect of alloying elements is manifested at the level of grain boundaries needs to be seen in the context of LME resulting in intergranular fracture. It should be obvious that for cases of LME where the embrittlement results in intergranular fracture the segregation to grain boundaries and the chemical composition at the grain boundary in general is of primordial importance.

In our study however, we did not encounter any intergranular fracture. The LME of the elevated Si steels was fully transgranular. Therefore, the composition of the bulk will play an important role.

As shown in section 5.1.3 of chapter 5, increasing the Si content of the ferritic/bainitic/martensitic steel increased the LME effect in LBE. Increasing the Si content increases the corrosion resistance to LBE of these steels but it also increases the material's DBTT (see Figure 2.27), the yield stress and the tensile strength. Furthermore, Si is a strong α-geneous element. It favours the formation of large grains and has a de-graphitising effect. Any one of these effects or a combination of them could be the cause of the increased LME. However, in the frame of the LME mechanism discussed in section 8.3, we will highlight which of these alloying effects is thought to be the cause of the increase in LME.

Furthermore, the composition of the solid metal is known to determine its microstructure and corrosion properties. The importance of these two aspects will be discussed further in the respective sections on microstructure and surface effect.

Microstructure of the solid

The increase in LME susceptibility of T91 due to thermal hardening shows that the bulk microstructure has a strong effect on the liquid metal embrittlement process. Although the grain size of the martensite was not altered by a decrease in tempering temperature, the increased LME susceptibility was obvious. By lowering the tempering temperature, the precipitation structure was changed and this decreased the dislocation mobility resulting in a higher hardness, yield stress and ultimate tensile strength. At lower tempering temperature (500°C), the amount of precipitation is small and precipitates are formed mostly inside the grains while higher tempering temperatures (730-780°C) will cause precipitation coarsening and precipitates will be dominantly at the grain boundaries.
It should be obvious that many microstructural aspects have an influence on the mechanical properties of steel and therefore on the material's susceptibility to LME and that this will make it very difficult to extract a simple relation on the effect of grain size on LME based on the SSRT tests of the complex steels used in this work.

In the ferritic/bainitic/martensitic elevated Si steels, the 2440 and 2441 steels had a ferritic microstructure with large grains while the 2439 steel had a bainitic microstructure with much smaller grains. As was discussed in section 5.1.3.1 of chapter 5, the LME was much worse for the 2440 and 2441 steels than for the 2439

steel. However, as mentioned above, this effect could be attributed to many other microstructural features.

The welded connections of T91 to T91 and T91 to 316L steel all showed significant embrittlement after pre-exposure in the 0 dpa capsule (see section 6.3.2.4 and section 6.3.2.5). For both the TIG and the EB welds the embrittlement was worse than for the base materials. Furthermore, the test results were well reproducible even though the same testing procedure was used as for testing the T91 base material. Thorough examination revealed that all welds broke in an area of increased hardness. The EB welds all broke in the weld while the T91/316L weld broke in the connection between the T91 base material and the buttering. The over alloyed 309 filler material used for TIG welding T91 also seemed to be more prone to LME than the T91 base material.
Despite pre-heating, the relatively rapid cooling after welding led to thermal stresses. Even after performing the recommended PWHT for these types of welds, the residual hardness in some areas of the welds was still elevated and significantly increased the susceptibility to LME in comparison to this of the base metals.

The cold worked 316L did not undergo any obvious embrittlement although the work hardening resulting from the cold work did significantly increase the material's hardness, yield strength and ultimate tensile strength. Cold work strongly increased the dislocation density in the 316L material creating dislocation forests, kinks and jogs which can hinder further dislocation movement. Furthermore, the cold work changed the microstructure from equi-axed austenite grains to long stretched grains. Despite these microstructural features hindering dislocation movement, the 316L material's susceptibility to LME was not increased.

Most likely, the difference in LME susceptibility between the ferritic-martensitic T91 and the austenitic 316L is caused by the difference in plastic deformation behaviour between the BCC and FCC lattice. As could be seen in the elevated Si steels, the austenitic varieties were also much less prone to LME than the ferritic/bainitic/martensitic elevated Si steels. The LME effect is manifested by brittle cleavage fracture in the solid metal – liquid metal systems studied here and it is known that brittle cleavage fracture can be observed in BCC or HCP metals but not in FCC metals [149]. For FCC metals, brittle fracture is manifested when there are factors contributing to grain boundary embrittlement. This is the case for several other examples of LME given in Chapter 1 but no intergranular embrittlement was observed for any of the austenitic steels tested in LBE.

Specificity solid metal – liquid metal couple

The intermediate nature of LME for the T91 – LBE couple are to be seen as a strong argument that LME is not a digital process. LME does not either occur catastrophically or not at all. It has become obvious based on the results presented in chapters 5, 6 and 7 and the discussion on the metallurgical parameters influencing LME above that many parameters influence the occurrence of LME however there is no specificity and all solid metals can be embrittled provided that the influencing parameters favour embrittlement.

Surface effect

In all cases of environmentally assisted cracking (hydrogen embrittlement, stress corrosion cracking, irradiation assisted stress corrosion cracking, liquid metal embrittlement,….) the surface plays a predominant role in the initiation of the cracking. Although the mechanisms of mechanical degradation in environmentally assisted cracking are not necessarily similar, the macroscopic effects are.

For LME, the surface condition strongly influences the wetting of the solid by the liquid. Since good wetting is required for LME to occur, the surface condition is a very important parameter.
Initially it was assumed that SSRT testing would break the oxide layer due to its much lower ductility compared to this of the bulk and therefore allow intimate contact between the liquid metal and the underlying bare solid metal. However, complete absence of LME in our initial study of the effects of temperature and strain rate on LME of T91 caused us to believe there was insufficient wetting [21]. Other authors [55] claimed the need to remove the oxide layer by either fluxing or ion sputtering followed by PVD deposition of LBE to perform valid LME tests.
Ion sputtering followed by PVD deposition of LBE was considered too laborious to allow a systematic study of the parameters influencing LME. Furthermore, it proved to be unsatisfactory due to the insufficient amount of LBE deposited on the surface to fully allow LME [56]. Fluxing was avoided because residual elements from the fluxing could influence the LME process.
To improve wetting under conditions as close to the application as possible, samples were pre-exposed in LBE under reducing conditions at a constant elevated temperature or under thermal cycling. As shown in section 6.3 of chapter 6, the pre-exposure did increase the material's susceptibility to LME. For the T91 steel, the LME phenomenon occurred more frequently than without pre-exposure and the fracture surfaces revealed more initiation sites. However, the embrittlement was still not fully reproducible.

The elevated Si steels however showed a very strong LME effect when tested in LBE without any prior surface treatment or pre-exposure. This was considered to be a clear indication that although the native oxide layer prevents wetting of the underlying bare metal, this oxide layer is in fact ruptured during testing allowing LME to occur when the solid metal is prone to LME or when the repassivation of the oxide layer is sufficiently slow to allow LME. Nevertheless, pre-exposure of the elevated Si steels also led to an increase in the severity of LME despite their excellent corrosion resistance in LBE [81],[82],[83]. The total elongation of the elevated Si steels was further decreased and the fracture surface was fully brittle. The shift of the occurrence of LME in the ferritic/bainitic/martensitic elevated Si steels to smaller elongations is most probably due to better wetting since these steels are more corrosion resistant in LBE and are therefore less likely to form corrosion cracks at the surface. It remains unclear however what exactly promotes wetting by pre-exposure in these very corrosion resistant elevated Si steels since the pre-exposure cannot remove their oxide layer based on their excellent corrosion properties in contact with LBE [81],[82],[83].

In the martensitic T91, surface cracks caused by either corrosion, EDM cutting [57] or machining, were found to strongly increase the susceptibility to LME. In this work, this was shown by the sample pre-exposed in low oxygen LBE at 450°C and tested at 450°C and by the notched specimens of T91, discussed in section 6.2, which had an increased susceptibility to LME. As shown in the fracture surface examination depicted by Figure 6.6, the LME effect was predominantly present near the root of the notch. This is because a notch increases the tendency for brittle cleavage fracture, because it produces high local stresses, introduces a tri-axial tensile stress state, produces high local strain hardening and cracking and produces a local increase in strain rate.

For the austenitic 316L steel, the notch had little or no effect on its susceptibility to LME since austenitic steels do not seem to suffer from LME by cleavage fracture due to their intrinsic resistance to cleavage by ductile deformation.
The 40% cold worked 316L, which contains a small amount of ferrite due to deformation induced transformation of austenite, is assumed to remain unaffected by the LBE due to the very good repassivation capability of the 316L oxide layer.

Neutron irradiation effect

As discussed in section 1.4, neutron irradiation introduces microstructural defects, causes hardening and embrittlement, radiation induced segregation and precipitation and causes swelling at high dpa. All these mechanical and microstructural effects of irradiation will to some extent influence the occurrence of LME. Based on the observations of increased susceptibility to LME of the thermally hardened T91 and of the welds, it is regarded highly probable that irradiation hardening and embrittlement will also increase the material's susceptibility to LME.

The TWIN ASTIR irradiation performed at 465-495°C did not cause any hardening in the austenitic 316L steel, nor in the martensitic T91 but the elevated Si steels did harden significantly due to the irradiation. Although the irradiation temperature is probably above stage V for the elevated Si steels, the high temperature irradiation must have caused precipitation and formation of NiSi and FeSi second phase particles.
The elevated Si steels were severely embrittled in LBE after irradiation. Unfortunately, we do not have any reference data on the mechanical properties of the elevated Si steels irradiated up to 1.5 dpa and tested in inert environment. However, when comparing to the results after pre-exposure in the 0 dpa capsule, the embrittlement has become worse after irradiation in contact with LBE.

The T91 irradiated in contact with LBE at 465-495°C in TWIN ASTIR revealed an increased susceptibility to LME at the low strain rate (1.10^{-6} s^{-1}) while no increased LME effect was observed at the high strain rate (1.10^{-3} s^{-1}). Both tests performed at the low strain rate revealed a significant decrease in total elongation even though the T91 steel was softened due to the irradiation. This might be an indication that the irradiation in contact with LBE promoted the wetting. However, the improved wetting might be due to the thermal corrosion in LBE at 465-495°C. As the 0 dpa capsule was programmed based on the initial gamma heating calculations, the materials were pre-exposed at significantly lower temperatures (350°C). Therefore, we are not able to distinguish whether the improved wetting is neutron irradiation enhanced or simply due to the thermal corrosion.
The test results from T91 irradiated in TWIN ASTIR do confirm the findings of the LiSoR experiments discussed in section 1.5.

Low temperature irradiation (200-350°C) in contact with LBE as well as reference tests of material irradiated in contact with gas or water will be needed to thoroughly assess the LME of the structural steels.

8.3 LIQUID METAL EMBRITTLEMENT MODELS CRITICALLY REVIEWED

The observed liquid metal embrittlement is very obvious for the ferritic/bainitic/martensitic elevated Si steels and to a much lesser extent for the conventional martensitic T91 steel. This means that the embrittlement of T91 is an intermediate case where the LME process is competing against conventional ductile behaviour.
For clarity, we will critically review the LME models using the most "pure" case of LME observed in this study being the Si enriched 2440 and 2441 steels in LBE and then examine if we can explain the competition between this model and conventional ductile behaviour for T91. Furthermore, we will try to explain why the 316L steel did not undergo any LME and explain the observed influence of parameters such as temperature, strain rate, grain size, etc. in the frame of the most likely LME model.

8.3.1 LME model

Based on the LME models discussed in section 1.3.2 of Chapter 1 and the critical review of the parameters influencing LME for the liquid metal – solid metal systems studied in this work, we need to conclude that the term "Liquid metal embrittlement" is used for at least 2 types of mechanical degradation.

When examining the reported liquid metal embrittlement causing predominantly intergranular failure as depicted in Figure 8.6, we have to conclude that the mechanism at the basis of this embrittlement is fundamentally different to this causing the full brittle cleavage failure we observed in the elevated Si steels tested in liquid LBE as depicted in Figure 6.21.
No intergranular penetration of LBE into the matrix of any of the studied structural steels has been found so far and none of the observed embrittled fracture surfaces revealed intergranular fracture. This is in very sharp contrast with some reported cases of LME such as for instance Al-Hg [18] and Al-Ga [18] and Ni-Pb [145], Ni-Bi [148].

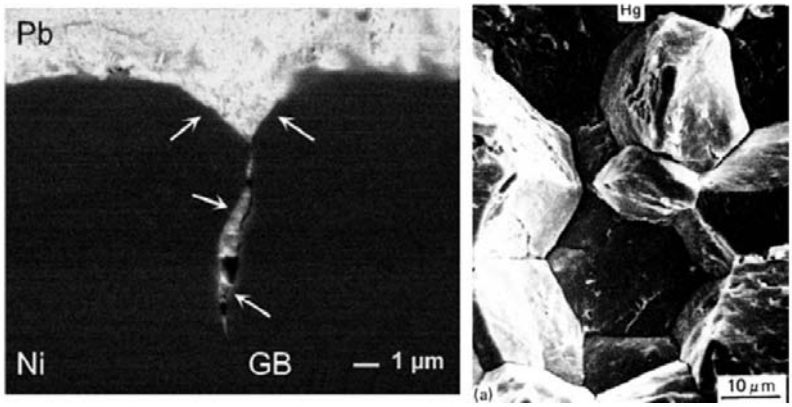

Figure 8.6: Intergranular penetration of liquid metal and intergranular failure reported in LME studies [145],[40].

Therefore we would propose to distinguish the 2 types of LME as:

- LME based on intergranular penetration of liquid metal into the solid;
- LME based on cleavage fracture.

The subdivision into different types of LME is currently becoming more and more accepted although the number of types of LME is not agreed upon. For instance T. Auger *et al.* [63] propose a third LME mechanism based on localised plastic flow according to the Lynch model (see section 1.3.2). In what follows however, we will try to explain that the localised work hardening in the path of the crack observed by both Lynch [37]-[40] and Popovich [41], [45] is actually the result of the embrittlement and not the cause.

As we divide the LME phenomenon into 2 types, this also implies that the models based on intergranular fracture or intergranular penetration of liquid metal into the bulk such as the Hancock and Ives' model and the grain boundary penetration model do not apply to the type of LME studied here. It is clear that these two models can not explain the LME phenomena observed in the enriched Si steels in contact with LBE. Which of the models is most suitable to explain the intergranular failure type of LME is considered to be outside the scope of this work since we did not observe any intergranular failure.

The stress assisted dissolution models by Robertson and Glickman could in principle not be discarded based on the observed fracture surfaces. However, it is very unlikely that the high velocity, fully brittle transgranular cleavage failures observed in the Si enriched steels tested in LBE are caused by stress assisted dissolution. The model is especially unlikely since these Si enriched steels were reported to be very corrosion resistant and show a lower dissolution rate in both static and flowing

exposure to LBE [81],[82],[83] than the conventional T91 steel [87],[151] which is less embrittled (see chapter 5).

Since the reduction in surface energy model is strongly based on thermodynamic considerations and furthermore the influence of the surface energy on the fracture properties can be determined in several ways (see section 1.3.2), we believe that the decrease in surface energy will contribute to a certain extent to the LME phenomenon. However, the model does not mention any mechanism on the atomic scale. Therefore, we also accept the reduction in surface energy as a contributing factor to LME but insufficient to fully explain the phenomenon.

By method of elimination this leaves the adsorption induced reduction in cohesion model and the localised plastic flow models by Lynch (enhanced dislocation emission model) and Popovich (enhanced work hardening model) both reinforced by the reduction in surface energy model. However, based on the observation of pure cleavage fracture of the 2440 and 2441 steels in LBE as depicted again in Figure 8.7, we have to conclude that the observed LME is due to the adsorption induced reduction in cohesion causing crystallographic planes to be separated by pure cleavage as described by the adsorption induced reduction in cohesion model in section 1.3.2 of chapter 1.

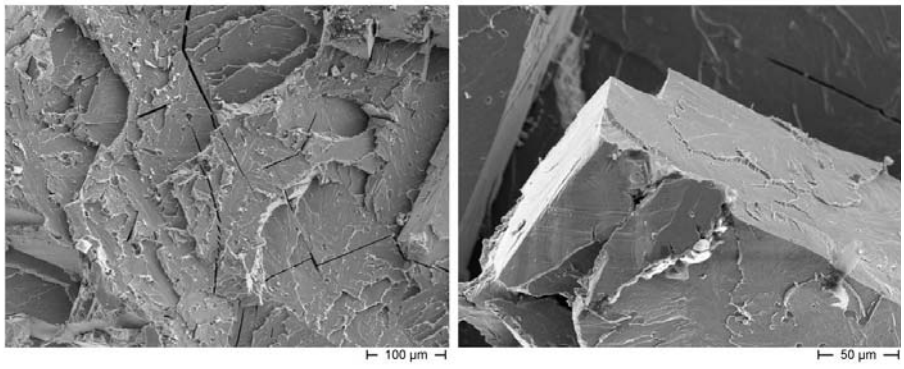

Figure 8.7: Cleavage fracture of 2441 steel after pre-exposure in the 0 dpa capsule.

8.3.2 LME mechanism and influencing parameters

To have a better understanding of the LME phenomenon in the frame of the adsorption induced reduction in cohesion model, we will briefly review the basics of brittle fracture and show how the reduction in cohesion can cause brittle cleavage fracture in a certain temperature range and furthermore be influenced by so many metallurgical parameters.

Brittle fracture

The theoretical stress to break atomic bonds is easily evaluated according to the simple formula given below where E is Young modulus, γ_s the reversible surface energy and a the interatomic distance.

$$\sigma_{cleavage}^{theor} = \sqrt{\frac{E\gamma_S}{a}} \approx \frac{E}{10} \qquad \textbf{(8.1)}$$

This theoretical stress is considerably larger (about 10 to 100 times) than the effective macroscopic fracture stress. Therefore, nucleation of fracture is possible only through the effect of local concentration of stress. However, notice that in this theoretical stress to break the atomic bonds, the surface energy is a very important factor. It again underlines the importance of the surface energy in environmental cracking but the decrease in surface energy is considered to be a necessary but not sufficient condition for LME as discussed before in section 1.3.2.

In metals, local stress concentrations can arise because plastic deformation (dislocation glide) is hindered by microstructural obstacles (see Figure 8.8) or by other dislocations. For instance, in BCC metals due to the combination of two dislocations which come together and react as follows:

$$\frac{a_0}{2}\left[\bar{1}\,\bar{1}\,1\right] + \frac{a_0}{2}\left[1\,1\,1\right] \rightarrow a_0\left[0\,0\,1\right] \qquad \textbf{(8.2)}$$

Since the (001) plane is not a close packed slip plane in the BCC lattice, the dislocation is immobile. Moreover, the (001) plane is the cleavage plane along which brittle cleavage fracture occurs.

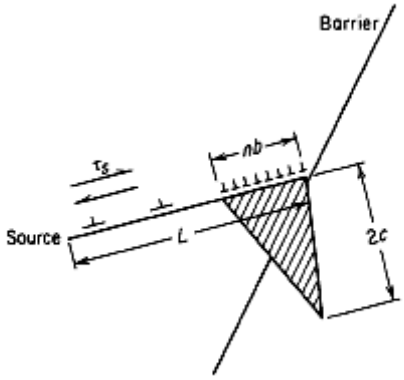

Figure 8.8: Model of microcrack formation at a pile-up of edge dislocations [149].

The first mechanism of build up of local stress at microstructural obstacles is very much the same mechanism as that for the stress concentration necessary to reach the yield point and actually, both mechanisms are locally in competition at the crack tip.

In BCC materials which have a ductile-to-brittle transition, the yield strength decreases with increasing temperature whereas the cleavage strength remains roughly constant. This is schematically depicted in Figure 8.9.

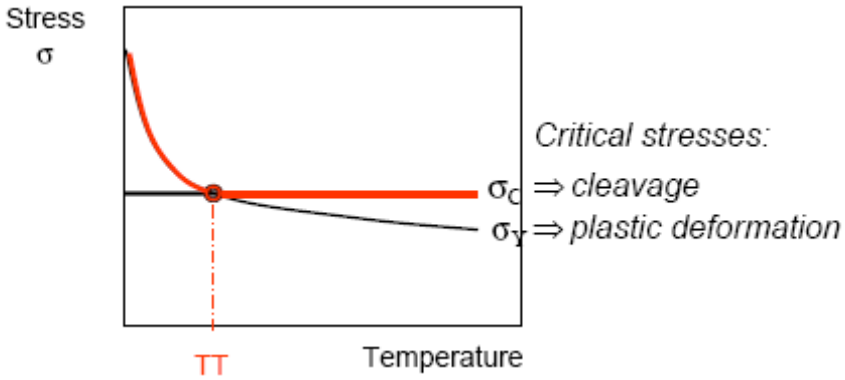

Figure 8.9: Schematic representation of the yield stress and cleavage stress as function of temperature, which causes the DBTT of BCC metals.

Below the cross-over temperature, fracture cannot occur until some local plastic deformation is produced, in order to build up the necessary stress concentration against grain boundaries. One must therefore increase the applied stress up to the yield point in order to trigger this, but as soon as this stress level is attained, brittle fracture occurs since the applied stress is now larger than the critical cleavage strength, and the effective fracture stress will be equal to the yield stress.

Conversely, above the cross over, the applied stress has to be increased above the yield point, that is, the material experiences general yield and strain-hardens until the critical fracture stress is reached and fracture takes place in the ductile range. This cross-over is the ductile-to-brittle transition temperature, and the effective fracture strength follows the red curve.

Based on the principle depicted in Figure 8.9, embrittlement can result from an increase in yield strength at constant cleavage strength or from a decrease in cleavage stress at constant yield strength. Both possibilities are schematically shown in Figure 8.10.

The adsorption induced reduction in cohesion model states, as discussed in section 1.3.2, that the presence of liquid metal atoms at the crack tip lowers the energy barrier that needs to be overcome to separate the two atoms at the crack tip. Macroscopically, this model therefore claims that the presence of liquid metal at the crack tip lowers the cleavage stress, indicated by σ_c in Figure 8.10.
As can be seen in the schematic representation, by decreasing the cleavage stress, the presence of liquid metal increases the DBTT temperature. This shift then defines the upper temperature of the ductility trough. The lower temperature of the ductility trough is defined by the ability of the liquid metal atoms to reach the crack tip and their influence on the cohesive energy as a function of temperature. This explains why for the majority of embrittling couples, the LME is very dominant near the melting temperature however not for all embrittling couples.

Electronic structure calculations on the surface energy reduction of pure iron by adsorption of LBE have shown there will be a reduction in the surface energy by between 16 and 35% depending on the crystallographic orientation (22% for (001)-plane; 35% for (011)-plane; 16% for (111)-plane) due to adsorption of LBE [152]. Although these values confirm a decrease in the cleavage stress due to a reduction in surface energy of the cleavage plane (the (001)-plane) it is unclear whether this is sufficient to explain the LME. The adsorption induced reduction in cohesion has not yet been confirmed by any structure calculations showing a decrease in cohesion of the atoms which can account for an additional decrease in cleavage stress. Furthermore, the available electronic structure calculations are based on pure iron in contact with LBE. Although all investigated steels in this work are mainly comprised of iron, their mechanical behaviour in contact with LBE is clearly different.
Despite these uncertainties, the adsorption induced reduction in cohesion model is the only model which accounts for the vast majority of the experimental observations.

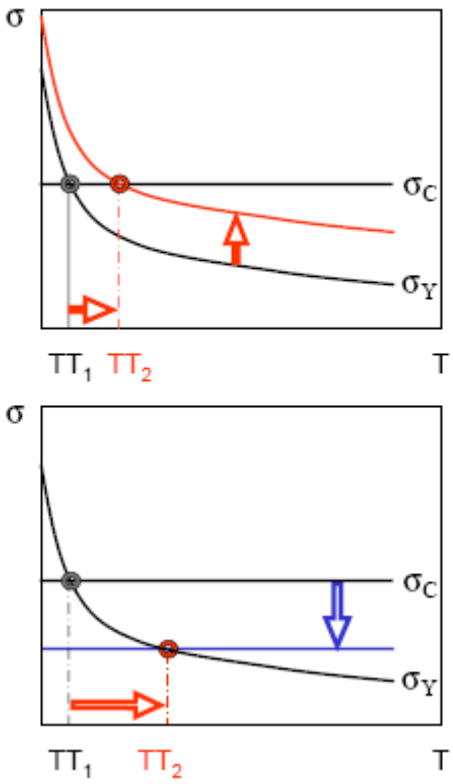

Figure 8.10: Schematic representation of increase in embrittlement by either an increase of yield strength at constant fracture stress (above) or by a decrease in cleavage stress at constant yield strength.

The first type of increased embrittlement caused by an increase in the yield stress is basically caused by any form of hardening. As can be seen above in Figure 8.10, this shifts the transition temperature to the right. Increased hardness or increased yield strength can be produced by any obstacles to dislocation glide, essentially finely dispersed clusters of point defects or solute atoms, and precipitates. The increased LME susceptibility of thermally hardened T91 should be attributed to this because the hardening was caused by a larger volume fraction of martensite and finely distributed precipitates inside the grains which strongly hindered the dislocation mobility.

Neutron irradiation at temperatures below stage V rapidly increases the yield strength and hardness even at rather low irradiation doses by introducing a large number of microstructural defects. At irradiation temperatures above stage V, the hardening effect is much slower since it is based on radiation induced segregation and precipitation as discussed in section 1.4. Furthermore, radiation induced

segregation and precipitation may lower the cleavage stress. These phenomena become important at rather high dpa.

As mentioned before, embrittlement can arise from a decrease in fracture strength at constant yield strength as well, and this can be produced through a variety of mechanisms, such as the increase in grain size, thermal or radiation induced segregation to the grain boundaries, or the precipitation of coarse particles of a second phase.

Unfortunately, the results discussed in chapter 7 are the result of relatively low dose irradiation above stage V. These conditions can not be conclusive by themselves. Not about the effect of irradiation hardening on LME due to the absence of hardening of the T91 and 316L steels above stage V, nor about the effects of RIS, precipitation and possible formation of phases on the LME process due to the relatively low dose and irradiation time.
Despite this, the parameters influencing LME in non irradiated materials discussed in section 1.3.1 can be very well explained by the above principles depicted in Figure 8.10.

Elastic and plastic behaviour

The elastic and plastic behaviour of the material in contact with liquid metal will be the same as under inert environment up to the point of fracture because there is no penetration of liquid metal into the bulk.

Fracture behaviour

The fracture behaviour of "pure" LME cases of the type studied here will be transgranular cleavage as was obviously observed in the ferritic/bainitic/martensitic elevated Si steels.

Temperature

The effect of temperature has been explained above. It is clear that fundamental study and modelling will be needed to fully understand the combination of the liquid metal properties and the solid (e.g. viscosity of the liquid, adsorption induced surface energy reduction, adsorption induced reduction in cohesion, etc.).

Strain rate

As for temperature, the strain rate of the test will have consequences on both the mechanical properties of some materials and the contact conditions of the liquid metal at the crack tip. Fast strain rates are known to increase the brittle nature of most materials but this may prevent adequate wetting of liquid metal at the crack tip preventing LME to occur.

Pressure

On the other hand, the influence of liquid metal pressure is rather clear. If the pressure is simply applied to the supply of the liquid metal to the crack as in [20] the pressure will benefit the supply of liquid metal to the crack tip and enhance the LME. However, when the sample is fully submerged in the liquid metal there will be competition between the hydrostatic pressure which promotes ductility and the supply to the crack tip which promotes LME.

Grain size

The effect of grain size deserves a special mention because grain refinement is practically the only metallurgical parameter which improves hardness and fracture behaviour of the solid metal simultaneously. The yield strength increases with the inverse square root of grain diameter according to the well known Hall-Petch equation.

$$\sigma_{YS} = \sigma_i + k_y d^{-1/2} \qquad \textbf{(8.3)}$$

Where σ_{YS} is the yield stress, σ_i the lattice friction stress which represents the overall resistance of the crystal lattice to dislocation movement, k_y is the locking parameter which measures the relative hardening contribution of the grain boundaries and d is the grain diameter.

On the other hand, Cottrell's model states that the cleavage stress exhibits a similar dependence, but with a larger slope and no threshold stress according to the following equation:

$$\sigma_C = \left(\frac{4\mu\gamma_m}{\pi(1-\nu^2)} \right)^{1/2} d^{-1/2} = \left(\frac{2\mu\gamma_m}{k_y} \right) d^{1/2} \qquad \textbf{(8.4)}$$

Where μ is the shear modulus, γ_m the surface creation energy and ν the Poisson ratio.

The resulting intersection again defines a transition, which is schematically represented in Figure 8.11, in very much the same way as for the temperature dependence.

Thus, similar to Figure 8.9, brittle fracture occurs at the yield point for large grain sizes (to the left) and ductile fracture occurs for the smaller grain sizes (to the right). However, as the coefficient for cleavage stress is larger than that for yield stress, the fracture strength increases more than the yield strength as the grain size decreases (to the right). This effect of grain size encountered when studying the "traditional" DBTT shift is also reported in LME studies as discussed in the part on microstructure of the solid in section 1.3.1 of chapter 1. Although we did not do a systematic grain size study, the LME encountered in the large grain ferritic elevated Si steels was considerably worse than the LME encountered in the bainitic 2439 elevated Si steel.

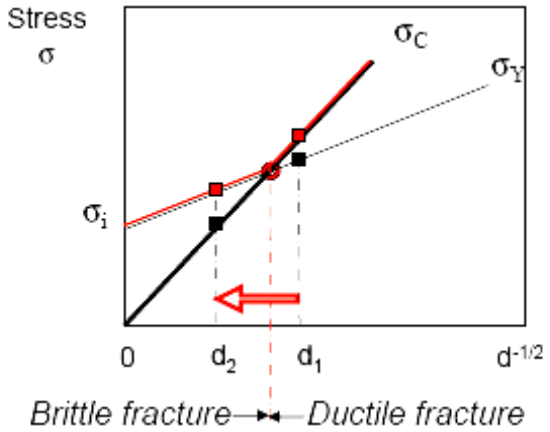

Figure 8.11: Schematic representation of the influence of grain size on the ductile to brittle transition in BCC metals.

Composition of the solid

The importance of the composition of the solid metal is underlined by the fact that even though all examined structural steels are predominantly comprised of iron, their mechanical behaviour is very differently affected by the liquid metal environment.

In our study it became obvious that by increasing the concentration of silicon in a BCC steel, its susceptibility to LME is strongly increased (see section 5.1.3.1 of chapter 5).

In air it was observed that the increase of Si in these steels caused an increase in the DBTT shift (see Figure 2.27). This increase in DBTT is rather strong as can be seen by comparison of T91 to T91-Si: -92°C for T91 vs. 48°C for T91-Si. Although the

solid solution strengthening of the Si will account for an increase in DBTT due to the increase of yield stress and hardness based on the principles explained above, the silicon addition also decreases the stacking fault energy and therefore also decreases the material's surface energy and cleavage stress.
When tested in liquid metal the DBTT is further increased due to the decrease in surface energy and the adsorption induced reduction in cohesion as can be seen from the upper limit of the ductility trough of the bainitic 2439 steel: DBTT at 93°C in air vs. 375°C in LBE.

Surface condition

The initiation of LME is determined by the surface condition, by the toughness of the oxide layer and by the kinetics of (re-)passivation of the oxide layer.
It was found by corrosion examination of elevated Si steels in LBE that in high Si steels a silica (SiO_2) layer is formed at the interface of the bulk and the oxide below the main oxide scale [82]. This very brittle oxide certainly breaks under application of strain during an SSRT test. Therefore, the underlying bare metal is exposed to the liquid metal environment as originally expected (see discussion section 5.1.2). In contrast to the reproducibility problems for LME testing of T91 steel which forms an oxide layer consisting of a spinel of Cr, the Si based oxide layer does not form protection from LME under strain. This difference in protection of the oxide layer against LME might be due to the kinetics of (re-)passivation or to the density of the formed oxide and should be studied in a detailed corrosion investigation.

8.3.3 Intermediate embrittlement: LME vs. ductile tearing

Despite the difference in protection by the oxide layers which might hinder liquid metal wetting and prevent LME, studies performed on de-oxidised T91 [56] or even thermally hardened T91 (see section 6.1.1, [58]) have not resulted in the degree of LME encountered in the elevated Si steels. Fracture surface examinations at most revealed mixed brittle – ductile fracture.
To explain the LME by adsorption induced reduction in cohesion of the intermediately embrittled couples, we need to examine more into detail what exactly is happening when materials are deformed to fracture.

Ductile fracture of metals in uniaxial tension is preceded by a localized reduction in diameter which is called necking. The stages in the development of a ductile cup and cone fracture are illustrated in Figure 8.12. Necking begins at the point of plastic instability where the increase in strength due to strain hardening fails to compensate

for the decrease in cross-sectional area (Figure 8.12a). This occurs at maximum load in the engineering stress – engineering strain curve. Many fine cavities form in the necked region (Figure 8.12b) and under continued straining these grow and coalesce into a central crack (Figure 8.12c). This crack grows in the direction perpendicular to the axis of the specimen until it approaches the surface of the specimen. Then, it propagates along localised shear planes at roughly 45° to the axis to form the cone part of the fracture (Figure 8.12d). Thus crack growth in ductile fracture is essentially a process of void coalescence initiated in the centre of the specimen.

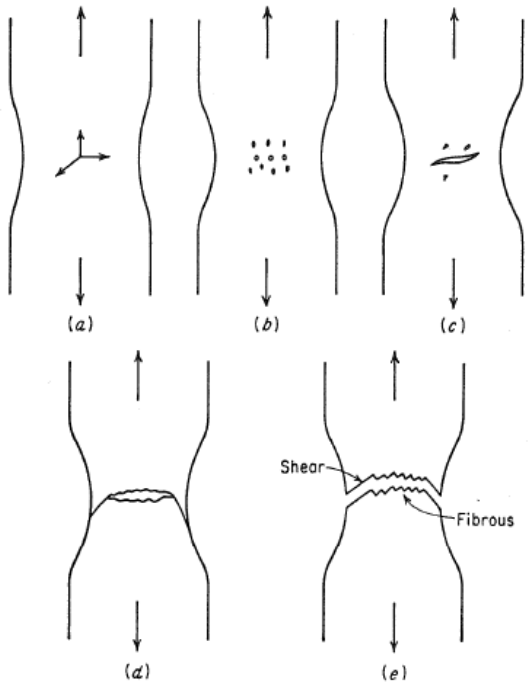

Figure 8.12: Stages in the formation of a ductile cup and cone fracture [149].

In contrast to ductile tearing, the LME process is initiated at the surface and progresses inward as shown by the semi-circular patterns initiated at the surface in the numerous fracture surface examinations discussed in chapters 5 & 6. If the rate of LME fracture is lower than ductile fracture progression or the LME initiation takes too long, the centre of the specimen will be fully ductile. Therefore, the effect of strain rate was examined to very low strain rates (down to 1.10^{-7} s^{-1}) as discussed in section 5.1.2. Even at very low strain rates, the fracture surface was fully ductile in the centre of the specimen.

However, based on this relative speed of LME fracture compared to ductile tearing discussion, the LME fractured part of the fracture surface should be fully brittle

while this was never observed. The competition between ductile fracture and LME brittle cleavage in the ferritic-martensitic T91 must therefore also be present on an atomic or more likely grain to grain basis. This is confirmed by the full brittle cleavage of a grain surrounded by ductile or mixed ductile – brittle fracture in the fracture surface of a DCT specimen shown in Figure 5.36B. Furthermore, the electronic structure calculations mentioned in section 8.2 above have shown that the amount of surface energy reduction caused by adsorption of LBE on pure iron depends on the crystallographic orientation [152].

Although it is clear that the orientation of the crystal lattice is important for the intermediately embrittled couples, fracture surface examination did not reveal areas where some grains are fully fractured in cleavage and others by ductile deformation. Therefore, it needs to be taken into account that the liquid metal does not penetrate the bulk and therefore only affects the outer atomic layers. The stress distribution near an advancing crack is however not at its maximum at the crack tip itself but reaches a maximum a certain distance from the crack tip depicted as r_y in Figure 8.13 for the case of plane strain conditions. This allows for conditions where the yield stress of the bulk will be exceeded at a certain distance into the bulk causing plastic deformation and strain hardening in the plastic zone before the cleavage stress of the atomic planes in contact with the liquid metal is reached. Furthermore, the local work hardening and formation of microvoids in the plastic zone ahead of the crack tip may prevent efficient adsorption of the liquid metal atoms onto the advancing cracked surface.

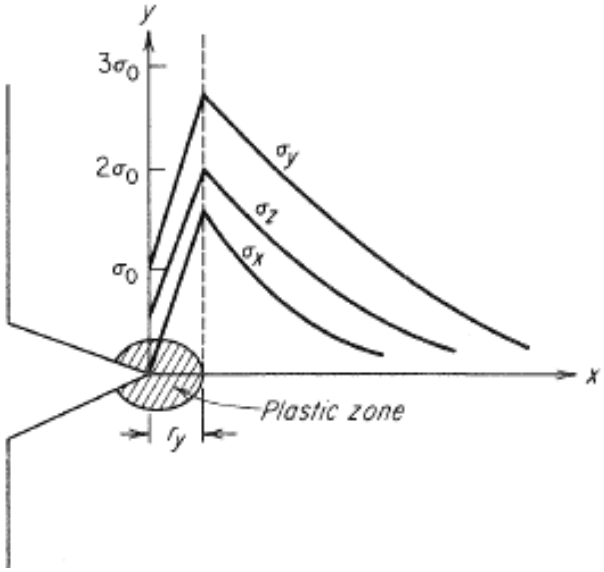

Figure 8.13: Distribution of stresses during local yielding (plane strain) [149].

This competition between ductile tearing and LME fracture is attributed to cause the mixed ductile – brittle fractures observed in chapters 5 and 6. Furthermore, this mechanism of local work hardening in the plastic zone to allow LME to occur at the crack tip will result in a more narrow plastically deformed zone in the path of the crack in comparison with the same material tested in air. This narrow plastic zone will become more and more narrow as the material is more and more susceptible to LME. The most "pure" form of LME being fractured by full brittle cleavage having the most narrow plastic zone resulting from the crack moving through the crystal along a number of parallel planes which form a series of plateaus and connecting ledges. This explains the observations of localised deformation made by Lynch and Popovich.

8.4 GENERAL CONCLUSIONS

The austenitic stainless steel 316L, the ferritic-martensitic T91 steel, TIG and EB welds of T91/T91 and T91/316L and several experimental silicon enriched steels were examined for their susceptibility to liquid metal embrittlement in contact with liquid lead bismuth eutectic before and after irradiation in contact with liquid lead bismuth eutectic. The mechanical properties of the investigated materials were assessed by tensile and fracture toughness tests in liquid metal environment and in gas environment at temperatures between 150 and 450°C with emphasis on the material's behaviour at 350°C which was found to be within the material's range of liquid metal embrittlement susceptibility.

In this section we summarize the general conclusions based on the literature and our experimental results shown in chapters 5, 6 and 7 and thoroughly discussed in the sections above.

316L

The austenitic stainless steel 316L is not embrittled by the liquid lead bismuth eutectic environment under any of the examined conditions. This is attributed to the FCC lattice which favours ductile deformation over cleavage fracture and the steel's dense oxide layer which prevents wetting by the LBE and allows it to repassivate when the oxide layer was damaged.

Plane strain fracture toughness measurements at 200 and 300°C revealed a decrease in fracture toughness by about 10%. However, these results need to be confirmed by additional fracture toughness analysis to increase the statistical reliability.

Neutron irradiation in contact with LBE at 460-490°C did not increase the material's susceptibility to LME.

T91

The ferritic-martensitic T91 steel is intermediately embrittled by LBE between 200 and 450°C. The material's susceptibility to embrittlement is increased by long term exposure in contact with LBE, thermal hardening and the presence of surface defects (cracks or notches). Fracture occurs in a mixed ductile – brittle mode.

Plane strain fracture toughness at 200 and 300°C is decreased by maximum 30% when the LBE is present at the crack tip. These measurements need to be confirmed by further fracture toughness assessment to improve their statistical reliability.

Neutron irradiation in contact with LBE at 460-490°C caused softening of the ferritic-martensitic steel by 50-100 MPa. The LME by LBE was more reproducible after neutron irradiation, which might indicate improved wetting due to corrosion.

Si enriched steels

The ferritic/bainitic/martensitic elevated Si steels were very susceptible to LME. The liquid LBE environment caused the material to break by full brittle cleavage fracture at 350°C. The 2439 steel had a distinct ductility trough between 250 and 375°C. The austenitic Si enriched steels revealed no susceptibility to LME for Si contents around 1.00 wt% while the high Si steels proved to be very susceptible to both hydrogen embrittlement and LME.

After neutron irradiation in contact with LBE at 460-490°C all examined Si enriched steels showed hardening and were strongly embrittled. Fracture surface examination and microstructural examination would be needed to draw further conclusions.

Welds

Both the T91/T91 TIG and EB welds are susceptible to LME in contact with LBE. The mechanical behaviour of these welds is the same up to the point of premature fracture. Fracture occurs gradually with several initiation sites for LME resulting in a significantly lower total elongation. However, despite the embrittlement the yield strength and tensile strength of the welds are reached and remain the same as under inert conditions. Fracture occurred in the areas of the weld which were hardened by the welding process. The increased susceptibility to LME of the examined T91/T91 welds is therefore also attributed to the increased hardness.

After neutron irradiation in contact with LBE at 460-490°C, both the T91/T91 TIG and EB welds are softened by 50 – 100 MPa and the degree of embrittlement when tested in liquid LBE is comparable to the LME observed prior to irradiation.

For the T91/316L TIG weld, it was shown that the 309 alloy, used for buttering is severely embrittled when tested in liquid metal environment after thermal cycling in contact with LBE.

The T91/316L EB weld does not have buttering and the T91 is directly fused onto the 316L. This however leads to very sudden changes in the chemical composition across the weld. Furthermore, it was shown that the T91/316L EB weld is embrittled by LBE and that the embrittlement is worse after thermal cycling in contact with LBE. The increased susceptibility to LME on the T91 side of the weld for the TIG weld and inside the weld for the EB weld is attributed to the elevated hardness in these parts of the respective welds.

After neutron irradiation in contact with LBE at 460-490°C, the T91/316L TIG weld was slightly less embrittled at the connection between the 309 buttering and the T91. The T91/316L weld however, was more embrittled after neutron irradiation than before. Fracture surface examination and chemical analyses would be needed to allow more precise conclusions.

LME mechanism

Based on the observations of full brittle transgranular cleavage fracture of the elevated Si steels in LBE above their DBTT temperature, the adsorption induced reduction in cohesion model was found to be the only model capable of explaining the majority of experimental results. Although the decrease in surface energy clearly plays a very important role in the LME process, it is doubtful whether this can fully account for the decrease in cleavage stress caused by the liquid metal atoms at the crack tip. Reliable surface energy data will be needed to allow for sound conclusions.

The intermediate embrittlement of the ferritic-martensitic steel T91 is attributed to the local competition between ductile tearing and LME induced brittle cleavage fracture. Initiation and propagation may be hindered by (re-)passivation of the surface or by difficulties in adsorption of the liquid metal onto the advancing cracked surface which is roughened by prior work hardening and microvoid formation.

9 OUTLOOK TO FUTURE WORK

My interest is in the future because I am going to spend the rest of my life there.
Charles F. Kettering
(1876-1958)

Losers live in the past. Winners learn from the past and enjoy working in the present toward the future.
Denis Waitley
(1924-…)

Knowing is not enough; we must apply. Willing is not enough; we must do.
Johann Wolfgang von Goethe
(1749-1832)

Chapter 9 summarises the related work which is currently in the pipeline and makes suggestions for future work which is highly needed towards realisation of possible applications or towards the understanding of LME.

First, the complementary research needed to optimally interpret the results presented in this PhD work will be summarized. These could not be performed due to a lack of time or due to restrictions in licensing but would strongly add to the scientific understanding of the work realised in this PhD.

Second, we will underline the importance of certain fundamental and engineering R&D work to be done to enable a more profound understanding of LME and to enable the realisation of a heavy liquid metal cooled nuclear facility.

Although in the last few years significant efforts and progress have been made in the field of heavy liquid metal cooled nuclear applications, it is clear that a huge amount of work still needs to be done to be able to fully understand and/or predict the relevant material degradation phenomena under irradiation in contact with heavy liquid metal coolants.

In this frame, we would like to distinguish between future work which can be realised with a minimum of effort in the near future, which would significantly improve the current data and understanding and future work which will need significant investment in both time and money and needs to be seen in the longer term.

9.1 SHORT TERM COMPLEMENTARY R&D

The first steps have been taken in the quantitative analysis of the embrittling effect of LBE on T91 and 316L as discussed in Chapters 3 and 5. However, these methods should be complemented by finite element modelling, the test facilities themselves need to be optimized to allow fracture toughness testing under controlled oxygen conditions and furthermore the materials database needs to be significantly expanded to increase the reliability of the quantitative results.
Since there are already DCT specimens irradiated in contact with LBE in the TWIN ASTIR irradiation, the optimized test procedure will need to be expanded to active testing in cell 12.

As mentioned in Chapter 7, the one-on-one parameterisation was lost due to the unexpected increase in the irradiation temperature. To resolve this issue a new 0 dpa capsule should be fabricated, filled with the identical materials in the same stacking order and be thermally exposed to the actual temperature profile of the TWIN ASTIR experiment. In fact, it would be beneficial to make a 0 dpa version of all capsules in the TWIN ASTIR irradiation to distinguish the thermal corrosion effects from the irradiation effects. Furthermore, a reference irradiation should be performed at 450-500°C in an "inert" environment (water or gas) to allow distinction between the effects of LBE corrosion under irradiation and the bulk irradiation effects.

Since the initial question of the TWIN ASTIR experiment (whether irradiation hardening would increase the structural material's susceptibility to LME) is still unresolved due to a complete lack of data on material irradiated in contact with LBE at temperatures between 200 and 350°C, it is clear that an irradiation campaign in contact with LBE at low temperature is of the utmost importance. Since the LME effect is expected to be maximum between 200 and 350°C and the corrosion increases with increasing temperature, the most interesting temperature to perform this irradiation in contact with LBE would still be 350°C.

Furthermore, to optimise the understanding of the produced data, it is of great importance to be able to examine fracture surfaces and liquid-solid interfaces of material irradiated in contact with liquid LBE. For this purpose the licensing efforts must be continued to allow the expansion of research possibilities in the field of liquid metal cooled nuclear facilities. SEM examination of the fracture surfaces of tensile tests discussed in Chapter 7 could reveal a treasure of information for a minimum of work load as soon as the licensing authorities agree to use the SEM. Examination of solid metal – liquid metal interfaces of specimens irradiated in

contact with LBE could give information on fracture initiation and corrosion. Therefore we strongly suggest to push licensing and experimental experience forward step by step and to optimally investigate the available material.

The results discussed in Chapter 7 were on the irradiated material from the low dose capsule A of TWIN ASTIR. The remaining five capsules were irradiated up to 2.5 dpa and have already been removed from the reactor at the time of writing this PhD and are in the process of cooling down by natural decay. It is clear that this material, irradiated under the same conditions as the low dose capsule, should be tested and compared to the results discussed in Chapter 7.

9.2 SUGGESTIONS FOR FUTURE FUNDAMENTAL AND ENGINEERING R&D

Fracture mechanics examinations will need to be further elaborated and mechanical testing in liquid metal environment will need to be standardised.

Apart from the irradiation at 350°C (which was mentioned in the previous section since it was in fact the initial goal of the TWIN ASTIR) a few other irradiation programmes in contact with heavy liquid metals need to be mentioned in the frame of future research. Although some of these irradiation experiments are already planned, they need all the work from design to PIE to be performed and can hardly be mentioned under short term R&D.
In first instance the irradiation experiments will remain to be in stagnant LBE conditions but up to higher dpa. Irradiations are foreseen in BR2 at 450°C under the name SPEED ASTIR up to 3.5 dpa and discussions are ongoing to extend the programme up to about 8 dpa. Furthermore, irradiations in contact with stagnant LBE are planned at NRG, The Netherlands at 300 and 550°C up to about 1.25 dpa.
In addition to the irradiations in LBE, SCK•CEN has planned an irradiation in pure lead in the Russian BOR60 sodium cooled fast reactor at 450 and 550°C up to 8 and 16 dpa.

Keeping in mind that the intended goal for the structural materials of an LFR or ADS are envisaged to reach 100-150 dpa, the extrapolation margins are still rather large. Furthermore, the production of hydrogen and helium might prove to worsen the embrittlement problem and prevent embrittlement saturation should be examined more in the future as well.

Apart from examining high dpa materials in terms of microstructure and high dpa material behaviour in contact with LBE, it will eventually be needed to examine all influential parameters together under conditions as close to the design conditions as possible. This will require in-pile heavy liquid metal loops placed into material test reactors and being subjected to a neutron spectrum which is as close to the spectrum of the final LFR or ADS as possible. This type of loop would enable material testing under flowing conditions under irradiation and eventually full component testing.

In the more fundamental field plenty of work is to be done as well.
Surface energy measurements will be needed. The experimental research on LME should be continued using model alloys and single crystals to examine the precise influence of alloying elements such as silicon and chromium and to examine the influence of crystallographic orientation on the occurrence of LME. In situ LME testing under microscopic examination of the crack tip should be further pursued. Furthermore, the phenomenon of LME will need multi-scale modelling to either prove our theories to be right or to prove us wrong.

REFERENCES

[1] Grübler, M. Jefferson, M. Makarova, A. McDonald, S. Messner, N. Nakicenovic, H.-H. Rogner, L. Schrattenholzer, M. Strubegger, "Global Energy Perspectives", Cambridge University Press (1998).

[2] E.O. Adamov, V.V. Orlov In: "Heavy Liquid Metal Coolants in Nuclear Technology", Edited by B.F. Gromov, State Scientific Center of Russian Federation Institute for Physics and Power Engineering, Obninsk, 1 (1999) 24-31.

[3] W. D'haeseleer, P. Klees, J. Albrecht, J. De Ruyck; P. Tonon, J.-M. Streydio, R. Belmans, L. Dufresne, B. Leduc, S. Proost, J.-P. van Ypersele, J.-M. Chevalier, W. Eichhammer, P. Terzian, "Belgium's Energy Challenges Towards 2030", Final Report of the Commission Energy 2030 (2007).

[4] A Technology Roadmap for Generation IV Nuclear Energy Systems, Issued by the U.S. DOE Nuclear Energy Research Advisory Committee and the Generation IV International Forum, http://www.ne.doe.gov/genIV/documents/gen_iv_roadmap.pdf (2002).

[5] T.R. Allen and D.C. Crawford, "Review article: Lead Cooled Fast Reactor Systems and the Fuels and Materials Challenges", Sci. and Tech. of Nucl. Inst. (2007) doi:10.1155/2007/97486.

[6] K. Tucek, J. Carlsson, H. Wider, "Comparison of Sodium and Lead Cooled Fast Reactors Regarding Reactor Physics Aspects, Severe Safety and Economical Issues", Nucl. Eng. Des. 236 (2006) 1589-1598.

[7] OECD/NEA Handbook of Pb-Bi Eutectic Alloy and Pb Properties, Materials Compatibility, Thermal Hydraulics and Technologies (2007)

[8] S. Andriamonje, A. Angelopoulos, A. Apostolakis, F. Attale, L. Brillard, S. Buono, J. Calero, F. Carminati, F. Casagrande and P. Cennini, S. Charalambous, R. Del Moral, C. Eleftheriadis, E. Gallego, J. Galvez, L. Garcia-Tabares, C. Geles, I. Goulas, A. Giorni, E. Gonzalez, M. Hussonnois, J. Jaren, R. Klapisch, P. Kokkas, F. Lemeilleur, G. Lindecker, A. Liolios, J.M. Loiseaux, C. Lopez, A. Lorente, M. Macri, J.M. Martinez-Val, H. Nifenecker, J. Oropesa, P. Pavlopoulos,

J.A. Pinston, J.-P. Revol, C. Roche, C. Rubbia, J.A. Rubio, K. Sakelariou, L. Sakelliou, F. Saldana, F. Schussler, J. Tamarit, D. Trubert, J.B. Viano, S. Vieira, S. Vlachos, X. Li, G. Zarris, " Experimental determination of the energy generated in nuclear cascades by a high energy beam", Phys. Letters B 348(3-4) (1995) 697-709.

[9] D. Maes, "Design of the small scale experimental ADS: MYRRHA", 12th International Conference on Emerging Nuclear Energy Systems (ICENES'05), Brussels, Belgium, August 21-26 (2005).

[10] D. Maisonnier, I. Cook, P. Sardain, R. Andreani, L. Di Pace, R. Forrest, L. Giancarli, S. Hermsmeyer, P. Norajitra, N. Taylor, D. Ward, "A Conceptual Study of Commercial Fusion Power Plants" Final Report of the European Fusion, Power Plant Conceptual Study (PPCS), EFDA-RP-RE-5.0, September 15th (2004) pp. 8-12.

[11] J. Zhang, N. Li, "Review of studies on fundamental issues in LBE corrosion", J. Nucl. Mater. 373, 1-3 (2008) 351-377.

[12] J.R. Weeks, "Mechanisms of Liquid Metal Corrosion", 4th NASA-AEC Liquid Metal Corrosion Meeting (1963)

[13] P.F. Tortorelli, O.K. Chopra, "Corrosion and compatibility considerations of liquid metals for fusion reactor applications", J. Nucl. Mater. 103 (1981) 621-632.

[14] M.H. Kamdar, "Embrittlement by Liquid Metals", Prog. Mater. Sci. 15 (1973) 289-373.

[15] N.S. Stoloff, In: Embrittlement by Liquid and Solid Metals. M.H. Kamdar, (1982) 3-26.

[16] P.J.L. Fernandes, D.R.H. Jones, "Mechanisms of Liquid metal induced embrittlement", Int. Mater. Rev. 42 (1997) 251-261.

[17] B. Joseph, M. Picat, F. Barbier, "Liquid metal embrittlement: A state-of-the-art appraisal", Eur. Phys. J.: Appl. Phys. 5 (1999) 19-31.

[18] A.R.C. Westwood, C.M. Preece, M.H. Kamdar, In: Adsorption Induced Brittle Fracture in Liquid Environments, 3, Academic Press, 1971, 589.

[19] V.V. Popovich, I.G. Dmukhovskaya, Sov. Mater. Sci. 365 (1978).

[20] W. Rostoker, J.M. McCaughey, H. Markus, "Embrittlement by Liquid Metals", Reinhold Publishing Corporation, New York (1960).

[21] J. Van den Bosch, D. Sapundjiev, A. Almazouzi, "Effects of temperature and strain rate on the mechanical properties of T91 material tested in liquid lead bismuth eutectic", J. Nucl. Mater. 356 (2006) 237-246.

[22] C.F. Old, "Liquid Metal Embrittlement of Nuclear Materials", J. Nucl. Mater. 92 (1980) 2-25.

[23] M.G. Nicholas, C.F. Old, "Review Liquid metal embrittlement", J. Mat. Sci. 14 (1979) 1-18.

[24] F. Shunk, W. Warke, "Specificity as an aspect of liquid metal embrittlement", Scr. Met., 8 (1974) 519-526.

[25] P. Gordon and H. An, "The mechanism of crack initiation and crack propagation in metal induced embrittlement of metals", Met. Trans. A., 13A (1982) 457-472.

[26] E. Glickman, “Mechanism of Liquid Metal Embrittlement by Simple Experiments: From Atomistics to Life-time”, In "Multiscale Phenomena in Plasticity", J. Lepinoux, *et al.* (Eds.), Kluwer Academic Publishers, The Netherlands (2000) 383-401.

[27] E. Rabkin, "Grain boundary embrittlement by liquid metals", In: "Multiscale Phenomena in Plasticity", J. Lepinoux, *et al.* (Eds.), Kluwer Academic Publishers, The Netherlands (2000) 403-413.

[28] M.H. Kamdar, "Liquid Metal Embrittlement", In: "The metals handbook", edited by J.M. Davis, ASM, Materials Park 13 (1983) 171-184.

[29] N.S. Stoloff, R.G. Davies, T.L. Johnston, "Environment sensitive mechanical behavior", edited by A.R.C. Westwood, N.S. Stoloff, Gordon and Breach, New York (1966) 613.

[30] I.G. Dmukhovskaya and V.V. Popovich, "The influence of the adsorption of a medium on the deformation of solids", translated from Fiz.-Khim. Mekh. Mater. 4 (1976) 60-66.

[31] V.V. Popovych, "The effect of strain rate on the plasticity of steel specimens in contact with a liquid metal medium.", translated from Fiz.-Khim. Mekh. Mater, 5 (1981) 9-13.

[32] H. Nichols, W. Rostoker, "Delayed failure of a Be-Cu alloy wetted with mercury", Trans ASM 58 (1965) 155-163.

[33] P.A. Rehbinder and E.D. Shchukin, "Surface phenomena in solids during deformation and fracture processes", Progress Surface Sci. 3, 22 (1972) 97-188.

[34] J.J. Gilman, In Proc. Conf. "Plasticity: 2nd symposium on naval structural mechanics", Rhode Island, RI, USA, Pergamon Press (1960) 43-99.

[35] S.P. Lynch, "Liquid-Metal Embrittlement in an Al 6% Zn 3% Mg Alloy", Acta Met. 29 (1981) 325-340.

[36] R.W. Vook, "Environment Sensitive Fracture Behaviour", edited by A.R.C. Westwood and N.S. Stoloff), Gordon and Breach, New York (1965) 657.

[37] S.P. Lynch, "A Fractographic study of gaseous hydrogen embrittlement and liquid metal embrittlement in a tempered-martensitic steel", Acta metall. 32 1 (1984) 79-90.

[38] S.P. Lynch, "Environmentally assisted cracking: overview of evidence for an adsorption-induced localised-slip process", Acta Metall. 36 10 (1988) 2639-2661.

[39] S.P. Lynch, "Environmentally assisted cracking at high velocities", Scripta Metall. 21 (1987) 157-162.

[40] S.P. Lynch, "Metal induced Embrittlement of Materials", Materials Characterization, 28 (1992) 279-289.

[41] V.V. Popovich, "Mechanisms of liquid metal embrittlement", translated from Fiz. Khim. Mekh. Mater. 15, 5 (1979) 11-20.

[42] I.G. Dmukhovskaya and V.V. Popovich, "A phenomenological model of embrittlement of metals under conditions of the adsorption action of liquid metal media", translated from Fiz. Khim. Mekh. Mater. 18, 6 (1982) 5-13.

[43] E. Glickman, "On the role of stress, strain and diffusion in dissolution-condensation mechanism of liquid metal embrittlement", Defect and Diffusion Forum 264 (2007) 141-149.

[44] I.H Dmukhovs'ka and V.V. Popovych, "Influence of stress concentrators on the temperature dependence of the liquid metal embrittlement of Armco iron", translated from Fiz. Khim. Mekh. Mater. 29, 5 (1993) 65-72.

[45] V.V. Popovich and I.G. Dmukhovskaya, "Rebinder effect in the fracture of Armco iron in liquid metals", translated from Fiz. Khim. Mekh. Mater. 14, 4 (1978) 30-36.

[46] W.R. Warke and N.N. Breyer, "Effect of steel composition on lead embrittlement", Journal of The Iron and Steel Institute, 10 (1971) 779-784.

[47] W.R. Warke, K.L. Johnson and N.N. Breyer, "Liquid metal embrittlement of steel by lead and lead alloys", In: Corrosion by Liquid Metals, edited by J.E. Draley, J.R. Weeks, Plenum Press (1970) 417-439.

[48] N.N. Breyer and P. Gordon, "Lead induced brittle failure of high strength steels", Illinois Institute of Technology, in: Microstruct. and. Design Alloys, Proc. Third Int. Conf. Strength Metals and Alloys, Cambridge, 1 (1973) 493-497.

[49] R.D. Zipp, W.R. Warke and N.N. Breyer, "A Comparison of Elevated Temperature Tensile Fractures in Nonleaded and Leaded 4145 Steel", ASTM STP 453, Electron Microfractography (1969) 111-133.

[50] P. Protsenko, A. Terlain, M. Jeymond, N. Eustathopoulos, "Wetting of Fe-7.5%Cr steel by molten Pb and Pb-17Li", J. Nucl. Mater. 307-311 (2002) 1396-1399.

[51] C. Fazio, I. Ricapito, G. Scaddozzo, G. Benamati, "Corrosion behaviour of steels and refractory metals and tensile features of steels exposed to flowing PbBi in the LECOR loop", J. Nucl. Mater. 318 (2003) 325-332.

[52] D. Kalkhof, M. Grosse, "Influence of PbBi environment on the low-cycle fatigue behavior of SNS target container materials", J. Nucl. Mater. 318 (2003) 143-150.

[53] F. Di Gabriele, A. Doubková, A. Hojná, "Investigation of the sensitivity to EAC of steel T91 in contact with liquid LBE", J. Nucl. Mater. 376, 3 (2008) 307-311.

[54] S. Guerin, J.-L. Pastol, C. Leroux, D. Gorse, "Synergy effect of LBE and hydrogenated helium on resistance to LME of T91 steel grade", J. Nucl. Mater. 318 (2003) 339-347.

[55] T. Auger, G. Lorang, S. Guérin, J.-L. Pastol, D. Gorse, "Effect of contact conditions on embrittlement of T91 steel by lead-bismuth", J. Nucl. Mater. 335 (2004) 227-231.

[56] T. Auger, G. Lorang, "Liquid metal embrittlement susceptibility of T91 steel by lead-bismuth", Scr. Mat. 52 (2005) 1323-1328.

[57] Y. Dai, B. Long, F. Gröschel, "Slow strain rate tensile tests on T91 in static lead-bismuth eutectic", 356, 1-3 (2006) 222-228.

[58] B. Long, Z. Tong, F. Gröschel, Y. Dai, "Liquid Pb-Bi embrittlement effects on the T91 steel after different heat treatments, J. Nucl. Mater. 377, 1 (2008) 219-224.

[59] H. Glasbrenner, F. Gröschel, "Bending tests on T91 steel in Pb-Bi eutectic, Bi and Pb-Li eutectic", J. Nucl. Mater. 335 (2004) 239-243.

[60] I. Serre, J.-B. Vogt, "Liquid metal embrittlement of T91 martensitic steel evidenced by small punch test", Nucl. Eng. Des. 237 (2007) 677-685.

[61] J.-B. Vogt, A. Verleene, I. Serre, F. Balbaud-Célérier, L. Martinelli, A. Terlain, "Understanding the liquid metal assisted damage sources in the T91 martensitic steel for safer use of ADS", Eng. Fail. Anal. 14 (2007) 1185-1193.

[62] A. Weisenburger, A. Heinzel, C. Fazio, G. Müller, V.G. Markow, A.D. Kastanov, "Low cycle fatigue tests of surface modified T91 steel in

10^{-6} wt% oxygen containing $Pb_{45}Bi_{55}$ at 550 °C", J. Nucl. Mater. 377, 1 (2008) 261-267.

[63] T. Auger, Z. Hamouche, L. Medina-Almazàn, D. Gorse, "Liquid Metal Embrittlement of T91 and 316L steels by heavy liquid metals: a fracture mechanics assessment", J. Nucl. Mater. 377, 1 (2008) 253-260.

[64] B. Long, Y. Dai, "Investigation of LBE embrittlement effects on the fracture properties of T91", J. Nucl. Mater. 376, 3 (2008) 341-345.

[65] S. Zinkle, J. Singh, "Analysis of displacement damage and defect production under cascade damage conditions", J. Nucl Mater. 199 (1993) 173-191.

[66] S.J. Zinkle, P.J. Maziasz and R.E. Stoller, "Dose dependence of the microstructural evolution in neutron-irradiated austenitic stainless steel", J. Nucl. Mater. 206 (1993) 266-286.

[67] S. Takaki, J. Fuss, H. Kugler, U. Dedek and H. Schultz, "The resistivity recovery of high purity and carbon doped iron following low temperature electron irradiation", Radiation Effects, 79 (1983) 87-123.

[68] T. Yamamoto, G.R. Odette, H. Kishimoto, J.-W. Rensman, P. Miao, "On the effects of irradiation and helium on the yield stress changes and hardening and non-hardening embrittlement of ~8% Cr Tempered martensitic steels: Compilation and analysis of existing data", J. Nucl. Mater. 356 (2006) 27-49.

[69] Y. de Carlan, X. Averty,J.-C. Brachet, J.-L. Bertin, F. Rozenblum, O. Rabouille, A. Bougault, "Post-Irradiation Tensile Behavior and Residual Activity of Several Ferritic/Martensitic and Austenitic Steels Irradiated in Osiris Reactor at 325°C up to 9 dpa", J. ASTM Int. 2, 8 (2005) 1-19.

[70] P.J. Maziasz, "Temperature dependence of the dislocation microstructure of PCA austenitic stainless steel irradiated in ORR spectrally-tailored experiments", J. Nucl. Mater. 191-194, 2 (1992) 701-705.

[71] F.A. Garner, M.B. Toloczko, B.H. Sencer, "Comparison of swelling and irradiation creep behavior of fcc-austenitic and bcc-ferritic/martensitic alloys at high neutron exposure", J. Nucl. Mater. 276 (2000) 123-142.

[72] D. Sapundjiev, A. Al Mazouzi, S. Van Dyck, "A study of the neutron irradiation effects on the susceptibility to embrittlement of A316L and T91 steels in lead-bismuth eutectic", J. Nucl. Mater. 356 (2006) 229-236.

[73] Y. Dai, H. Glasbrenner, V. Boutelier, R. Bruetsch, X. Jia, F. Groeschel, "Preliminary results of post-irradiation examinations on LiSoR-2 test section", J. Nucl. Mater. 335 (2004) 232-238.

[74] Y. Dai, B. Long, X. Jia, H. Glasbrenner, K. Samec, F. Groeschel, "Tensile tests and TEM investigations on LiSoR-2 to -4", J. Nucl. Mater. 356 (2006) 256-263.

[75] H. Glasbrenner, R. Brütsch, F. Gröschel, "Experience with irradiation of LiSoR test section no. 3", Nucl. Eng. Des. 236 (2006) 2494-2500.

[76] H. Glasbrenner, R. Brütsch, Y. Dai, F. Gröschel, M. Martin, "Post-irradiation examination on LiSoR 3 experiment", J. Nucl. Mater. 356 (2006) 247-255.

[77] H. Glasbrenner, F. Gröschel, "Liquid metal compatibility under irradiation: The LiSoR 5 experiment", J. Nucl. Mater. 367-370 (2007) 1590-1595.

[78] Y. Dai, D. Gavillet, R. Restani, "Stressed capsules of austenitic and martensitic steels irradiated in SINQ Target-4 in contact with liquid lead-bismuth eutectic", J. Nucl. Mater. 377 (2008) 225-231.

[79] P. Hosemann, R.R. Greco, I. Usov, Y. Wang, S.A. Maloy, N. Li, "The design, setup and operational testing of the irradiation and corrosion experiment (ICE)", J. Nucl. Mater. 376 (2008) 392-395.

[80] A. L. Johnson, E. P. Loewen, T. T. Ho, D. Koury, B. Hosterman, U. Younas, J. Welch, J. W. Farley, "Spectroscopic and microscopic study of the corrosion of iron silicon steel by lead–bismuth eutectic (LBE) at elevated temperatures", J. Nucl. Mater. 350 (2006) 221-231.

[81] T.R. Allen, D.C. Crawford, "Review article: Lead cooled fast reactor systems and the fuels and materials challenges", Sci. Tech. Nucl. Inst. (2007) doi:10.1155/2007/97486.

[82] Y. Kurata, M. Futakawa, "Excellent corrosion resistance of 18Cr-20Ni-5Si steel in liquid PbBi", J. Nucl. Mater. 325 (2004) 217-222.

[83] F. Barbier, G. Benamati, C. Fazio, A. Rusanov, "Compatibility tests of steels in flowing liquid lead-bismuth", J. Nucl. Mater. 295 (2001) 149-156.

[84] R.W.K. Honeycombe and P. Hancock, "Steels" in Metallurgy and Material Science Series, Edward Arnold publication (1981).

[85] R.L. Klueh and D.R. Harries, "High-Chromium Ferritic and Martensitic Steels for Nuclear Application", Library of Congress Cataloging in publication data by American Society of Testing and Materials (ASTM) (2001).

[86] F.A. Garner, M.B. Toloczko, B.H. Sencer, "Comparison of swelling and irradiation creep behaviour of fcc-austenitic and bcc-ferritic/martensitic alloys at high neutron exposure", J. Nucl. Mater. 273 (2000) 123-142.

[87] D. Sapundjiev, S. Van Dijck, W. Bogaerts, "Liquid Metal Corrosion of T91 and A316L in Pb-Bi eutectic at temperatures 400-600°C", Corrosion Science, 48, 3 (2006) 577-594.

[88] E. Lucon, "Mechanical Properties of the European Reference RAFM Steel (EUROFER97) before and after Irradiation at 300°C (0.3-2dpa)", (2003) BLG-962.

[89] E. Lucon, A. Almazouzi, "Mechanical Response to Irradiation at 200°C for EM10, T91 and HT9 Steels – Final Report: Specimens Irradiated to 2.6 and 3.9 dpa", (2004) BLG-986.

[90] R. Chaouadi and A. Fabry, " On the utilization of the instrumented charpy impact test for characterizing the flow and fracture behavior of reactor pressure vessel steels", In "From charpy to present impact testing", eds, D.François and A.Pineau, France, (2002) 103-105.

[91] T. Sourmail, C. Garcia-Mateo, "Critical assessment of models for predicting the M_s temperature of steels", Comp. Mat. Sci. 34, 2 (2005) 213-218.

[92] X.Q. Li, W. Van Renterghem, A. Almazouzi, "Stacking fault energy determination – Theory and Experimental Procedure", Restricted SCK•CEN Report, R-4331, (2007).

[93] K. Coleman, D. Gandy, "Guideline for welding P(T) 91", document 1006590, EPRI, 1300 W.T. Harris Blvd., Charlotte, NC 28262, USA, (2002).

[94] M.L. Santella, R.W. Swindeman, R.W. Reed and J.M. Tanzoch, "Martensite transformation, microsegregation, and creep strength of 9 Cr-1Mo-V steel weld metal", paper presented at the EPRI Conference on 9Cr Materials Fabrication and Joining Technologies, July 10-11, Myrtle Beach, South Carolina, USA, (2001).

[95] H. Okamura, R. Ohtani, K. Saito, K. Kimura, R. Ishii, K. Fujiyama, S. Hongo, T. Iseki, H. Uchida, "Basic investigation for life assessment technology of modified 9Cr-1Mo steel", Nucl. Eng. & Design, 193 (1999) 243-254.

[96] K. Haarmann, J.C. Vaillant, W. Bendick, A. Arbab, "The T91/P91 Book", Vallourec & Mannesmann Tubes, (1999).

[97] E. Ayala, M.A. Roman, J. Vega, X. Gomez, T. Gomez-Acebo and J. Echeberria, "Delta Ferrite Formation in 9-12% Chromium Steel Weldments, Advanced Heat Resistant Steels for Power Generation, San Sebastián (1998) 633-643.

[98] L. Yajiang, W. Juan, Z. Bing and F. Tao, "XRD and TEM analysis of microstructure in the welding zone of 9Cr-1Mo-V-Nb heat-resisting steel", Bull. Mater. Sci., 25 (2002) 213-217.

[99] X. Jia, Y. Dai, "Micro-hardness measurement and micro-structure characterization of T91 weld metal irradiated in SINQ Target-3", J. Nucl. Mater., 343 (2005) 212-218.

[100] Y. Li, B. Zhou, T. Feng and J. REN, "Microstructure and Fracture Morphology in the Welding Zone of T91 Heat-resisting Steel Used in Power Station", J. Mater. Sci. Technol., 18 (2002) 427-430.

[101] S. Spigarelli, E. Quadrini, "Analysis of the creep behaviour of modified P91 (9Cr-1Mo-NbV) welds", Materials & Design, 23 (2002) 547-552.

[102] C.J. Middleton, J.M. Brear, R. Munson and R. Viswanathan, "An Assessment of the Risk of Type IV Cracking in Welds to Header, Pipework and Turbine Components constructed from the Advanced Ferritic 9% and 12% Chromium Steels", In: Advances in Materials Technology for Fossil Power Plants, Proceedings of the 3rd Conference held at University of Wales Swansea, (2001) 69-78.

[103] S.R. Collins, P.C. Williams, "Weldability and Corrosion Studies of AISI 316L Electropolished Tubing", Swagelok Company, (2000).

[104] H. Nakagawa, H. Fujii and M. Tamura, "Effect of Heat Treatment on Low Temperature Toughness of Reduced Pressure Electron Beam Weld Metal of type 316L Stainless Steel", In: Advances in Cryogenic Engineering: Proceedings of the International Cryogenic Materials Conference – ICMC, 52 (2006).

[105] V. Sobolev, "Compatibility of Structure Materials of a Typical ADS with Heavy Liquid Metal Coolants: Brief review of experimental results", SCK•CEN report, R-3532 (2001).

[106] V. Sobolev, "Myrrha ADS database: Part I. Thermophysical properties of molten lead-bismuth eutectic, Version I", SCK•CEN report, BLG-1014 (2005).

[107] J. Van den Bosch, R.W. Bosch, D. Sapundjiev, A. Almazouzi, " Liquid Metal Embrittlement Susceptibility of Ferritic-martensitic Steel in Liquid Lead Alloys", J. Nucl. Mater., 376, 3 (2008) 322-329.

[108] D. Sapundjiev, "Compatibility of structural materials with liquid lead-bismuth eutectic", PhD thesis from KULeuven, ISBN 978-90-5682-759-5, (2007).

[109] Ph. Antoine, F. Joppen, M. Van Haesendonck, "Uitbatingsvergunning cel 12 - βγ materiaal", IDPBW/FC/Pan/M060668/F160, 27/11/2006.

[110] Ph. Antoine, F. Hardeman, M. Van Haesendonck, "Uitbatingsvergunning cel 12 – werk met α-materiaal", IDPBW/PAN/PAN/2008/305/F73, 21/04/2008.

[111] L. Eysermans, "Bedrijfshandboek voor het gebruik van de installatie LIMETS 2", Internal Technical SCK•CEN Note (2007).

[112] B.F. Gromov, G.I. Toshinsky, V.V. Checkunov, Yu.I. Orlov, Yu.S. Belomytsev, I.N. Gorelov, A.G. Karabash, M.P. Leonchuk, D.V. Pankratov, Yu.G. Pashkin, "Designing the Reactor Installation with Lead-Bismuth Coolant for Nuclear Submarines. The brief history, summarized operation results", In Proceedings of the conference on Heavy Liquid Metal Coolants in Nuclear Technology", Obninsk: SCC RF-IPPE, 1 (1999) 14-17.

[113] D.V. Pankratov, E.I. Yefimov, V.N. Bolkhovitinov, V.D. Kuranov, M.I. Bugreev, "Polonium Problem in Nuclear Power Plants with Lead Bismuth as a Coolant", In Proceedings of the conference on Heavy Liquid Metal Coolants in Nuclear Technology", Obninsk:SCC RF-IPPE, 1 (1999) 101.

[114] F. Vermeersch, "Evaluatie van de radiologische gevolgen van de release van een hoeveelheid Po-210 in het kader van het ASTIR project op BR2", Technical Note NS/Fve/IDPBW/05-041 (2005).

[115] Ch. Perret, "MEGAPIE Preliminary safety assessment report", FIKW-CT-2001-00159, D11 (2004).

[116] H. Dekien, "Ontwerp van een ontmantelingsinstallatie voor bestraalde capsules in een hotcel", Afstudeerwerk Hogeschool West-Vlaanderen (2005).

[117] V. Sobolev, F. Vermeersh, Th. Aoust, "Activation of LBE Polonium release in the TECLA Capsule, SCK•CEN internal report IR0016 (2002).

[118] R.-W. Bosch, "Polonium handling in hot cell 12", SCK•CEN internal scientific note, NMS/RWB/01 (2007).

[119] S. Katseva, "MCNP Neutronics Calculations of TWIN ASTIR, BR2-SCU/SK/B044434/twin_astir2/14/10/05, Technical note, SCK•CEN (2005).

[120] J. Neuhausen, Y. Köster, B. Eichler, "Investigation of evaporation characteristics of polonium and its lighter homoloques selenium and tellurium from liquid Pb-Bi-eutecticum", Radiochim. Acta 92 (2004) 917.

[121] M. Matijasevic, E. Lucon, A. Almazouzi, " Behavior of ferritic/martensitic steels after n-irradiation at 200 and 300 °C", J. Nucl. Mater. 377, 1 (2008) 101-108.

[122] J. Van den Bosch, A. Almazouzi, Ph. Benoit, R.W. Bosch, W. Claes, B. Smolders, P. Schuurmans, H. Aït Abderrahim, "TWIN ASTIR: an irradiation experiment in liquid PbBi eutectic environment", J. Nucl. Mater., 377 (2008) 206-212.

[123] A. Zucchini, P. Agostini, E. Baicchi, "Lead-bismuth recrystallization studies for the MEGAPIE target", J. Nucl. Mater., 336 (2005) 291-298.

[124] P. Agostini, E. Baicchi, A. Zucchini, G. Benamati, "The re-crystallization issue in lead-bismuth technology", J. Nucl. Mater., 335 (2004) 275.

[125] C. Foletti, G. Scaddozzo, M. Tarantino, A. Gessi, G. Bertacci, P. Agostini and G. Benamati, "ENEA experience in LBE technology", J. Nucl. Mater., 356 (2006) 264-272.

[126] J. Buongiorno, C. Larson and K.R. Czerwinski, Speciation of polonium released from molten lead bismuth", Radiochim. Acta, 91 (2003) 153-158.

[127] E. Loewen, "Investigation of polonium removal systems for lead-bismuth cooled fbrs", Innovative Nuclear Energy Systems for Sustainable Development of the World, 47 (2005) 586-595.

[128] T. Obara, T. Miura, H. Sekimoto, "Fundamental study of polonium contamination by neutron irradiated lead–bismuth eutectic", J. Nucl. Mater., 343 (2005) 297-301.

[129] V.I. Levanov, D.V. Pankratov, E.I. Yefimov, "The Estimation of Radiation Danger of Gaseous and Volatile Radionuclides in Accelerator Driven System with Pb-Bi Coolant", In Proceedings of the Third International Conference on Accelerator Driven Transmutation Technologies and Applications, Prague, Czech Republic, June (1999).

[130] M. Haïssinsky, In: "Nouveau traité de chimie minerale, t.13 : oxygene - ozone - oxydes - eau oxygene - la combustion - soufre - selenium - tellure – polonium", Masson (1960) 2041-2046.

[131] F. Vermeersch, SCK•CEN intern report NS/Fve/IDPBW/05-041 (2005).

[132] J.B.J. Hegeman, J. Rensman, Window Materials for ADS, NRG deliverable 16 part 1: Contract no. FIKW-CT-2000-00058.

[133] E. Lucon, A. Almazouzi, Scientific Report SCK•CEN-BLG-973, (2004).

[134] Y. de Carlan, S. Urvoy, Y. Tournie, P. Wident, Technical document DMN/SRMA/LA2M/NT/2004-2581/A

[135] M. Matijasevic, D.E.A. Métallurgie et Matériaux-Rapport de Stage, Institut National des Sciences et Techniques Nucléaires de Paris, Soutenance: 23/06/2003.

[136] Y. Dai, X. Jia, R. Thermer and F. Groeschel, FP5 Euratom Framework Programme, 1998-2002, Deliverable no 47, Month 48, Contract no. FIKW-CT-2000-00058.

[137] C. Fazio, F. Gröschel, W. Wagner, K. Thomsen, B.L. Smith, R. Stieglitz, L. Zanini, A. Guertin, A. Cadiou, J. Henry, P. Agostini, Y. Dai,

H. Heyck, S. Dementjev, S. Panebianco, A. Almazouzi, J. Eikenberg, A. Letourneau, J.C. Toussaint, A. Janett, Ch. Perret, S. Joray, J. Patorski, W. Leung, P. Meloni, P. Turroni, A. Zucchini, G. Benamati, J. Konys, T. Auger, A. Gessi, D. Gorse, I. Serre, A. Terlain, J.-B. Vogt, A. Batta, A. Class, X. Cheng, F. Fellmoser, M. Daubner, S. Gnieser, G. Grötzbach, R. Milenkovic, C. Latgé, J.U. Knebel, "The MEGAPIE-TEST project: Supporting research and lessons learned in first-of-a-kind spallation target technology", Nucl. Eng. Des. 238, 6 (2008) 1471-1495.

[138] R. Chaouadi, "An Energy-based Crack Extension Formulation for Crack Resistance Characterization of Ductile Materials." J. Test. Eval. 32, 6 (2004) 469-475.

[139] J.R. Donoso, J. Zahr, J.D. Landes, "Construction of J-R Curves Using the Common and Concise Formats", J. ASTM Int. 2, 3 (2005) 1-17.

[140] J.R. Donoso, J.D. Landes, "Common Format for Developing Calibration Curves in Elastic-Plastic Fracture Mechanics", Eng. Fract. Mech. 47, 5 (1994) 619-628.

[141] J.R. Donoso, J.D. Landes, "The role of constraint on the calibration functions for the prediction of ductile fracture in structural components", Int. J. Fract. 63 (1993) 275-285.

[142] J.R. Donoso, J.D. Landes, "A unifying principle for evaluating fracture toughness in the elastic and plastic regimes with planar fracture specimens", Fatigue and Fracture Mechanics, 30 (2002) 34-50.

[143] E. Lucon, M. Scibetta, E. van Walle, "Applying the Normalization Technique for Measuring the Upper Shelf Toughness Properties of RPV Steels", SCK•CEN report, BLG-915 (2002)

[144] D. Maugis, "Review: Subcritical crack growth, surface energy, fracture toughness, stick-slip and embrittlement", J. Mater. Sci. 20 (1985) 3041-3073.

[145] D. Chatain, "Role of the solid/liquid interface faceting in rapid penetration of a liquid phase along grain boundaries", Acta Mat. 49, 7 (2001) 1123-1128.

[146] D. Maes, S. Van Dyck, A. Al Mazouzi, D. Lamberts, "XT-ADS Primary system Operating temperature", Version 2.1.0, Internal SCK•CEN technical note ANS-DM/dm.3930.B044122/825/07-24.

[147] AAA Materials Handbook, "Materials Data for Particle Accelerator Applications", revision 3 (2006).

[148] N. Marie, K. Wolski and M. Biscondi, "Intergranular penetration and embrittlement of solid nickel through bismuth vapour condensation at 700°C", J. Nucl. Mater. 296, 1-3 (2001) 282-288.

[149] G.E. Dieter, "Mechanical Metallurgy", McGraw-Hill series in Materials Science and Engineering, ISBN 0-07-016893-8 (1986)

[150] J. Van den Bosch, G. Coen, A. Almazouzi, J. Degrieck, "Fracture toughness assessment of ferritic-martensitic steel in liquid lead-bismuth eutectic.", accepted for publication in J. Nucl. Mater. (2009).

[151] G. Benamati, A. Gessi, G. Scaddozzo, "Corrosion behaviour of steels and refractory metals in flowing Lead-Bismuth Eutectic at low oxygen activity", J. Mater. Sci. 40, 9-10 (2005) 2465-2470.

[152] A. Legris, G. Nicaise, J.-B. Vogt, J. Foct, "Liquid metal embrittlement of the martensitic steel 91: influence of the chemical composition of the liquid metal. Experiments and electronic structure calculations", J. Nucl. Mater. 301 (2002) 70-76.

BIOGRAPHY

Joris Van den Bosch was born in Aarschot, Belgium on 21 November 1980.
In 2004, he obtained his Master in Civil Engineering, Metallurgy and Materials Science from the university of Ghent, Belgium with a thesis on "Archeometallurgic study of metal slags from the Roman era, Excavated in Flandres".
Since 2004, he has worked at SCK•CEN, Belgium in the Institute for Nuclear Materials Science (NMS) on this PhD thesis.

LIST OF PUBLICATIONS

Journal papers

1. J. Van den Bosch, K. Verbeken, D. Vanderschueren and B.C. De Cooman, "Hot band transverse temperature profiles analysis", Steel Grips, 3, 5 (2005) 370-374.
2. J. Van den Bosch, D. Sapundjiev, A. Almazouzi, "Effects of temperature and strain rate on the mechanical properties of T91 material tested in liquid lead bismuth eutectic", J. Nucl. Mat. 356 (2006) 237-246.
3. J. Van den Bosch, A. Almazouzi, Ph. Benoit, R.W. Bosch, W. Claes, B. Smolders, P. Schuurmans, H. Aït Abderrahim, "TWIN ASTIR: An irradiation experiment in liquid Pb-Bi eutectic environment", J. Nucl. Mat., 377 (2008) 206-212.
4. J. Van den Bosch, R.W. Bosch, D. Sapundjiev, A. Almazouzi, "Liquid metal embrittlement susceptibility of ferritic-martensitic steel in lead alloys", J. Nucl. Mat., 376, 3 (2008) 322-329.
5. J. Van den Bosch, G. Coen, A. Almazouzi, J. Degrieck, " Fracture toughness assessment of ferritic-martensitic steel in liquid lead-bismuth eutectic.", Accepted for publication in J. Nucl. Mater.
6. J. Van den Bosch, A. Almazouzi, "Compatibility of T91/316L welds with liquid lead bismuth eutectic environment", Accepted for publication in J. Nucl. Mater.

SCK•CEN reports

1. J. Van den Bosch, A. Al Mazouzi, "Eurotrans-Demetra-Task 4.1.2: Reference materials procurement, dispatching and characterisation", SCK•CEN, R-4197, 2005.
2. J. Van den Bosch, A. Al Mazouzi, "Characterization of TIG and EB welds of T91 and 316L", SCK•CEN, R-4399, 2006.
3. J. Van den Bosch, Ph. Benoit, A. Al Mazouzi, R.W. Bosch, W. Claes, B. Smolders, P. Schuurmans, H. Aït Abderrahim, "Rig design, Fabrication and Assembly: Twin Astir at BR2", SCK•CEN, R-4395, 2006.
4. J. Van den Bosch, A. Al Mazouzi, "Mechanical properties after irradiation of the first batch of TWIN-ASTIR experiment", SCK•CEN, R-4695, 2008

Proceedings International Conferences

1. J. Van den Bosch, A. Al Mazouzi, J. Degrieck, "ADS candidate materials compatibility with Liquid Metal in neutron irradiation environment", In: International Youth Conference on Energetics 2007 (IYCE'07) Proceedings, Budapest, Hungary, 31 May - 2 June 2007, Budapest, Hungary, Budapest University of Technology and Economics, 2007.

Oral presentations at International Conferences/Workshops

1. Effect of temperature and strain rate on the mechanical properties of T91 material tested in liquid lead bismuth eutectic, IWSMT-7, Thun, Switzerland, May 30th – June 3rd, 2005.
2. Assessment of the Behaviour of TIG and EB Welds of T91 and 316L in LBE., IWSMT-8, Taos, New Mexico, USA, Octobre 16th – 20th, 2006.
3. TWIN ASTIR: an Irradiation Experiment in Liquid Pb-Bi Eutectic Environment, IWSMT-8, Taos, New Mexico, USA, Octobre 16th – 20th, 2006.
4. Liquid Metal Embrittlement of ferritic-martensitic steel in lead-alloys, IWSMT-8, Taos, New Mexico, USA, Octobre 16th – 20th, 2006.
5. TWIN ASTIR: an Irradiation Experiment in Liquid Pb-Bi Eutectic Environment, 4th International Workshop on Materials for heavy liquid metal cooled reactors and related technologies, Rome, Italy, May 21st – 23rd, 2007.
6. Liquid Metal Embrittlement of ferritic-martensitic steel in lead-alloys, 4th International Workshop on Materials for heavy liquid metal cooled reactors and related technologies, Rome, Italy, May 21st – 23rd, 2007.
7. ADS candidate materials compatibility with liquid metals in neutron irradiation environment, International Youth Conference on Energetics 2007 (IYCE'07), Budapest, Hungary, May 30th – June 6th, 2007.
8. Fracture toughness assessment of T91 in liquid lead-bismuth eutectic, E-MRS Spring Meeting 2008, Strasbourg, France, May 26th – May 30th, 2008.
9. Compatibility of T91/316L welds with liquid lead bismuth eutectic environment., E-MRS Spring Meeting 2008, Strasbourg, France, May 26th – May 30th, 2008.
10. Liquid metal embrittlement of silicon enriched steels for nuclear applications, International Workshop on Spallation Materials Technology 9 (IWSMT-9), Sapporo, Japan, October 19th – October 24th, 2008.
11. Twin Astir: tensile results of T91 and 316L steel after neutron irradiation in contact with liquid lead bismuth eutectic, International Workshop on

Spallation Materials Technology 9 (IWSMT-9), Sapporo, Japan, October 19th – October 24th, 2008.

12. Investigation of embrittlement effects of lead-bismuth eutectic on the fracture properties of T91 and 316L, International Workshop on Spallation Materials Technology 9 (IWSMT-9), Sapporo, Japan, October 19th – October 24th, 2008.

Poster presentations

1. ADS candidate materials compatibility with PbBi in n-irradiation environment, ISQUID (international school on quantification of irradiation damage), Rochehaut, Belgium 25th – 29th September, 2006.
2. ADS candidate materials compatibility with PbBi in n-irradiation environment, 7e FirW Doctoraatssymposium, Gent, Belgium, 29th November, 2006.
3. Limets 2: Hot-cell test set-up for Liquid Metal Embrittlement (LME) studies in liquid lead alloys, Workshop on Structural Materials for Innovative Nuclear Systems (SMINS).- Karlsruhe, Germany, 4-6 June 2007.
4. TWIN ASTIR: An Irradiation Experiment in Liquid Pb-Bi Eutectic Environment, NATO Advanced Study Institute on Materials for Generation-IV Nuclear Reactors, Cargese, Corsica, France, September 24th - October 6th, 2007.